Mesoporous ceria catalyst synthesis: effects of composition on thermal stability and oxygen depletion in methane rich and lean environments

Thomas Di Nardo

Thesis submitted to
The Faculty of Graduate and Postdoctoral Studies
In partial fulfillment of the requirements
For the M.Sc. degree in the Ottawa-Carleton Chemistry Institute

Department of Chemistry
Faculty of Science
University of Ottawa

Table of Contents

LIST OF TABLES ..... **VI**

LIST OF EQUATIONS ..... **VI**

LIST OF FIGURES ..... **VI**

LIST OF ABBREVIATIONS ..... **XVII**

ABSTRACT ..... **XIX**

NOVEL CLAIM ..... **XIX**

OBJECTIVE ..... **XIX**

ACKNOWLEDGMENT ..... **XXI**

CHAPTER 1 ..... **1**

INTRODUCTION **1**

1.1 PROJECT OVERVIEW 1

1.2 SOLID OXIDE FUEL CELLS 1

1.3 SELF-ASSEMBLY METHOD 2

1.3.1 Precursor *4*

1.3.2 Surfactants *4*

1.4 MESOPOROUS MATERIALS 5

1.5 THERMAL STABILITY 5

1.6 METHODS OF SYNTHESIS 5

1.7 FUEL PROCESSING 8

1.7.1 Fuels *8*

1.8 METHANE OXIDATION 9

1.9 METHODS OF CATALYSIS 10

1.10 SCOPE 10

CHAPTER 2 ..... **12**

EXPERIMENTAL PROCEDURE **12**

2.1 SUMMARY 12

2.2 SYNTHESIS 14

2.2.1 080610001x *14*

2.2.2 080611002x *15*

2.2.3 080618003x *15*

2.2.4 080620004x *15*

2.2.5 080620005x *15*

2.2.6 080620006x *15*

2.2.7 080704007x *15*

2.2.8 080711008x *16*

2.2.9 080711009x *16*

2.2.10 080711010x *16*

2.2.11 080711011x *16*

2.2.12 080717012x *16*

2.2.13 080717013x *17*

2.2.14 080717014x *17*

2.2.15 080717015x *17*

2.2.16 090715016x *17*

2.2.17 090715017x *17*
2.2.18 090715018x *18*
2.2.19 090715019x *18*
2.2.20 090715020x *18*
2.2.21 080611CG001 Synthesis of cerium glycolate[38] *18*
2.2.22 Sm glycolate synthesis *18*
2.2.23 Ce glycolate synth 080818CG002 ..... *19*
2.2.24 Cerium isopropoxide[42] *Ce Iso 001* *19*
2.2.25 Cerium isopropoxide Ce Iso 002 ..... *19*
2.3 MICROREACTOR PROCEDURE 20
2.3.1 Alumina tube setup *21*
2.3.2 Mass spectrometry Residual Gas Analyzer *21*
2.3.3 Range of experiments *21*
2.4 CATALYSIS PARAMETERS 21
Experiment set A *22*
2.4.1 Experiment 1 ..... *22*
Experiment set B *22*
2.4.2 Experiment 2 ..... *22*
2.4.3 Experiment 3 ..... *22*
2.4.4 Experiment 4 ..... *22*
2.4.5 Experiment 5 ..... *22*
2.4.6 Experiment 6 ..... *22*
Experiment set C *23*
2.4.7 Experiment 7 ..... *23*
2.4.8 Experiment 8 ..... *23*
Experiment set D *23*
2.4.9 Experiment 9 ..... *23*
Experiment set E *23*
2.4.12 Experiment 12 ..... *23*
Experiment set F *24*
2.4.13 Experiment 13 ..... *24*
2.4.14 Experiment 14 ..... *24*
Experiment set G *24*
2.4.15 Experiment 15 ..... *24*
2.4.16 Experiment 16 ..... *24*
2.4.17 Experiment 17 ..... *24*
Experiment set H *25*
2.4.18 Experiment 18 ..... *25*
Experiment set I *25*
2.4.19 Experiment 19 ..... *25*
2.4.20 Experiment 20 ..... *25*
2.4.21 Experiment 21 ..... *25*
2.4.22 Experiment 22 ..... *25*
Experiment set J *26*
2.4.23 Experiment 23 ..... *26*
2.4.24 Experiment 24 ..... *26*
2.4.25 Experiment 25 ..... *26*
Experiment set K *26*
2.4.26 Experiment 26 ..... *26*
2.4.27 Experiment 27 ..... *26*

CHAPTER 3 ..... **27**

CHARACTERIZATION **27**

3.1 POWDER X-RAY DIFFRACTION 27

3.1.1 Diffractogram *27*

3.1.2 Peak width and crystallite size *28*

3.2 GAS ADSORPTION – PHYSISORPTION 30

3.2.1 Isotherms *30*

3.2.2 BET Surface area *33*

3.2.3 Total pore volume and average pore radius *34*

3.2.4 Pore size distribution *35*

3.3 RGA – MASS SPECTROSCOPY 36

CHAPTER 4 ..... **38**

SYNTHESIS ANALYSIS **38**

4.1 SUMMARY 38

4.2 EXPERIMENTAL CONDITIONS IN SYNTHESIS 41

4.2.1 Precursors *41*

4.2.2 Surfactants *41*

4.2.3 Doping *42*

4.2.4 Solvent systems *42*

4.2.5 Surfactant concentration *43*

4.3 XRD DIFFRACTOGRAM ANALYSIS AND ISOTHERM INTERPRETATION 43

4.3.1 Sample 001 ..... *45*

4.3.2 Sample 002 ..... *46*

4.3.3 Sample 003 ..... *46*

4.3.4 Sample 004 ..... *47*

4.3.5 Sample 005 ..... *47*

4.3.6 Sample 006 ..... *47*

4.3.7 Sample 007 ..... *47*

4.3.8 Sample 008 ..... *48*

4.3.9 Sample 009 ..... *48*

4.3.10 Sample 010 ..... *48*

4.3.11 Sample 011 ..... *48*

4.3.12 Sample 012 ..... *49*

4.3.13 Sample 013 ..... *49*

4.3.14 Sample 014 ..... *49*

4.3.15 Sample 015 ..... *49*

4.3.16 Sample 016 ..... *49*

4.3.17 Sample 017 ..... *51*

4.3.18 Sample 018 ..... *53*

4.3.19 Sample 019 ..... *55*

4.3.20 Sample 020 ..... *55*

4.4 SEM 55

4.5 TEM 56

4.6 CONCLUSION 57

CHAPTER 5 ..... **60**

CATALYSIS **60**

5.1 SUMMARY 60

5.2 CATALYSIS 61
Experiment set A *61*
5.2.1 Test run 006C4 ..... *61*
Experiment set B *62*
5.2.2 Catalysis 007C6 ..... *62*
Experiment set C *66*
5.2.3 Catalysis 006C4 fuel rich and fuel lean *66*
Experiment set D *67*
5.2.4 Catalysis 015C4 ..... *67*
Experiment set E *68*
5.2.5 Catalysis 006C4 Fuel rich doubling the mass flow of reactants *68*
Experiment set F *70*
5.2.6 Bubble tests *70*
Experiment set G *73*
5.2.7 Catalysis 006C4 Mass flow of reactants further increased *73*
Experiment set H *76*
5.2.8 Blank *76*
Experiment set I *77*
5.2.9 further investigation into oxygen depletion *77*
Experiment set J *81*
5.2.10 Catalysis 017C4 new oxygen methane ratio discovery and pursuit *81*
5.2.11 Catalysis 017C4 fuel lean *83*
Experiment set K *84*
5.2.12 Catalysis 017C6 fuel lean *84*
5.3 CONCLUSION 86

CHAPTER 6 ..... **91**

CONCLUSION **91**
6.1 SYNTHESIS 91
6.2 CATALYSIS 92

REFERENCES **94**

APPENDICES **96**
APPENDIX A 96
Powder x-ray diffractograms *96*
APPENDICES B 124
Isotherms and pore size distribution *124*

List of tables

Table 1 Catalyst synthesis components identifying the variations between the different samples detailing finalization (A- as synthesized, C4 – calcinated at 673K, and C6 – calcinated 873K), precursor, surfactant, solvent system and base.....13
Table 2 Catalyst synthesis components identifying the variations between the different samples detailing finalization (A- as synthesized, C4 – calcinated at 673K, and C6 – calcinated 873K), precursor, surfactant, solvent system and base. (same as table 1).....39
Table 3 Catalyst synthesis components characterization data between different samples detailing finalization (A- as synthesized, C4 – calcinated at 673K, and C6 – calcinated 873K), multipoint BET, single point BET, total pore volume, and average pore volume.....40
Table 4 Bubble test comparison table comparing flow for methane, oxygen and helium, with or without a catalyst.....71

List of equations

Equation 1.....28
Equation 2.....28
Equation 3.....29
Equation 4.....29
Equation 5.....30
Equation 6.....33
Equation 7.....34
Equation 8.....35
Equation 9.....35
Equation 10.....35
Equation 11.....36
Equation 12.....36
Equation 13.....37

List of figures

Figure 1 Mechanism of formation of cerium glycolate; Triethylenetetramine (TETA) and NaOH are used as catalysts.....3
Figure 2 Micelle formation with cerium glycolate disassembly.....3
Figure 3 Mechanism of formation of mesoporous ceria by self-assembly method.....3
Figure 4 Sodium dodecyl sulfate (SDS) an anionic surfactant.....4
Figure 5 Cetyltrimethylammonium bromide (CTAB) a cationic surfactant.....4
Figure 6 n-Hexadecylamine a neutral surfactant.....5
Figure 7 Microreactor setup showing alumina tube (a) as reaction chamber surrounded by a furnace (b) and thermocouple (c).....20
Figure 8 Isotherm types I-VI[44].....31
Figure 9 Types of hysteresis loops, H1-H4.....32
Figure 10 Multipoint BET liner plot.....34
Figure 11 Pore size distribution of sample 001A, synthesized from cerium (IV) hydroxide, CTAB, water, ethanol, and sodium hydroxide.....44
Figure 12 Isotherm of sample 001A uncalcinated; synthesized from cerium (IV) hydroxide, CTAB, water, ethanol, and sodium hydroxide, showing type IV with hysteresis type H3.....44

Figure 13 pXRD of sample 001C4 calcinated at 673K, synthesized from cerium (IV) hydroxide, CTAB, water, ethanol, and sodium hydroxide 45
Figure 14 pXRD of sample 001C6 calcinated at 873K, synthesized from cerium (IV) hydroxide, CTAB, water, ethanol, and sodium hydroxide 46
Figure 15 pXRD of sample 016A uncalcinated, synthesized from cerium (III) nitrate hexahydrate, samarium (III) nitrate hexahydrate, CTAB, water, ethanol, and sodium hydroxide 50
Figure 16 pXRD of sample 016C4 calcinated at 673K, synthesized from cerium (III) nitrate hexahydrate, samarium (III) nitrate hexahydrate, CTAB, water, ethanol, and sodium hydroxide 51
Figure 17 pXRD of sample 017A uncalcinated, synthesized from cerium (III) nitrate hexahydrate, titanium isopropoxide, CTAB, water, ethanol, and sodium hydroxide 52
Figure 18 pXRD of sample 017C4 calcinated at 673K, synthesized from cerium (III) nitrate hexahydrate, titanium isopropoxide, CTAB, water, ethanol, and sodium hydroxide 52
Figure 19 pXRD of sample 018A uncalcinated, synthesized from cerium (III) nitrate hexahydrate, copper (II) nitrate hemipentahydrate, CTAB, water, ethanol, and sodium hydroxide 53
Figure 20 pXRD of sample 018C4 calcinated at 673K, synthesized from cerium (III) nitrate hexahydrate, copper (II) nitrate hemipentahydrate, CTAB, water, ethanol, and sodium hydroxide 54
Figure 21 pXRD of sample 018C6 calcinated at 873K, synthesized from cerium (III) nitrate hexahydrate, copper (II) nitrate hemipentahydrate, CTAB, water, ethanol, and sodium hydroxide 54
Figure 22 SEM of sample 006C4 (a) synthesized from cerium (III) nitrate hexahydrate, CTAB, water:ethanol, and NaOH, calcinated at 673K; sample 008C4 (b) synthesized from cerium (IV) hydroxide, CTAB:paraffin, water:ethanol, and NaOH,, calcinated at 673K; sample 008A (c,d) synthesized from cerium (IV) hydroxide, CTAB:paraffin, water:ethanol, and NaOH,, as-synthesized. 56
Figure 23 TEM images of sample 017A, synthesized from cerium (III) nitrate hexahydrate, titanium isopropoxide, CTAB, water, ethanol, and sodium hydroxide; uncalcinated, synthesized from cerium (III) nitrate hexahydrate, titanium isopropoxide, CTAB, water, ethanol, and sodium hydroxide (a) 8,000x (b) 10,000x (c) 30,000x (d) 40,000x; all at 200kV 57
Figure 24 Single gas monitor RGA of sample 006C4 synthesized from cerium nitrate hexahydrate, CTAB, water, ethanol, and sodium hydroxide 61
Figure 25 Single gas monitor RGA of sample 007C6 synthesized from cerium hydroxide, CTAB/paraffin, water, ethanol, methylene chloride, and sodium hydroxide 62
Figure 26 Single gas monitor RGA of sample 007C6 synthesized from cerium hydroxide, CTAB/paraffin, water, ethanol, methylene chloride, and sodium hydroxide 63
Figure 27 Single gas monitor RGA of sample 007C6 synthesized from cerium hydroxide, CTAB/paraffin, water, ethanol, methylene chloride, and sodium hydroxide 63
Figure 28 Single gas monitor RGA of sample 007C6 synthesized from cerium hydroxide, CTAB/paraffin, water, ethanol, methylene chloride, and sodium hydroxide 64
Figure 29 Single gas monitor RGA of sample 007C6 synthesized from cerium hydroxide, CTAB/paraffin, water, ethanol, methylene chloride, and sodium hydroxide 65
Figure 30 Single gas monitor RGA of sample 006C4 synthesized from cerium nitrate hexahydrate, CTAB, water, ethanol, and sodium hydroxide 66
Figure 31 Single gas monitor RGA of sample 006C4 synthesized from cerium nitrate hexahydrate, CTAB, water, ethanol, and sodium hydroxide 67

Figure 32 Single gas monitor RGA of sample 015C4 synthesized from cerium hydroxide, n-hexadecylamine, water, ethanol, and sodium hydroxide....68
Figure 33 Single gas monitor RGA of sample 006C4 synthesized from cerium nitrate hexahydrate, CTAB, water, ethanol, and sodium hydroxide....69
Figure 34 Single gas monitor RGA of bubble test, WC (with catalyst), NC (no catalyst), B4 (before stabilization), after (after stabilization). When a catalyst used it was sample 006C4 synthesized from cerium nitrate hexahydrate, CTAB, water, ethanol, and sodium hydroxide....72
Figure 35 Single gas monitor RGA of bubble test, WC (with catalyst), after (after stabilization). When a catalyst used it was sample 006C4 synthesized from cerium nitrate hexahydrate, CTAB, water, ethanol, and sodium hydroxide....73
Figure 36 Single gas monitor RGA of sample 006C4 synthesized from cerium nitrate hexahydrate, CTAB, water, ethanol, and sodium hydroxide....74
Figure 37 Single gas monitor RGA of sample 006C4 synthesized from cerium nitrate hexahydrate, CTAB, water, ethanol, and sodium hydroxide....75
Figure 38 Single gas monitor RGA of sample 006C4 synthesized from cerium nitrate hexahydrate, CTAB, water, ethanol, and sodium hydroxide....76
Figure 39 Single gas monitor RGA of a blank alumina tube....77
Figure 40 Single gas monitor RGA of sample 006C4 synthesized from cerium nitrate hexahydrate, CTAB, water, ethanol, and sodium hydroxide....78
Figure 41 Single gas monitor RGA of sample 006C4 synthesized from cerium nitrate hexahydrate, CTAB, water, ethanol, and sodium hydroxide....79
Figure 42 Single gas monitor RGA of sample 006C4 synthesized from cerium nitrate hexahydrate, CTAB, water, ethanol, and sodium hydroxide....80
Figure 43 Single gas monitor RGA of sample 006C4 synthesized from cerium nitrate hexahydrate, CTAB, water, ethanol, and sodium hydroxide....81
Figure 44 Single gas monitor RGA of sample 017C4 synthesized from cerium nitrate hexahydrate, titanium isopropoxide, CTAB, water, ethanol, and sodium hydroxide....82
Figure 45 Single gas monitor RGA of sample 017C4 synthesized from cerium nitrate hexahydrate, titanium isopropoxide, CTAB, water, ethanol, and sodium hydroxide....83
Figure 46 Single gas monitor RGA of sample 017C4 synthesized from cerium nitrate hexahydrate, titanium isopropoxide, CTAB, water, ethanol, and sodium hydroxide....84
Figure 47 Single gas monitor RGA of sample 017C6 synthesized from cerium nitrate hexahydrate, titanium isopropoxide, CTAB, water, ethanol, and sodium hydroxide....85
Figure 48 Single gas monitor RGA of sample 017C6 synthesized from cerium nitrate hexahydrate, titanium isopropoxide, CTAB, water, ethanol, and sodium hydroxide....86
Figure 49 pXRD of sample 001A, synthesized from cerium (IV) hydroxide, CTAB, water, ethanol, and sodium hydroxide, uncalcinated....96
Figure 50 pXRD of sample 001C4, synthesized from cerium (IV) hydroxide, CTAB, water, ethanol, and sodium hydroxide, calcinated at 673K....96
Figure 51 pXRD of sample 001C6 synthesized from cerium (IV) hydroxide, CTAB, water, ethanol, and sodium hydroxide, calcinated at 873K....97
Figure 52 pXRD of sample 002A synthesized from cerium (IV) hydroxide, myristyl trimethylammonium bromide, water, ethanol, and sodium hydroxide, uncalcinated....97
Figure 53 pXRD of sample 002C4, synthesized from cerium (IV) hydroxide, myristyl trimethylammonium bromide, water, ethanol, and sodium hydroxide, calcinated at 673K....98
Figure 54 pXRD of sample 002C6, synthesized from cerium (IV) hydroxide, myristyl trimethylammonium bromide, water, ethanol, and sodium hydroxide, calcinated at 873K....98
Figure 55 pXRD of sample 003A synthesized from cerium (IV) hydroxide, CTAB, hexane, ethanol, and sodium hydroxide, uncalcinated....99

Figure 56 pXRD of sample 003C4 synthesized from cerium (IV) hydroxide, CTAB, hexane, ethanol, and sodium hydroxide, calcinated at 673K 99
Figure 57 pXRD of sample 003C6 synthesized from cerium (IV) hydroxide, CTAB, hexane, ethanol, and sodium hydroxide, calcinated at 873K 100
Figure 58 pXRD of sample 004A synthesized from cerium glycolate, CTAB, water, ethanol, and sodium hydroxide, uncalcinated 100
Figure 59 pXRD of sample 004C4 synthesized from cerium glycolate, CTAB, water, ethanol, and sodium hydroxide, calcinated at 673K 101
Figure 60 pXRD of sample 004C6 synthesized from cerium glycolate, CTAB, water, ethanol, and sodium hydroxide, calcinated at 873K 101
Figure 61 pXRD of sample 005A synthesized from cerium (III) chloride heptahydrate, CTAB, water, ethanol, and sodium hydroxide, uncalcinated 102
Figure 62 pXRD of sample 005C4 synthesized from cerium (III) chloride heptahydrate, CTAB, water, ethanol, and sodium hydroxide, calcinated at 673K 102
Figure 63 pXRD of sample 005C6 synthesized from cerium (III) chloride heptahydrate, CTAB, water, ethanol, and sodium hydroxide, calcinated at 873K 103
Figure 64 pXRD of sample 006A synthesized from cerium (III) nitrate hexahydrate, CTAB, water, ethanol, and sodium hydroxide, uncalcinated 103
Figure 65 pXRD of sample 006C4 synthesized from cerium (III) nitrate hexahydrate, CTAB, water, ethanol, and sodium hydroxide, calcinated at 673K 104
Figure 66 pXRD of sample 006C6 synthesized from cerium (III) nitrate hexahydrate, CTAB, water, ethanol, and sodium hydroxide, calcinated at 873K 104
Figure 67 pXRD of sample 007A synthesized from cerium hydroxide, CTAB, paraffin, water, ethanol, dichloromethane, and sodium hydroxide, uncalcinated 105
Figure 68 pXRD of sample 007C4 synthesized from cerium hydroxide, CTAB, paraffin, water, ethanol, dichloromethane, and sodium hydroxide, calcinated at 673K 105
Figure 69 pXRD of sample 007C6 synthesized from cerium hydroxide, CTAB, paraffin, water, ethanol, dichloromethane, and sodium hydroxide, calcinated at 873K 106
Figure 70 pXRD of sample 008A synthesized from cerium hydroxide, CTAB, paraffin, water, ethanol, and sodium hydroxide, uncalcinated 106
Figure 71 pXRD of sample 008C4 synthesized from cerium hydroxide, CTAB, paraffin, water, ethanol, and sodium hydroxide, calcinated at 673K 107
Figure 72 pXRD of sample 008C6 synthesized from cerium hydroxide, CTAB, paraffin, water, ethanol, and sodium hydroxide, calcinated at 873K 107
Figure 73 pXRD of sample 009A synthesized from cerium hydroxide, SDS, water, ethanol, and sodium hydroxide, uncalcinated 108
Figure 74 pXRD of sample 009C4 synthesized from cerium hydroxide, SDS, water, ethanol, and sodium hydroxide, calcinated at 673K 108
Figure 75 pXRD of sample 009C6 synthesized from cerium hydroxide, SDS, water, ethanol, and sodium hydroxide, calcinated at 873K 109
Figure 76 pXRD of sample 010A synthesized from cerium hydroxide, CTAB/SDS, water, ethanol, and sodium hydroxide, uncalcinated 109
Figure 77 pXRD of sample 010C4 synthesized from cerium hydroxide, CTAB/SDS, water, ethanol, and sodium hydroxide, calcinated at 673K 110
Figure 78 pXRD of sample 010C6 synthesized from cerium hydroxide, CTAB/SDS, water, ethanol, and sodium hydroxide, calcinated at 873K 110
Figure 79 pXRD of sample 011A synthesized from cerium hydroxide, CTAB, toluene, pyridine, uncalcinated 111
Figure 80 pXRD of sample 011C4 synthesized from cerium hydroxide, CTAB, toluene, pyridine, calcinated at 673K 111

Figure 81 pXRD of sample 011C6 synthesized from cerium hydroxide, CTAB, toluene, pyridine, calcinated at 873K 112
Figure 82 pXRD of sample 012A synthesized from cerium hydroxide, CTAB (300mM), water, ethanol, and sodium hydroxide, uncalcinated 113
Figure 83 pXRD of sample 012C4 synthesized from cerium hydroxide, CTAB (300mM), water, ethanol, and sodium hydroxide, calcinated at 673K 113
Figure 84 pXRD of sample 012C6 synthesized from cerium hydroxide, CTAB (300mM), water, ethanol, and sodium hydroxide, calcinated at 873K 114
Figure 85 pXRD of sample 013A synthesized from cerium hydroxide, SDS (300mM), water, ethanol, and sodium hydroxide, uncalcinated 114
Figure 86 pXRD of sample 013C4 synthesized from cerium hydroxide, SDS (300mM), water, ethanol, and sodium hydroxide, calcinated at 673K 115
Figure 87 pXRD of sample 013C6 synthesized from cerium hydroxide, SDS (300mM), water, ethanol, and sodium hydroxide, calcinated at 873K 115
Figure 88 pXRD of sample 014A synthesized from cerium hydroxide, triton-X, water, ethanol, and sodium hydroxide, uncalcinated 116
Figure 89 pXRD of sample 014C4 synthesized from cerium hydroxide, triton-X, water, ethanol, and sodium hydroxide, calcinated at 673K 116
Figure 90 pXRD of sample 014C6 synthesized from cerium hydroxide, triton-X, water, ethanol, and sodium hydroxide, calcinated at 873K 117
Figure 91 pXRD of sample 015A synthesized from cerium hydroxide, n-hexadecylamine, water, ethanol, and sodium hydroxide, uncalcinated 117
Figure 92 pXRD of sample 015C4 synthesized from cerium hydroxide, n-hexadecylamine, water, ethanol, and sodium hydroxide, calcinated at 673K 118
Figure 93 pXRD of sample 015C6 synthesized from cerium hydroxide, n-hexadecylamine, water, ethanol, and sodium hydroxide, calcinated at 873K 118
Figure 94 pXRD of sample 016A synthesized from cerium (III) nitrate hexahydrate, samarium (III) nitrate hexahydrate, CTAB, water, ethanol, and sodium hydroxide, uncalcinated 119
Figure 95 pXRD of sample 016C4 synthesized from cerium (III) nitrate hexahydrate, samarium (III) nitrate hexahydrate, CTAB, water, ethanol, and sodium hydroxide, calcinated at 673K 119
Figure 96 pXRD of sample 016C6 synthesized from cerium (III) nitrate hexahydrate, samarium (III) nitrate hexahydrate, CTAB, water, ethanol, and sodium hydroxide, calcinated at 873K 120
Figure 97 pXRD of sample 017A synthesized from cerium (III) nitrate hexahydrate, titanium isopropoxide, CTAB, water, ethanol, and sodium hydroxide, uncalcinated 120
Figure 98 pXRD of sample 017C4 synthesized from cerium (III) nitrate hexahydrate, titanium isopropoxide, CTAB, water, ethanol, and sodium hydroxide, calcinated at 673K 121
Figure 99 pXRD of sample 017C6 synthesized from cerium (III) nitrate hexahydrate, titanium isopropoxide, CTAB, water, ethanol, and sodium hydroxide, calcinated at 873K 121
Figure 100 pXRD of sample 018A synthesized from cerium (III) nitrate hexahydrate, copper (III) hemi pentahydrate, CTAB, water, ethanol, and sodium hydroxide, uncalcinated 122
Figure 101 pXRD of sample 018C4 synthesized from cerium (III) nitrate hexahydrate, copper (III) hemi pentahydrate, CTAB, water, ethanol, and sodium hydroxide, calcinated at 673K 122
Figure 102 pXRD of sample 018C6 synthesized from cerium (III) nitrate hexahydrate, copper (III) hemi pentahydrate, CTAB, water, ethanol, and sodium hydroxide, calcinated at 873K 123
Figure 103 isotherm of sample 001A, synthesized from cerium (IV) hydroxide, CTAB, water, ethanol, and sodium hydroxide, uncalcinated 124
Figure 104 pore size distribution of sample 001A, synthesized from cerium (IV) hydroxide, CTAB, water, ethanol, and sodium hydroxide, uncalcinated 124
Figure 105 isotherm of sample 001C4, synthesized from cerium (IV) hydroxide, CTAB, water, ethanol, and sodium hydroxide, calcinated at 673K 125

Figure 106 pore size distribution of sample 001C4, synthesized from cerium (IV) hydroxide, CTAB, water, ethanol, and sodium hydroxide, calcinated at 673K 125
Figure 107 isotherm of sample 001C6 synthesized from cerium (IV) hydroxide, CTAB, water, ethanol, and sodium hydroxide, calcinated at 873K 126
Figure 108 pore size distribution of sample 001C6 synthesized from cerium (IV) hydroxide, CTAB, water, ethanol, and sodium hydroxide, calcinated at 873K 126
Figure 109 isotherm of sample 002A synthesized from cerium (IV) hydroxide, myristyl trimethylammonium bromide, water, ethanol, and sodium hydroxide, uncalcinated 127
Figure 110 pore size distribution of sample 002A synthesized from cerium (IV) hydroxide, myristyl trimethylammonium bromide, water, ethanol, and sodium hydroxide, uncalcinated 127
Figure 111 isotherm of sample 002C4, synthesized from cerium (IV) hydroxide, myristyl trimethylammonium bromide, water, ethanol, and sodium hydroxide, calcinated at 673K 128
Figure 112 pore size distribution of sample 002C4, synthesized from cerium (IV) hydroxide, myristyl trimethylammonium bromide, water, ethanol, and sodium hydroxide, calcinated at 673K 128
Figure 113 isotherm of sample 002C6, synthesized from cerium (IV) hydroxide, myristyl trimethylammonium bromide, water, ethanol, and sodium hydroxide, calcinated at 873K 129
Figure 114 pore size distribution of sample 002C6, synthesized from cerium (IV) hydroxide, myristyl trimethylammonium bromide, water, ethanol, and sodium hydroxide, calcinated at 873K 129
Figure 115 isotherm of sample 003A synthesized from cerium (IV) hydroxide, CTAB, hexane, ethanol, and sodium hydroxide, uncalcinated 130
Figure 116 pore size distribution of sample 003A synthesized from cerium (IV) hydroxide, CTAB, hexane, ethanol, and sodium hydroxide, uncalcinated 130
Figure 117 isotherm of sample 003C4 synthesized from cerium (IV) hydroxide, CTAB, hexane, ethanol, and sodium hydroxide, calcinated at 673K 131
Figure 118 pore size distribution of sample 003C4 synthesized from cerium (IV) hydroxide, CTAB, hexane, ethanol, and sodium hydroxide, calcinated at 673K 131
Figure 119 isotherm of sample 003C6 synthesized from cerium (IV) hydroxide, CTAB, hexane, ethanol, and sodium hydroxide, calcinated at 873K 132
Figure 120 pore size distribution of sample 003C6 synthesized from cerium (IV) hydroxide, CTAB, hexane, ethanol, and sodium hydroxide, calcinated at 873K 132
Figure 121 isotherm of sample 004A synthesized from cerium glycolate, CTAB, water, ethanol, and sodium hydroxide, uncalcinated 133
Figure 122 pore size distribution of sample 004A synthesized from cerium glycolate, CTAB, water, ethanol, and sodium hydroxide, uncalcinated 133
Figure 123 isotherm of sample 004C4 synthesized from cerium glycolate, CTAB, water, ethanol, and sodium hydroxide, calcinated at 673K 134
Figure 124 pore size distribution of sample 004C4 synthesized from cerium glycolate, CTAB, water, ethanol, and sodium hydroxide, calcinated at 673K 134
Figure 125 isotherm of sample 004C6 synthesized from cerium glycolate, CTAB, water, ethanol, and sodium hydroxide, calcinated at 873K 135
Figure 126 pore size distribution of sample 004C6 synthesized from cerium glycolate, CTAB, water, ethanol, and sodium hydroxide, calcinated at 873K 135
Figure 127 isotherm of sample 005A synthesized from cerium (III) chloride heptahydrate, CTAB, water, ethanol, and sodium hydroxide, uncalcinated 136
Figure 128 pore size distribution of sample 005A synthesized from cerium (III) chloride heptahydrate, CTAB, water, ethanol, and sodium hydroxide, uncalcinated 136

Figure 129 isotherm of sample 005C4 synthesized from cerium (III) chloride heptahydrate, CTAB, water, ethanol, and sodium hydroxide, calcinated at 673K 137
Figure 130 pore size distribution of sample 005C4 synthesized from cerium (III) chloride heptahydrate, CTAB, water, ethanol, and sodium hydroxide, calcinated at 673K 137
Figure 131 isotherm of sample 005C6 synthesized from cerium (III) chloride heptahydrate, CTAB, water, ethanol, and sodium hydroxide, calcinated at 873K 138
Figure 132 pore size distribution of sample 005C6 synthesized from cerium (III) chloride heptahydrate, CTAB, water, ethanol, and sodium hydroxide, calcinated at 873K 138
Figure 133 isotherm of sample 006A synthesized from cerium (III) nitrate hexahydrate, CTAB, water, ethanol, and sodium hydroxide, uncalcinated 139
Figure 134 pore size distribution of sample 006A synthesized from cerium (III) nitrate hexahydrate, CTAB, water, ethanol, and sodium hydroxide, uncalcinated 139
Figure 135 isotherm of sample 006C4 synthesized from cerium (III) nitrate hexahydrate, CTAB, water, ethanol, and sodium hydroxide, calcinated at 673K 140
Figure 136 pore size distribution of sample 006C4 synthesized from cerium (III) nitrate hexahydrate, CTAB, water, ethanol, and sodium hydroxide, calcinated at 673K 140
Figure 137 isotherm of sample 006C6 synthesized from cerium (III) nitrate hexahydrate, CTAB, water, ethanol, and sodium hydroxide, calcinated at 873K 141
Figure 138 pore size distribution of sample 006C6 synthesized from cerium (III) nitrate hexahydrate, CTAB, water, ethanol, and sodium hydroxide, calcinated at 873K 141
Figure 139 isotherm of sample 007A synthesized from cerium hydroxide, CTAB, paraffin, water, ethanol, dichloromethane, and sodium hydroxide, uncalcinated 142
Figure 140 pore size distribution of sample 007A synthesized from cerium hydroxide, CTAB, paraffin, water, ethanol, dichloromethane, and sodium hydroxide, uncalcinated 142
Figure 141 isotherm of sample 007C4 synthesized from cerium hydroxide, CTAB, paraffin, water, ethanol, dichloromethane, and sodium hydroxide, calcinated at 673K 143
Figure 142 pore size distribution of sample 007C4 synthesized from cerium hydroxide, CTAB, paraffin, water, ethanol, dichloromethane, and sodium hydroxide, calcinated at 673K 143
Figure 143 isotherm of sample 007C6 synthesized from cerium hydroxide, CTAB, paraffin, water, ethanol, dichloromethane, and sodium hydroxide, calcinated at 873K 144
Figure 144 pore size distribution of sample 007C6 synthesized from cerium hydroxide, CTAB, paraffin, water, ethanol, dichloromethane, and sodium hydroxide, calcinated at 873K 144
Figure 145 isotherm of sample 008A synthesized from cerium hydroxide, CTAB, paraffin, water, ethanol, and sodium hydroxide, uncalcinated 145
Figure 146 pore size distribution of sample 008A synthesized from cerium hydroxide, CTAB, paraffin, water, ethanol, and sodium hydroxide, uncalcinated 145
Figure 147 isotherm of sample 008C4 synthesized from cerium hydroxide, CTAB, paraffin, water, ethanol, and sodium hydroxide, calcinated at 673K 146
Figure 148 pore size distribution of sample 008C4 synthesized from cerium hydroxide, CTAB, paraffin, water, ethanol, and sodium hydroxide, calcinated at 673K 146
Figure 149 isotherm of sample 008C6 synthesized from cerium hydroxide, CTAB, paraffin, water, ethanol, and sodium hydroxide, calcinated at 873K 147
Figure 150 pore size distribution of sample 008C6 synthesized from cerium hydroxide, CTAB, paraffin, water, ethanol, and sodium hydroxide, calcinated at 873K 147
Figure 151 isotherm of sample 009A synthesized from cerium hydroxide, SDS, water, ethanol, and sodium hydroxide, uncalcinated 148
Figure 152 pore size distribution of sample 009A synthesized from cerium hydroxide, SDS, water, ethanol, and sodium hydroxide, uncalcinated 148
Figure 153 isotherm of sample 009C4 synthesized from cerium hydroxide, SDS, water, ethanol, and sodium hydroxide, calcinated at 673K 149

Figure 154 pore size distribution of sample 009C4 synthesized from cerium hydroxide, SDS, water, ethanol, and sodium hydroxide, calcinated at 673K 149
Figure 155 isotherm of sample 009C6 synthesized from cerium hydroxide, SDS, water, ethanol, and sodium hydroxide, calcinated at 873K 150
Figure 156 pore size distribution of sample 009C6 synthesized from cerium hydroxide, SDS, water, ethanol, and sodium hydroxide, calcinated at 873K 150
Figure 157 isotherm of sample 010A synthesized from cerium hydroxide, CTAB/SDS, water, ethanol, and sodium hydroxide, uncalcinated 151
Figure 158 pore size distribution of sample 010A synthesized from cerium hydroxide, CTAB/SDS, water, ethanol, and sodium hydroxide, uncalcinated 151
Figure 159 isotherm of sample 010C4 synthesized from cerium hydroxide, CTAB/SDS, water, ethanol, and sodium hydroxide, calcinated at 673K 152
Figure 160 pore size distribution of sample 010C4 synthesized from cerium hydroxide, CTAB/SDS, water, ethanol, and sodium hydroxide, calcinated at 673K 152
Figure 161 isotherm of sample 010C6 synthesized from cerium hydroxide, CTAB/SDS, water, ethanol, and sodium hydroxide, calcinated at 873K 153
Figure 162 pore size distribution of sample 010C6 synthesized from cerium hydroxide, CTAB/SDS, water, ethanol, and sodium hydroxide, calcinated at 873K 153
Figure 163 isotherm of sample 011A synthesized from cerium hydroxide, CTAB, toluene, pyridine, uncalcinated 154
Figure 164 pore size distribution of sample 011A synthesized from cerium hydroxide, CTAB, toluene, pyridine, uncalcinated 154
Figure 165 isotherm of sample 011C4 synthesized from cerium hydroxide, CTAB, toluene, pyridine, calcinated at 673K 155
Figure 166 pore size distribution of sample 011C4 synthesized from cerium hydroxide, CTAB, toluene, pyridine, calcinated at 673K 155
Figure 167 isotherm of sample 011C6 synthesized from cerium hydroxide, CTAB, toluene, pyridine, calcinated at 873K 156
Figure 168 pore size distribution of sample 011C6 synthesized from cerium hydroxide, CTAB, toluene, pyridine, calcinated at 873K 156
Figure 169 isotherm of sample 012A synthesized from cerium hydroxide, CTAB (300mM), water, ethanol, and sodium hydroxide, uncalcinated 157
Figure 170 pore size distribution of sample 012A synthesized from cerium hydroxide, CTAB (300mM), water, ethanol, and sodium hydroxide, uncalcinated 157
Figure 171 isotherm of sample 012C4 synthesized from cerium hydroxide, CTAB (300mM), water, ethanol, and sodium hydroxide, calcinated at 673K 158
Figure 172 pore size distribution of sample 012C4 synthesized from cerium hydroxide, CTAB (300mM), water, ethanol, and sodium hydroxide, calcinated at 673K 158
Figure 173 isotherm of sample 012C6 synthesized from cerium hydroxide, CTAB (300mM), water, ethanol, and sodium hydroxide, calcinated at 873K 159
Figure 174 pore size distribution of sample 012C6 synthesized from cerium hydroxide, CTAB (300mM), water, ethanol, and sodium hydroxide, calcinated at 873K 159
Figure 175 isotherm of sample 013A synthesized from cerium hydroxide, SDS (300mM), water, ethanol, and sodium hydroxide, uncalcinated 160
Figure 176 pore size distribution of sample 013A synthesized from cerium hydroxide, SDS (300mM), water, ethanol, and sodium hydroxide, uncalcinated 160
Figure 177 isotherm of sample 013C4 synthesized from cerium hydroxide, SDS (300mM), water, ethanol, and sodium hydroxide, calcinated at 673K 161
Figure 178 pore size distribution of sample 013C4 synthesized from cerium hydroxide, SDS (300mM), water, ethanol, and sodium hydroxide, calcinated at 673K 161

Figure 179 isotherm of sample 013C6 synthesized from cerium hydroxide, SDS (300mM), water, ethanol, and sodium hydroxide, calcinated at 873K 162
Figure 180 pore size distribution of sample 013C6 synthesized from cerium hydroxide, SDS (300mM), water, ethanol, and sodium hydroxide, calcinated at 873K 162
Figure 181 isotherm of sample 014A synthesized from cerium hydroxide, triton-X, water, ethanol, and sodium hydroxide, uncalcinated 163
Figure 182 pore size distribution of sample 014A synthesized from cerium hydroxide, triton-X, water, ethanol, and sodium hydroxide, uncalcinated 163
Figure 183 isotherm of sample 014C4 synthesized from cerium hydroxide, triton-X, water, ethanol, and sodium hydroxide, calcinated at 673K 164
Figure 184 pore size distribution of sample 014C4 synthesized from cerium hydroxide, triton-X, water, ethanol, and sodium hydroxide, calcinated at 673K 164
Figure 185 isotherm of sample 014C6 synthesized from cerium hydroxide, triton-X, water, ethanol, and sodium hydroxide, calcinated at 873K 165
Figure 186 pore size distribution of sample 014C6 synthesized from cerium hydroxide, triton-X, water, ethanol, and sodium hydroxide, calcinated at 873K 165
Figure 187 isotherm of sample 015A synthesized from cerium hydroxide, n-hexadecylamine, water, ethanol, and sodium hydroxide, uncalcinated 166
Figure 188 pore size distribution of sample 015A synthesized from cerium hydroxide, n-hexadecylamine, water, ethanol, and sodium hydroxide, uncalcinated 166
Figure 189 isotherm of sample 015C4 synthesized from cerium hydroxide, n-hexadecylamine, water, ethanol, and sodium hydroxide, calcinated at 673K 167
Figure 190 pore size distribution of sample 015C4 synthesized from cerium hydroxide, n-hexadecylamine, water, ethanol, and sodium hydroxide, calcinated at 673K 167
Figure 191 isotherm of sample 015C6 synthesized from cerium hydroxide, n-hexadecylamine, water, ethanol, and sodium hydroxide, calcinated at 873K 168
Figure 192 pore size distribution of sample 015C6 synthesized from cerium hydroxide, n-hexadecylamine, water, ethanol, and sodium hydroxide, calcinated at 873K 168
Figure 193 isotherm of sample 016A synthesized from cerium (III) nitrate hexahydrate, samarium (III) nitrate hexahydrate, CTAB, water, ethanol, and sodium hydroxide, uncalcinated 169
Figure 194 pore size distribution of sample 016A synthesized from cerium (III) nitrate hexahydrate, samarium (III) nitrate hexahydrate, CTAB, water, ethanol, and sodium hydroxide, uncalcinated 169
Figure 195 isotherm of sample 016C4 synthesized from cerium (III) nitrate hexahydrate, samarium (III) nitrate hexahydrate, CTAB, water, ethanol, and sodium hydroxide, calcinated at 673K 170
Figure 196 pore size distribution of sample 016C4 synthesized from cerium (III) nitrate hexahydrate, samarium (III) nitrate hexahydrate, CTAB, water, ethanol, and sodium hydroxide, calcinated at 673K 170
Figure 197 isotherm of sample 016C6 synthesized from cerium (III) nitrate hexahydrate, samarium (III) nitrate hexahydrate, CTAB, water, ethanol, and sodium hydroxide, calcinated at 873K 171
Figure 198 pore size distribution of sample 016C6 synthesized from cerium (III) nitrate hexahydrate, samarium (III) nitrate hexahydrate, CTAB, water, ethanol, and sodium hydroxide, calcinated at 873K 171
Figure 199 isotherm of sample 017A synthesized from cerium (III) nitrate hexahydrate, titanium isopropoxide, CTAB, water, ethanol, and sodium hydroxide, uncalcinated 172

Figure 200 pore size distribution of sample 017A synthesized from cerium (III) nitrate hexahydrate, titanium isopropoxide, CTAB, water, ethanol, and sodium hydroxide, uncalcinated 172
Figure 201 isotherm of sample 017C4 synthesized from cerium (III) nitrate hexahydrate, titanium isopropoxide, CTAB, water, ethanol, and sodium hydroxide, calcinated at 673K 173
Figure 202 pore size distribution of sample 017C4 synthesized from cerium (III) nitrate hexahydrate, titanium isopropoxide, CTAB, water, ethanol, and sodium hydroxide, calcinated at 673K 173
Figure 203 isotherm of sample 017C6 synthesized from cerium (III) nitrate hexahydrate, titanium isopropoxide, CTAB, water, ethanol, and sodium hydroxide, calcinated at 873K 174
Figure 204 pore size distribution of sample 017C6 synthesized from cerium (III) nitrate hexahydrate, titanium isopropoxide, CTAB, water, ethanol, and sodium hydroxide, calcinated at 873K 174
Figure 205 isotherm of sample 018A synthesized from cerium (III) nitrate hexahydrate, copper (III) hemi (pentahydrate), CTAB, water, ethanol, and sodium hydroxide, uncalcinated 175
Figure 206 pore size distribution of sample 018A synthesized from cerium (III) nitrate hexahydrate, copper (III) hemi (pentahydrate), CTAB, water, ethanol, and sodium hydroxide, uncalcinated 175
Figure 207 isotherm of sample 018C4 synthesized from cerium (III) nitrate hexahydrate, copper (III) hemi (pentahydrate), CTAB, water, ethanol, and sodium hydroxide, calcinated at 673K 176
Figure 208 pore size distribution of sample 018C4 synthesized from cerium (III) nitrate hexahydrate, copper (III) hemi (pentahydrate), CTAB, water, ethanol, and sodium hydroxide, calcinated at 673K 176
Figure 209 isotherm of sample 018C6 synthesized from cerium (III) nitrate hexahydrate, copper (III) hemi (pentahydrate), CTAB, water, ethanol, and sodium hydroxide, calcinated at 873K 177
Figure 210 pore size distribution of sample 018C6 synthesized from cerium (III) nitrate hexahydrate, copper (III) hemi (pentahydrate), CTAB, water, ethanol, and sodium hydroxide, calcinated at 873K 177
Figure 211 isotherm of sample 019A synthesized from cerium (III) nitrate hexahydrate, copper (III) hemi (pentahydrate), CTAB, water, ethanol, and sodium hydroxide, uncalcinated 178
Figure 212 pore size distribution of sample 019A synthesized from cerium (III) nitrate hexahydrate, copper (III) hemi (pentahydrate), CTAB, water, ethanol, and sodium hydroxide, uncalcinated 178
Figure 213 isotherm of sample 019C4 synthesized from cerium (III) nitrate hexahydrate, copper (III) hemi (pentahydrate), CTAB, water, ethanol, and sodium hydroxide, calcinated at 673K 179
Figure 214 pore size distribution of sample 019C4 synthesized from cerium (III) nitrate hexahydrate, copper (III) hemi (pentahydrate), CTAB, water, ethanol, and sodium hydroxide, calcinated at 673K 179
Figure 215 isotherm of sample 019C6 synthesized from cerium (III) nitrate hexahydrate, copper (III) hemi (pentahydrate), CTAB, water, ethanol, and sodium hydroxide, calcinated at 873K 180
Figure 216 pore size distribution of sample 019C6 synthesized from cerium (III) nitrate hexahydrate, copper (III) hemi (pentahydrate), CTAB, water, ethanol, and sodium hydroxide, calcinated at 873K 180
Figure 217 isotherm of sample 020A synthesized from cerium (III) nitrate hexahydrate, samarium (III) nitrate hexahydrate, CTAB, water, ethanol, and sodium hydroxide, uncalcinated 181

Figure 218 pore size distribution of sample 020A synthesized from cerium (III) nitrate hexahydrate, samarium (III) nitrate hexahydrate, CTAB, water, ethanol, and sodium hydroxide, uncalcinated 181
Figure 219 isotherm of sample 020C4 synthesized from cerium (III) nitrate hexahydrate, samarium (III) nitrate hexahydrate, CTAB, water, ethanol, and sodium hydroxide, calcinated at 673K 182
Figure 220 pore size distribution of sample 020C4 synthesized from cerium (III) nitrate hexahydrate, samarium (III) nitrate hexahydrate, CTAB, water, ethanol, and sodium hydroxide, calcinated at 673K 182
Figure 221 isotherm of sample 020C6 synthesized from cerium (III) nitrate hexahydrate, samarium (III) nitrate hexahydrate, CTAB, water, ethanol, and sodium hydroxide, calcinated at 873K 183
Figure 222 pore size distribution of sample 020C6 synthesized from cerium (III) nitrate hexahydrate, samarium (III) nitrate hexahydrate, CTAB, water, ethanol, and sodium hydroxide, calcinated at 873K 183

List of abbreviations

A_{cs} - cross-sectional area of the absorbate

B4 - before

BET - Brunauer-Emmett-Teller model for surface area calculation

C - BET C constant related to the energy of adsorption of the first adsorbed layer.

CTAB - cetyltrimethylammonium bromide

d - interplanar distance

DMFC – direct methanol fuel cell

e - charge on the ion

EtOH - ethanol

FL - fuel lean

FR - fuel rich

FWHM - full width half maximum

H - strength of the magnetic field

i - Y-intercept

L -crystallite size in Å

m - mass of the ion

M - molecular weight of the adsorbate

MCM-41 - Mobil Crystalline Materials (meso ordered silica)

Me - methane

MFC – mass flow controller

mM - millimolar

n - an integer representing the order of the reflection

N - Avagadro's number;

NC - no catalyst

p/p_{He} – relative pressure to pressure of helium

P/Po - relative pressure of nitrogen

P_a - ambient pressure

pXRD - powder x-ray diffraction

r - radius of curvature of the path

R - gas constant, 8.314x107 $erg/deg^{-1}mol^{-1}$

r_K - Kelvin radius of the pore

r_n - radius of neck

r_p - average pore radius, For a cylindrical pore

RT - room temperature

r_w - radius of width

s - slope

S - Surface area resolved from BET

SBA-15 – Santa Barbara Amorphous type material (meso ordered silica)

sccm - standard cubic centimeter per minute

SDC - Samarium-doped ceria

SDS - sodium dodecyl sulfate

SEM – scanning electron microscope

SOFC – solid oxide fuel cell

T - ambient temperature

T - boiling point of nitrogen, 77K

t - thickness of the adsorbed layer

TEM – transmission electron microscope

V - potential difference of the ion-accelerating plates

v - velocity of the ion

V_{ads} - volume adsorbed

V_{liq} - volume of adsorbed nitrogen as liquid nitrogen

V_m - molar volume of the liquid adsorbate, 34.7cm^3/mol for nitrogen

W - weight of gas adsorbed at relative pressure, P/ Po

WC - with catalyst

W_m - weight of adsorbate constituting a monolayer of surface coverage

XRD- x-ray diffraction

β - line broadening at half the maximum intensity in radians (full width half maximum)

γ - surface tension of nitrogen at boiling point, 8.85 ergs/cm^2

η - amount of strain

Θ - Bragg angle related to the peak position

λ - wavelength of the x-ray

Abstract

This work takes a closer look at ceria catalyst synthesis through micelle self-assembly. We compare surfactants, precursors, solvent systems, and doping. The surfactants are the building blocks upon which the ceria can crystallize. Using different surfactants we can form different sized micelles as well as manipulate the surface interactions between the surfactant head and the other materials in solution, such as the precursors, which provide the metal, for the oxide formation. The samples are calcinated to test their thermal stability. Characterization is performed using pXRD as well as physisorption. The samples that exhibited a higher thermal stability were characterized to have a high surface area as well as low fluctuations in crystallite size, pore volume, and pore size. Ceria synthesized with cerium (III) nitrate hexahydrate and CTAB in a water:ethanol mixture using sodium hydroxide showed to be the most effective at providing a thermally stable product. Doping the catalyst with titanium increased the thermal stability significantly.

We also investigate these catalysts' effects in methane oxidation in a microreactor. Select samples were run in a variety of fuel to oxygen ratios to determine the best conditions in which we could perform partial oxidation to recuperate hydrogen gas. Most of the experiments show oxygen depletion with minor changes in other gas levels indicating that there is no oxidation occurring. Curiously the oxygen levels do decrease. There is a possibility that there is a reaction occurring initially at room temperature and being exacerbated with further temperature increase.

Novel claim

This project is a collection of ceria synthesis parameters and their effects on the yielding product. It also attempts to perform methane conversion at low temperatures. Due to the demonstration of methane dependant oxygen consumption there is a unique interaction that has been uncovered, possibly room temperature oxidation. I don't have the understanding to explain what is happening in the system but it is new and interesting.

Objective

We wanted to produce thermally stable high surface area mesoporous ceria. We also wanted to modify and enhance the properties of the ceria through doping. We also wanted to investigate

methane oxidation with these catalysts and in the course of doing so we looked at oxygen depletion in our system with respect to the conditions necessary to make it happen.

Acknowledgment

First and foremost I would like to thank Dr Giorgi for the opportunity to complete my masters as part of his group. I would also like to thank Richard, Arif, Julie, Munawer, Dave, and John for their partnership and overall entertainment during lab hours. I especially want to thank my mom for being an amazing person and a constant inspiration. Thanks to all my friends and loved ones that have dealt with me, my ramblings, and my absences.

Chapter 1

Introduction

1.1 Project Overview

This project started with the idea of developing a catalyst for conversion of methane to syngas. Syngas[1] is a gas mixture of various amounts of carbon monoxide and hydrogen gases. Of which, hydrogen gas can then be used as fuel in fuel cells. Ceria was chosen as a catalyst because of low temperature ionic conductivities[2,3,4]. Our aim was to create high surface area catalysts using ceria, more specifically mesoporous ceria. To do this, a self-assembly[5,6,7] system using surfactants was used which aids in the formation of the porous ceria by creating micelles over which ceria can form crystals. Attention was also given to surfactant concentration, doping, solvent systems, and precursors. Finally a micro-reactor test was conducted to view the kinetics of these catalysts in oxidation of methane.

We have delved into the processes of making the catalyst, improving its thermal stability and maximizing its total surface area while keeping the pore size within mesoporous range of 2-50nm. The size of the pores is required to allow the flow of larger particles through the catalyst while maintaining a high surface area. The mixture, which allows for the crystallization of ceria in a porous complex, contains a precursor, a surfactant, a solvent, and a base. The precursor, solvent and surfactant were looked at with hopes of improving the interactions between the ceria and the surfactant. The solvent can affect the direction the micelle formation, polar solvents form typical micelles with the polar heads out. A non-polar solvent forms a reverse micelle[7], which would form a different final structure for the ceria. Trying solvents with different polarities can affect the interaction of not only the surfactants but also the other molecules present in solution such as the precursors.

1.2 Solid Oxide Fuel cells

Fuel cells are composed mainly of three parts: the anode, the cathode, and the electrolyte[8]. The anode and the cathode are porous so as to allow gas flow whereas the electrolyte must be dense to prevent gas mixing. The fuel must be able to flow through the anode and air must flow through the cathode. Oxygen gets ionized at the cathode; the oxygen ions then travel through

the electrolyte to react with the hydrogen on the anode side to produce electricity and water. The electrons run back to the cathode through a circuit. Doped ceria[2,21,23] is of great interest as a fuel cell electrolyte because of its high oxygen ion conductivity. Ceria can be doped with samarium or gadolinium, which can increase ionic conductivity by introducing oxygen vacancies in the crystals. This also causes ceria to go under chemical expansion when reduced from the 4+ to 3+ oxidation state in order to compensate for oxygen vacancy formation. Depending on ambient partial pressures of oxygen, ceria can give up or take in oxygen without decomposing. However, this can cause defects in the fluorite structure of ceria. It also has catalytic properties that are useful for the anode of the fuel cell. Although the initial interest of this thesis was for ceria as an anode, the development of a porous framework as a part of the anode is due to the use of ceria as a low temperature electrolyte because of its high ionic conductivity. The use of these ceria and doped ceria samples for SOFC is not experimentally explored in this thesis but is discussed here as a potential use.

1.3 Self-Assembly Method

A self-assembly method uses surfactants which assemble as micelles in a polar solution. There are three types of surfactants, which can be used; neutral[35], cationic[34], and anionic[36]. By selecting the surfactant, it is possible to control the crystallite pore size. Surfactants have a lipophilic tail and a hydrophilic head, which line up forming spheres in solution. By using a cerium salt dissolved in solution, the cerium ionically binds to the hydrophilic heads of the surfactant, which forms a layer of cerium over the micelle. The base allows for the transformation of the cerium precursor to ceria. The ceria has a positive charge on the cerium and negative charges on the oxygen, which allow for interactions with the polar head of the surfactants. Sometimes other polar small molecules are used to bind between the ceria and the polar heads, (glycolate, figure 1) which can come from the precursor (Figure 2). Order of the micelle and ultimately the pores is an important point to note when trying to increase the surface area especially as a marketable product. After crystallizing, there would exist, in theory, uniform spheres of ceria. The catalyst is filtered and dried and the surfactant is then burnt off leaving the ceria shell (figure 3). By doing so a large surface area is provided which will increase the triple phase boundary[37], when a metal catalyst is added to the framework. The triple phase boundary is a catalytic site where the gas pore, electrolyte, and electrode particles intersect. The reaction occurs at the surface of ceria, which is why maximizing the surface is important. The sample is calcinated at different temperatures to assess the thermal

stability of the mesostructure. Through XRD the low angle peaks, smaller than 3 degrees, can tell us of the long-range order[24] of the pores in the catalyst while physisorption can give us information about the surface area. Long-range order of the mesopores would allow for better fuel delivery and greater surface area, this is when the mesopores are stacked in a two-dimensional or even three-dimensional order.

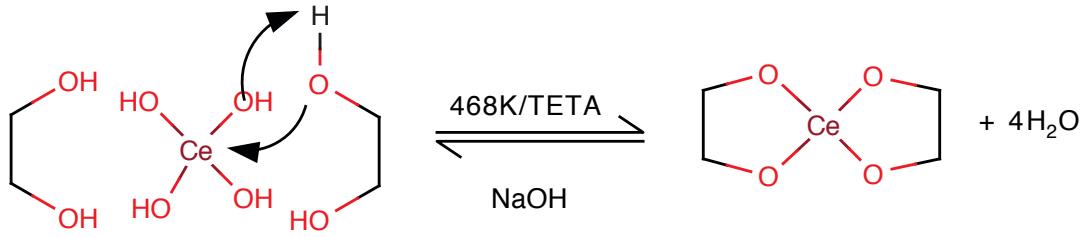

Figure 1 Mechanism of formation of cerium glycolate; Triethylenetetramine (TETA) and NaOH are used as catalysts

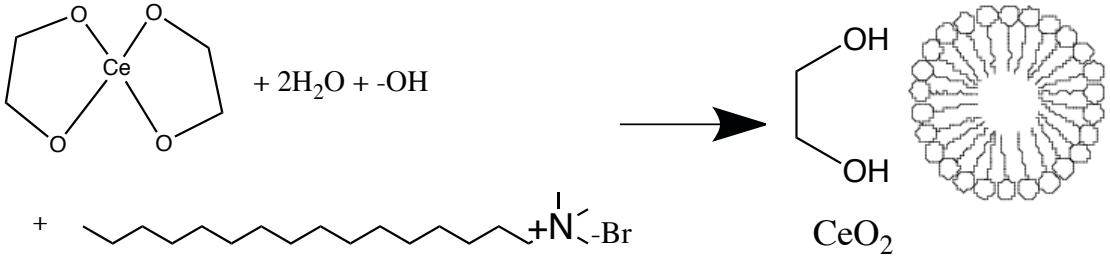

Figure 2 Micelle formation with cerium glycolate disassembly

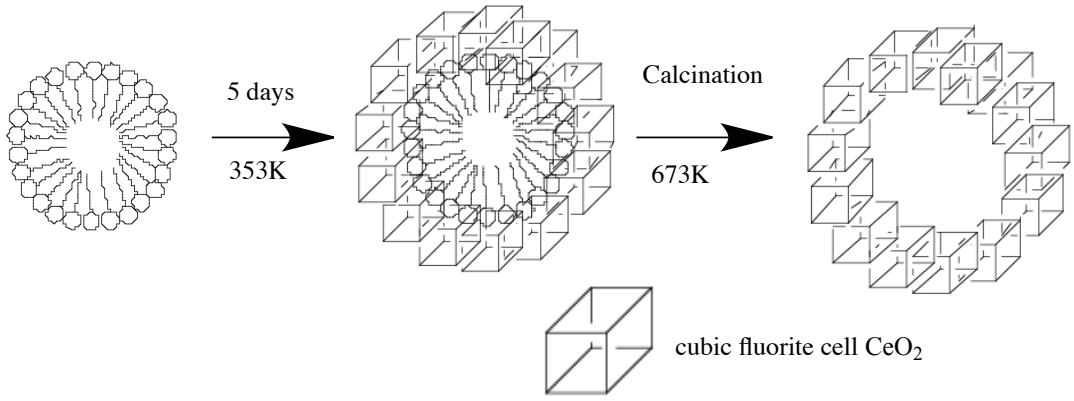

Figure 3 Mechanism of formation of mesoporous ceria by self-assembly method

1.3.1 Precursor

A precursor is a molecule that can supply a necessary component during a reaction. In this case the precursor supplies the metal ion for the ultimate formation of the metal oxide. The precursor also contains a counter ion, which may or may not play a significant role in the synthetic process. In these experiments we use cerium(IV)hydroxide, cerium glycolate, cerium (III) chloride heptahydrate, cerium (III) nitrate hexahydrate, samarium(III) nitrate hexahydrate, titanium isopropoxide, copper(III) nitrate hemi pentahydrate.

1.3.2 Surfactants

Surface-active agents, surfactants are amphiphilic compounds, which have polar heads, and lipophilic tails that can interacts with polar and non-polar solvents in various manners. Surfactants in a polar solution can go through a multilevel assembly from thin film formation at the surface of the solution to micelle formation when the concentration of the surfactant reaches the necessary level, critical micelle concentration (CMC), above which micelles are formed. Elongated formations are also possible at a second CMC. In a non-polar solution a reverse micelle can be formed where the lipophilic tail sticks out in the solvent while the hydrophilic heads pull in together away from the solvent. Three types of surfactants are available and are categorized by the head. There are anionic surfactants, which have a negatively charged polar head such as, sodium dodecyl sulphate (figure 4). There are cationic surfactants with a positively charged polar head such as cetyl trimethylammonium bromide (figure 5). The third type are non-ionic (neutral) surfactants with neutral heads such as alkyl poly(ethylene oxides), like Triton –X100 or n-hexadecylamine (figure 6). In the experiments we use cetyl trimethylammonium bromide, myristyl trimethylammonium bromide, sodium dodecyl sulphate, triton-x, n-hexadecylamine.

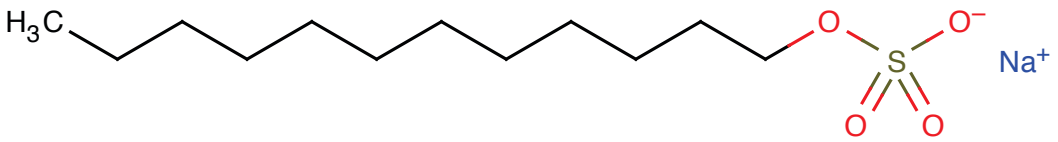

Figure 4 Sodium dodecyl sulfate (SDS) an anionic surfactant

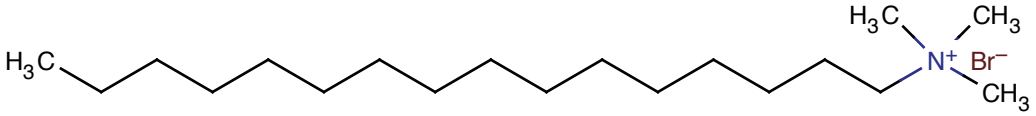

Figure 5 Cetyltrimethylammonium bromide (CTAB) a cationic surfactant

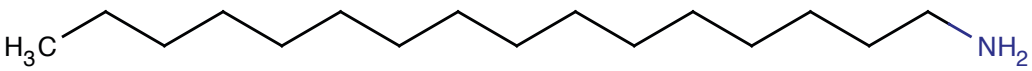

Figure 6 n-Hexadecylamine a neutral surfactant

1.4 Mesoporous materials

Mesoporous materials contain pores with sizes within a 2-50nm[35] range. These differ from macroporous and microporous materials, which have larger and smaller pore sizes, respectively. These materials are of particular interest because this size of pores gives an increased catalyst contact surface while maintaining accessibility of pores and maximizing surface area. Materials like MCM-41[39] and SBA-15[27] are highly ordered silicates, which were some of the first exemplary forms of mesoporous compounds synthesized. With high surface areas of over 1000 m^2/g they showed how order and porosity could be utilized to create improved catalysts. This synthesis method was then applied to various and numerous base materials to form other mesoporous oxides.

1.5 Thermal Stability

Thermal stability is an important factor for a fuel cell catalyst. Generally high temperatures[8] are necessary for a fuel cell to function depending on the fuel cell type. Ceria has high catalytic activity[15] but poor thermal stability[15,38]. As the catalyst is heated the pores collapse as it sinters. Using other metals as dopants the pores can be stabilized and can perform at higher temperatures[15].

Use of these catalysts for hydrogen production through methane oxidation[14] has also been investigated. Flowing a methane/oxygen mixture through the catalysts at various temperatures and different flow ratios has yielded selectivity for different products with different activation energies. Several groups have investigated the use of various fuels to produce hydrogen gas. Methane has been one of the primary fuels for SOFC but ethanol[30] and other hydrocarbon gases[19,40] have been of interest.

1.6 Methods of synthesis

Several groups have reported different procedures to make mesoporous ceria. Some groups have provided useful tools or procedures not necessarily meant for mesoporous ceria but which can be utilized for this purpose. Lyons et al. report thermally stable mesoporous ceria synthesized with a neutral surfactant, hexadecylamine, in a 50% aqueous ethanol solution[15].

Cerium was added by hydrated cerium acetate. The products were calcinated at 673K and 873K to compare characteristics at lower and higher temperatures. XRD shows low angle peaks in the 1-5° giving pore distances of 4 and 7nm. TEM shows loss of order in structure at the higher calcinations temperature it also shows that the sample calcinated at 673K is absent of surfactants when compared to the as-synthesized sample (473K). Physisorption of the sample provided surface areas of 245 m^2/g and 105m^2/g at 573K and 873K respectively. This again shows degradation of the mesoporous structure at higher temperatures. This is a fairly standard procedure, which looks at changing the polarity of the solvent slightly by using a 50% aqueous ethanol solution rather than just water. This produces similar surface areas as without the change.

Ksapabutr et al reports a one-pot synthesis of the precursor, cerium glycolate, to use to make ceria[38]. The precursor is made by combining cerium hydroxide in ethylene glycol with sodium hydroxide. This mixture is then heated for 18h to produce cerium glycolate. Furthermore this can be used to make mesoporous ceria in similar conditions as stated above and has been shown to increase surface area of the final catalyst.

With a slightly different approach Yue et al. attempt to decrease sintering at higher temperatures but don't focus on the pores themselves, instead using nanoparticles[26]. They report on texture stability of mesoporous ceria from nanoparticle assembly. Using an aqueous ammonia solution with ceria trinitrate pumped through the solution created a purple precipitate which turned yellow when Ce(IV) oxidation state was reached. The precipitate formed ceria nanoparticles of about 5nm. The nanoparticles were assembled in a solution containing HF and P123. The samples were dried and then heated to temperatures ranging from 573-973K. The samples were then exposed to steam at 773-973K. XRD showed low angle peaks below 1 degree, which equates to pores of about 7nm. Physisorption showed surface areas between 43-126 m^2/g decreasing as the temperature rose and further still when treated with steam at high temperatures. TEM shows the separations between the nanoparticles even at 973K. Fusion and sintering would cause the surface area to decrease even more.

Zhang et al. report the use of amino acids to control the hierarchical nanostructure of mesoporous ceria[34]. Using L-lysine dissolved in water with addition of nitric acid and cerium chloride heptahydrate, sodium oxalate is added to produce cerium oxalate as a precipitate.

After crystallization and filtration the powder was calcinated at 633K. No low angle XRD were taken only higher angle to show the presence of ceria fluorite crystals. The surface areas achieved were fairly consistent with other groups at this temperature, ranging from 83-125m^2/g. SEM shows dumbbell-like shapes overlapped in crosses with cauliflower-like ends. Although interesting, this overall shape is not necessarily the most efficient in terms of surface area as a catalyst.

Calles et al investigated the use of SBA-15 as a framework on which Ce and La is deposited.[27] Cu and Ni were also used but to aid in the activity of the catalyst specifically in its product selectivity. Physisorption comparison shows the highest surface area, 631m^2/g, when SBA was measured alone. The greater the amount of ceria deposited on the SBA the lower the surface area per gram gets, from 562-480m^2/g, since as layers get added the area decreases and mass increases. XRD of the ceria planes shows distances of 4.9 to 7.4nm again decreasing as more ceria is deposited. Although these surface areas are high it is important to consider how much of the surface area is actually ceria and other metals compared to silica.

Sinha et al utilizes titania to stabilize ceria mesopores[21]. Using hexadecylamine as a surfactant with a mixture of cerium and titanium in a mixed propanol/water solvent triethanolamine added as a complexing agent for the inorganic precursor ions. Cerium was added as cerium (III) acetate monohydrate and titanium as titanium isopropoxide. After filtering washing and drying, the sample was calcinated at 723K. Some samples were further heated to temperatures up to 1073K. XRD shows low angle peaks reflecting pore sizes of about 3-4nm while physisorption showed surface areas of 357m^2/g at 673K and 286m^2/g at 1073K.[11] This shows degradation at higher temperatures but still with a surface area greater than most have in as-synthesized form. The dispersion of titania in the ceria inhibits sintering in the ceria and helps with thermal stability. Sinha also shows that the addition of Pt improves catalytic activity in the case of toluene removal, which could be investigated for use as an oxidation catalyst for hydrogen production.

The idea behind creating these catalysts with thermal stability and high surface area is that generally fuel cells, especially SOFC's, are run at high temperatures and if the catalyst changes or degrades at those temperatures its function and efficiency will change as well, especially decrease. The use of these catalysts to oxidize methane and ethanol has also been investigated extensively. The facile production of hydrogen gas is a well sought after achievement.

1.7 Fuel Processing

For fuel cell power generation there are three main parts, the fuel processor, the fuel cell stack and the power conditioner[40]. Besides the use of ceria in the fuel cell itself, it could be useful for fuel processing. Fuel processing is the conversion of commercially available fuels to suitable fuel for a fuel cell. This imparts several steps. There is cleaning or removal of problematic compounds in the fuel, such as removing sulphur, halides, and ammonia to prevent catalyst degradation. As well as converting the fuel to a fuel gas reformate as in methane to hydrogen gas rich reformate (syngas). Another step is altering the gas reformate to specific fuel cell requirements by reacting carbon monoxide and water to form more hydrogen and carbon dioxide by the water-gas shift reaction. Considering a low temperature methane oxidation could provide a one step on demand processing for hydrogen gas production.

1.7.1 Fuels

Fuel cells typically use hydrogen gas as a fuel[40]. The source of the hydrogen gas can be from several hydrocarbon gases. Another source of hydrogen is from metal hydrides, which we will not be discussing here. The hydrogen can be produced in a facility and then used directly in a fuel cell or can be produced at the fuel cell site itself.

Fuel cells can be run from various fuels such as; methane, ethane, butane, propane, and bio-diesel just to name a few. With longer hydrocarbon chains there is a greater amount of side products produced and possible polymerization, which decreases efficiency of the fuel cell and can cause poisoning of the cells[15], which render the fuel cell ineffective. Light molecular weight alcohols can also be used as a source of protons for a fuel cell. Direct methanol fuel cells[40] have been used and are being used efficiently for many applications. The toxicity of methanol has come into question for long-term use since it can cause blindness by damaging the retina. One possible solution has been direct ethanol fuel cells, which are being investigated with great success and difficulty. Another idea from Bricker et al reports oxidation of methane to methanol using a Mn_2O_3 catalyst[28]. In time this could be used in sequence with DMFC's as a safe fuelling alternative. Methane could be fuelled into the vehicle then converted to methanol for the fuel cell to function on. Methane is one the fuels which produce the lowest amount of CO_2 per joules of energy. For this project methane was used as the only fuel. Methane has a 5-15% explosive limit with an auto-ignition temperature of 580^0C and its flash point is -188^0C. Activation energy on non-doped ceria is 160 kJ mol^{-1}.

1.7.2 Carbon emission

Methane is known to be a more harmful greenhouse gas than carbon dioxide. The global warming potential of methane compared to carbon monoxide is 25 over 100 years and 72 over 20 years. The global warming potential is a measuring system used to classify how much heat a greenhouse gas can trap in the atmosphere over a time interval compared to carbon dioxide.

1.8 Methane oxidation

Catalysis is a process by which a catalyst is used to accelerate a reaction by reducing the activation energy making it possible at lower temperatures. Methane oxidation is an important process for fuel cells. Methane gas can undergo full or partial oxidation depending on the conditions and the environment. Full oxidation of methane yields carbon dioxide and water, whereas partial oxidation yields carbon monoxide and hydrogen gas[12]. The production of syngas is a step in the indirect conversion of methane to liquid fuel. This conversion is of great importance in the utilization of natural gas resources, and both direct and indirect routes have been suggested. The indirect routes require conversion of methane to syngas, which can then be converted to liquid fuel by a Fischer-Tropsch reaction[1]. Conversion of methane to syngas is mildly exothermic, producing syngas with an H_2/CO ratio smaller or equal to two. Methane oxidation can depend on oxygen/methane ratios. By balanced chemical equation, full oxidation ($CH_4 + 2O_2 \rightarrow 2H_2O + CO_2$) for one mole of methane requires 2 moles of oxygen. This 2:1 of oxygen to methane, which can be regulated by flow with conversion factors, is simply a minimum. Using ratios of 3:1 oxygen to methane would assure full oxidation. In the same manner, partial oxidation ($CH_4 + ½O_2 \rightarrow 2H_2 + CO$) for one mole of methane requires ½ a mole of oxygen. This 1:2 of oxygen to methane is a maximum. Using 1:3 oxygen to methane ratio would make partial oxidation more likely.

For the purpose of running these reactions in a timely manner, we attempted to build a microreactor. The idea came from Younes-Metzler et al who created a tiny plate reactor, which helped with stabilization of temperature changes as well as reaching gas equilibrium fairly quickly[14]. Our microreactor was larger due to design changes made in order to increase structural strength. The microreactor was then loaded with catalyst then methane and oxygen were flowed over it. Using a residual gas analyzer the products of the reaction could then be detected, mainly searching for H_2, CO, H_2O, CO_2, methane, and O_2.

1.9 Methods of catalysis

Fu et al describe a mechanism of methane oxidation over several metal oxides.[29] None of these are ceria but still shed light on possible applicable mechanisms. In general the M=O bond has a polarity that allows for a certain alignment of methane onto the metal oxide. This alignment depends on the type of addition that is initially occurring on the surface. The main focus is on H abstraction from methane and less on CO/CO_2 formation. Further work on ceria would be useful for H abstraction as well as CO/CO_2 formation to determine if there is exchange of oxygen from the catalyst itself to the carbon or does it merely hold it in a transition state to allow the binding of oxygen onto the carbon or even if additional oxygen binds to the surface of the catalyst to give proximity of available carbon and oxygen.

Using ethanol as a fuel, H. Idriss focuses on platinum, palladium, rhodium, and gold supported ceria surfaces to test for selectivity of product formation. Specifically H_2 is the desired product of the reaction. Other products consisted of acetaldehyde and crotonaldehyde as well as methane, CO and CO_2. All four catalysts formed acetaldehyde in the as-synthesized stage. The rhodium/ceria catalyst directs the acetaldehyde further still to CO; the rhodium is an efficient catalyst for carbon-carbon bond dissociation. Using an additional component in the catalyst, such as Pd, converts the CO to Methane. At lower temperatures Rh-Au/Ceria was the best combination for hydrogen gas production and at higher temperatures the Pt-Rh/Ceria gives the best hydrogen gas production. The ethanol would first undergo dehydrogenation to form acetaldehyde, and then it's converted to CO and CH_4 then to H_2 gas. Acetaldehyde can also be converted into acetone in a secondary reaction. Overall there are two steps to converting ethanol into hydrogen gas. First breaking the carbon-carbon bond for which Rhodium works best, the second is oxidizing CO to CO_2 in which case the gold is best suited for the job. At higher temperatures Pt would be the most effective instead of gold.

1.10 Scope

When making mesoporous ceria several factors require attention. Precursors, surfactants, solvent systems, and dopants are fine-tuneable[9] to achieve thermal stability, long-range order, and high surface area. Dopants have shown to give necessary thermal stability to utilize the micelle shape from the surfactants. Titanium specifically has shown to be a great addition for thermal stability[21]. Long-range order and high surface area followed suite to give a surface area of $286 m^2/g$ at 1073K. Interesting trials could be performed combining this one by Sinha et al and using HF like Yue et al to see if it would stabilize the catalyst even more from sintering.

Furthermore using amino acids, as done by Zhang et al, in sequence with surfactants, there could be an interesting hierarchal structure formation. Using these catalysts for methane or even ethanol oxidation would prove to be an exciting endeavour for future application in our time. Although methane is simpler to oxidize, ethanol would be a welcomed alternative fuel since it is regarded as a renewable green fuel. Ethanol produces many side products but by combining catalysts and additional dopants selectivity of product formation can be achieved as described by H. Idriss. When targeting hydrogen gas, a combination of ceria/Rh with either Au or Pt has been shown to yield the greatest amount. All in all within a few years a highly functioning hydrogen production system could be available and used for all fuel cells whether the choice of fuel is ethanol, methanol, methane, propane, or butane.

Chapter 2

Experimental Procedure

2.1 Summary

This chapter covers the method of sample synthesis for every catalyst and precursor made as well as the procedure for testing the reactivity of certain samples. The samples are originally labelled based on date of production and sample number, starting with 001. (see table 1) For ease of use, beyond this chapter, catalyst samples are referred to by the sample number only, excluding production date. The experiments are numbered one through twenty-seven excluding ten and eleven because of air leaks.

Table 1 Catalyst synthesis components identifying the variations between the different samples detailing finalization (A- as synthesized, C4 – calcinated at 673K, and C6 – calcinated 873K), precursor, surfactant, solvent system and base.

Sample	finalization	Precursor	Surfactant	Solvent System	Base
o01	A	$Ce(OH)_4$	CTAB	water/EtOH	NaOH
o01	C4	$Ce(OH)_4$	CTAB	water/EtOH	NaOH
o01	C6	$Ce(OH)_4$	CTAB	water/EtOH	NaOH
o02	A	$Ce(OH)_4$	myristyl trimethylammonium bromide	water/EtOH	NaOH
o02	C4	$Ce(OH)_4$	myristyl trimethylammonium bromide	water/EtOH	NaOH
o02	C6	$Ce(OH)_4$	myristyl trimethylammonium bromide	water/EtOH	NaOH
o03	A	$Ce(OH)_4$	CTAB	Hexane	NaOH
o03	C4	$Ce(OH)_4$	CTAB	Hexane	NaOH
o03	C6	$Ce(OH)_4$	CTAB	Hexane	NaOH
o04	A	Cerium Glycolate	CTAB	water/EtOH	NaOH
o04	C4	Cerium Glycolate	CTAB	water/EtOH	NaOH
o04	C6	Cerium Glycolate	CTAB	water/EtOH	NaOH
o05	A	$CeCl_3$ - $7H_2O$	CTAB	water/EtOH	NaOH
o05	C4	$CeCl_3$ - $7H_2O$	CTAB	water/EtOH	NaOH
o05	C6	$CeCl_3$ - $7H_2O$	CTAB	water/EtOH	NaOH
o06	A	Ce(III) $(NO_3)_3$-$6H_2O$	CTAB	water/EtOH	NaOH
o06	C4	Ce(III) $(NO_3)_3$-$6H_2O$	CTAB	water/EtOH	NaOH
o06	C6	Ce(III) $(NO_3)_3$-$6H_2O$	CTAB	water/EtOH	NaOH
o07	A	$Ce(OH)_4$	CTAB/paraffin	water/EtOH/$MeCl_2$	NaOH
o07	C4	$Ce(OH)_4$	CTAB/paraffin	water/EtOH/$MeCl_2$	NaOH
o07	C6	$Ce(OH)_4$	CTAB/paraffin	water/EtOH/$MeCl_2$	NaOH
o08	A	$Ce(OH)_4$	CTAB/paraffin	water/EtOH	NaOH
o08	C4	$Ce(OH)_4$	CTAB/paraffin	water/EtOH	NaOH
o08	C6	$Ce(OH)_4$	CTAB/paraffin	water/EtOH	NaOH
o09	A	$Ce(OH)_4$	SDS	water/EtOH	NaOH
o09	C4	$Ce(OH)_4$	SDS	water/EtOH	NaOH
o09	C6	$Ce(OH)_4$	SDS	water/EtOH	NaOH
o10	A	$Ce(OH)_4$	CTAB/SDS	water/EtOH	NaOH
o10	C4	$Ce(OH)_4$	CTAB/SDS	water/EtOH	NaOH
o10	C6	$Ce(OH)_4$	CTAB/SDS	water/EtOH	NaOH
o11	A	$Ce(OH)_4$	CTAB	toluene	Pyridine
o11	C4	$Ce(OH)_4$	CTAB	toluene	Pyridine
o11	C6	$Ce(OH)_4$	CTAB	toluene	Pyridine
o12	A	$Ce(OH)_4$	CTAB (300mM)	water/EtOH	NaOH
o12	C4	$Ce(OH)_4$	CTAB (300mM)	water/EtOH	NaOH
o12	C6	$Ce(OH)_4$	CTAB (300mM)	water/EtOH	NaOH
o13	A	$Ce(OH)_4$	SDS (300mM)	water/EtOH	NaOH
o13	C4	$Ce(OH)_4$	SDS (300mM)	water/EtOH	NaOH
o13	C6	$Ce(OH)_4$	SDS (300mM)	water/EtOH	NaOH
o14	A	$Ce(OH)_4$	triton-X	water/EtOH	NaOH
o14	C4	$Ce(OH)_4$	triton-X	water/EtOH	NaOH
o14	C6	$Ce(OH)_4$	triton-X	water/EtOH	NaOH
o15	A	$Ce(OH)_4$	n-hexadecylamine	water/EtOH	NaOH
o15	C4	$Ce(OH)_4$	n-hexadecylamine	water/EtOH	NaOH
o15	C6	$Ce(OH)_4$	n-hexadecylamine	water/EtOH	NaOH
o16	A	Ce(III) $(NO_3)_3$-$6H_2O$/Sm(III) $(NO_3)_3$-$6H_20$	CTAB	water/EtOH	NaOH
o16	C4	Ce(III) $(NO_3)_3$-$6H_2O$/Sm(III) $(NO_3)_3$-$6H_20$	CTAB	water/EtOH	NaOH
o16	C6	Ce(III) $(NO_3)_3$-$6H_2O$/Sm(III) $(NO_3)_3$-$6H_20$	CTAB	water/EtOH	NaOH
o17	A	Ce(III) $(NO_3)_3$-$6H_2O$/Titanium Isopropoxide	CTAB	water/EtOH	NaOH
o17	C4	Ce(III) $(NO_3)_3$-$6H_2O$/Titanium Isopropoxide	CTAB	water/EtOH	NaOH
o17	C6	Ce(III) $(NO_3)_3$-$6H_2O$/Titanium Isopropoxide	CTAB	water/EtOH	NaOH
o18	A	Ce(III) $(NO_3)_3$-$6H_2O$/Cu(II) $(NO_3)_2$-$2.5H_2O$	CTAB	water/EtOH	NaOH
o18	C4	Ce(III) $(NO_3)_3$-$6H_2O$/Cu(II) $(NO_3)_2$-$2.5H_2O$	CTAB	water/EtOH	NaOH
o18	C6	Ce(III) $(NO_3)_3$-$6H_2O$/Cu(II) $(NO_3)_2$-$2.5H_2O$	CTAB	water/EtOH	NaOH
o19	A	Ce(III) $(NO_3)_3$-$6H_2O$/Cu(II) $(NO_3)_2$-$2.5H_2O$	CTAB	water/EtOH	NaOH
o19	C4	Ce(III) $(NO_3)_3$-$6H_2O$/Cu(II) $(NO_3)_2$-$2.5H_2O$	CTAB	water/EtOH	NaOH
o19	C6	Ce(III) $(NO_3)_3$-$6H_2O$/Cu(II) $(NO_3)_2$-$2.5H_2O$	CTAB	water/EtOH	NaOH
o20	A	Ce(III) $(NO_3)_3$-$6H_2O$/Sm(III) $(NO_3)_3$-$6H_20$	CTAB	water/EtOH	NaOH
o20	C4	Ce(III) $(NO_3)_3$-$6H_2O$/Sm(III) $(NO_3)_3$-$6H_20$	CTAB	water/EtOH	NaOH
o20	C6	Ce(III) $(NO_3)_3$-$6H_2O$/Sm(III) $(NO_3)_3$-$6H_20$	CTAB	water/EtOH	NaOH

2.2 Synthesis

Catalyst synthesis always consists of a surfactant, base, precursor, and a solvent system (table 1).

2.2.1 080610001x

4.1g of Cetyl trimethylammonium bromide (CTAB) and 2.3g of NaOH are added to 120mL of a 50:50 solution of distilled water and methanol in a 500mL propylene bottle equipped with a Teflon coated stirring bar. The mixture is stirred until a homogeneous solution is formed. Then 2.36g of Cerium Hydroxide is added to the solution and stirred for 30mins until the mixture is uniform.

After uniform mixture every sample goes through the following procedure. It should be noted that beginning with sample 012 to sample 020 the propylene bottle was replaced with a 125mL Erlenmeyer flask.

The bottle is capped and then placed in an oven at 353K (80^0C) for five days. Once the bottle is removed from the oven it is cooled to room temperature. The mixture is filtered and washed by suction filtration. It is poured into a Buchner filter over a Whatman filter paper. The bottle is then rinsed 3 times with 20mL of distilled water and poured over the filter paper to remove any remnants left in the bottle. The sample is then washed 3 times with 50mL of distilled water. The resulting compound and filter paper are then placed on a watch glass and dried overnight in an oven at 393K (120^0C). The sample is removed from the filter paper and ground with a mortar and pestle until it is uniform and smooth in size as determinable visually. Half of the sample is kept, placed in a vial and labelled with the suffix A for as-synthesized. The remaining half is then split into two parts, one of which is heated to 673K (400^0C) and the other portion to 873K (600^0C) and held at that temperature for 4 hours to calcinate the samples. These are then labelled with the suffixes C4 and C6 respectively to indicate calcinated at 673K (400^0C) or 873K (600^0C). The samples are placed in long ceramic crucibles and set in a large furnace with a quartz tube, which uses a temperature control box to supply current to the furnace and monitor its temperature. The furnace is also closed off with its exhaust sent to the fume hood because of the gaseous side products that are formed when burning off the surfactants from the metal oxide sample such as HBr, NOx, CO, and CO_2.

2.2.2 080611002x

3.36g of myristyl trimethylammonium bromide and 2.3g of NaOH are added to 120mL of a 50:50 solution of distilled water and methanol in a 500mL propylene bottle equipped with a Teflon coated stirring bar. The mixture is stirred until a homogeneous solution is formed. Then 2.36g of Cerium Hydroxide is added to the solution and stirred for 30mins until the mixture is uniform.

2.2.3 080618003x

4.1g of Cetyl trimethylammonium bromide (CTAB) and 2.3g of NaOH are added to 120mL of hexane in a 500mL propylene bottle equipped with a Teflon coated stirring bar. The mixture is stirred for 30mins then 10mL of ethanol is added and stirred for an additional 30mins. Then 2.36g of Cerium Hydroxide is added to the solution and stirred for 30mins until the mixture is uniform.

2.2.4 080620004x

3.075g of Cetyl trimethylammonium bromide (CTAB) and 1.725g of NaOH are added to 90mL of a 50:50 solution of distilled water and ethanol in a 125mL propylene bottle equipped with a Teflon coated stirring bar. The mixture is stirred until a homogeneous solution is formed. Then 3.4965g of Cerium glycolate is added to the solution and stirred for 30mins until the mixture is uniform.

2.2.5 080620005x

3.075g of Cetyl trimethylammonium bromide (CTAB) and 1.725g of NaOH are added to 90mL of a 50:50 solution of distilled water and ethanol in a 125mL propylene bottle equipped with a Teflon coated stirring bar. The mixture is stirred until a homogeneous solution is formed. Then 5.145g of Cerium chloride heptahydrate is added to the solution and stirred for 30mins until the mixture is uniform.

2.2.6 080620006x

3.075g of Cetyl trimethylammonium bromide (CTAB) and 1.725g of NaOH are added to 90mL of a 50:50 solution of distilled water and ethanol in a 125mL propylene bottle equipped with a Teflon coated stirring bar. The mixture is stirred until a homogeneous solution is formed. Then 6.0250g of Cerium(III) nitrate hexahydrate is added to the solution and stirred for 30mins until the mixture is uniform.

2.2.7 080704007x

Melt 2.0g of paraffin wax and mix with 10mL of methylene chloride. Add this to a solution of 90mL 50:50 distilled water and ethanol in a 125mL propylene bottle equipped with a Teflon

coated stirring bar followed by the addition of 3.075g of Cetyl trimethylammonium bromide (CTAB) and 1.725g of NaOH. The mixture is stirred until a homogeneous solution is formed. Then 5.145g of Cerium chloride heptahydrate is added to the solution and stirred for 30mins until the mixture is uniform.

2.2.8 080711008x

Melt 1.0g of paraffin wax and mix a solution of 100mL 50:50 distilled water and ethanol in a 125mL propylene bottle equipped with a Teflon coated stirring bar followed by the addition of 3.6448g of Cetyl trimethylammonium bromide (CTAB) and 4.0g of NaOH. The mixture is stirred until a homogeneous solution is formed. Then 3.21g of Cerium hydroxide is added to the solution and stirred for 30mins until the mixture is uniform.

2.2.9 080711009x

2.8838g of sodium dodecyl sulphate (SDS) and 4.0g of NaOH are added to 100mL of a 50:50 solution of distilled water and ethanol in a 125mL propylene bottle equipped with a Teflon coated stirring bar. The mixture is stirred until a homogeneous solution is formed. Then 3.21g of Cerium hydroxide is added to the solution and stirred for 30mins until the mixture is uniform.

2.2.10 080711010x

1.4419g of sodium dodecyl sulphate (SDS), 1.8244g cetyl triethylammonium bromide and 4.0g of NaOH are added to 100mL of a 50:50 solution of distilled water and ethanol in a 125mL propylene bottle equipped with a Teflon coated stirring bar. The mixture is stirred until a homogeneous solution is formed. Then 3.21g of Cerium hydroxide is added to the solution and stirred for 30mins until the mixture is uniform.

2.2.11 080711011x

3.075g cetyl triethylammonium bromide and 5mL pyridine are added to 90mL of toluene in a 125mL propylene bottle equipped with a Teflon coated stirring bar. The mixture is stirred until a homogeneous solution is formed. Then 2.80g of Cerium hydroxide is added to the solution and stirred for 30mins until the mixture is uniform.

2.2.12 080717012x

10.934g cetyl triethylammonium bromide and 4.0g of NaOH are added to 100mL of a 50:50 solution of distilled water and ethanol in a 125mL Erlenmeyer flask equipped with a Teflon coated stirring bar. The mixture is stirred until a homogeneous solution is formed. Then 5.00g

of Cerium hydroxide is added to the solution and stirred for 30mins until the mixture is uniform.

2.2.13 080717013x

8.6514g sodium dodecyl sulphate and 4.0g of NaOH are added to 100mL of a 50:50 solution of distilled water and ethanol in a 125mL Erlenmeyer flask equipped with a Teflon coated stirring bar. The mixture is stirred until a homogeneous solution is formed. Then 5.00g of Cerium hydroxide is added to the solution and stirred for 30mins until the mixture is uniform.

2.2.14 080717014x

6.25g (5.811mL) triton-x and 4.0g of NaOH are added to 100mL of a 50:50 solution of distilled water and ethanol in a 125mL Erlenmeyer flask equipped with a Teflon coated stirring bar. The mixture is stirred until a homogeneous solution is formed. Then 3.21g of Cerium hydroxide is added to the solution and stirred for 30mins until the mixture is uniform.

2.2.15 080717015x

2.4146g n-hexadecylamine and 4.0g of NaOH are added to 100mL of a 50:50 solution of distilled water and ethanol in a 125mL Erlenmeyer flask equipped with a Teflon coated stirring bar. The mixture is stirred until a homogeneous solution is formed. Then 3.21g of Cerium hydroxide is added to the solution and stirred for 30mins until the mixture is uniform.

2.2.16 090715016x

3.075g of Cetyl trimethylammonium bromide (CTAB) and 2.36g of NaOH are added to 90mL of a 50:50 solution of distilled water and ethanol in a 125mL Erlenmeyer flask equipped with a Teflon coated stirring bar. The mixture is stirred until a homogeneous solution is formed. Then 6.0250g Cerium(III) nitrate hexahydrate and 6.1614g Samarium(III)nitrate hexahydrate are added to the solution and stirred for 30mins until the mixture is uniform.

2.2.17 090715017x

3.075g of Cetyl trimethylammonium bromide (CTAB) and 2.36g of NaOH are added to 90mL of a 50:50 solution of distilled water and ethanol in a 125mL Erlenmeyer flask equipped with a Teflon coated stirring bar. The mixture is stirred until a homogeneous solution is formed. Then 6.0250g Cerium(III) nitrate hexahydrate and 3.790mL of Titanium Isopropoxide are added to the solution and stirred for 30mins until the mixture is uniform.

2.2.18 090715018x

3.075g of Cetyl trimethylammonium bromide (CTAB) and 2.36g of NaOH are added to 90mL of a 50:50 solution of distilled water and ethanol in a 125mL Erlenmeyer flask equipped with a Teflon coated stirring bar. The mixture is stirred until a homogeneous solution is formed. Then 6.0250g Cerium(III) nitrate hexahydrate and 6.1614g Copper(II) nitrate hemipentahydrate are added to the solution and stirred for 30mins until the mixture is uniform.

2.2.19 090715019x

3.41g of Cetyl trimethylammonium bromide (CTAB) and 1.92 g of NaOH are added to 100mL of a 50:50 solution of distilled water and ethanol in a 125mL Erlenmeyer flask equipped with a Teflon coated stirring bar. The mixture is stirred until a homogeneous solution is formed. Then 6.2466g Cerium(III) nitrate hexahydrate and 0.86058g Copper(II) nitrate hemipentahydrate are added to the solution and stirred for 30mins until the mixture is uniform.

2.2.20 090715020x

3.41g of Cetyl trimethylammonium bromide (CTAB) and 1.92 g of NaOH are added to 100mL of a 50:50 solution of distilled water and ethanol in a 125mL Erlenmeyer flask equipped with a Teflon coated stirring bar. The mixture is stirred until a homogeneous solution is formed. Then 6.2466g Cerium(III) nitrate hexahydrate and 1.6445g Samarium(III) nitrate hexahydrate are added to the solution and stirred for 30mins until the mixture is uniform.

2.2.21 080611CG001 Synthesis of cerium glycolate[38]

5.20g of Cerium hydroxide is dissolved in a 250mL round bottom flask containing 90mL ethylene glycol and a Teflon coated stir bar by stirring for 20mins until uniform. Then 3.55mL of triethylene tetramine and 0.12g of NaOH are added to the mixture and stirred again for 5 mins. The mixture is then refluxed at 468K (195^0C) using a water cooled condenser and wrapping the round bottom flask in alumina wool for 18 hours. Then the remaining ethylene glycol is distilled for 2 hours from the round bottom flask by wrapping the condenser with alumina wool. The sample is then filtered by suction filtration and washed with 5x20mL acetonitrile. Methanol is used to rinse out the round bottom flask the remaining parts of the sample from the round bottom flask. The sample is then dried at room temperature.

2.2.22 Sm glycolate synthesis

12.0g of samarium acetate is dissolved in a 250mL round bottom flask containing 100mL ethylene glycol and a Teflon coated stir bar by stirring for 20mins under nitrogen gas until

uniform. The mixture is then refluxed at 463K (190^{0}C) using a water cooled condenser and wrapping the round bottom flask in alumina wool for 1.5 hours. Then the remaining ethylene glycol is distilled for 2 hours from the round bottom flask by wrapping the condenser with alumina wool. The sample is then filtered by suction filtration and washed with 5x20mL acetonitrile. Methanol is used to rinse out the round bottom flask the remaining parts of the sample from the round bottom flask. The sample is then dried overnight at room temperature.

2.2.23 Ce glycolate synth 080818CG002

10.4g of Cerium hydroxide is dissolved in a 250mL round bottom flask containing 180mL ethylene glycol and a Teflon coated stir bar by stirring for 20mins until uniform. Then 7.10mL of triethylene tetramine and 0.36g of NaOH are added to the mixture and stirred again for 5 mins. The mixture is then refluxed at 468K (195^{0}C) using a water cooled condenser and wrapping the round bottom flask in alumina wool for 18 hours. Then the remaining ethylene glycol is distilled for 2 hours from the round bottom flask by wrapping the condenser with alumina wool. The sample is then filtered by suction filtration and washed with 5x20mL acetonitrile. Methanol is used to rinse out the round bottom flask the remaining parts of the sample from the round bottom flask. The sample is then dried at room temperature.

2.2.24 Cerium isopropoxide[42] Ce Iso 001

10.4g of Cerium hydroxide is dissolved in a 250mL round bottom flask containing 95mL isopropanol and a Teflon coated stir bar by stirring for 20mins until uniform. Then 3.75g of NaOH is added to the mixture and stirred again for 5 mins. The mixture is then refluxed at 354K (81^{0}C) using a water-cooled condenser for 12 hours. Then the remaining isopropanol is distilled for 2 hours from the round bottom flask by wrapping the condenser with alumina wool. The sample is then filtered by suction filtration and washed with 5x20mL methanol. Methanol is used to rinse out the round bottom flask the remaining parts of the sample from the round bottom flask. The sample is then dried at room temperature. The sample is then crushed with the mortar and pestle air-dried and sealed in a vial.

2.2.25 Cerium isopropoxide Ce Iso 002

10.4g of Cerium hydroxide is dissolved in a 100mL round bottom flask containing 48mL isopropanol and a Teflon coated stir bar by stirring for 20mins until uniform. Then 3.75g of NaOH is added to the mixture and stirred again for 5 mins. The mixture is then refluxed at 354K (81^{0}C) using a water-cooled condenser for 12 hours. Then the remaining isopropanol is distilled for 2 hours from the round bottom flask by wrapping the condenser with alumina wool. The sample is then filtered by suction filtration and washed with 5x20mL methanol.

Methanol is used to rinse out the round bottom flask the remaining parts of the sample from the round bottom flask. The sample is then dried in the oven at 393K (120^0C). The sample is then crushed with the mortar and pestle air-dried and sealed in a vial.

2.3 Microreactor Procedure

A microreactor was used to test catalytic performance of the prepared ceria catalysts for methane oxidation. The exhaust of the micro-reactor was connected to a mass spectrometer, ACCUQUAD residual gas analyzer (RGA), for partial pressure readings, most of the exhaust flow was sent to a fume hood. The intake of the micro-reactor was connected to a cross union joining three gases, helium, methane, and oxygen (BOC Gases). The gases were sourced from large gas cylinders, which had an interrupted connection to the cross union by mass flow controllers (MFC) which independently control the flow of gasses. The catalyst was inserted into the center of the alumina tube and blocked with alumina wool on both ends. The tube and wool are weighed, the sample is loaded with the final wool plug being inserted then the final weight is measured. A small catalyst furnace was slipped around the alumina tube with an Omega thermocouple aligned to the center of the alumina tube (Figure 7). The temperature was controlled with a temperature control power supply/readout. All tubing seals were made with stainless steel nut and ferrule sets with exception of the use of Teflon ferrule sets on the alumina tube. All tubing was 1/8“ stainless steel with the exceptions of a connection to the mass spectrometer, which was 1/4 “ stainless steel and tubing from the gas cylinders to the MKS mass flow controllers were 1/4” plastic tubing.

Figure 7 Microreactor setup showing alumina tube (a) as reaction chamber surrounded by a furnace (b) and thermocouple (c).

2.3.1 Alumina tube setup

To test the catalyst we used fuel lean, fuel rich, and equal fuel to oxygen conditions, by flow volume. The mass spec chamber pressure was kept constant at $1.0x10^{-5}$mbar. Any adjustments made to the chamber pressure to correct any fluctuations were marked and accounted for. Helium was used a constant background pressure against which we could calibrate the pressures of the system. The time of the temperature change, temperature stabilization, and pressure stabilization were marked.

2.3.2 Mass spectrometry Residual Gas Analyzer

The mass spectrometer program, RGA (Residual Gas Analyzer v2.3) was set to identify peaks at m/z=2(H_2), 4(He), 15(methyl), 18(water), 28(N_2, CO), 31(MeO) 32(O_2), 40(Ar), 44(CO_2) on a single gas monitor RGA or Pressure vs Time scan. Cross section values must be noted when looking at the partial pressures of different ions vs the partial pressures of the initial volumes of gas as well as correction factors for the major peak fragmentation during ionization. Helium is used as a non-reactive background gas to correct for any pressure fluctuations.

2.3.3 Range of experiments

The experiment parameters for catalysis include temperature and fuel flow ratios. Some experiments range from room temp (RT) to 673K or 873K. Some experiments were maintained at RT to determine activity without additional energy to the system. The flow ratios range from fuel rich, fuel lean, or equilibrated. Some of the experiments have more variations on the fuel ratios to determine activity based on fuel/oxygen ratios.

2.4 Catalysis parameters

The following list will detail all experiment parameters.

Prior to every experiment, the lines are flushed with helium, then the gas flow rates are be adjusted and allowed to stabilize in the reactor.

Experiment set A

2.4.1 Experiment 1

The sample 006C4 is run under fuel lean conditions oxygen (O_2) at 0.9sccm, methane (Me) at 0.3sccm, helium (He) at 8.8sccm. The temperature is initially set to RT then to 623K, increasing to 873K. The runs were saved under file names FL006C41 and FL006C42.

Experiment set B

2.4.2 Experiment 2

The sample 007C6 is run under fuel lean conditions Oxygen (O_2) at 0.9sccm, Methane (Me) at 0.3sccm, Helium (He) at 8.8sccm. The temperature is initially set to RT then to 573K, increasing to 873K followed by a return to RT. The runs were saved under file names T007C6FL, 2007C6FL, and 3007C6FL.

2.4.3 Experiment 3

The sample 007C6 is run under fuel rich conditions Oxygen (O_2) at 0.3sccm, Methane (Me) at 0.9sccm, Helium (He) at 8.8sccm. The temperature is initially set to RT then to 873K. The runs were saved under file names 1007C6FR, 2007C6FR.

2.4.4 Experiment 4

The sample 007C6 is run under equal fuel and oxygen conditions Oxygen (O_2) at 0.6sccm, Methane (Me) at 0.6sccm, Helium (He) at 8.8sccm. The temperature is initially set to RT then to 673K. The run was saved under file name 1007C6EQ.

2.4.5 Experiment 5

The sample 007C6 is run under fuel rich conditions Oxygen (O_2) at 0.4sccm, Methane (Me) at 0.8sccm, Helium (He) at 8.8sccm. The temperature is initially set to RT then to 373K. The run was saved under file name 1007C648.

2.4.6 Experiment 6

The sample 007C6 is run under varying conditions;
Oxygen (O_2) at 0.4sccm, Methane (Me) at 0.8sccm, Helium (He) at 8.8sccm,
Oxygen (O_2) at 0.39sccm, Methane (Me) at 0.81sccm, Helium (He) at 8.8sccm
Oxygen (O_2) at 0.38sccm, Methane (Me) at 0.82sccm, Helium (He) at 8.8sccm
Oxygen (O_2) at 0.37sccm, Methane (Me) at 0.83sccm, Helium (He) at 8.8sccm

Oxygen (O_2) at 0.36sccm, Methane (Me) at 0.84sccm, Helium (He) at 8.8sccm

Oxygen (O_2) at 0.35sccm, Methane (Me) at 0.85sccm, Helium (He) at 8.8sccm

Oxygen (O_2) at 0.20sccm, Methane (Me) at 1.00sccm, Helium (He) at 8.8sccm

The temperature is maintained at RT. The runs were saved under file names T007C623, T007C624, and T007C625.

Experiment set C

2.4.7 Experiment 7

The sample 006C4 is run under fuel rich conditions oxygen (O_2) at 0.3sccm, methane (Me) at 0.9sccm, helium (He) at 8.8sccm. The temperature is initially set to RT then to 673K. The runs were saved under file names RN2006C4, RN3006C4, and RN4006C4.

2.4.8 Experiment 8

The sample 006C4 is run under fuel lean conditions oxygen (O_2) at 0.9sccm, methane (Me) at 0.3sccm, helium (He) at 8.8sccm. The temperature is initially set to RT then to 673K. The run was saved under file name RN5006C4.

Experiment set D

2.4.9 Experiment 9

The sample 015C4 is run under fuel less conditions oxygen (O_2) at 0.9sccm, methane (Me) at 0.0sccm, helium (He) at 8.8sccm. The temperature is initially set to RT then to 673K. Methane is then added into the system at 0.3sccm while maintaining 673K. This is followed by a temperature ramp back down to room temperature. The runs were saved under file names Testrun1, Testrun2, and Testrun3.

Experiment set E

2.4.12 Experiment 12

The sample 006C4 is run under fuel rich conditions oxygen (O_2) at 0.6sccm, methane (Me) at 1.8sccm, helium (He) at 7.6sccm. Initially the flow is set through the stainless steel blank and stabilized. The flow is then switched to the catalyst. The run was saved under file name 006C4004.

Experiment set F

2.4.13 Experiment 13

The bubble test, vary the flow rates isolating one gas then another and so on while switching from the blank, stainless steel tubing, and the alumina with the catalyst at every step you count the bubbles produced in the exhaust over a 30 second period to compare exhaust flow rates to see if there's any loss. The data is saved under file name bubbletest1.

2.4.14 Experiment 14

The bubble test 2, vary the flow rates isolating one gas then another and so on while switching from the blank, stainless steel tubing, and the alumina with the catalyst at every step you count the bubbles produced in the exhaust over a 5min period to compare exhaust flow rates to see if there's any loss.

Experiment set G

2.4.15 Experiment 15

The sample 006C4 is run under fuel rich conditions oxygen (O_2) at 1.25sccm, methane (Me) at 3.75sccm, helium (He) at 5.0sccm. The temperature is initially set to RT then to 473K then back to RT. The run was saved under file name 006C4005, 006C4006, and 006C4007.

2.4.16 Experiment 16

The sample 006C4 is run under fuel rich conditions oxygen (O_2) at 1.25sccm, methane (Me) at 3.75sccm, helium (He) at 5.0sccm. The temperature is initially set to RT then to 673K then back to RT. The run was saved under file name 006C4008, 006C4009, and 006C4010.

2.4.17 Experiment 17

The sample 006C4 is run under fuel rich conditions oxygen (O_2) at 1.25sccm, methane (Me) at 3.75sccm, helium (He) at 5.0sccm. The temperature is initially set to RT then to 423K then back to RT. The run was saved under file name 006C4011, 006C4012, 006C4013, and 006C4014.

Experiment set H

2.4.18 Experiment 18

The blank is run under fuel rich conditions oxygen (O_2) at 1.25sccm, methane (Me) at 3.75sccm, helium (He) at 5.0sccm. The temperature is initially set to RT then to 423K. The run was saved under file name 006C4BLK.

Experiment set I

2.4.19 Experiment 19

The sample 006C4 is run under fuel rich conditions oxygen (O_2) at 1.25sccm, helium (He) at 8.75sccm. The temperature is initially set to RT then to 423K. Then methane (Me) was set at 3.75sccm while reducing helium (He) to 5.0sccm and maintaining oxygen. The run was saved under file name 006C4023.

2.4.20 Experiment 20

The sample 006C4 is run under fuel rich conditions oxygen (O_2) at 1.25sccm, methane (Me) at 3.75sccm, helium (He) at 5.0sccm. The temperature is initially set to RT then to 423K then Oxygen (O_2) was set to 1.50sccm. The run was saved under file name 006C4025.

2.4.21 Experiment 21

The sample 006C4 is run under fuel rich conditions oxygen (O_2) at 1.25sccm, methane (Me) at 3.75sccm, helium (He) at 5.0sccm. The temperature is initially set to RT then to 673K. The run was saved under file name 006C4027, and 006C4028.

2.4.22 Experiment 22

The sample 006C4 is run under fuel lean conditions oxygen (O_2) at 3.75sccm, methane (Me) at 1.25sccm, helium (He) at 5.0sccm. The temperature is initially set to RT then to 673K. The run was saved under file name 006C4029, and 006C4030.

Experiment set J

2.4.23 Experiment 23

The sample 017C4 is run under fuel rich conditions oxygen (O_2) at 1.25sccm, methane (Me) at 3.75sccm, helium (He) at 5.0sccm. The temperature is set to RT. The oxygen levels are then increased until they appear and varied to find a more precise point of presence. The run was saved under file name 017C4001, 017C4002, and 017C4003.

2.4.24 Experiment 24

The sample 017C4 is run under fuel lean conditions oxygen (O_2) at 7.00sccm, methane (Me) at 3.75sccm, helium (He) at 5.0sccm. The temperature is initially set to RT then to 673K then back to RT. The run was saved under file name 017C4004, and 017C4005.

2.4.25 Experiment 25

The sample 017C4 is run under fuel lean conditions oxygen (O_2) at 3.75sccm, methane (Me) at 1.25sccm, helium (He) at 5.0sccm. The temperature is initially set to RT then to 673K. The run was saved under file name 017C4007, 017C4008, and 017C4009.

Experiment set K

2.4.26 Experiment 26

The sample 017C6 is run under fuel lean conditions oxygen (O_2) at 3.75sccm, methane (Me) at 1.25sccm, helium (He) at 5.0sccm. The temperature is initially set to RT then to 873K. The run was saved under file name 017C4010, 017C4011, and 017C4012.

2.4.27 Experiment 27

The sample 017C6 is run under fuel lean conditions oxygen (O_2) at 3.75sccm, methane (Me) at 1.25sccm, helium (He) at 5.0sccm. The temperature is set to RT then to 473K followed by 673K. The run was saved under file name 017C4013, 017C4014, and 017C4015.

Chapter 3

Characterization

3.1 Powder X-ray diffraction

Powder x-ray diffraction was used as a fingerprint tool by comparison with a database. As a method of characterization it is widely used to determine structural properties of crystals. We can learn about the composition of the crystals, their size, possible presence of order, microstrains, and its lattice parameters.

Powder X-Ray diffraction is used for structural characterization of materials. Ideally, every possible crystalline orientation is represented equally in the sample, leading to smooth diffraction rings around the beam axis. In accordance with Bragg's law[13], each ring corresponds to a particular reciprocal lattice vector in the sample crystal, with intensity proportional to the number of planes. Using the Williamson-Hall equation we can determine the crystallite size.

3.1.1 Diffractogram

The x-ray diffractogram is a plot of gathered data graphing the intensity versus the 2Θ angle of signal acquisition. From this we can easily determine 2Θ angle of the peak position as well as the peak breadth, which is taken as full width half-maximum. A Phillips PW 130 x-ray diffraction with a Cu K α radiation of 1.54Å wavelength connected to a Kevex Psi Peltier cooled solid-state detector. The sample was loaded onto a Vaseline coated silica disc.

Using a diffractometer[13], X-rays are scattered across a powder, which is spinning, allowing for many different crystals to diffract the beams giving a higher possibility of getting a pattern of positive interference from the crystals. The spinning disc is tilted at an angle, θ, while a detector rotates around it on an arm at an angle of 2θ; the detector is a scintillation counter, which measures ionizing radiation. This is known as a Bragg-Brentano type of configuration. The reciprocal lattice vectors can be determined by the diffraction pattern of the crystal, which is the momentum difference between incoming and diffracted X-rays of a crystal. Each point in a reciprocal lattice (h, k, l) corresponds to a set of lattice planes (H, K, L) in the real space lattice. The direction of the reciprocal lattice vector corresponds to the normal in the real space planes. The magnitude of the

reciprocal lattice vector is equal to the reciprocal of the interplanar spacing of the real space planes. This allows us to determine the atomic arrangement of the lattice.

From the 2Θ angle we can determine interplanar distances using Bragg's law[31].

Equation 1

$$n\lambda = 2d\sin\theta$$

Where,

n is an integer representing the order of the reflection

λ is the wavelength of the x-ray

d is the interplanar distance

Θ is the Bragg angle related to the peak position

Peaks in the lower angle range of the diffractogram signify larger interplanar distances, which for porous compounds are a sign or order in those pores.

3.1.2 Peak width and crystallite size

From the peak breadth we can determine crystal size, strain. The width of the peak from the raw data is affected by crystal size, crystal strain, instrumental factors, and the presence of defects in the crystal lattice. The peak width is measured at full width half maximum (FWHM).

To determine the size of the crystallites we can use the Scherrer equation[31], which ignores the effect of strain in the breadth of the peak.

Equation 2

$$L = \frac{0.94\lambda}{\beta\cos\theta}$$

Where,

L is the crystallite size in Å

λ is the wavelength of the x-ray

β is the line broadening at half the maximum intensity in radians (full width half maximum)

Θ is the Bragg angle related to the peak position

The wavelength of the x-ray depends on the x-ray source. In this case copper was used as the x-ray source, which has a wavelength of 1.54 Å. β and Θ are from the collected data and these values, obtained from a diffraction pattern are dependant of peak refinement. We refine the raw data for subsequent analysis by first subtracting the background noise (because there is a constant measuring of noise, and $K_{\alpha 2,}$ ($K_{\alpha 2}$ is determined to be half the intensity of $K_{\alpha 1}$). The $K_{\alpha 1}$-$K_{\alpha 2}$ doublet cannot be separated with filters. The resulting emission x-ray collected is the $K_{\alpha 1,}$ which is used for analysis of the crystallite structure.

A portion of the breadth of the peak is due to strain in the crystallite. Stokes and Wilson[25] described its effect based on the Bragg angle and the amount of strain or distortion compared to the perfect structure.

Equation 3

$$\beta = \eta \tan\theta$$

where,

β is the line broadening at half the maximum intensity in radians (full width half maximum)

η is the amount of strain

Θ is the Bragg angle related to the peak position

The Williamson-Hall[25] method combines both of these definitions to form a more complete description of the breadth.

Equation 4

$$\beta = \eta\tan\theta + \frac{\lambda}{L\cos\theta}$$

Where

β is the line broadening at half the maximum intensity in radians (full width half maximum)

η is the amount of strain

Θ is the Bragg angle related to the peak position

λ is the wavelength of the x-ray

L is the crystallite size in Å

Furthermore it allows for a method to determine the values based on the experimental data.

If the formula is rearranged as a linear expression as follows

Equation 5

$$\frac{\beta\cos\theta}{\lambda} = \frac{1}{L} + \eta\frac{\sin\theta}{\lambda}$$

Plotting (βcosθ)/λ versus (sinθ)/λ we get a linear plot where the slope is equal to the value of microstrains in the crystallite and the reciprocal of the intercept is equal to the size of the crystallite.

3.2 Gas adsorption – physisorption

Quantum Autosorb1 has been used to analyze the surface area, the pore volume and pore size distribution of the mesoporous samples. Generally the samples are degassed under heat then transferred to undergo physisorption analysis. Both processes are done using a liquid nitrogen bath to remove impurities from the system. Nitrogen gas is used as the adsorbate to give an adsorption and desorption isotherm of nitrogen gas. Through the isotherm data several other graphs can be created giving rise to more information about the sample. High surface area as well as long-range order is necessary for the mesoporous samples to be efficient as SOFC anodes. To verify this we determine pore volume and pore size distribution as well as surface area.

3.2.1 Isotherms

The construction of an adsorption spectrum can reveal an understanding of the surface area and porosity of an adsorbent. An adsorption isotherm can be created measuring the quantity of adsorbate on a surface over a range of relative pressures at a constant temperature. The isotherm spectrum consist of adsorption points gathered when gas is being adsorbed as well as desorption points of when gas is removed from the sample. During adsorption fixed volumes of gas are introduced to the system and the relative pressure is then measured in a stepwise manner. Upon desorption the pressure is reduced to match that of the adsorption spectrum and the volume released is then measured. There are six types of adsorption isotherms[44] shown in Figure 8.

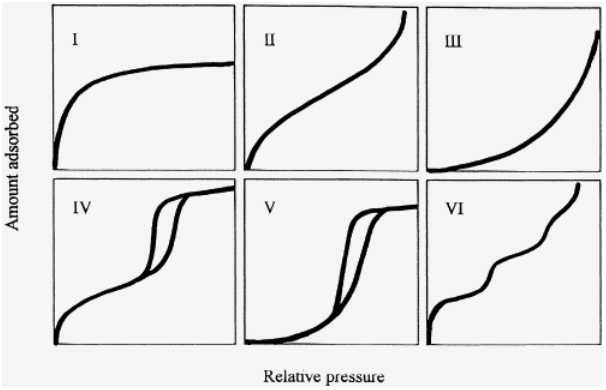

Figure 8 Isotherm types I-VI[44]

Type I – Langmuir isotherms are concave which depict microporous solids with small external surfaces. The limited uptake of adsorbent is governed by the accessibility of the micropore and not it's internal surface area.

Type II – isotherms are generally macroporous or non-porous adsorbents. This represents an easy access to the surface area allowing unrestricted monolayer-multilayer adsorption.

Type III – Isotherms are convex and are rarely encountered. They display an immediate formation of multilayers. They can represent non-porous adsorbents.

Type IV – Isotherms are associated with capillary condensation in mesopores indicated by the steep slope at higher pressures. Shows monolayer formation and transition to multilayer formation.

Type V – Isotherms are uncommon and can contain mesopores. There is no monolayer formation only unrestricted multilayer formation. Represent microporous or mesoporous solids

Type VI – Isotherms are also uncommon. There is complete monolayer formation followed by other monolayer formations. Represent adsorption on homogeneous, non-porous surfaces.

Types I, II, and III are generally reversible, some type I isotherms from macroporous materials sometimes exhibit hysteresis. Type IV and V usually exhibit hysteresis between adsorption and desorption points. de Boer has identified five types of hysteresis loops[45] correlating them with distinct pore shapes. IUPAC has since redefined the hysteresis to 4 types (Figure 9), H1-H4[16, 43, 44].

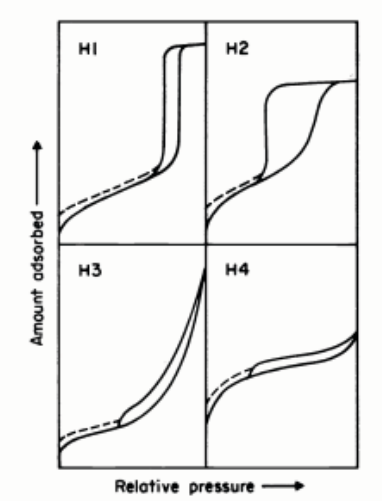

Figure 9 Types of hysteresis loops, H1-H4

Type H1

Results from agglomerates, an assemblage of particles rigidly joined together, or compacts of uniform spheres in a regular array. Giving a narrow distribution of pore size. The two branches of the isotherm are vertical and parallel for a significant range. Both adsorption and desorption branches are steep at intermediate relative pressures. Adsorption is determined by the internal radius whereas desorption is determined by the access radius or neck radius. With increasing relative pressures, capillaries give rise to condensation and a meniscus has been formed. Upon desorption, the capillaries will empty at lower relative pressure when it corresponds to the radius r.

Type H2

Results from poorly defined pore size distribution and pore shape, meaning a variety of shapes and sizes. Adsorption branch is sloping from intermediate to saturation relative pressure, desorption is steep at intermediate relative pressure. Adsorption occurs with a varying radius but desorption is limited by the pore access and is therefore at one fix relative pressure. Varying r_w's (width) but constant r_n's (neck) and imagine the width of the wide parts vary but not the width of the neck.

Type H3

Results from aggregates, an assembly of particles, which are loosely coherent, of plate-like particles forming slit-shaped pores. The adsorption branch is steep at saturation pressure. The desorption branch is steep at intermediate relative pressure. Upon adsorption the meniscus cannot be formed

until the pressure of the vapour is saturated. On the desorption branch the space is emptied when the relative pressure corresponds to the width of the capillary (the effective radius of the curvature of the meniscus)

Type H4

Results from narrow slit-like pores. The two branches remain nearly horizontal and parallel over a wide range of relative pressure. This indicates a varying radius upon adsorption and desorption without a capillary effect

3.2.2 BET Surface area

The Brunauer-Emmett-Teller (BET) method is a widely used procedure to determine the surface area of solid materials. To do this we use the BET equation[32],

Equation 6

$$\frac{1}{\mathrm{W}((\mathrm{Po}/\mathrm{P})-1)} = \frac{1}{\mathrm{WmC}} + \frac{(C-1)}{\mathrm{WmC}}\frac{(P)}{(\mathrm{Po})}$$

W is the weight of gas adsorbed at relative pressure, P/ P_o

W_m is the weight of adsorbate constituting a monolayer of surface coverage

C is the BET C constant related to the energy of adsorption of the first adsorbed layer.

Multipoint BET method using the BET equation requires a linear plot of $1/[W((P_o/P)-1)]$ vs P/P_o which is restricted to a limited region of the adsorption isotherm in the P/P_o range of 0.05 to 0.35 of the isotherm. The following is a typical BET plot (Figure 10).

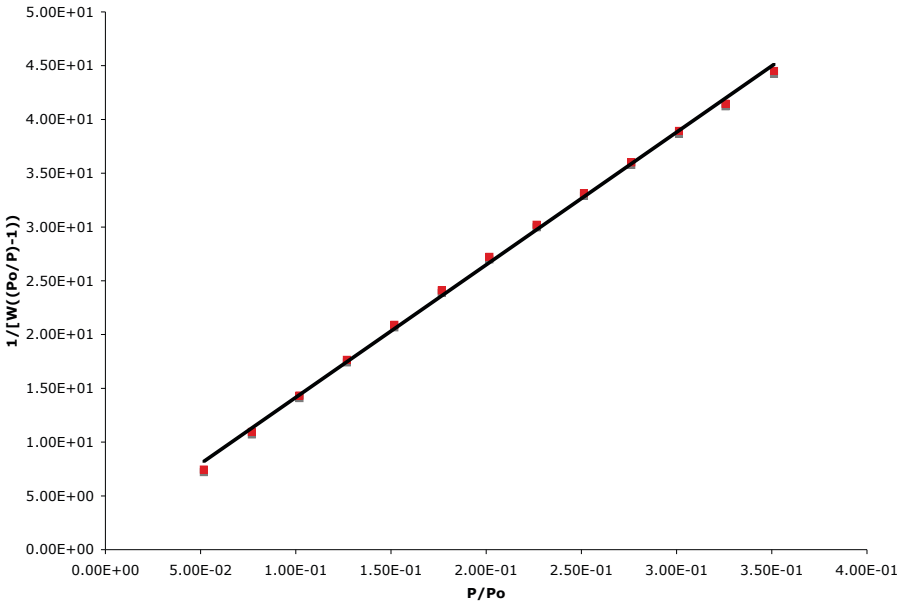

Figure 10 Multipoint BET liner plot

The BET plot in figure 10 requires a minimum of three point from which you can obtain the slope, s, and Y-intercept, i. Using $W_m=1/(s+i)$ you can calculate the weight of the adsorbate monolayer. Then using equation 7 you can calculate the surface area of the monolayer.

N is Avagadro's number;

M is the molecular weight of the adsorbate;

A_{cs} is cross-sectional area of the absorbate, which can be looked up. For nitrogen at 77K is A_{cs}=16.2Å.

Equation 7

$$St = \frac{W_{\mathrm{m}} N A c s}{M}$$

3.2.3 Total pore volume and average pore radius

Total pore volume is obtained from the amount of vapour adsorbed at a relative pressure close to one, by assuming that all the pores are filled with liquid adsorbate (nitrogen). The volume of nitrogen absorbed, V_{ads}, can be converted to the volume of liquid nitrogen[10], V_{liq}, contained in the pores using,

Equation 8

$$Vliq = \frac{Pa\ Vads\ Vm}{RT}$$

P_a and T are ambient pressure and temperature

V_m is the molar volume of the liquid adsorbate, 34.7cm^3/mol for nitrogen

The average pore size is derived from the pore volume. For a cylindrical pore the average pore radius, $r_{p,}$ can be determined by using,

Equation 9

$$rp = \frac{2Vliq}{S}$$

V_{liq} is the volume of adsorbed nitrogen as liquid nitrogen

S is the Surface area resolved from BET

3.2.4 Pore size distribution

The distribution of pore volume with respect to pore size is called pore size distribution. The desorption isotherms are considered the most appropriate data points to evaluate the pore size distribution since the desorption isotherm is closer to true thermodynamic stability. Assuming cylindrical pore shape and use of nitrogen as adsorbate, we can use the Kelvin equation[10],

Equation 10

$$rk = \frac{-2\gamma\ Vm}{\mathrm{RTln(P/Po)}}$$

γ is the surface tension of nitrogen at boiling point, 8.85 ergs/cm^2

V_m is the molar volume of liquid nitrogen, 34.7cm^3/mol

R is the gas constant, 8.314x10^{7}ergs/deg/mol

T is the boiling point of nitrogen, 77K

P/P_o is the relative pressure of nitrogen

r_K is the Kelvin radius of the pore

The Kelvin radius represents the radius of the pore in which condensation occurs but prior to condensation some adsorption has taken place on the walls of the pore, therefore r_K does not represent the actual pore radius. The actual pore radius[10], r_p, is given by,

Equation 11

$$rp = rK + t$$

t is the thickness of the adsorbed layer

Statistically the thickness can be assumed to be $3.54(V_{ads}/V_m)$, where 3.54 is the thickness of one molecular layer of nitrogen (in Å) and V_{ads}/V_m is the ratio of the volume of nitrogen adsorbed to the volume adsorbed at completion of the monolayer.

A more convenient way of estimating t is using de Boer's equation[10],

Equation 12

$$t(\text{Å}) = [\frac{(13.99)}{(log(\frac{Po}{P})} / + 0.034)] \, 1/2$$

The BJH method can be used to increase the accuracy of the measurements by taking into account a reduction of the physically adsorbed layer upon decrease of relative pressure. Each step in pressure decrease results in emptying the largest pore size as well as a reduction in thickness of the physically adsorbed layer from the previously emptied pores, which still contained residues of the adsorbate.

3.3 RGA – Mass spectroscopy

The mass spectrometer program was set to identify peaks at m/e = 2(H), 4(He), 15(methyl), 18(water), 28(N_2,CO), 30(NO), 31(MeO), 32(O_2), 44(CO_2) on a Pressure vs Time scan. Cross section values must be noted when looking at the partial pressures of different ions vs the partial pressures of the initial volumes of gas. Note: for these experiments the m/z value of 28 is only associated with CO since N_2 is not present in any of the reagents and would only become present if there were a leak.

The gas phase sample is first bombarded by a stream of high-energy electrons at the ionizer converting some molecules to ions, which are then accelerated by an electric field[11]. The ions are then separated according to their mass to charge ratio, m/z, in an electrostatic field.

The kinetic energy of an accelerated ion is equal to,

Equation 13

$$½mv^2 = eV$$

where,

m is the mass of the ion

v is the velocity of the ion

e is the charge on the ion

V is the potential difference of the ion-accelerating plates

In these experiments, we use a quadrupole mass filter. This system comprises four parallel rods in the direction of the ion beam. The rods generate a two-dimensional oscillating electrostatic field, which is controlled by a combination of direct current (DC) and radio frequency (RF) voltages. One set of rods is connected with a positive DC voltage while the other is connected with a negative DC voltage. Each set of rods is also superimposed with a sinusoidal RF voltage 180 degrees out of phase with one another. In the X direction of the field, light ions are in phase with the RF drive, in turn will gain energy and oscillate with increasing amplitudes until they collide with one of the rods and are discharged from the system. High mass ions will be able to pass through the quadrupole without hitting the X electrodes. The X direction is called a high-pass mass filter. The Y direction is a low-pass mass filter. Heavy ions will be unstable due to the effect of the negative DC component but light ions will be stabilized by the RF component, allowing the light ions to pass through the quadrupole without hitting the Y electrodes. Varying the DC/RF ratio allows for filter selectivity and scanning of the entire mass spectra.

The ion passes through to the detector, which measures the ions current directly using a Faraday cup or an electron multiplier detector. The detector output is amplified and fed to the recorder. The signal from the recorder is a mass spectrum. The mass spectrometer is run under ultra high vacuum obtained by a turbo pump combined with a mechanical pump.

Chapter 4

Synthesis analysis

4.1 Summary

For the synthesis portion of the experimentation, we tested variations in precursors, surfactants, solvent systems as well as doping by additional precursors with alternate source metals (table2). With characterization you can then determine pore volume, pore size, surface area, thermal stability, crystal size, and long-range order. In an overall comparison from synthesis by pore size, surface area, pore volume, crystal size we can compare them at different calcination levels (table 3).

For thermal stability we have to look at changes in pore volume, pore size, crystal size, surface area. Values of various methods of surface area interpretation were tabulated but only the multi point BET method will be discussed (table 3). Pore size can increase or decrease with temperature with this synthesis method. Heating the sample at 673K burns off the carbon based surfactants, which are locked inside the catalyst pores, thus increasing the available space in the pores. Alternately if thermal stability is low the pore size also increases because the surrounding walls collapse. The difference between the two situations is pore volume. When the surfactant is removed the total pore volume will greatly increase whereas when the walls collapse it will only slightly change and possibly decrease. Surface area will follow in the same suite as pore size but surface area will increase as surfactants are removed while it will decrease as pores collapse. Typically crystal size increases with increasing temperature. Larger crystals also represent thermal stability but changing crystal size shows low thermal stability. The samples are also calcinated to 873K to consider thermal stability. The as synthesized sampled is used for comparison.

Table 2 Catalyst synthesis components identifying the variations between the different samples detailing finalization (A- as synthesized, C4 – calcinated at 673K, and C6 – calcinated 873K), precursor, surfactant, solvent system and base. (same as table 1)

Sample	finalization	Precursor	Surfactant	Solvent System	Base
o01	A	$Ce(OH)_4$	CTAB	water/EtOH	NaOH
o01	C4	$Ce(OH)_4$	CTAB	water/EtOH	NaOH
o01	C6	$Ce(OH)_4$	CTAB	water/EtOH	NaOH
o02	A	$Ce(OH)_4$	myristyl trimethylammonium bromide	water/EtOH	NaOH
o02	C4	$Ce(OH)_4$	myristyl trimethylammonium bromide	water/EtOH	NaOH
o02	C6	$Ce(OH)_4$	myristyl trimethylammonium bromide	water/EtOH	NaOH
o03	A	$Ce(OH)_4$	CTAB	Hexane	NaOH
o03	C4	$Ce(OH)_4$	CTAB	Hexane	NaOH
o03	C6	$Ce(OH)_4$	CTAB	Hexane	NaOH
o04	A	Cerium Glycolate	CTAB	water/EtOH	NaOH
o04	C4	Cerium Glycolate	CTAB	water/EtOH	NaOH
o04	C6	Cerium Glycolate	CTAB	water/EtOH	NaOH
o05	A	$CeCl_3$ - $7H_2O$	CTAB	water/EtOH	NaOH
o05	C4	$CeCl_3$ - $7H_2O$	CTAB	water/EtOH	NaOH
o05	C6	$CeCl_3$ - $7H_2O$	CTAB	water/EtOH	NaOH
o06	A	Ce(III) $(NO_3)_3$-$6H_2O$	CTAB	water/EtOH	NaOH
o06	C4	Ce(III) $(NO_3)_3$-$6H_2O$	CTAB	water/EtOH	NaOH
o06	C6	Ce(III) $(NO_3)_3$-$6H_2O$	CTAB	water/EtOH	NaOH
o07	A	$Ce(OH)_4$	CTAB/paraffin	water/EtOH/$MeCl_2$	NaOH
o07	C4	$Ce(OH)_4$	CTAB/paraffin	water/EtOH/$MeCl_2$	NaOH
o07	C6	$Ce(OH)_4$	CTAB/paraffin	water/EtOH/$MeCl_2$	NaOH
o08	A	$Ce(OH)_4$	CTAB/paraffin	water/EtOH	NaOH
o08	C4	$Ce(OH)_4$	CTAB/paraffin	water/EtOH	NaOH
o08	C6	$Ce(OH)_4$	CTAB/paraffin	water/EtOH	NaOH
o09	A	$Ce(OH)_4$	SDS	water/EtOH	NaOH
o09	C4	$Ce(OH)_4$	SDS	water/EtOH	NaOH
o09	C6	$Ce(OH)_4$	SDS	water/EtOH	NaOH
o10	A	$Ce(OH)_4$	CTAB/SDS	water/EtOH	NaOH
o10	C4	$Ce(OH)_4$	CTAB/SDS	water/EtOH	NaOH
o10	C6	$Ce(OH)_4$	CTAB/SDS	water/EtOH	NaOH
o11	A	$Ce(OH)_4$	CTAB	toluene	Pyridine
o11	C4	$Ce(OH)_4$	CTAB	toluene	Pyridine
o11	C6	$Ce(OH)_4$	CTAB	toluene	Pyridine
o12	A	$Ce(OH)_4$	CTAB (300mM)	water/EtOH	NaOH
o12	C4	$Ce(OH)_4$	CTAB (300mM)	water/EtOH	NaOH
o12	C6	$Ce(OH)_4$	CTAB (300mM)	water/EtOH	NaOH
o13	A	$Ce(OH)_4$	SDS (300mM)	water/EtOH	NaOH
o13	C4	$Ce(OH)_4$	SDS (300mM)	water/EtOH	NaOH
o13	C6	$Ce(OH)_4$	SDS (300mM)	water/EtOH	NaOH
o14	A	$Ce(OH)_4$	triton-X	water/EtOH	NaOH
o14	C4	$Ce(OH)_4$	triton-X	water/EtOH	NaOH
o14	C6	$Ce(OH)_4$	triton-X	water/EtOH	NaOH
o15	A	$Ce(OH)_4$	n-hexadecylamine	water/EtOH	NaOH
o15	C4	$Ce(OH)_4$	n-hexadecylamine	water/EtOH	NaOH
o15	C6	$Ce(OH)_4$	n-hexadecylamine	water/EtOH	NaOH
o16	A	Ce(III) $(NO_3)_3$-$6H_2O$/Sm(III) $(NO_3)_3$-$6H_20$	CTAB	water/EtOH	NaOH
o16	C4	Ce(III) $(NO_3)_3$-$6H_2O$/Sm(III) $(NO_3)_3$-$6H_20$	CTAB	water/EtOH	NaOH
o16	C6	Ce(III) $(NO_3)_3$-$6H_2O$/Sm(III) $(NO_3)_3$-$6H_20$	CTAB	water/EtOH	NaOH
o17	A	Ce(III) $(NO_3)_3$-$6H_2O$/Titanium Isopropoxide	CTAB	water/EtOH	NaOH
o17	C4	Ce(III) $(NO_3)_3$-$6H_2O$/Titanium Isopropoxide	CTAB	water/EtOH	NaOH
o17	C6	Ce(III) $(NO_3)_3$-$6H_2O$/Titanium Isopropoxide	CTAB	water/EtOH	NaOH
o18	A	Ce(III) $(NO_3)_3$-$6H_2O$/Cu(II) $(NO_3)_2$-$2.5H_2O$	CTAB	water/EtOH	NaOH
o18	C4	Ce(III) $(NO_3)_3$-$6H_2O$/Cu(II) $(NO_3)_2$-$2.5H_2O$	CTAB	water/EtOH	NaOH
o18	C6	Ce(III) $(NO_3)_3$-$6H_2O$/Cu(II) $(NO_3)_2$-$2.5H_2O$	CTAB	water/EtOH	NaOH
o19	A	Ce(III) $(NO_3)_3$-$6H_2O$/Cu(II) $(NO_3)_2$-$2.5H_2O$	CTAB	water/EtOH	NaOH
o19	C4	Ce(III) $(NO_3)_3$-$6H_2O$/Cu(II) $(NO_3)_2$-$2.5H_2O$	CTAB	water/EtOH	NaOH
o19	C6	Ce(III) $(NO_3)_3$-$6H_2O$/Cu(II) $(NO_3)_2$-$2.5H_2O$	CTAB	water/EtOH	NaOH
o20	A	Ce(III) $(NO_3)_3$-$6H_2O$/Sm(III) $(NO_3)_3$-$6H_20$	CTAB	water/EtOH	NaOH
o20	C4	Ce(III) $(NO_3)_3$-$6H_2O$/Sm(III) $(NO_3)_3$-$6H_20$	CTAB	water/EtOH	NaOH
o20	C6	Ce(III) $(NO_3)_3$-$6H_2O$/Sm(III) $(NO_3)_3$-$6H_20$	CTAB	water/EtOH	NaOH

Table 3 Catalyst synthesis components characterization data between different samples detailing finalization (A- as synthesized, C4 – calcinated at 673K, and C6 – calcinated 873K), multipoint BET, single point BET, total pore volume, and average pore volume.

Sample	finalization	M BET (m^2/g)	crystal size (Å)	Avg pore size (Å)	total pore volume (cc/g)
o01	A	1.08E+02	38	9.86E+01	2.65E-01
o01	C4	9.03E+01	63	9.35E+01	2.11E-01
o01	C6	2.41E+01	161	2.68E+02	1.62E-01
o02	A	1.12E+02	41	1.11E+02	3.12E-01
o02	C4	7.89E+01	73	1.20E+02	2.37E-01
o02	C6	3.27E+01	141	2.01E+02	1.65E-01
o03	A	1.24E+02	33	7.26E+01	2.25E-01
o03	C4	7.88E+01	78	1.12E+02	2.21E-01
o03	C6	2.16E+01	192	2.56E+02	1.39E-01
o04	A	7.32E+01	106	9.97E+01	1.82E-01
o04	C4	7.04E+01	46	1.05E+02	1.85E-01
o04	C6	4.11E+01	53	1.54E+02	1.58E-01
o05	A	1.12E+02	74	1.48E+02	4.15E-01
o05	C4	9.49E+01	87	1.56E+02	3.69E-01
o05	C6	4.12E+01	190	3.09E+02	3.18E-01
o06	A	6.58E+01	144	1.81E+02	2.98E-01
o06	C4	9.77E+01	140	1.37E+02	3.35E-01
o06	C6	6.03E+01	175	1.57E+02	2.37E-01
o07	A	9.24E+01	37	1.11E+02	2.55E-01
o07	C4	5.37E+01	44	1.83E+02	2.45E-01
o07	C6	2.03E+01	109	3.88E+02	1.97E-01
o08	A	6.56E+01	30	1.37E+02	2.25E-01
o08	C4	4.93E+01	48	1.53E+02	1.89E-01
o08	C6	1.71E+01	222	3.64E+02	1.55E-01
o09	A	6.79E+01	40	1.23E+02	2.09E-01
o09	C4	3.14E+01	32	1.93E+02	1.52E-01
o09	C6	1.90E+01	169	3.19E+02	1.52E-01
o10	A	4.88E+00	43	3.41E+02	4.16E-02
o10	C4	4.96E+01	51	1.46E+02	1.81E-01
o10	C6	3.11E+01	108	2.07E+02	1.61E-01
o11	A	9.37E+01	31	1.12E+02	2.61E-01
o11	C4	6.56E+01	64	1.19E+02	1.95E-01
o11	C6	4.72E+01	94	1.61E+02	1.90E-01
o12	A	1.79E+01	29	3.40E+02	1.53E-01
o12	C4	6.16E+01	24	1.81E+02	2.78E-01
o12	C6	7.55E+00	88	4.38E+02	8.26E-02
o13	A	7.97E+01	49	1.44E+02	2.86E-01
o13	C4	5.99E+01	22	1.70E+02	2.54E-01
o13	C6	2.19E+01	127	4.49E+02	2.46E-01
o14	A	5.79E+01	102	1.59E+02	2.30E-01
o14	C4	7.89E+01	31	1.35E+02	2.67E-01
o14	C6	1.33E+01	139	5.62E+02	1.87E-01
o15	A	4.60E+01	28	2.00E+02	2.31E-01
o15	C4	7.98E+01	29	1.28E+02	2.56E-01
o15	C6	2.68E+01	107	3.44E+02	2.31E-01
o16	A	2.75E+01	340	1.98E+02	1.36E-01
o16	C4	6.63E+01	57	1.05E+02	1.74E-01
o16	C6	4.90E+01	74	1.36E+02	1.67E-01
o17	A	1.17E+02	52	2.01E+02	5.89E-01
o17	C4	1.15E+02	57	2.14E+02	6.13E-01
o17	C6	7.70E+01	59	2.94E+02	5.66E-01
o18	A	1.69E+01	80	4.40E+02	1.85E-01
o18	C4	7.46E+01	88	1.41E+02	2.63E-01
o18	C6	7.24E+01	120	1.29E+02	2.34E-01
o19	A	1.07E+01		1.71E+02	4.56E-02
o19	C4	8.76E+01		2.27E+02	4.98E-01
o19	C6	4.75E+01		3.84E+02	4.56E-01
o20	A	3.64E+01		1.52E+01	1.38E-02
o20	C4	2.00E+01		1.25E+02	6.24E-02
o20	C6	1.32E+01		1.57E+02	5.18E-02

4.2 Experimental Conditions in synthesis

4.2.1 Precursors

Precursors offer the metal ion in the metal oxide synthesis. Using CTAB, and the 50:50 water:ethanol mixture, we can test for the effects of various precursors. The precursors included in these experiments are $Ce(OH)_4$, $Ce(III)(NO_3)_3 – 6H_2O$, $CeCl_3$-$7H_2O$, and Cerium Glycolate.

For precursor effects, sample 001 is termed as the standard synthesis model with Cerium Hydroxide as the precursor. The other samples looked at are 004 with cerium Glycolate, 005 with cerium chloride hepta-hydrate, and 006 with cerium nitrate hexa-hydrate. In all circumstances the pore sizes fall within the mesoporous range. At 873K 005 shows the largest pores with 15.6nm as well as at 673K with 30.9nm whereas 006 shows the largest pore size at 393K with 18.1nm, followed by 005 with 14.8nm. For 005 the pore sizes increase with every calcination level, which shows surfactant removal from 14.8nm to 15.6nm, to 30.9nm. For 006 it decreases and reincreases going from 18.1nm to 13.7nm to 15.7nm, showing crystal growth and pore degradation, although 006 shows the largest surface area at 673K and at 873K. Based on this and pore volume sample 006 is the most thermally stable

4.2.2 Surfactants

The surfactants can be cationic, anionic, and neutral. The interaction of the surfactant with the precursor ions and solvent system can vary with the different ionic ends. Keeping the $Ce(OH)_4$ precursor, the 50:50 water:ethanol mixture, we test for the effects of various surfactants. The surfactants included in these experiments are CTAB, myristyl trimethyl ammonium bromide, CTAB with paraffin, SDS, CTAB with SDS, high concentration CTAB, high concentration SDS, triton-x, and n-hexadecylamine. CTAB, and myristyl trimethyl ammonium bromide are cationic surfactants, the latter being shorter. SDS is an anionic surfactant. Triton-X, and n-hexadecylamine are neutral surfactants. Paraffin is used as a surfactant aid, with the idea that it will bulk up the micelle size.

For surfactant effects we compare samples, 001 (CTAB), 002(myristyl trimethyl ammonium bromide) , 007(CTAB:paraffin:MeCl2), 008(CTAB:paraffin), 009 (SDS), 010(CTAB:SDS), 014(triton-x), and 015(n-hexadecylamine). At 693K the surface area is greatest for sample 001 at 90.3m^2/g and the lowest is for sample 009 at 31.4 m^2/g. Samples 015, 014, 002 have fairly high surface area at 79.8 m^2/g, 78.9 m^2/g and 78.9 m^2/g. Sample 002 has the highest surface area at 873K of 32.7 m^2/g.

As for pore size, sample 009 had has the largest pore size at 19.3nm at 673K. While sample 014 has the largest pore volume at 0.230cc/g. Comparing these data we can determine that sample 002, with the cationic myristyl trimethyl ammonium bromide, is the most thermally stable in this category; it has a smaller change in final pore size and fairly consistent pore volume. CTAB was ultimately used the doped ceria synthesis because it yielded the highest surface area at 673K.

4.2.3 Doping

We doped ceria using Samarium, Titanium, and Copper. Samarium is used because it increases electrical conductivity, titanium is used because it increases thermal stability and copper is known to improve low temperature oxidation activity of ceria. As a precursor for cerium we used $Ce(III)(NO_3)_3 – 6H_2O$ with CTAB as a surfactant and 50:50 water:ethanol solvent mixture. For the dopant precursors we used $Sm(III)(NO_3)_3 – 6H_2O$, Titanium Isopropoxide and $Cu(III)(NO_3)_3$-$2.5H_20$.

For doping effects we compare samples 001 (non-doped ceria), 016(samarium (50%) doped ceria), 017(titania (48%) doped ceria), 018 (copper (66%) doped ceria), 019(copper (25%) doped ceria) and 020(samarium (25%) doped ceria). At 693K the surface area is greatest with sample 017; the titanium doping increases thermal stability. Pore volume and pore size also were highest with 017. At 893K the lowest surface area was from 001 without any doping. At 873K the pore volume and pore size is the lowest in sample 001, which shows that doping in general does increase thermal stability.

4.2.4 Solvent systems

The solvent system will greatly influence the synthesis process as well. Using CTAB, and $Ce(OH)_4$ we used 50:50 water:ethanol mixture, hexane and toluene as solvent systems. It should be noted that by using a non-polar solvent the base had to be adjusted as well. A non-polar solvent will induce a reverse micelle structure.

For solvent systems, sample 001(water:ethanol:NaOH), 003(hexane:NaOH), and 011(toluene:pyridine) are compared. At 693K the surface area is largest with 001 with 90.3 m^2/g but at 873K it is largest at 011 with 47.2 m^2/g. Pore size is largest with 011 with 11.9nm at 673K and remains the most stable when compared with 873K at 16.1nm. It also has the most stable pore volume from 673K to 873K with 0.195cc/g and 0.190cc/g.

4.2.5 Surfactant concentration

For CTAB concentration effect we compare samples 001(100mM) and 012(300mM). At 693K the surface area is larger at lower concentration with 90.33 m^2/g for 001 compared to 61.6 m^2/g for 012 both dropping, to 24.1 m^2/g and 7.55 m^2/g respectively at 873K. Similarly the crystal size for 001 increases 6.3nm to 16.1nm and for 012 from 2.4nm to 8.8nm. The pore sizes in sample 012 appear to be larger and have similar pore volume. Both samples have low thermal stability.

For SDS concentration effect we compare samples 009(100mM) and 013(300mM). At 693K the surface area is greater at higher concentration with 59.9 m^2/g for 013 compared to 31.4 m^2/g for 009 both dropping, 013 to 21.9 m^2/g and 009 to 18.7 m^2/g at 873K. The crystal size for sample 013 increases from 2.2nm to 12.7nm and for sample 009 increases from 3.2nm to 16.9nm. The pore size is fairly similar for both and total pore volume is greater at the higher concentration. Thermal stability is comparable for both samples. Sample 013 appears to be better at 673K but falls just as short as sample 009 at 873K.

4.3 XRD diffractogram analysis and isotherm interpretation

X-ray diffraction analysis shows that all samples were monophasic materials consistent with cubic ceria, with the exception of samples 016 and 018, which show phase separation coinciding with samarium and copper respectively. pXRD of most samples (with the exception of 002,014, 015), show a low angle peak at $2\Theta = 1.55$ giving an interplanar distance of 5.7nm, which is fairly consistent with the average pore size of most samples (considering that this value would represent only the pores that have order and periodicity, whereas the pore size from physisorption is an average of all pores). This peak is maintained throughout yet decreases with increasing temperature. A few samples, 003A, 007A, 012A, 013A also exhibit a secondary low angle peak at $2\Theta = 3.175$ giving an interplanar distance of 2.8nm at as-synthesized which disappears after calcination. This would represent pores that still have surfactant in them and therefore retain the long-range order of the structure. Upon calcination, the periodicity is broken and the peaks disappear

For the most part the pore size distribution shows a narrow breadth and a conservative area of distribution within the mesoporous range (figure 11). The isotherms for all samples are type IV with hysteresis type H3, representing slit-shaped pores (figure 12).

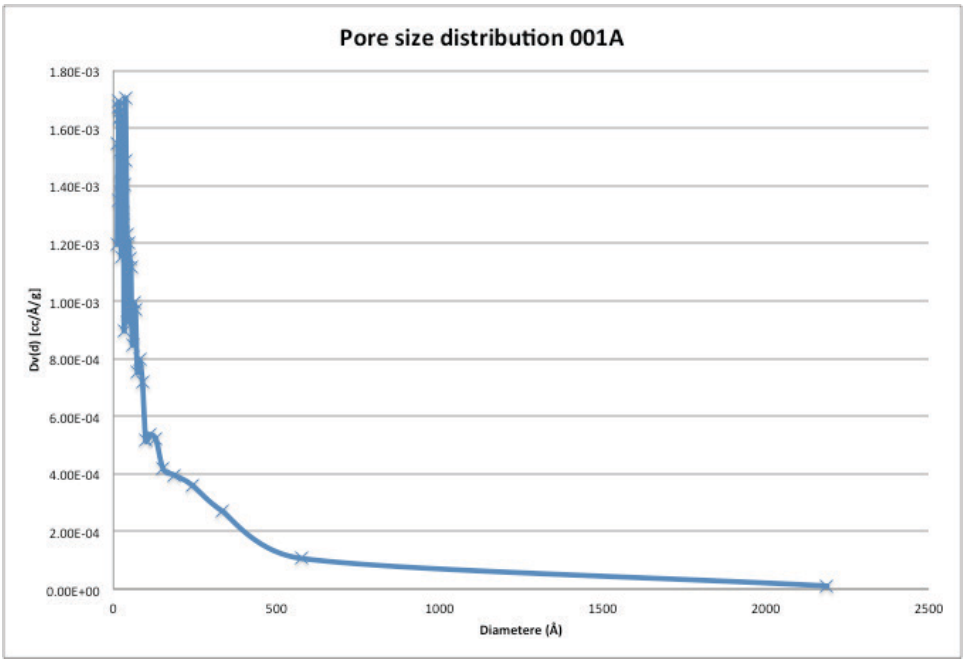

Figure 11 Pore size distribution of sample 001A, synthesized from cerium (IV) hydroxide, CTAB, water, ethanol, and sodium hydroxide

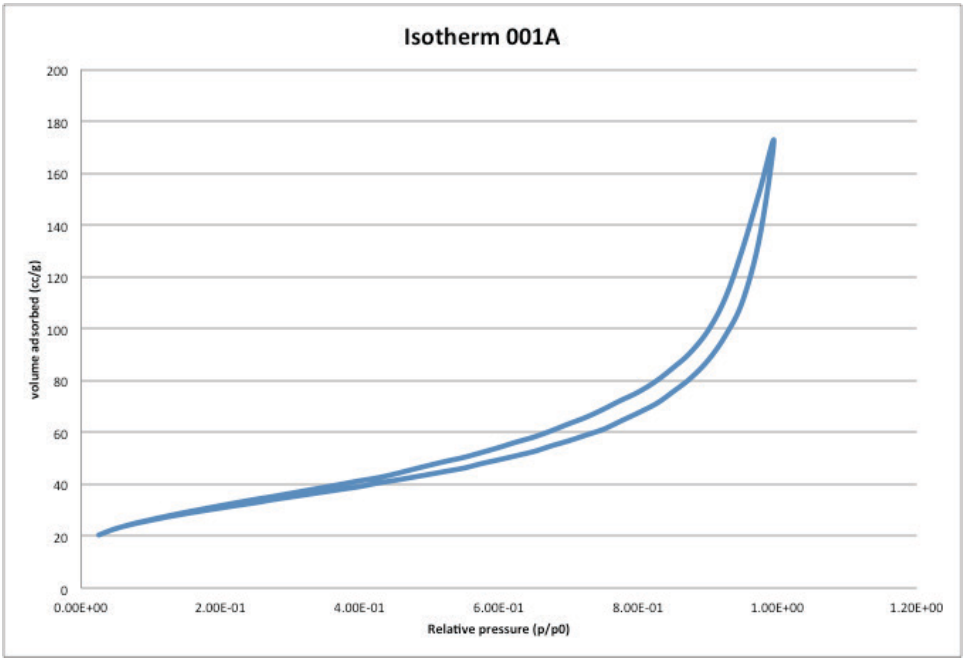

Figure 12 Isotherm of sample 001A uncalcinated; synthesized from cerium (IV) hydroxide, CTAB, water, ethanol, and sodium hydroxide, showing type IV with hysteresis type H3

4.3.1 Sample 001

There are nominal changes in pore size from 393K to 673K with 9.85nm to 9.35nm, while more than doubling at 873K with 26.8nm. The total pore volume decreases with each level, from 0.265cc/g to 0.211cc/g to 0.162cc/g showing that pores are collapsing. This is further demonstrated by the surface area, which drops from 107.7 m^2/g to 90.3 m^2/g, to 24.1 m^2/g at 873K. Crystal sizes are 3.8nm, 6.3nm and 16.1nm at 393K, 673K, and 873K respectively. The increasing crystal size and growth is another sign of poor thermal stability. Overall this implies poor thermal stability. In figures 13 and 14, we see the low angle peak, which degrades at the higher temperature and plane labelling[33] for cubic fluorite ceria.

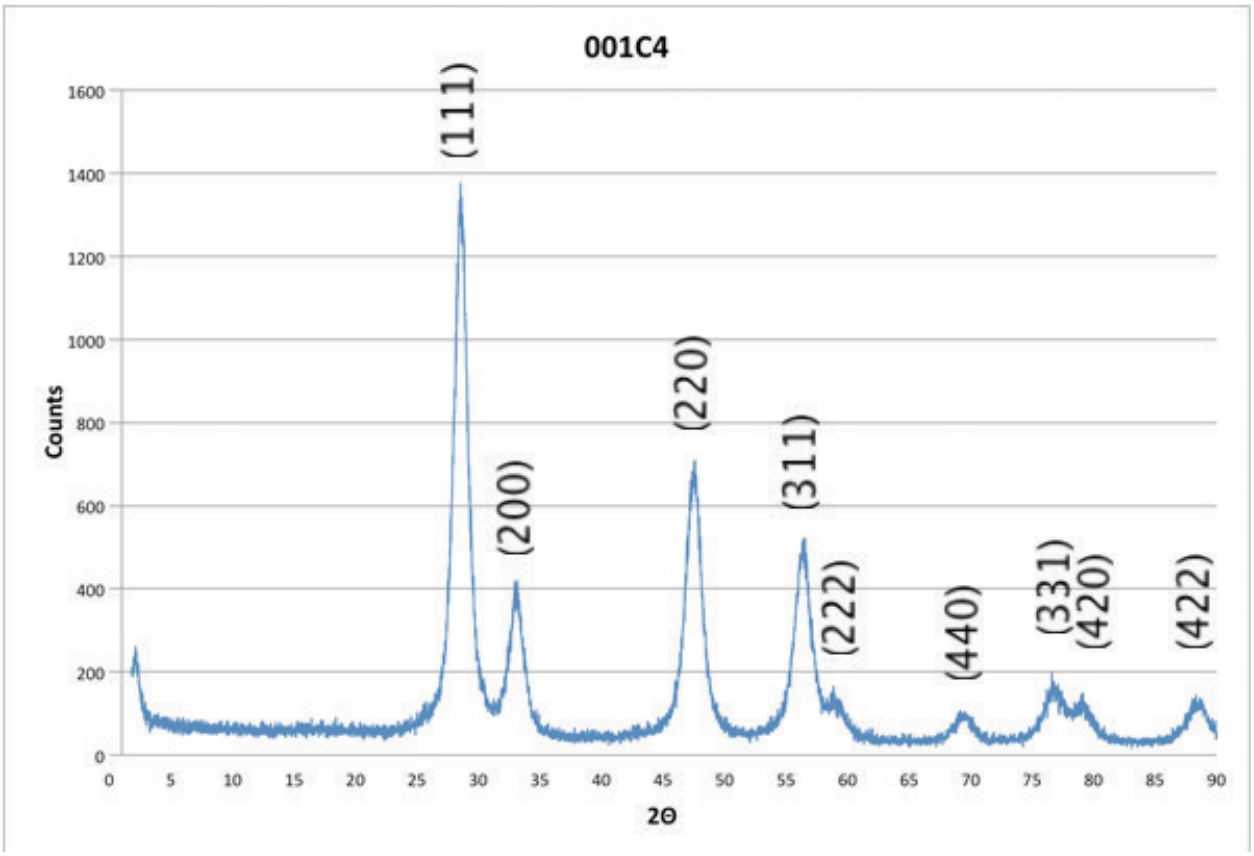

Figure 13 pXRD of sample 001C4 calcinated at 673K, synthesized from cerium (IV) hydroxide, CTAB, water, ethanol, and sodium hydroxide

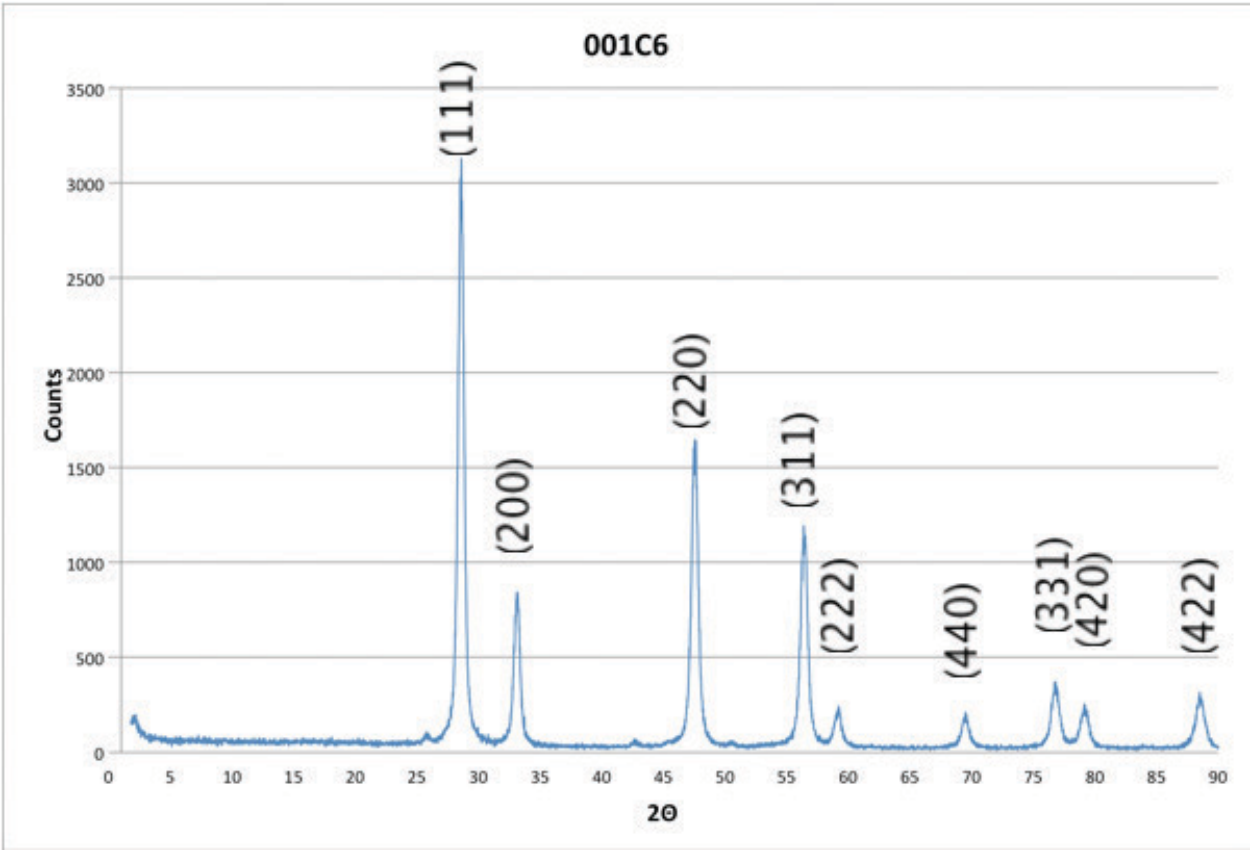

Figure 14 pXRD of sample 001C6 calcinated at 873K, synthesized from cerium (IV) hydroxide, CTAB, water, ethanol, and sodium hydroxide

4.3.2 Sample 002

The pore size is similar at 393K and 673K with 11.1nm and 12.0nm respectively. At 873K the average pore size is 20.1nm. The total pore volume decreases with each level, from 0.312cc/g to 0.237cc/g to 0.165cc/g showing that pores are collapsing. This is further demonstrated by the surface area, which drops from 112.3 m^2/g to 78.9 m^2/g, to 32.7 m^2/g at 873K. Crystal sizes are 4.1nm, 7.3nm and 14.1nm at 393K, 673K, and 873K respectively. Overall this implies poor thermal stability.

4.3.3 Sample 003

There is a consistent increase in pore size with each level from 7.3nm to 11.2nm to 25.6nm. The pore volume stays steady at 673K going from 0.225cc/g to 0.221cc/g but drops at 873K at 0.139cc/g, showing that pores are collapsing. This is further demonstrated by the surface area, which drops from 123.7 m^2/g at 393K, 78.8 m^2/g at 673K, and 21.6 m^2/g at 873K. Crystal sizes are

3.3nm, 7.8nm and 19.2nm at 393K, 673K, and 873K respectively. Overall this implies poor thermal stability.

4.3.4 Sample 004

There is increasing pore size with each level, from 9.97nm to 10.5nm to 15.4nm. Pore volume stays fairly consistent with a minor decrease at 873K going from 0.1823cc/g to 0.1848cc/g to 0.1584cc/g. The effect of pore collapse is seen more in the surface area decrease with 73.2 m^2/g at 393K, 70.4 m^2/g at 673K, and 41.1 m^2/g at 873K. Crystal sizes are 10.6nm, 4.6nm and 5.3nm at 393K, 673K, and 873K respectively. Overall there is decent thermal stability.

4.3.5 Sample 005

There is a consistent pore size with an increase at 873K going from 14.8nm to 15.6nm to 30.9nm. Pore volume decreases at each level going from 0.415cc/g to 0.369cc/g then to 0.318cc/g. The effect of pore collapse is reflected with the surface area decrease with 111.9 m^2/g at 393K, 94.9 m^2/g at 673K, and 41.2 m^2/g at 873K. Crystal sizes are 7.4nm, 8.7nm and 19.0nm at 393K, 673K, and 873K respectively. Pore size increases, while pore volume decreases and surface area decreases, while crystal size increases. Overall this shows poor thermal stability.

4.3.6 Sample 006

There is a decrease in pore size going from 18.1nm to 13.7nm followed by an increase in pore size to 15.7nm and an increase then a decrease in pore volume starting at 0.298cc/g going to 0.335cc/g to 0.237cc/g. The surface area is 65.8 m^2/g at 393K, 97.7m2.g at 673K, and 60.3 m^2/g at 873K. Crystal sizes are 14.4nm, 14.0nm and 17.5nm at 393K, 673K, and 873K respectively. At 873K the rise in pore size and decrease in pore volume and surface area show that there is greater collapse in the final step. Overall showing mild thermal stability.

4.3.7 Sample 007

Pore size increases slightly at 673k from 11.1nm to 18.3nm and greatly at 873K to 38.8nm. Pore volume stays similar at 673K from 0.255cc/g to 0.245cc/g then decreases at 873K with 0.197cc/g. There is a significant surface area decrease at each step as well from92.4 m^2/g to 53.7 m^2/g to 20.3 m^2/g. Crystal sizes are 3.7nm, 4.4nm and 10.9nm at 393K, 673K, and 873K respectively. In this case there are pores collapsing to form larger pores at 673K, which explains the surface area drop as well. At 873K the pore size increases even more with a drop in volume and a severe drop in surface area, which indicate that pore walls collapse as especially forming open-ended pores.

4.3.8 Sample 008

Pore size increases slightly at 673K from 13.7nm to 15.3nm and significantly at 873K to 36.4nm. Pore volume decrease from an initial 0.225cc/g to 0.189cc/g at 673K and 0.155cc/g at 873K. This shows pore degradation and therefore low thermal stability especially at 873K. This is further demonstrated by the decrease in surface area, going from 65.6 m^2/g to 49.3 m^2/g then to 17.1 m^2/g. Crystal sizes are 4.1nm, 7.3nm and 14.1nm at 393K, 673K, and 873K respectively. All factors are indicative of poor thermal stability.

4.3.9 Sample 009

Pore size increases from 12.3nm at 393K to 19.3nm at 673K then further increases to 31.9nm at 873K. Pore volume decreases initially then maintains starting at 0.209cc/g at 393K going to 0.152cc/g at 673K and staying there at 873K. This shows pore degradation throughout and low thermal stability. This is also demonstrated by the decrease in surface area going from 67.9 m^2/g to 31.4 m^2/g then to 19.0 m^2/g and the crystal size increase from 4.1nm, 7.3nm and 14.1nm at 393K, 673K, and 873K respectively.

4.3.10 Sample 010

pore size decreases then reincreases going from 34.1nm to 14.6nm then back up to 20.7nm. Pore volume increased from the 0.042cc/g to 0.181cc/g then down a little bit to 0.161cc/g. The surface area increases at every step from 4.88 m^2/g to 49.6 m^2/g then to 31.1 m^2/g. Crystal size increases from 4.3nm, 5.1nm and 10.8nm at 393K, 673K, and 873K respectively. The surface area results are consistent with the pore volume changes and the differences with pore sizes can be explained by crystallization, which thickens the pore walls decreasing the internal pore size then pore degradation due to poor thermal stability.

4.3.11 Sample 011

Pore size increases slightly from 11.2nm at 393K to 11.9nm at 673K then increases to 16.1nm 873K. Pore volume decreases from 0.261cc/g to 0.195cc/g then to 0.190cc/g. The surface area decreases from 93.7 m^2/g to 65.6 m^2/g then finally to 47.2 m^2/g. Crystal size increases from 3.1nm, 6.4nm and 9.4nm at 393K, 673K, and 873K respectively. This shows pore degradation and low thermal stability.

4.3.12 Sample 012

Pore size is 34.0nm at 393K then drops to 18.1nm at 673K and increases to 43.8nm at 873K. The volume increases from 0.153cc/g to 0.278cc/g then goes down to 0.083cc/g. The surface area increases from 17.9 m^2/g to 61.6 m^2/g then drops back down to 7.55 m^2/g. This shows signs of pore degradation. Crystal size increases from 2.9nm, 2.4nm and 8.8nm at 393K, 673K, and 873K respectively.

4.3.13 Sample 013

Pore size is 14.4nm at 393K then increases to 17.0nm at 673K and further to 44.9nm at 873K. The pore volume decreases from 0.286cc/g to 0.254cc/g then to 0.246cc/g at 873K. The surface area decreases from 79.7 m^2/g to 59.9 m^2/g then to 21.9 m^2/g. Crystal size decreases from 4.9nm to 2.2nm and increases to 12.7nm at 393K, 673K, and 873K respectively. This shows overall pore degradation.

4.3.14 Sample 014

Pore size is 15.9nm at 393K then decreases to 13.5nm at 673K and increases to 56.2nm at 873K. The pore volume increases from0.230cc/g to 0.267cc/g then decreases down to 0.187cc/g. The surface area reflects the same trend, increasing from 57.9 m^2/g to 78.9 m^2/g then decreasing to 13.3 m^2/g. Crystal size increases from 10.2nm, 3.1nm and 13.9nm at 393K, 673K, and 873K respectively. This shows the calcination process followed by pore degradation at higher temperatures.

4.3.15 Sample 015

Pore size is 20nm at 393K then decreases to 12.8nm at 673K then increases to 34.4nm at 873K. The pore volume increases from 0.231cc.g to 0.256cc/g and back to 0.231cc/g. The surface area follows a similar trend increasing 46.0 m^2/g to 79.8 m^2/g then down to 26.8 m^2/g. Crystal size increases from 2.8nm, 2.9nm and 10.7nm at 393K, 673K, and 873K respectively. This shows the calcination process and pore degradation at higher temperatures.

4.3.16 Sample 016

Pore size is 19.8nm at 393K decreasing to 10.5nm at 673K then increasing up to 13.6nm at 873K. Pore volume follows and opposite trend going from 0.136cc/g to 0.174cc/g to 0.167cc/g. Surface area is 27.5 m^2/g at 393K then increases to 66.3 m^2/g and drops to 49.0m^2/g. Crystal size decreases from 34.0nm, 5.7nm and 7.4nm at 393K, 673K, and 873K respectively. This shows the calcination

process and slight pore degradation at higher temperatures. The pXRD of 016A (figure 15) shows phase separation indicating samarium wasn't fully integrated into the ceria fluorite crystal. The phase separation is evident with the additional peaks that appear on the pXRD in addition to the peaks for ceria. For 016C4 (figure 16) this phase separation is non-existent indicating integration.

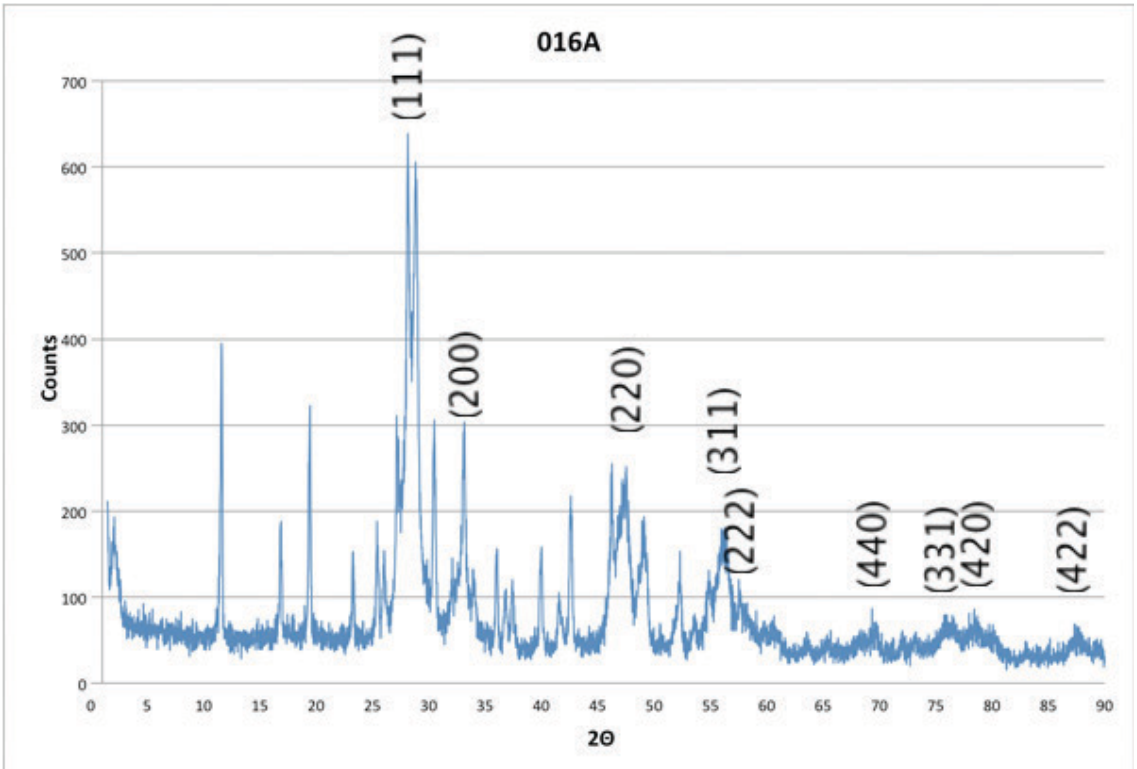

Figure 15 pXRD of sample 016A uncalcinated, synthesized from cerium (III) nitrate hexahydrate, samarium (III) nitrate hexahydrate, CTAB, water, ethanol, and sodium hydroxide

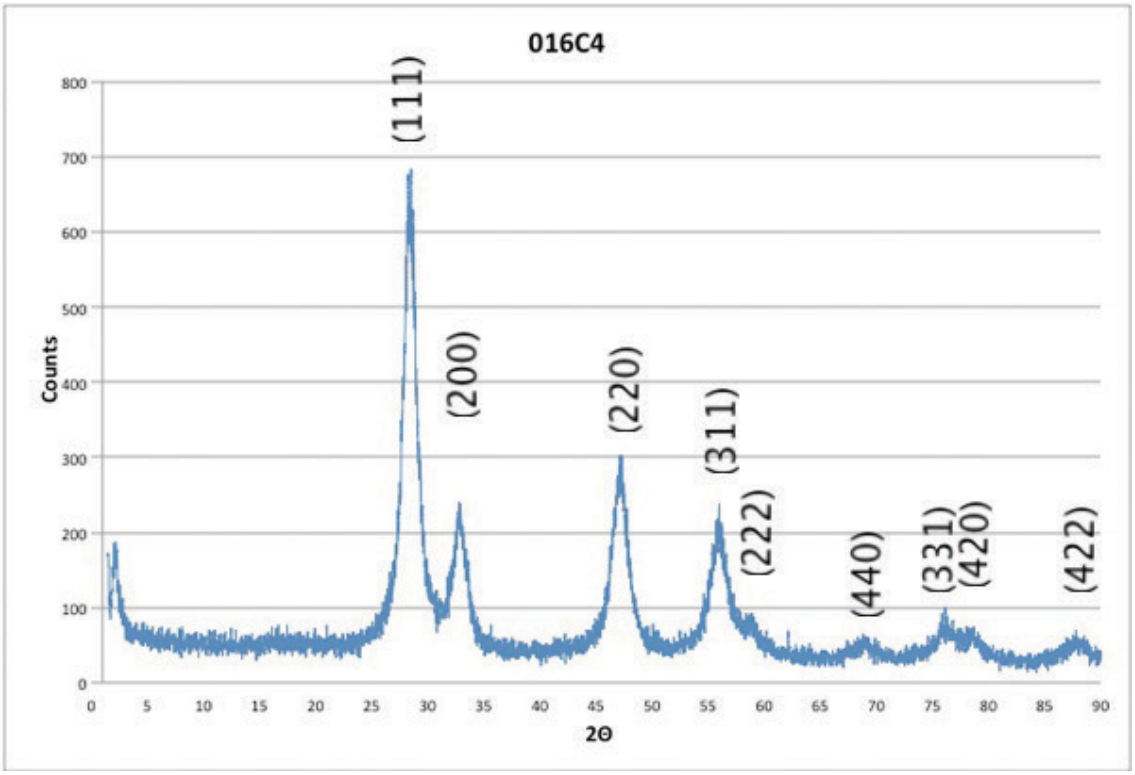

Figure 16 pXRD of sample 016C4 calcinated at 673K, synthesized from cerium (III) nitrate hexahydrate, samarium (III) nitrate hexahydrate, CTAB, water, ethanol, and sodium hydroxide

4.3.17 Sample 017

Pore size is 20.1nm at 393K increasing to 21.4nm at 673K and to 29.4nm at 873K. Pore volume increases from 0.589cc/g to 0.613cc/g then decreases to 0.566cc/g. The surface area is 117.3 m^2/g at 393K then slightly decreasing to 114.9 m^2/g at 693K decreasing to 77.0 m^2/g at 873K. Crystal size increases from 5.2nm, 5.7nm and 5.9nm at 393K, 673K, and 873K respectively. This sample shows good thermal stability. The pXRD of 017A (figure 17) and 017C4 (figure 18) show integration of titanium into the ceria fluorite crystal by only having peaks for ceria.

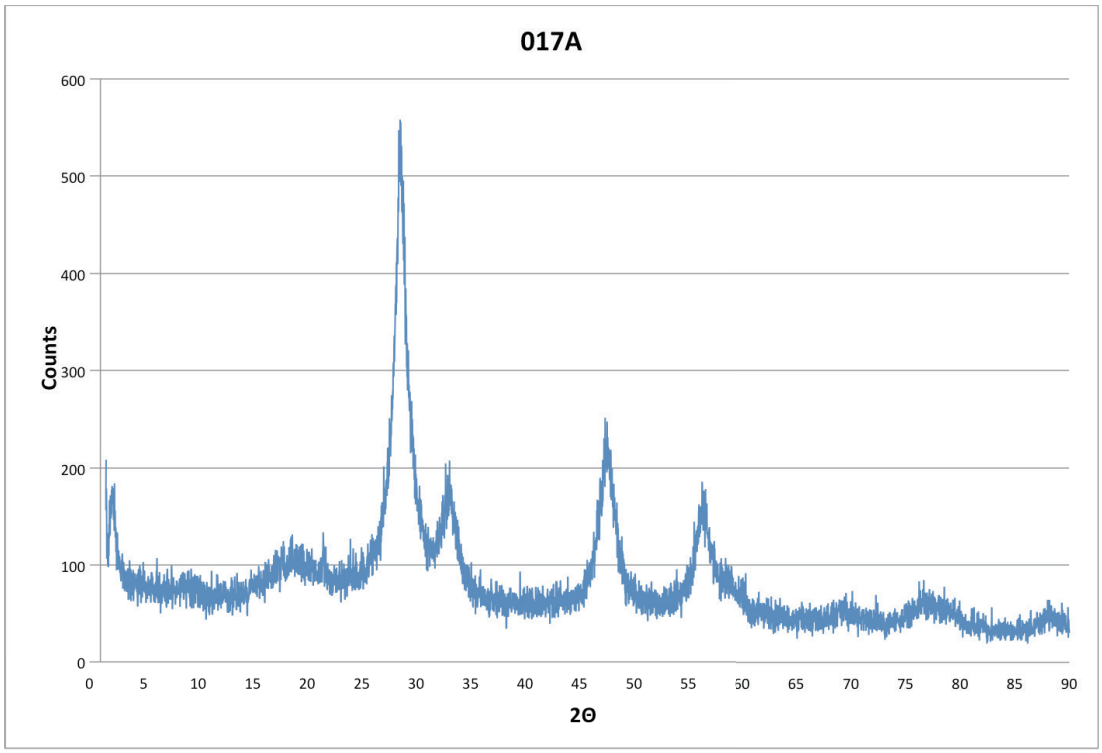

Figure 17 pXRD of sample 017A uncalcinated, synthesized from cerium (III) nitrate hexahydrate, titanium isopropoxide, CTAB, water, ethanol, and sodium hydroxide

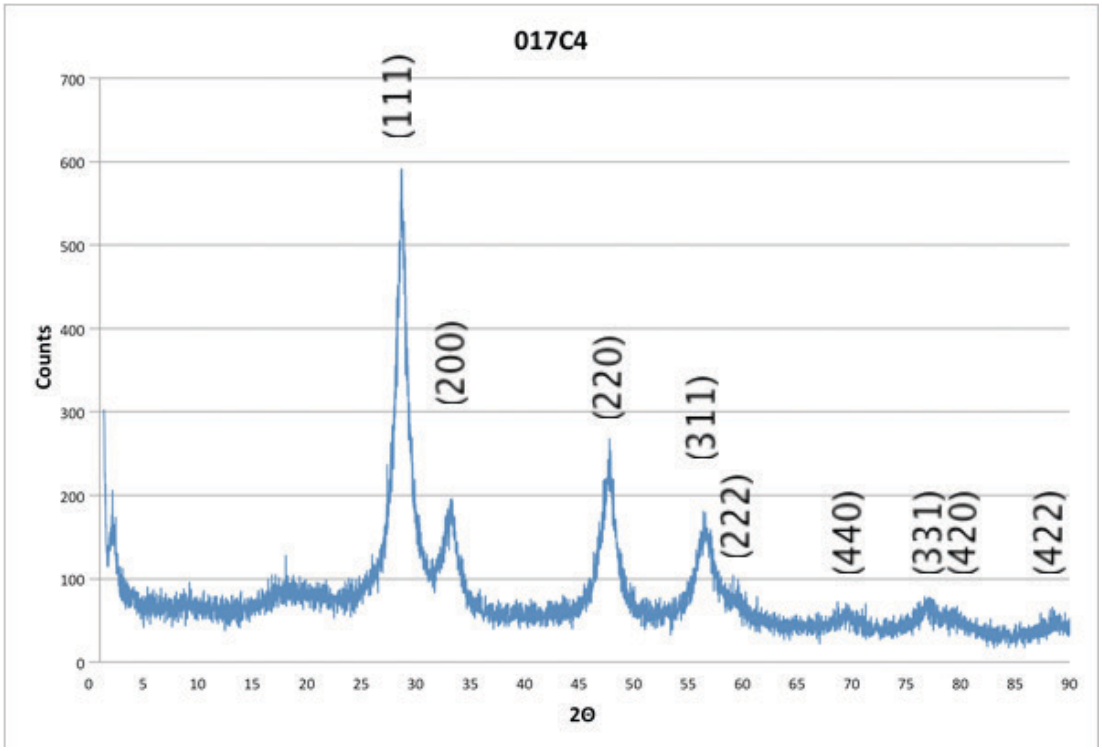

Figure 18 pXRD of sample 017C4 calcinated at 673K, synthesized from cerium (III) nitrate hexahydrate, titanium isopropoxide, CTAB, water, ethanol, and sodium hydroxide

4.3.18 Sample 018

Pore size is 44nm at 393K decreasing to 14.1nm at 673K then to 12.9nm at 873K. The pore volume increases from 0.185c/g to 0.263cc/g then decreasing to 0.234cc/g. Surface area increases from 16.9 m^2/g to 74.6 m^2/g and staying similar with 72.4 m^2/g at 873K. Crystal size increases from 8.0nm, 8.8nm and 12.0nm at 393K, 673K, and 873K respectively. This shows the calcination process and fair thermal stability. The pXRD of 018 (figure 19, 20, and 21) shows copper integration at 293K, then disintegration at 673K and 873K.

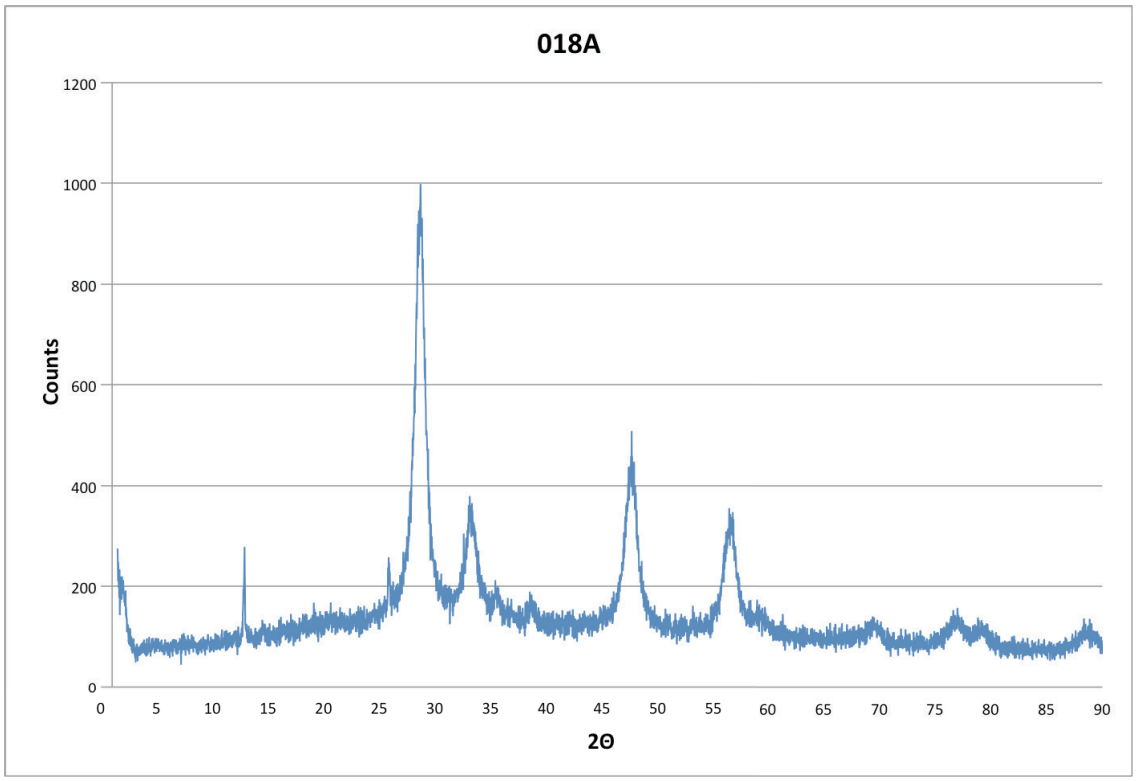

Figure 19 pXRD of sample 018A uncalcinated, synthesized from cerium (III) nitrate hexahydrate, copper (II) nitrate hemipentahydrate, CTAB, water, ethanol, and sodium hydroxide

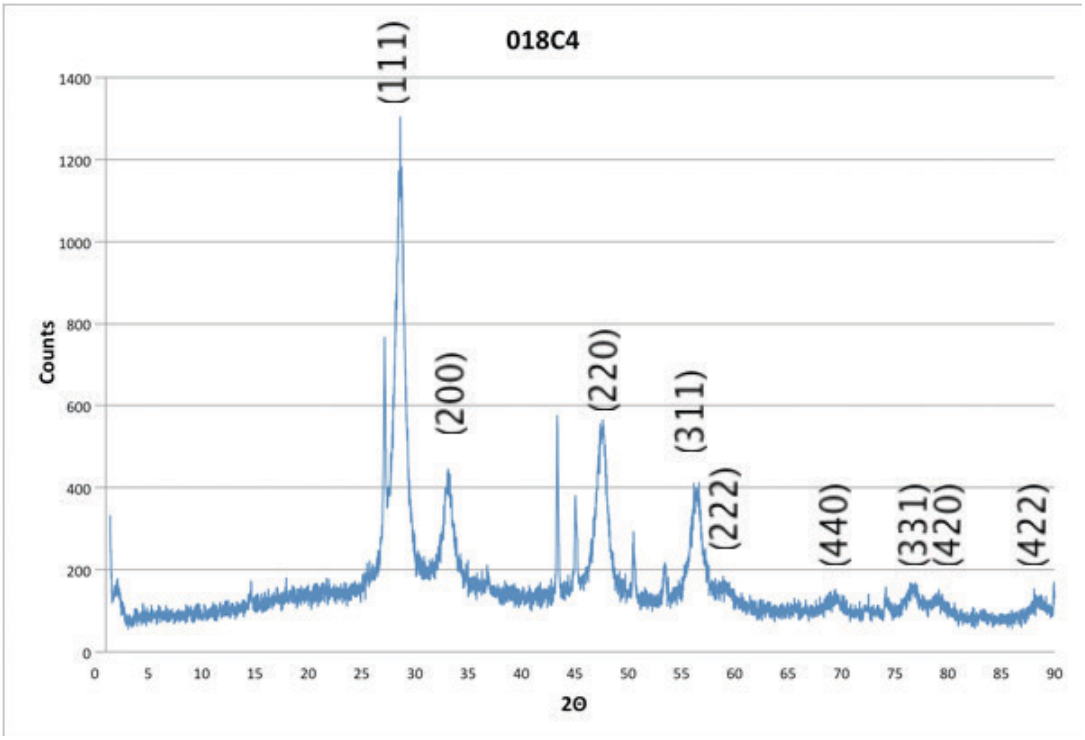

Figure 20 pXRD of sample 018C4 calcinated at 673K, synthesized from cerium (III) nitrate hexahydrate, copper (II) nitrate hemipentahydrate, CTAB, water, ethanol, and sodium hydroxide

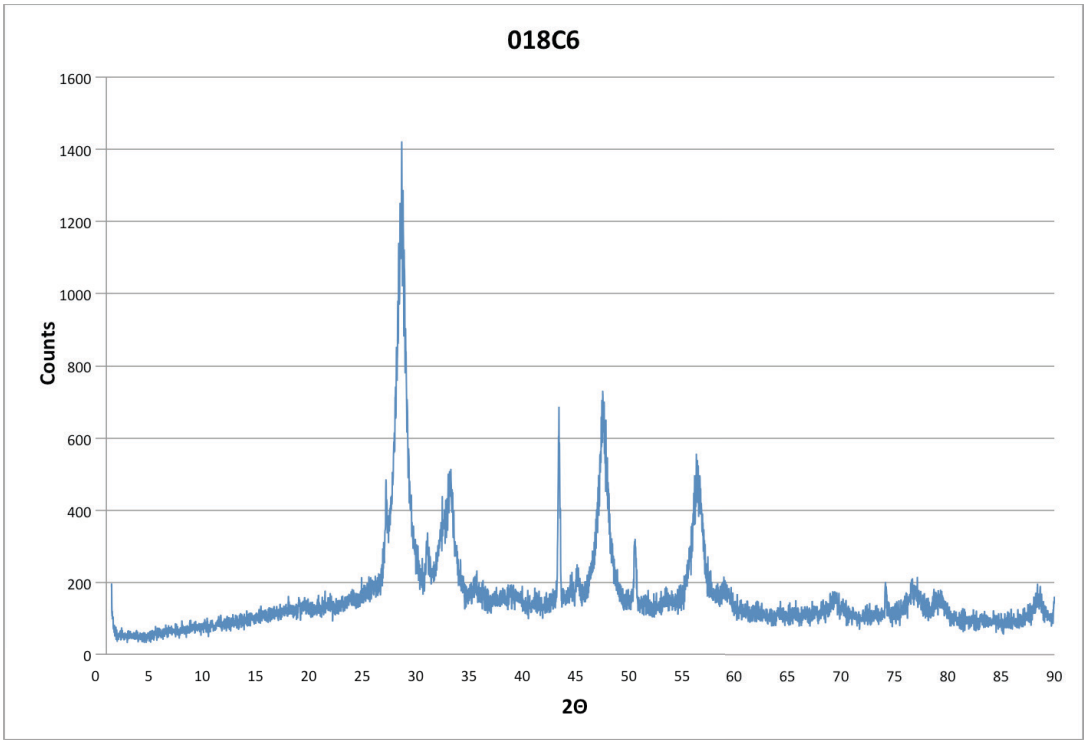

Figure 21 pXRD of sample 018C6 calcinated at 873K, synthesized from cerium (III) nitrate hexahydrate, copper (II) nitrate hemipentahydrate, CTAB, water, ethanol, and sodium hydroxide

4.3.19 Sample 019

Pore size is 17.1nm at 393K increasing to 22.7nm at 673K then to 38.4nm at 873K. Pore volume increases from 0.0456cc/g at 393K to 0.498cc/g at 673K maintaining a similar pore volume at 873K with 0.456cc/g. Surface area increases from 10.7 m^2/g to 87.6 m^2/g decreasing to 47.5 m^2/g at 393K, 673K and 873K respectively. This shows the calcination process and low thermal stability.

4.3.20 Sample 020

Pore size is 1.52nm at 393K increasing to 12.5nm at 673K and 15.7nm at 873K. Pore volume increases from 0.0138cc/g at 393K to 0.0624cc/g at 673K with a small decrease to 0.0518cc/g at 873K. Surface area decrease constantly from 36.4 m^2/g to 20.0 m^2/g to 13.2 m^2/g at 393K, 673K and 873K respectively. This shows the calcination process and low thermal stability.

4.4 SEM

Through SEM imaging we can see that samples 006C4, figure 22 a) and 008C4, figure 22 b), resemble a spherical-like sponges with varied pore shapes. When we compare the uncalcinated sample 008A to 008C4, calcinated at 673K, we see a smoother surface, figure 22 c), d); representing filled pores in sample 008A whereas 008C4, figure 22 b), has a very porous surface comparable to a uniform, small scale pumice stone. In sample 008A the pores filled with surfactants, while 008C4 shows the porous ceria shell left behind. For 008C6 (not shown) we'd expect to see collapsed pores on a denser structure.

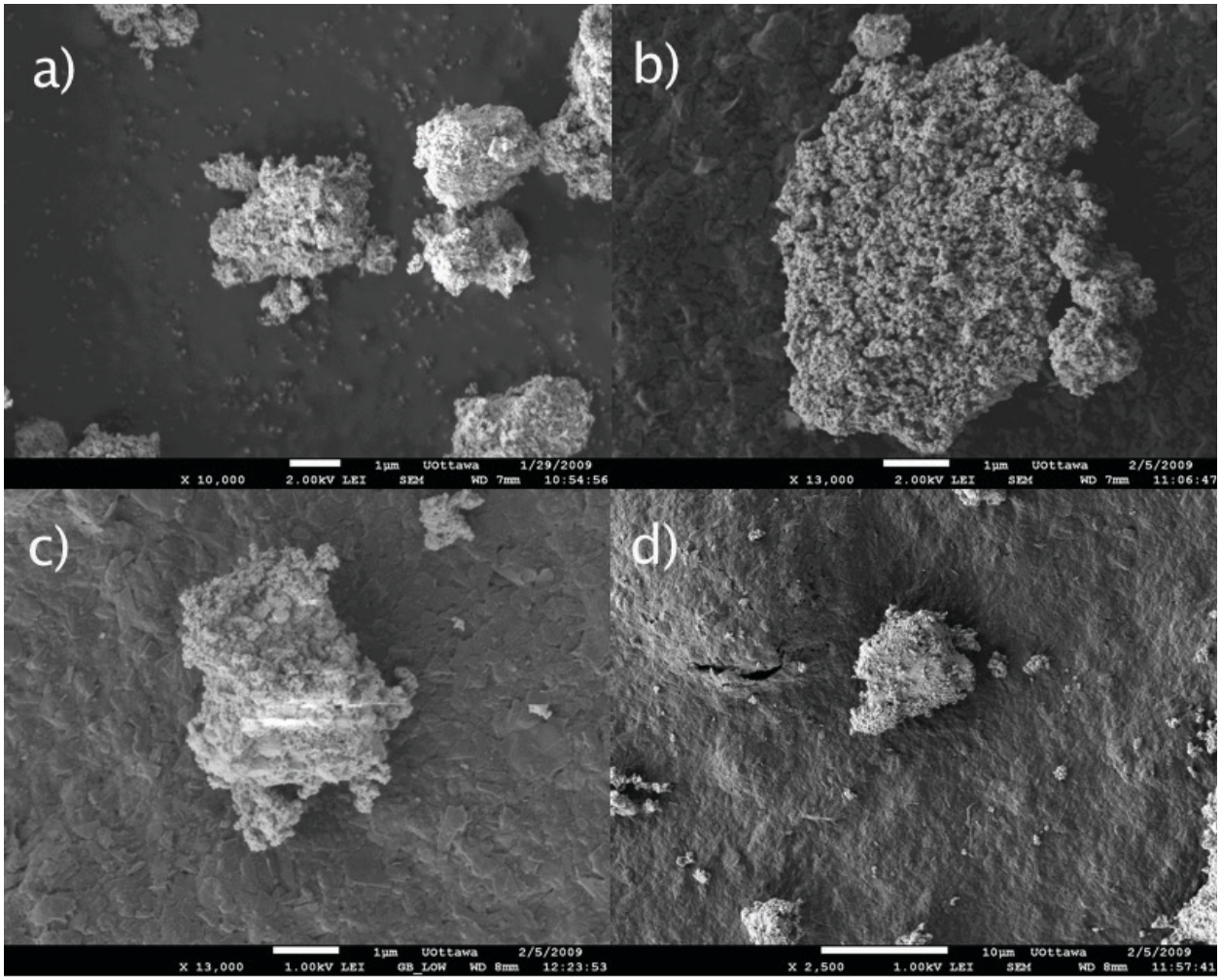

Figure 22 SEM of sample 006C4 (a) synthesized from cerium (III) nitrate hexahydrate, CTAB, water:ethanol, and NaOH, calcinated at 673K; sample 008C4 (b) synthesized from cerium (IV) hydroxide, CTAB:paraffin, water:ethanol, and NaOH,, calcinated at 673K; sample 008A (c,d) synthesized from cerium (IV) hydroxide, CTAB:paraffin, water:ethanol, and NaOH,, as-synthesized.

4.5 TEM

From TEM imaging of sample 017A uncalcinated titania doped ceria we can see aggregation of particles in figure 23 a). We can also confirm the cubic shape of ceria crystals in figure 23 b) and from measurement of crystal size in figure 23 b) there is a mean crystallite size of 12.35nm compared to the 5.2nm from pXRD. Note: in the TEM image the measurements are from visible and clearly defined crystals, which tend to be the larger ones. In figure 23 c) and 23 d) we can also see the lattice spacing.

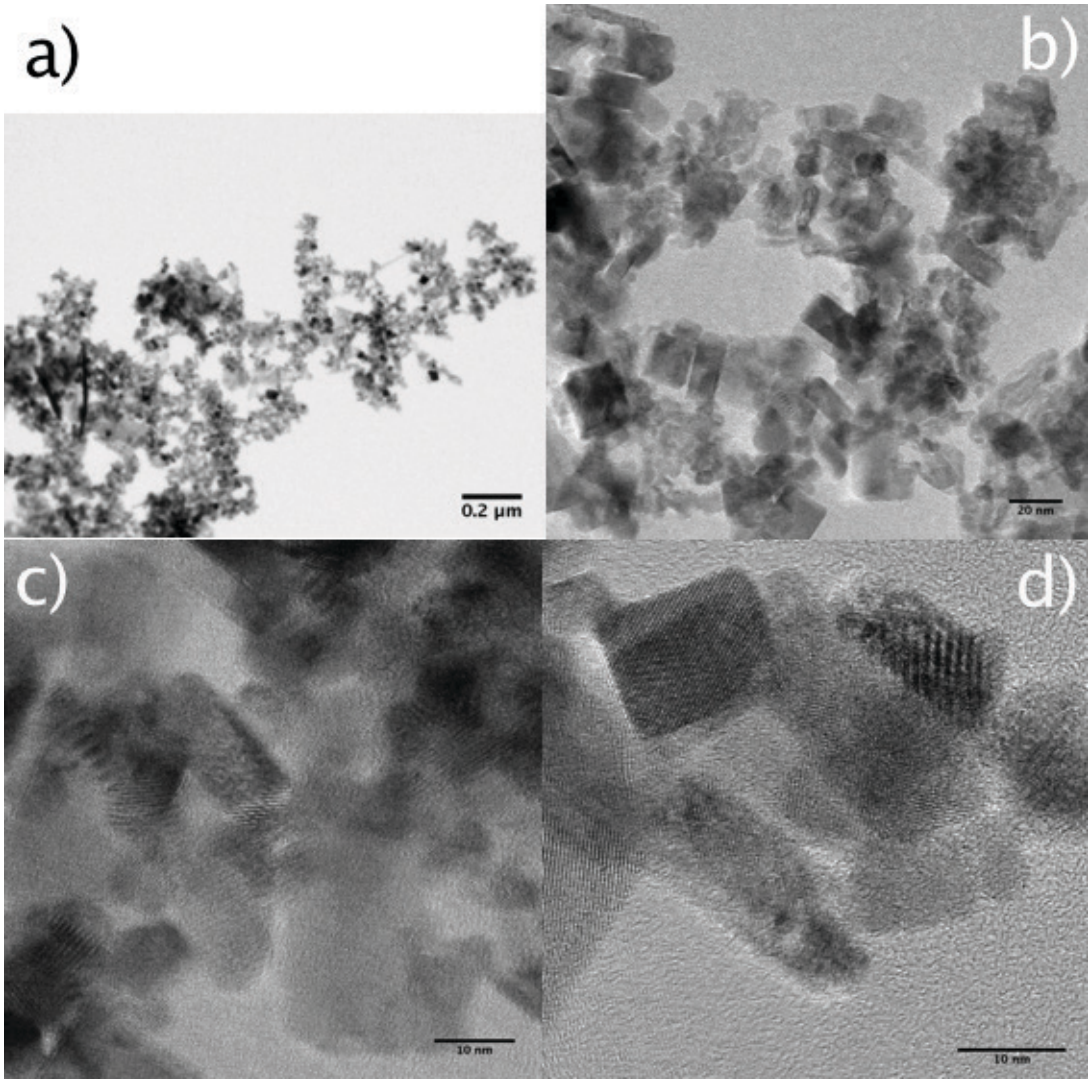

Figure 23 TEM images of sample 017A, synthesized from cerium (III) nitrate hexahydrate, titanium isopropoxide, CTAB, water, ethanol, and sodium hydroxide; uncalcinated, synthesized from cerium (III) nitrate hexahydrate, titanium isopropoxide, CTAB, water, ethanol, and sodium hydroxide (a) 8,000x (b) 10,000x (c) 30,000x (d) 40,000x; all at 200kV

4.6 Conclusion

Analysis of each sample was conducted through characterization techniques, comparing them with XRD and gas adsorption for crystallite size long-range order, pore volume, average pore size, and surface area. Crystallite size varied from 34.0nm to 2.2nm. Typically trending to have a larger crystallite size at higher temperatures, save for a few samples exhibiting high thermal stability. Pore volume and pore size follow a similar trend, although it should increase initially because of the calcination process, it also increases at higher temperatures because or pore degradation, again

except for a few thermally stable sample. Surface area follows an inverted trend of pore size and pore volume since pore degradation decreases the applicable surface of the catalyst.

Further more select samples were chosen to test methane oxidation with a microreactor. XRD and gas adsorption assume spherical shape of particles. SEM and TEM were used to take a closer look at the actual particles and determine shape.

CTAB concentration effects show that a lower concentration of CTAB has greater thermal stability and surface area at 673K. While SDS concentration effects show that a higher concentration of SDS has greater thermal stability and surface area at 673K. Doping ceria with titanium provides the most stability to give great thermal stability and high surface area at 673K.

Cationic surfactant showed to be the most effective surfactant yielding a high surface area and showing higher thermal stability over the other surfactants. Sodium dodecyl sulphate (SDS), an anionic surfactant, yields a lower surface area but a slightly better thermal stability. Since the target temperature is 673K CTAB is considered to be the best-suited surfactant.

Cerium nitrate hexahydrate produces the most thermally stable product out the four precursors, yielding the highest surface area at 673K.

Solvent system effects show that using hexane with NaOH yields a high surface area, at 393K, with very poor thermal stability. Water/ethanol with NaOH yields the highest surface area at 673K while using toluene and pyridine yields the highest surface area at 873K and demonstrating the greater thermal stability. Since the target temperature is 673K water/ethanol with NaOH is considered to be the best-suited solvent system.

The ideal synthesis method that was understood to be the most thermally stable was low concentration CTAB as a surfactant, cerium nitrate hexahydrate as a precursor, and water/ethanol with NaOH as the solvent system. Individually these factors provide the building blocks for thermally stable ceria Coincidently, sample 006 shows to be the most thermally stable version of non-doped ceria. This method was then applied to the synthesis of doped ceria. At 693K the

surface area is greatest with sample 017; the titanium doping increases thermal stability. Pore volume and pore size also were highest with 017.

Chapter 5

Catalysis

5.1 Summary

When monitoring the oxidation of methane, one would expect methane and oxygen levels to decrease upon reaction either in the gas phase or on the surface of the catalysts. Correspondingly, the reaction products such as water and carbon dioxide should go up or hydrogen and carbon monoxide levels should go up depending on the prevalent reaction[12,14]. The carbon monoxide can also further react with water to create hydrogen and carbon dioxide. The representation of relative pressure change in this section is shown in percentage, positive for an increase in relative pressure and negative for a decrease in relative pressure. All partial pressures are corrected using gas corrections factors and ionization cross sections[46,47]. All experiments use helium as a background constant against which the partial pressures were calibrated to correct for any pressure fluctuations in the system, unless otherwise indicated.

The experiments are mainly run under fuel lean, 1:3 methane to oxygen, and fuel rich, 3:1 methane to oxygen, conditions to elucidate which would cause partial methane oxidation and full methane oxidation. Some experiments were also run at other ratios for the same purpose. The length of the experiments varied from a few hours to a few days. This was dependant on the time it took for the pressure levels to stabilize in the system at each temperature level.

During the catalysis experiments samples 006C4, a high surface area ceria calcinated at 673K; 007C6, a low surface area ceria calcinated at 673K; 015C4, a high surface area ceria calcinated at 673K; 017C4, a high surface area titania doped ceria calcinated at 673K; and 017C6, a high surface area titania doped ceria calcinated at 873K were used compare reactivity for methane oxidation. The main ideas were to compare high and low surface area reactivity as well as reactivity between ceria and titania doped ceria.

5.2 Catalysis

Experiment set A

5.2.1 Test run 006C4

For catalysis, Experiment 1 the sample 006C4 is run in fuel lean conditions. The temperature is set to 623K to which is just below the known reactivity temperature for methane oxidation, to slowly ramp through to 873K. It should be noted that this sample being calcinated at 673K shouldn't be heated past that temperature since it alters the catalyst.

This was a test run of the system and setup. For experiment 1, with sample 006C4 under fuel lean conditions there are no significant changes with temperature. In figure 24, we see there is a slight decrease in oxygen levels (-18.7%), and a slight increase in hydrogen levels (11.47%) as well as methane levels (9.9%). If there were a reaction we would expect a decrease in oxygen and methane while having an increase in hydrogen gas. There doesn't appear to be any methane oxidation. Since the experiment temperature was greater than that of the calcination the catalyst was changed for the next step.

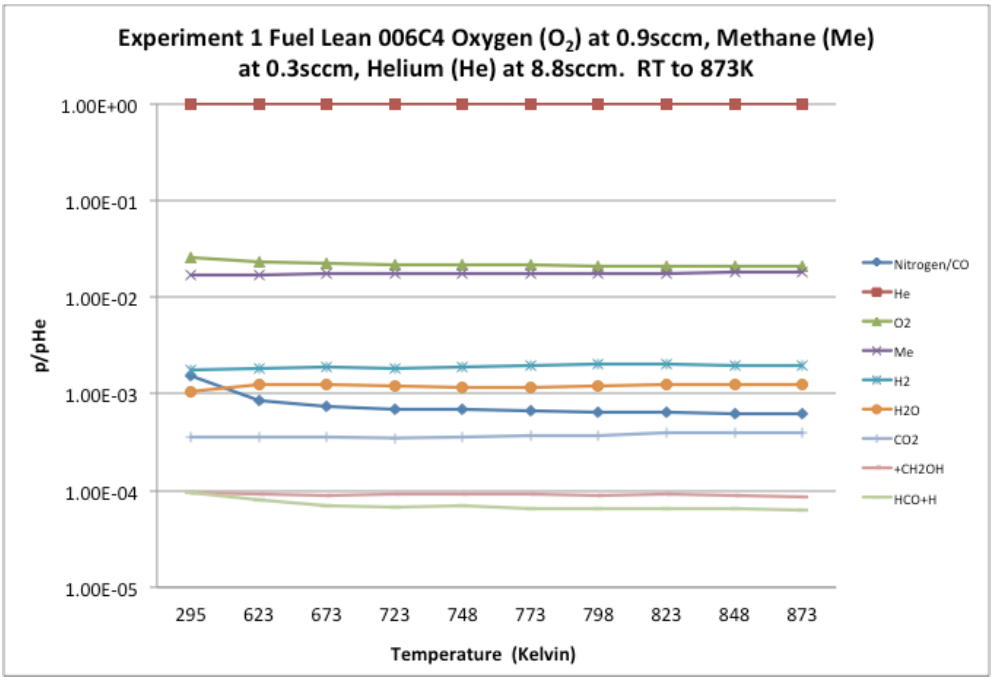

Figure 24 Single gas monitor RGA of sample 006C4 synthesized from cerium nitrate hexahydrate, CTAB, water, ethanol, and sodium hydroxide

Experiment set B

5.2.2 Catalysis 007C6

In Experiments 2, 3, 4, 5 and 6 the sample 007C6 is run under fuel lean, fuel rich, and equal fuel to oxygen ratio conditions from room temperature to 873K. Then fuel rich conditions were investigated more thoroughly to determine the ratio at which the oxygen levels return.

For experiment 2, with sample 007C6 under fuel lean conditions we can see in figure 25 that there is an extensive decrease in oxygen levels (-68.2%) with a mild increase in hydrogen levels (37.84%). Methane levels increase a little as well (6.69%), which seem very odd.

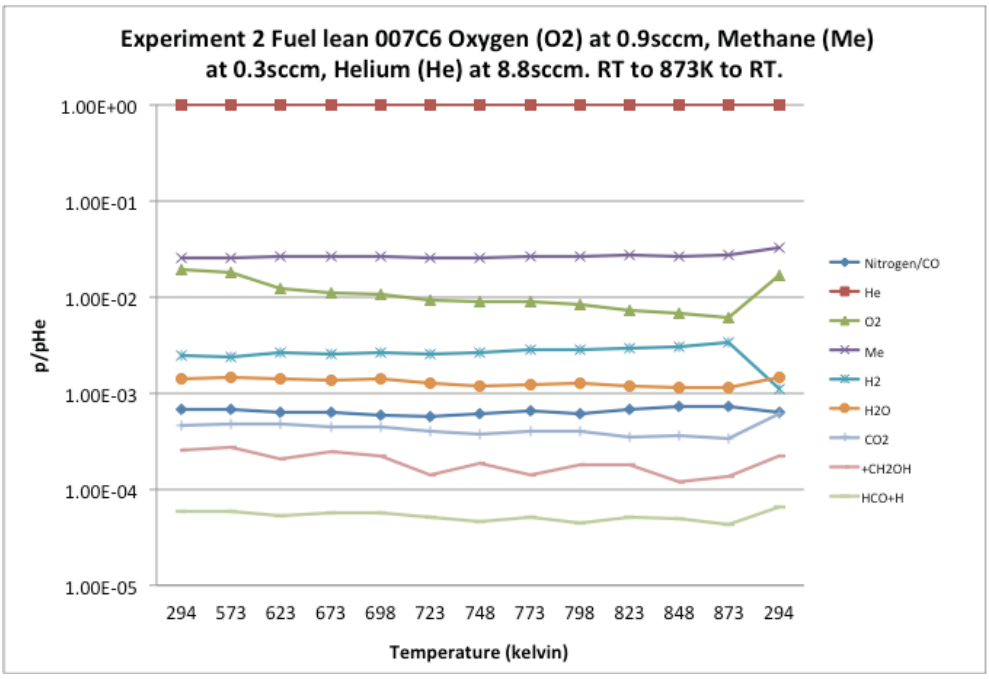

Figure 25 Single gas monitor RGA of sample 007C6 synthesized from cerium hydroxide, CTAB/paraffin, water, ethanol, methylene chloride, and sodium hydroxide

For experiment 3, with sample 007C6, under fuel rich conditions there is an extensive decrease in oxygen levels (-76.6%), no change in methane levels (0.1%) and little in hydrogen levels (-4.7%) in figure 26. Unless the reaction occurs at room temperature there is no sign of changes in oxygen products.

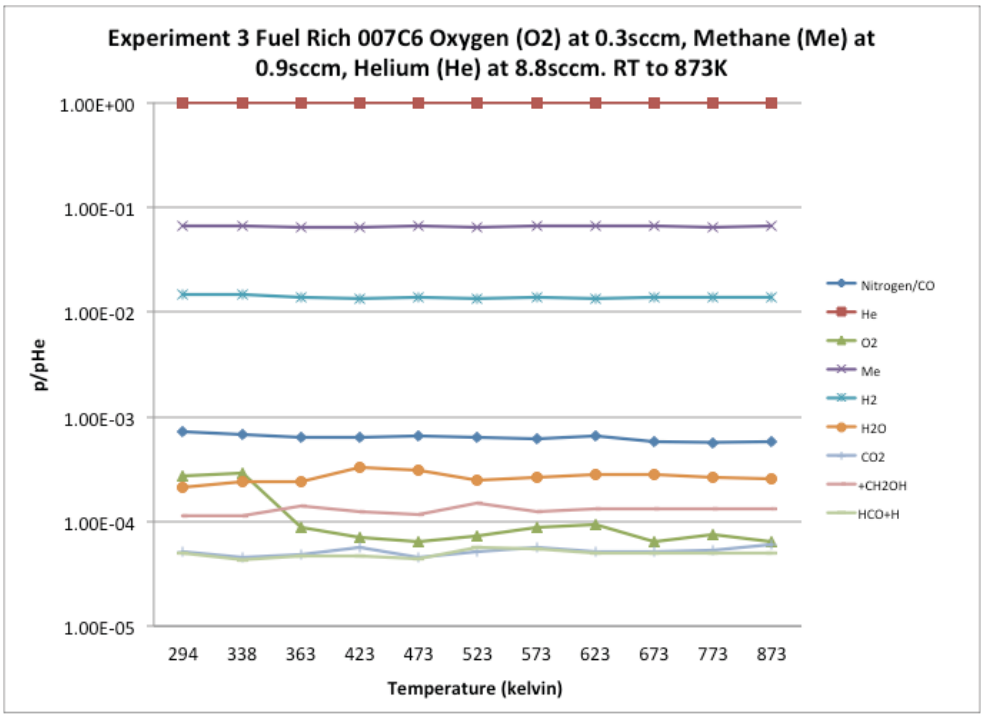

Figure 26 Single gas monitor RGA of sample 007C6 synthesized from cerium hydroxide, CTAB/paraffin, water, ethanol, methylene chloride, and sodium hydroxide

For experiment 4, with sample 007C6 under equal fuel and oxygen conditions, we can see in figure 27 there is a continuous decrease in oxygen levels (-97.3%) with a very slight increase in hydrogen levels (14.2%). Methane also has a slight increase (9.0%).

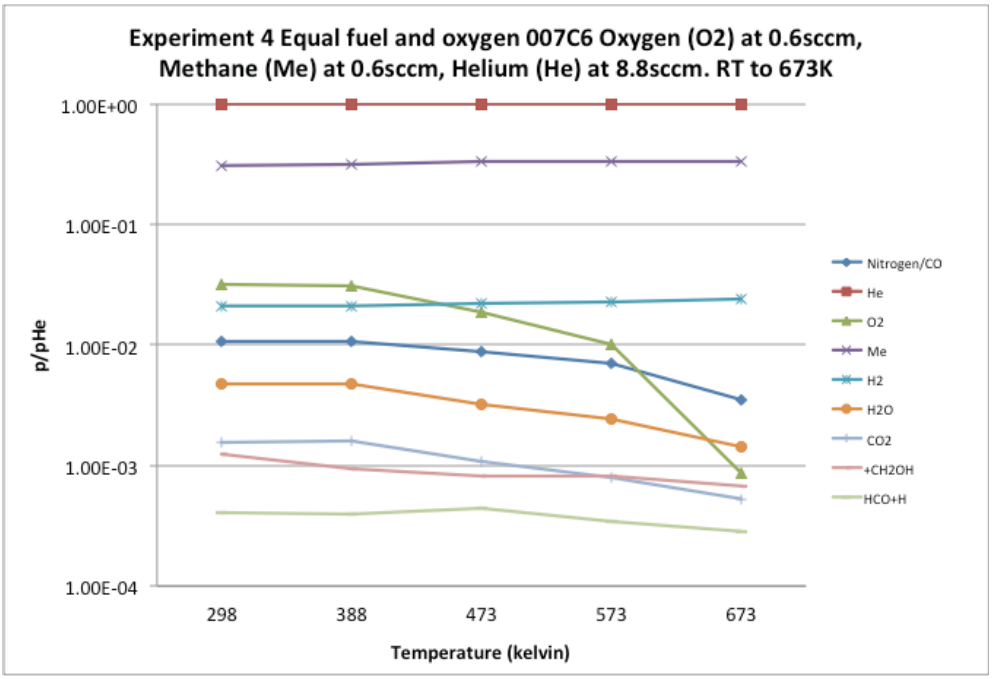

Figure 27 Single gas monitor RGA of sample 007C6 synthesized from cerium hydroxide, CTAB/paraffin, water, ethanol, methylene chloride, and sodium hydroxide

For experiment 5, with sample 007C6 under fuel rich 2:1 conditions, we see in figure 28 that oxygen levels quickly drop (-81.5%) after an increase in temperature. Methane (3.4%), carbon dioxide (0%) and hydrogen (1.7%) levels remain constant. Carbon monoxide/Nitrogen levels drop a little bit (-25.6%) as does water (-26.0%). There appears to only be a loss in oxygen with no explanation.

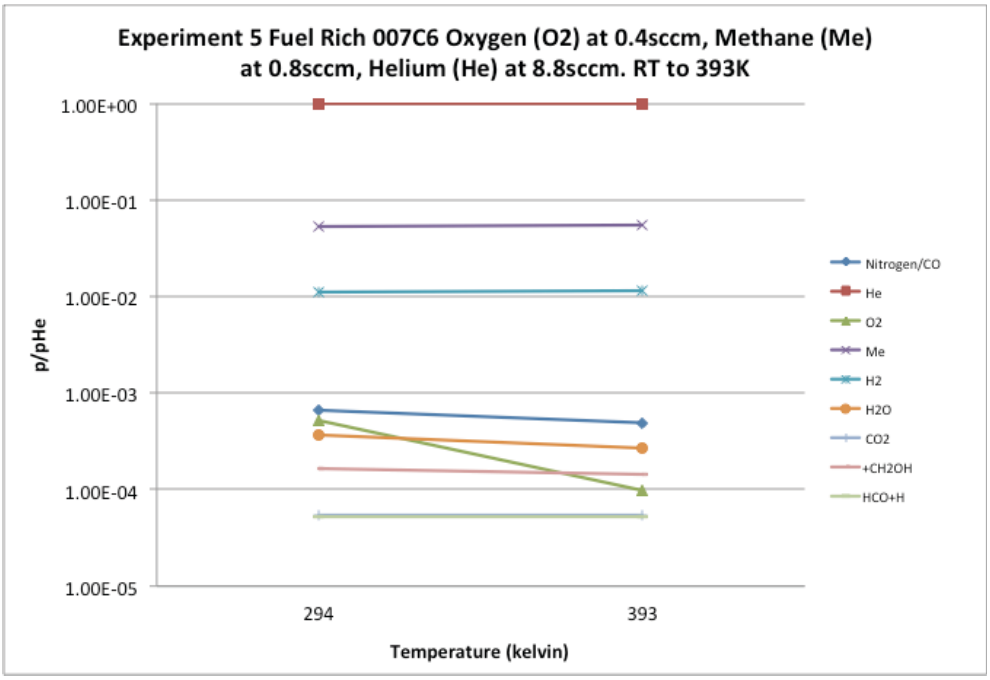

Figure 28 Single gas monitor RGA of sample 007C6 synthesized from cerium hydroxide, CTAB/paraffin, water, ethanol, methylene chloride, and sodium hydroxide

For experiment 6, with sample 007C6 under increasing fuel/decreasing oxygen conditions, in figure 29 we see oxygen levels decrease (-88.2%) as expected, water (8.26%) and methane show a slight increase (24.1%). Water (8.26%) and hydrogen (24.1%) also increase slightly. Carbon monoxide (-26.3%) and carbon dioxide (-26.2%) also show a slight decrease. When the mass of oxygen input is dropped to 0.38sccm from 0.40sccm the reading in the mass spec drops by 50%. Further the 50% change in oxygen input results in an 88.2% decrease. This shows that oxygen is being consumed as well.

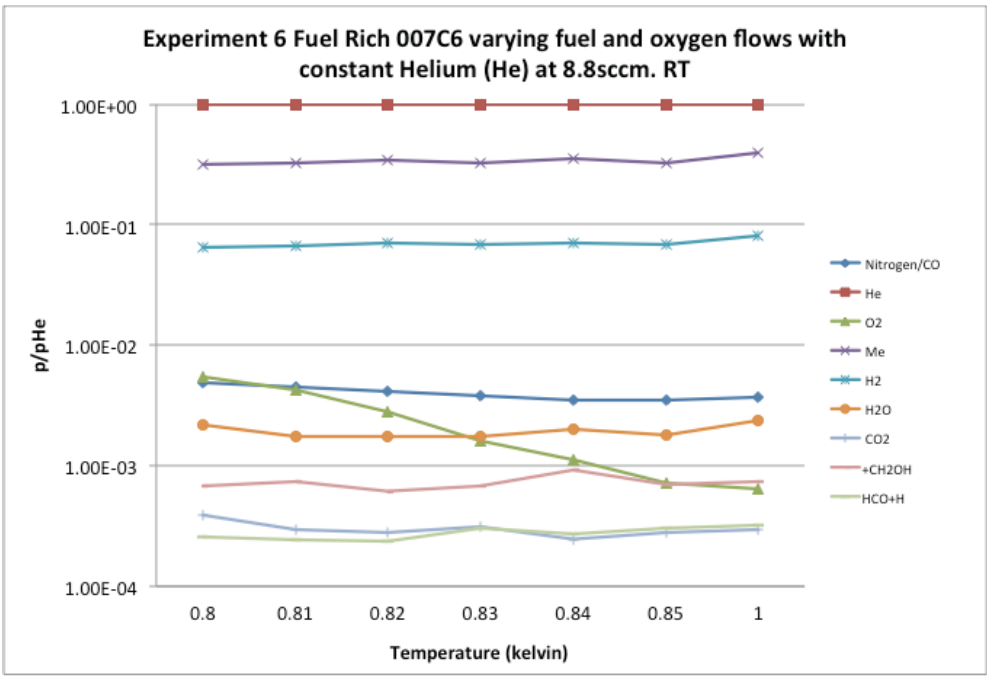

Figure 29 Single gas monitor RGA of sample 007C6 synthesized from cerium hydroxide, CTAB/paraffin, water, ethanol, methylene chloride, and sodium hydroxide

When comparing the initial experiments, we investigate different fuel to oxygen ratios. In experiments 2-5 we have fuel to oxygen ratios of 1:3, 3:1, 1:1, and 2:1. In all of the conditions the oxygen levels drop significantly with varying changes in hydrogen. 1:1 displays the greatest change in oxygen while 1:3 shows the greatest increase in hydrogen and the smallest decrease in oxygen.

When investigating the change in oxygen and methane ratios, in experiment 6, there appears to be a further loss in oxygen other than that warranted by the change in input flow. Oxygen is being consumed. The expected signs of methane oxidation are not seen. Therefore no methane oxidation is occurring.

Experiment set C

5.2.3 Catalysis 006C4 fuel rich and fuel lean

In Experiments 7 and 8, sample 006C4 is run under fuel rich and fuel lean conditions from room temperature to 673K.

For experiment 7, with sample 006C4 under fuel rich conditions, in figure 30 methane levels increase while oxygen significantly decreases (-97.1%). Hydrogen levels increase very slightly (8.5%) while carbon monoxide (-63.3%), carbon dioxide (-55.8%) and water decrease (-44.3%).

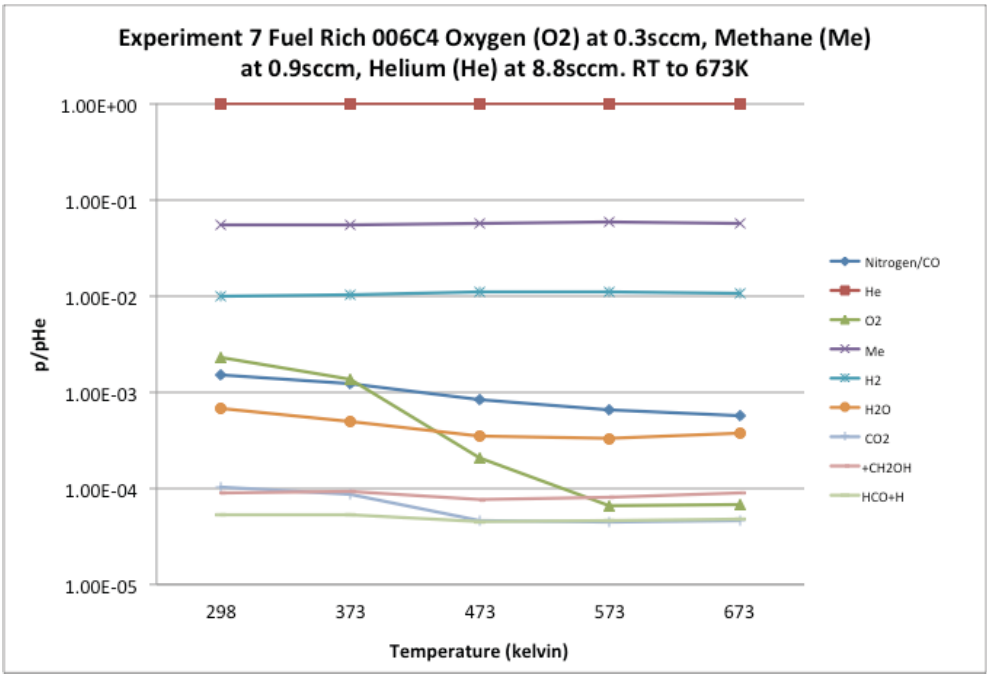

Figure 30 Single gas monitor RGA of sample 006C4 synthesized from cerium nitrate hexahydrate, CTAB, water, ethanol, and sodium hydroxide

For experiment 8, with sample 006c4 under fuel lean conditions, Figure 31 shows methane levels remain consistent (0.016%), oxygen levels drop (-27.1%). Water levels drop a little bit (-9.2%) as well as carbon monoxide (-21.9%) and carbon dioxide levels (-9.3%). Hydrogen levels increase a little bit (12.0%).

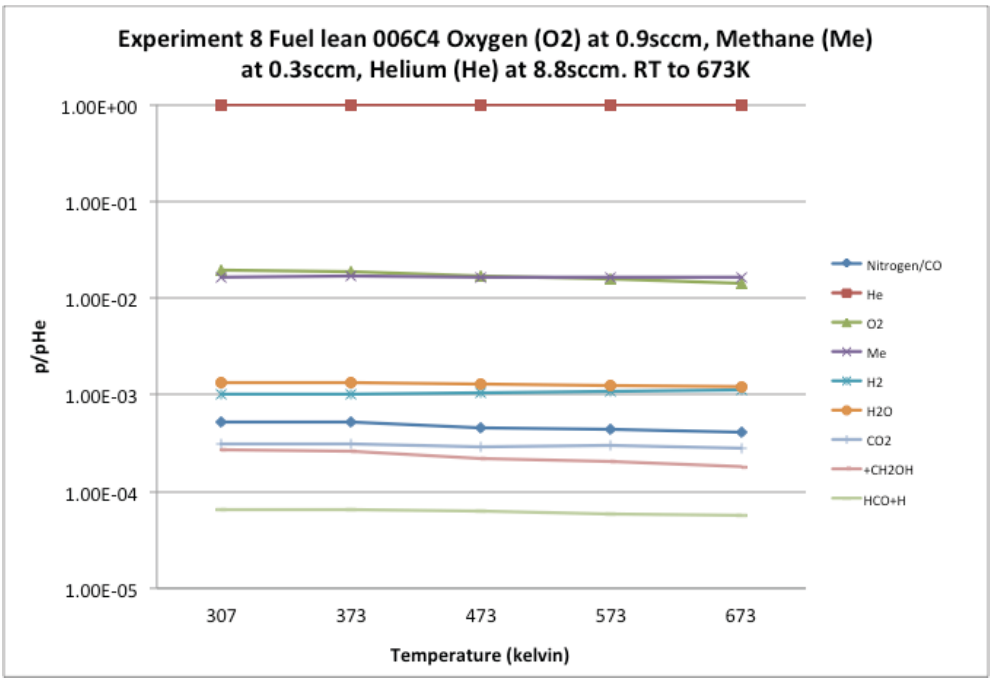

Figure 31 Single gas monitor RGA of sample 006C4 synthesized from cerium nitrate hexahydrate, CTAB, water, ethanol, and sodium hydroxide

The comparison of fuel lean and fuel rich conditions for 006C4 both show oxygen decrease and minor increases in hydrogen. These confirm the results that we have seen in the previous set of experiments yet still do not provide a full picture of what is happening in the reaction chamber. Oxygen levels percent decrease is greatest in fuel rich conditions but still decrease in fuel lean conditions yet in converted mass flow values the decrease is greater in fuel lean conditions, with a drop of 0.0461sccm, where there is a greater abundance of oxygen to begin with compared to fuel rich with a drop of 0.0196. The typical methane oxidation products are not being seen; there is no methane oxidation occurring.

Experiment set D

5.2.4 Catalysis 015C4

In experiment 9 sample 015C4 is run under fuel less conditions with methane introduction after gas pressure stabilization at 673K. This was to see the reaction of the oxygen in the system when the fuel is introduced to better understand the oxygen depletion.

In figure 32, we see that with the initial temperature increase, oxygen (-12.6%) and methane (-7.2%) drop in levels. There is little change in the other gases. After the introduction of methane,

oxygen decreases (-41.6%) while there's a rise in water (199.3%), carbon dioxide (244.2%) and hydrogen (56.5%). As the temperature decreases oxygen (44.7%) and methane (9.5%) levels increase. Carbon monoxide (6.4%), water (2.7%), carbon dioxide (4.1%) and hydrogen (1.9%) stay similar.

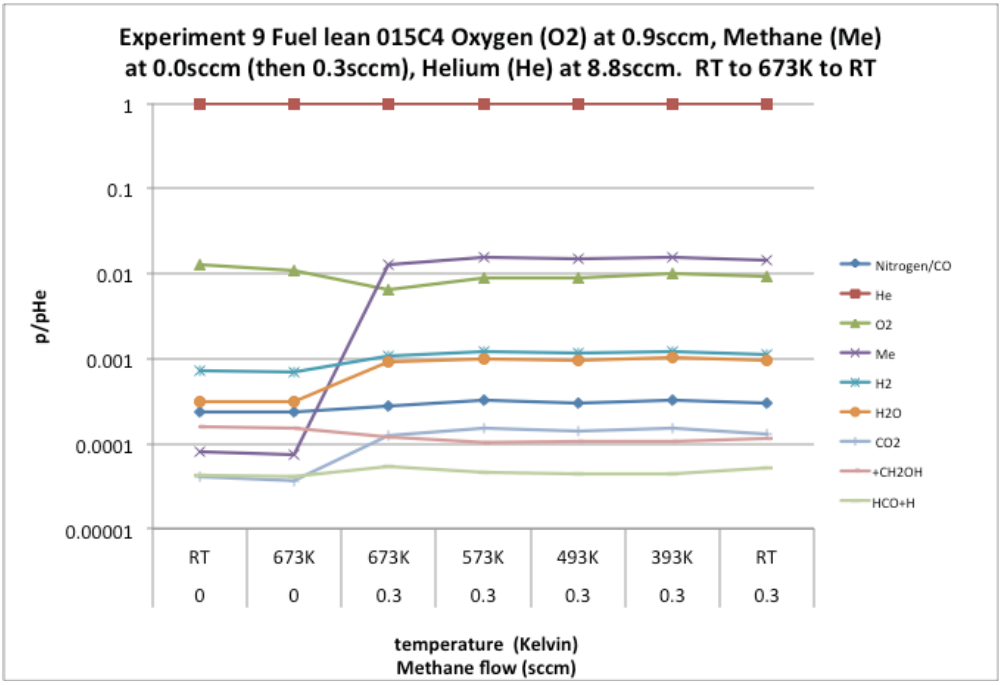

Figure 32 Single gas monitor RGA of sample 015C4 synthesized from cerium hydroxide, n-hexadecylamine, water, ethanol, and sodium hydroxide

A test in which methane is reintroduced into the system at high temperature shows oxygen decreases after the introduction of methane by 41.6% and hydrogen increases by 56.5%. Comparing the initial levels with 0sccm of methane at RT to those with 0.3sccm of methane at RT also show that there is a decrease in initial oxygen with the mere presence of methane this effect is further exacerbated by increasing the temperature. These results imply that the oxygen level decrease is methane dependant.

Experiment set E

5.2.5 Catalysis 006C4 Fuel rich doubling the mass flow of reactants

In experiment 12, sample 006C4 is run under fuel rich conditions with double the mass flow of oxygen and methane while lowering that of the helium to keep total mass flow at 10sccm. This was

done to further investigate the oxygen depletion with hopes that any small variations would show up on a bigger scale at these overall ratios while maintaining comparative ratios.

In figure 33, the initial levels reflect that of catalytic absence. With time level stabilization shows oxygen depletion (-96.9%) and a rise in hydrogen (45.2%), methane (24.1%). There is a decrease in carbon monoxide (-79.23%), carbon dioxide (-50.7%), and water (-49.9).

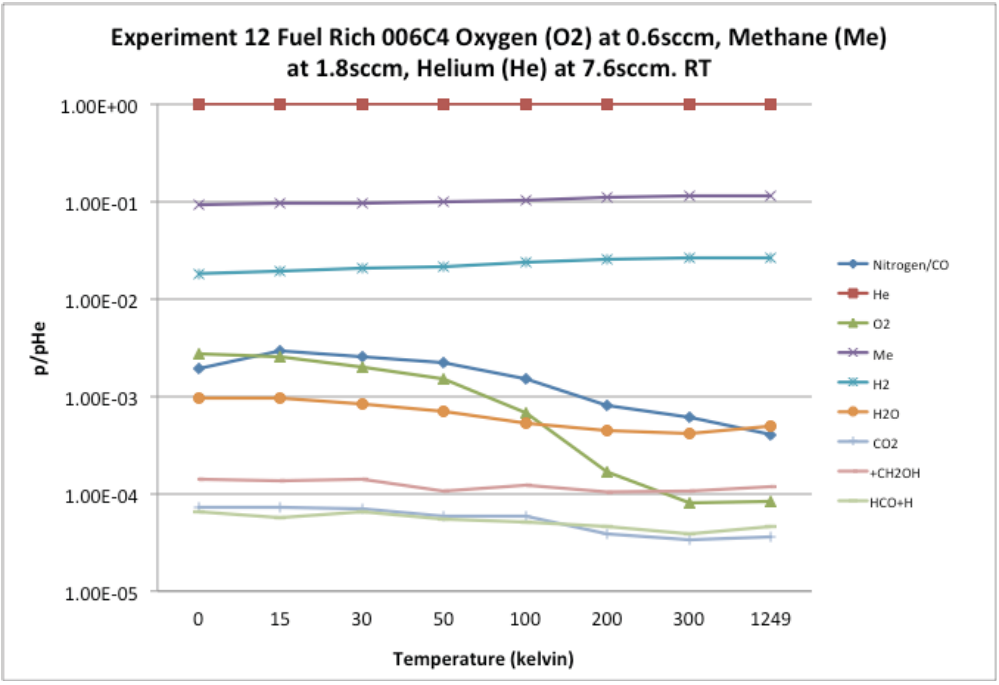

Figure 33 Single gas monitor RGA of sample 006C4 synthesized from cerium nitrate hexahydrate, CTAB, water, ethanol, and sodium hydroxide

The test runs the gas flow in fuel rich conditions until stabilization without a catalyst, and then the system is switched to flow through the catalyst. After stabilization oxygen shows depletion and hydrogen shows a large increase.

Beyond the idea of hydrogen production, which is present in some experiments in certain conditions, there is an overwhelming decrease in oxygen, which is consistently present. As discussed previously, there is an appreciable amount of oxygen level decrease in the presence of methane at RT. This experiment, with a greater quantity of methane and oxygen while preserving the same 3:1 ratio, exhibits a further quantitative decrease of oxygen all the while at RT.

This experiment, repeated without a catalyst, shows little to no changes in oxygen and other gases (as shown in experiment 18).

Experiment set F

5.2.6 Bubble tests

Experiments 13 and 14 cover an extensive set of parameters to see if the overall exhaust flow rate varied throughout the reactions. Initially comparing each gas individually then in combination all with and without catalyst (006C4). The oxygen level drop, in the previous experiments, does not produce any reaction products containing oxygen. To investigate the possibility of overall flow change, the execution of the bubble test could rule out any setup issues that could be resulting in oxygen level decrease such as filtering or absorption.

For experiment 13 with 006C4 the overall flow rate was compared for the different gases alone and in combination by counting bubbles from the exhaust. The bubble count for this experiment was taken over a 30 second period. We see in table 4 that the exhaust flow (in bubbles) doesn't vary much. It is greater with no catalyst and slower with the catalyst and when oxygen is in the mix there tends to be a slightly more favourable flow.

Table 4 Bubble test comparison table comparing flow for methane, oxygen and helium, with or without a catalyst

Nominal flow (sccm)	Oxygen	Methane	Helium	Catalyst	# of bubbles
5	■			N	8
5		■		N	7
5			■	N	7
5	■			Y	6
5		■		Y	6
5			■	Y	6
10	■			N	17
10		■		N	16
10			■	N	16
10	■			Y	14
10		■		Y	12
10			■	Y	12
5+5	■		■	N	17
5+5	■		■	Y	14
5+5		■	■	N	17
5+5		■	■	Y	12
5+5	■	■		N	17
5+5	■	■		Y	14

For experiment 14 with 006C4 the overall flow rate was compared for the different gases alone and in combination by counting bubbles from the exhaust this time over a longer period of time. Every step compares 5.0sccm flow. From figure 34 we see the overall bubble count varies from 67 to 87 over the 5minute span. In figure 35 we see that with the catalyst after stabilization the bubble counts vary between 67 and 79.

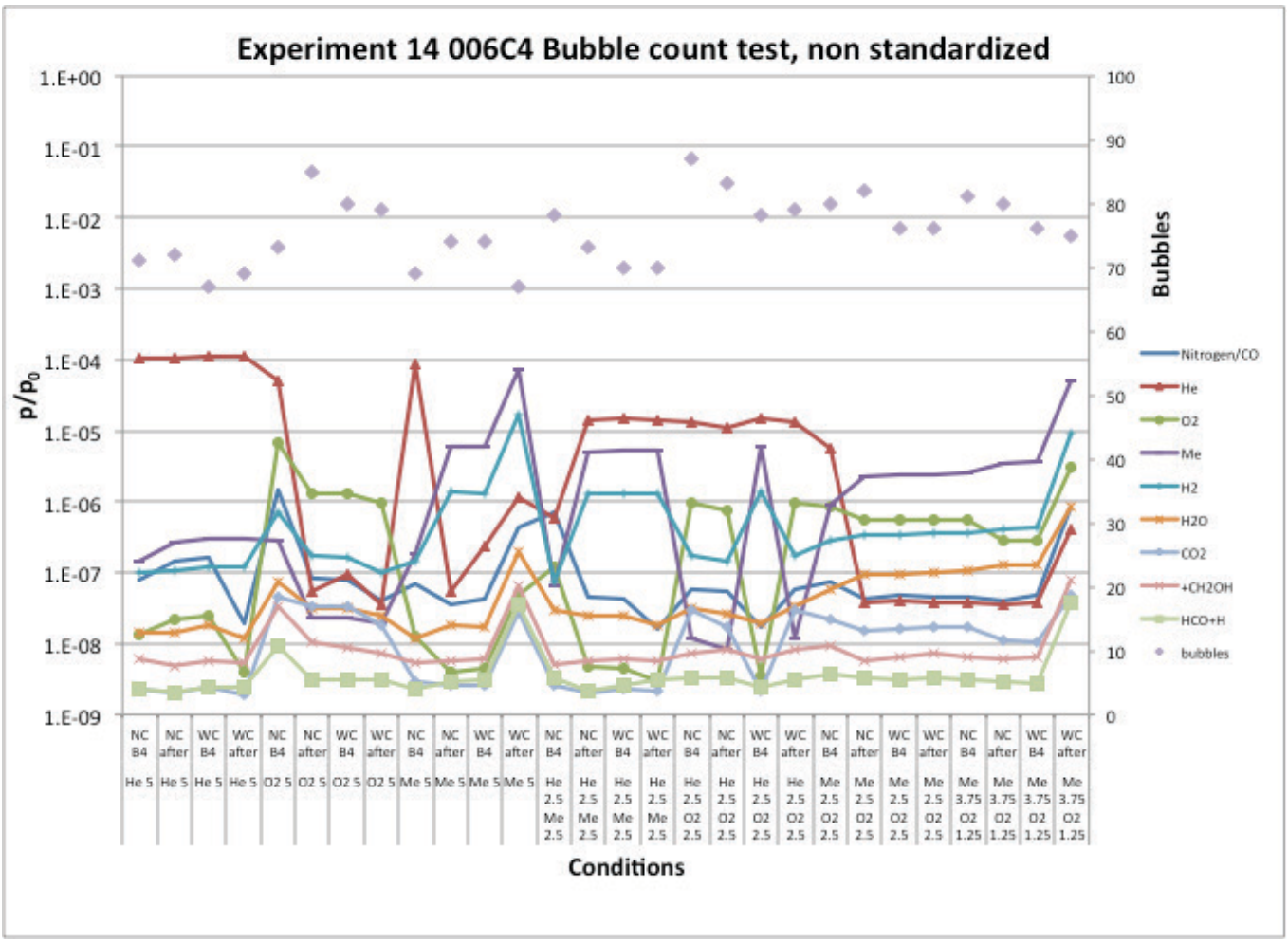

Figure 34 Single gas monitor RGA of bubble test, WC (with catalyst), NC (no catalyst), B4 (before stabilization), after (after stabilization). When a catalyst used it was sample 006C4 synthesized from cerium nitrate hexahydrate, CTAB, water, ethanol, and sodium hydroxide

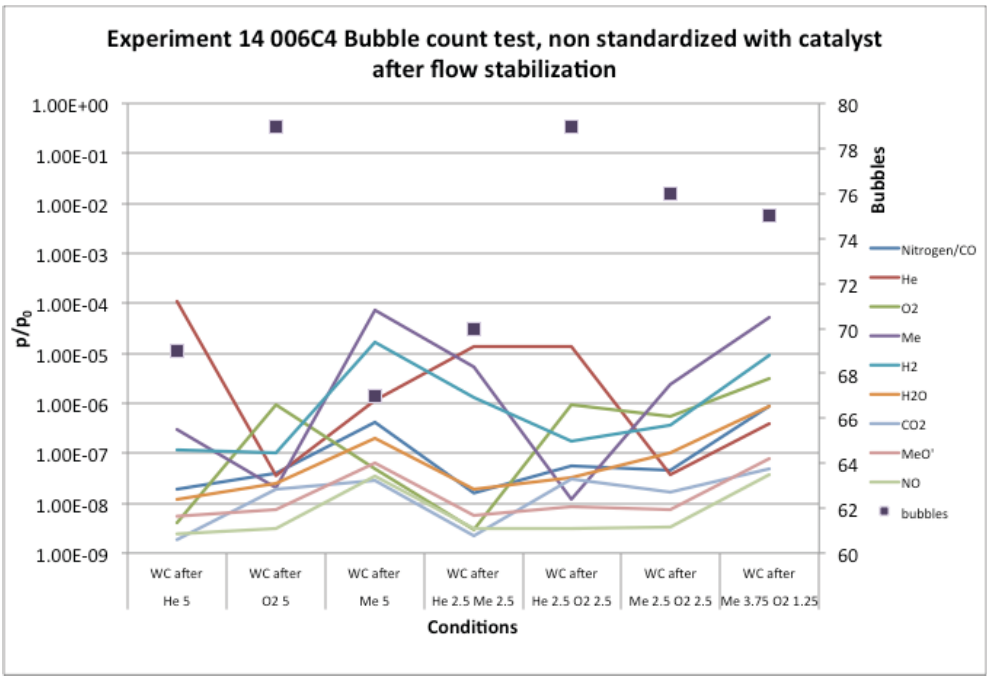

Figure 35 Single gas monitor RGA of bubble test, WC (with catalyst), after (after stabilization). When a catalyst used it was sample 006C4 synthesized from cerium nitrate hexahydrate, CTAB, water, ethanol, and sodium hydroxide

The conducted bubble test measured the exhaust volume for the experiment and conditions. The experiments show that the mass flow through the catalyst does vary but only by 15% at the most, of which the lows account for situations where oxygen wasn't in the conditions, presenting high exhaust flow rates for condition sets that include oxygen. It is expected with the catalyst that overall flow could decrease slightly based on the obstruction it imposes on the system. The largest exhaust flow rates in bubbles come from scenarios where oxygen is involved. There isn't a great flow variation through the catalyst. There is no inhibition of oxygen flow through the catalyst.

Experiment set G

5.2.7 Catalysis 006C4 Mass flow of reactants further increased

Experiments 15, 16 and 17 study the effects of maintaining comparative ratios in fuel rich conditions while changing the overall ratios this time to a further extent. The sample 006C4 is ramped to 673K then back to room temperature as well a more focused run to 423K and back to room temperature.

For experiment 15 with sample 006C4 under fuel rich conditions, figure 36 shows that carbon monoxide (-84.9%), water (-51.2%), and carbon dioxide (-81.2%) levels decrease with increasing temperature with oxygen levels decreasing very significantly (-98.5%). Methane (10.0%) and hydrogen (3.5%) levels don't vary very much. Upon return to room temperature the levels that had decreased have returned to similar initial levels. Bubble counts were also made in this experiment to see if there were any changes in flow with temperature change. At all steps the bubble count is 146-7 bubbles in 5 minutes.

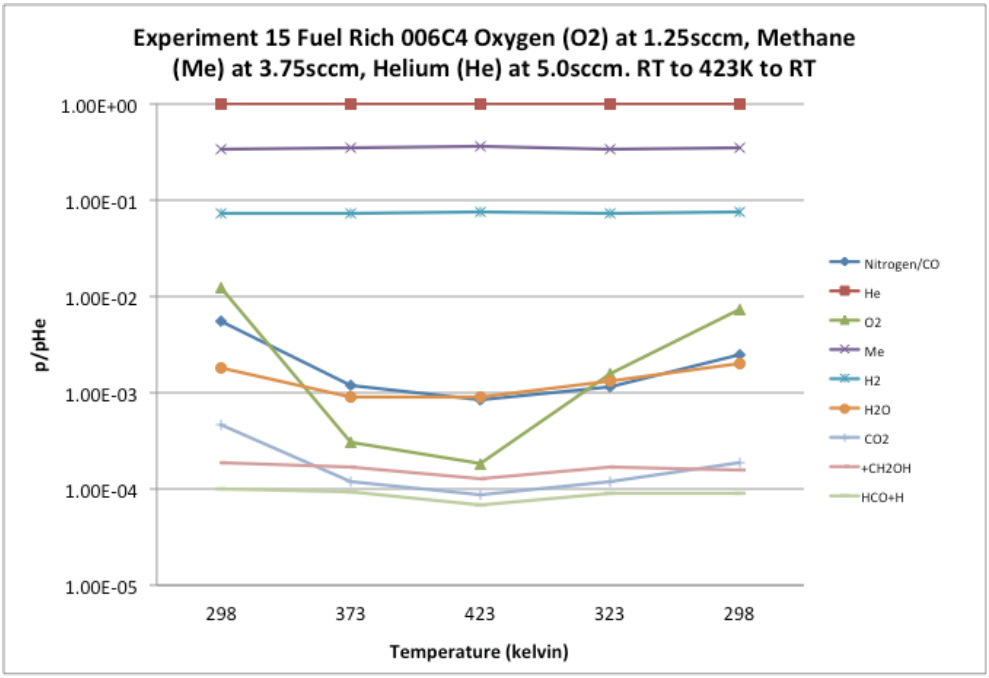

Figure 36 Single gas monitor RGA of sample 006C4 synthesized from cerium nitrate hexahydrate, CTAB, water, ethanol, and sodium hydroxide

For experiment 16 with sample 006C4 under fuel rich conditions figure 37 shows that carbon monoxide (-71.6%), carbon dioxide (-54.9%) and water (-55.9%) levels decrease while oxygen levels decrease significantly (-97.1%). Methane levels varied slightly (12.3%) while hydrogen levels increased (10.9%).

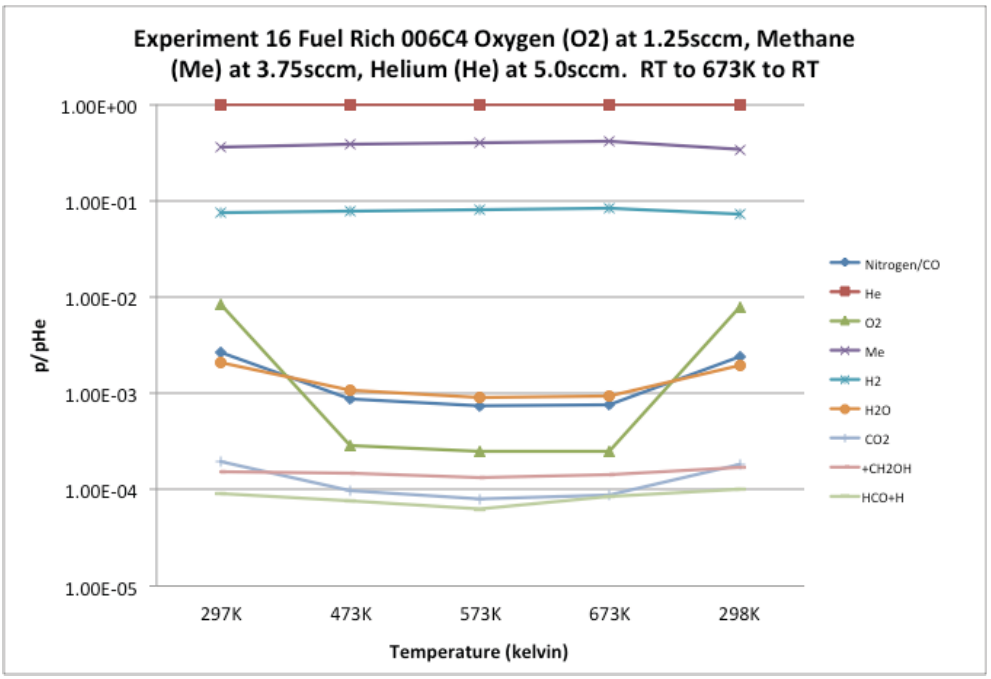

Figure 37 Single gas monitor RGA of sample 006C4 synthesized from cerium nitrate hexahydrate, CTAB, water, ethanol, and sodium hydroxide

Figure 38 shows that for experiment 17 with sample 006C4 under fuel rich conditions as temperature increases, water (-55.9%) and carbon monoxide (-69.8%) levels drop, as does carbon dioxide (-48.1%). Oxygen levels drop significantly (-96.9%) while methane (3.2%) and hydrogen levels (-1.9%) don't vary.

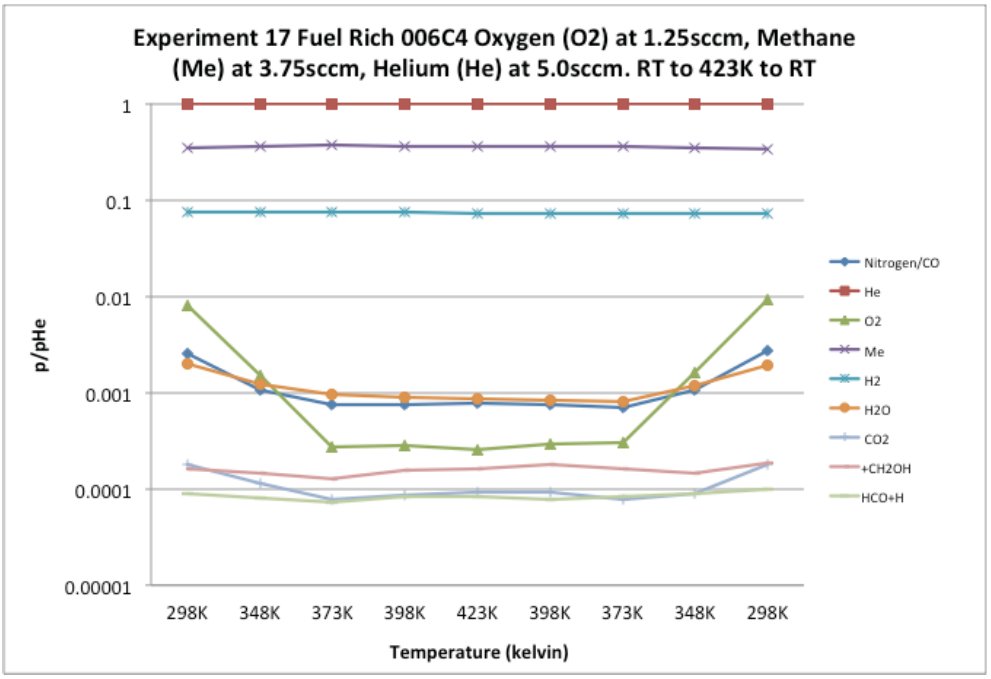

Figure 38 Single gas monitor RGA of sample 006C4 synthesized from cerium nitrate hexahydrate, CTAB, water, ethanol, and sodium hydroxide

The experiments continue to show oxygen depletion. Reversibility is demonstrated, initially from RT to 423K to RT followed by RT to 673K to RT, both showing similar values in the low points of oxygen levels regardless of the further extent in temperature increase. Experiment 17 looks at a more stepwise approach at the reversibility of the experiment. The results of which shows a fairly symmetric pattern with most gases returning within a 5% change of the initial values with the exception of oxygen, which returns at a 14.7% increase.

Experiment set H

5.2.8 Blank

Experiment 18 follows a blank run under the same conditions as experiment 17.

Experiment 18 is run with a blank under fuel lean conditions to determine the possibility of thermal reaction in the gas phase or simply in part of the microreactor setup without a catalyst. In figure 39 we see some minor changes as the temperature increases, mainly being an initial increase in levels due to the rise in temperature. The gases changes are as follows carbon monoxide (4.3%), oxygen (3.2%), methane (1.0%), hydrogen (0.8%), water (3.9%), carbon dioxide (6.2%). We can clearly see that without the catalyst the oxygen levels do not deplete.

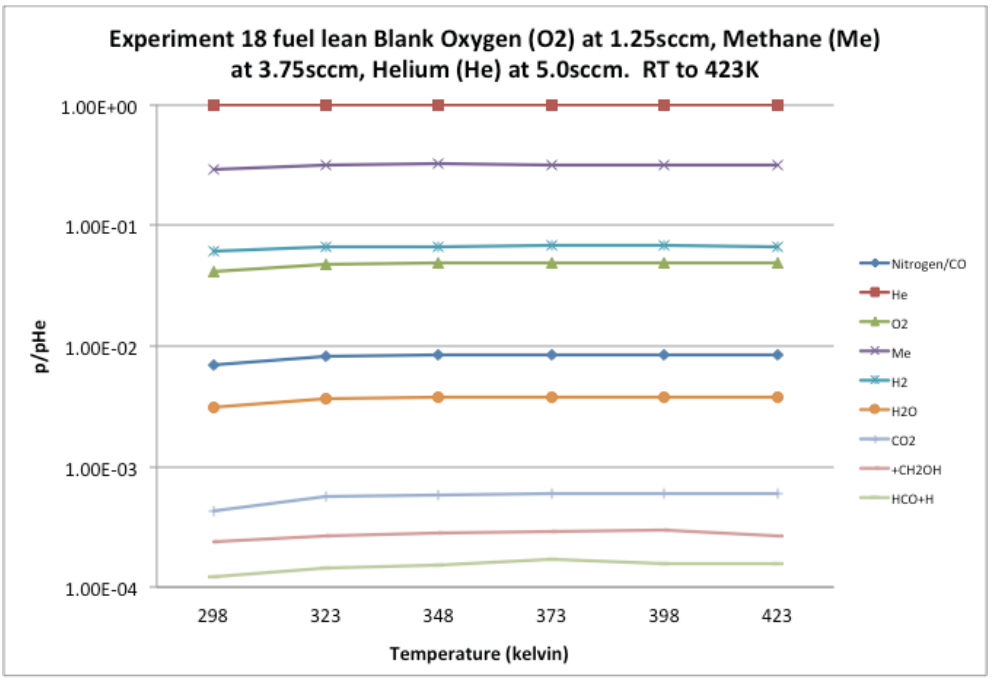

Figure 39 Single gas monitor RGA of a blank alumina tube

Experiment set I

5.2.9 further investigation into oxygen depletion

Experiment 19 is run in a similar fashion as experiment 17 but fuel-less with the reintroduction of methane and reduction of helium to see its effects on oxygen depletion. Experiment 20 follows in the same manner while increasing the oxygen levels to 1.50sccm while keeping the other levels the same. Oxygen levels are high; there might be a leak. Experiment 21 is the same as experiment 16 but with a slower ramp in temperature. Experiment 22 is the fuel lean equivalent to experiment 16.

In figure 40 we have experiment 19 where sample 006C4 is run with only helium and oxygen then heated to 423K followed by introduction of methane to fuel rich conditions. The methane level is expected to rise as it does. All levels rise extensively, which is due to standardization with helium and during introduction of methane in the system the helium mass flow was decreased to compensate and conserve a 10sccm flow. The overall flow was less important to conserve, as it was more important to conserve the mass flow of the control.

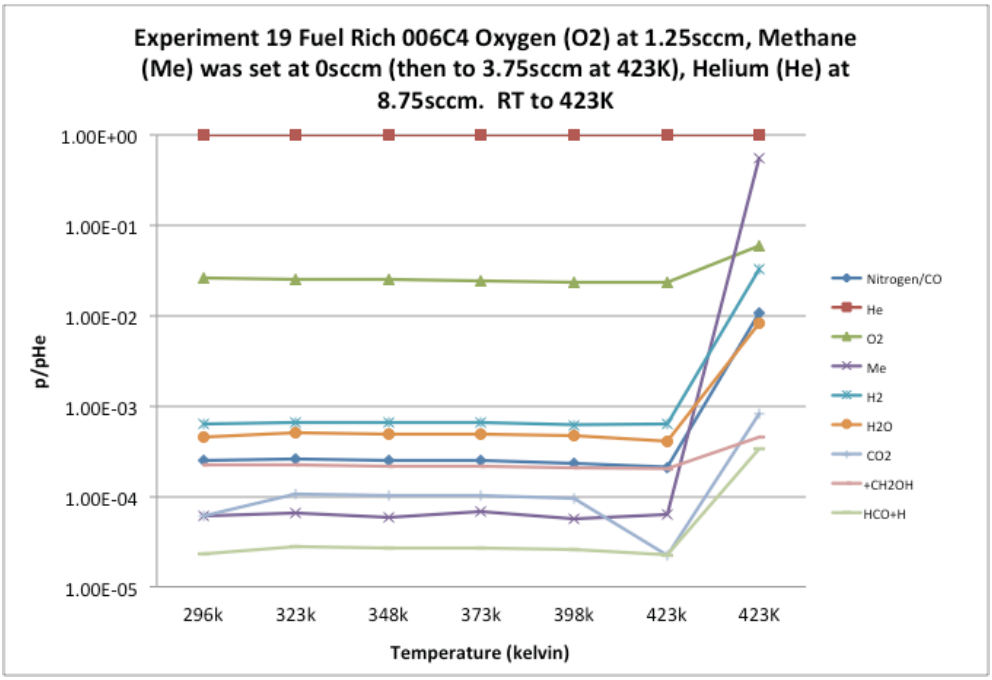

Figure 40 Single gas monitor RGA of sample 006C4 synthesized from cerium nitrate hexahydrate, CTAB, water, ethanol, and sodium hydroxide

In experiment 20, sample 006C4, under fuel rich conditions, is heated to 423K. In figure 41, there doesn't appear to be much of a difference in levels with the addition of oxygen in the system. The gas levels changed as follows, carbon monoxide (0.5%), oxygen (-0.6%), methane (0.5%), hydrogen (0.4%), water (1.2%), and carbon dioxide (5.3%). In an attempt to see the effect of increasing the mass flow of oxygen at elevated temperatures we see that oxygen levels actually go down which coincides with the previous results showing greater oxygen loss at higher oxygen to methane ratios. See figure 36.

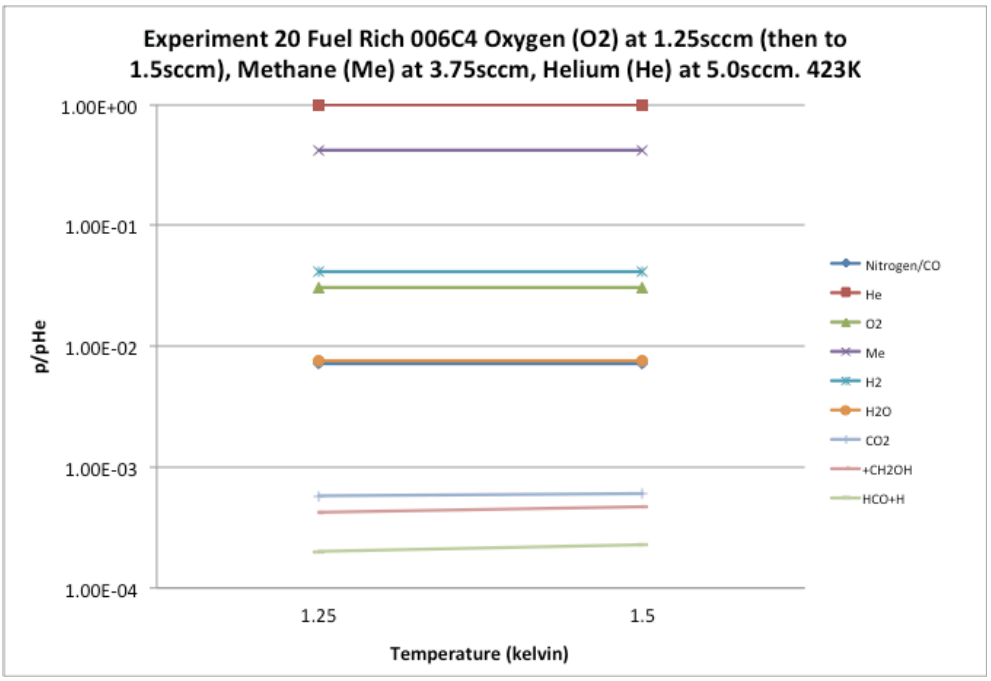

Figure 41 Single gas monitor RGA of sample 006C4 synthesized from cerium nitrate hexahydrate, CTAB, water, ethanol, and sodium hydroxide

For Experiment 21, figure 42, sample 006C4 is under fuel rich conditions there doesn't appear to be much of a change in methane levels (-3.8%) yet between 523K and 573K oxygen levels decrease (-13.4%) and hydrogen levels increase (12.7%) giving final changes of -26.0% and -2.0% respectively. Carbon dioxide (-9.1%), carbon monoxide (-7.3%) and water (-6.1%) all drop a little.

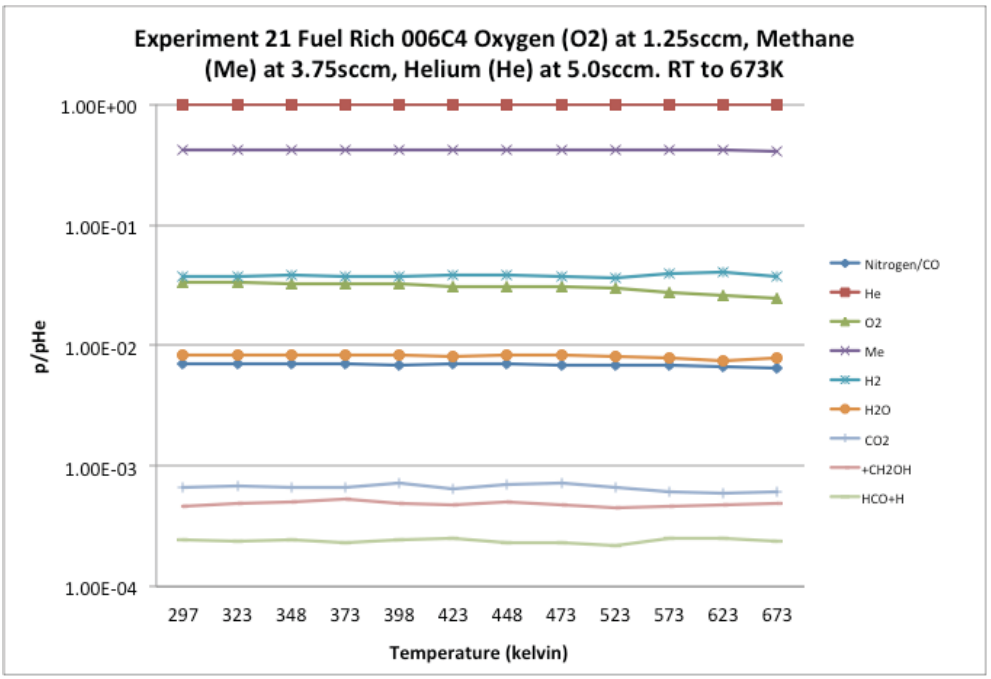

Figure 42 Single gas monitor RGA of sample 006C4 synthesized from cerium nitrate hexahydrate, CTAB, water, ethanol, and sodium hydroxide

Experiment 22, figure 43, sample 006C4 under fuel lean conditions the oxygen levels decrease (-83.2%) simultaneously hydrogen (56.2%) and carbon monoxide (28.0%) levels increase. Carbon dioxide (-53.6%) and water levels (-43.2%) also decrease. There are minor changes in methane (10%).

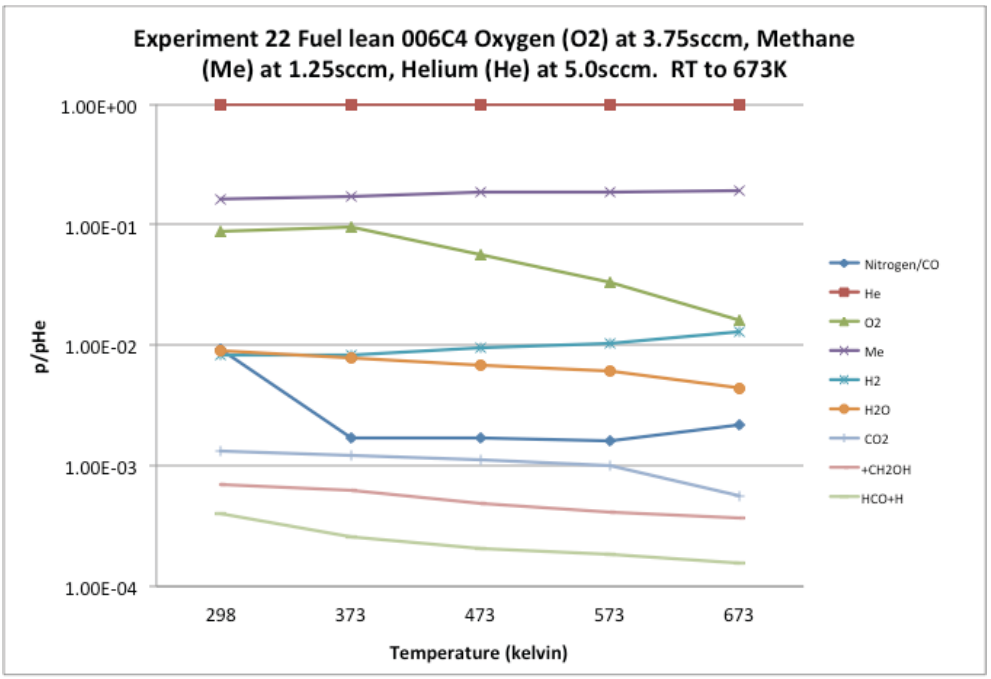

Figure 43 Single gas monitor RGA of sample 006C4 synthesized from cerium nitrate hexahydrate, CTAB, water, ethanol, and sodium hydroxide

Again we see reduction in oxygen levels, experiment 21 shows a more significant drop at 573K with a simultaneous increase in hydrogen but no decrease in methane, therefore there is no methane oxidation. Experiment 22 shows similar results at lower temperatures. At 373K, oxygen and water begin to decrease while hydrogen and carbon monoxide begin to increase. Under fuel lean conditions there appears to be partial oxidation of methane.

Experiment set J

5.2.10 Catalysis 017C4 new oxygen methane ratio discovery and pursuit

Experiment 23 runs sample 017C4 under fuel rich conditions. There appears to be immediate oxygen depletion. The oxygen levels are varied to find a flow rate that allows for oxygen to be present at room temperature. Experiment 24 follows with the new ratios and tests them up to 673K. Experiment 25 is the fuel lean equivalent.

For experiment 23, in figure 44, we see that at 1.25sccm of oxygen the levels are fairly low. The idea is to increase the oxygen levels until we see resurgence. Initially slowly increasing the flow without much change in results, the flow is increased drastically, which yields a higher level of oxygen. The jump between 6 and 7sccm of oxygen is where the shift occurs that allows the oxygen to come forth.

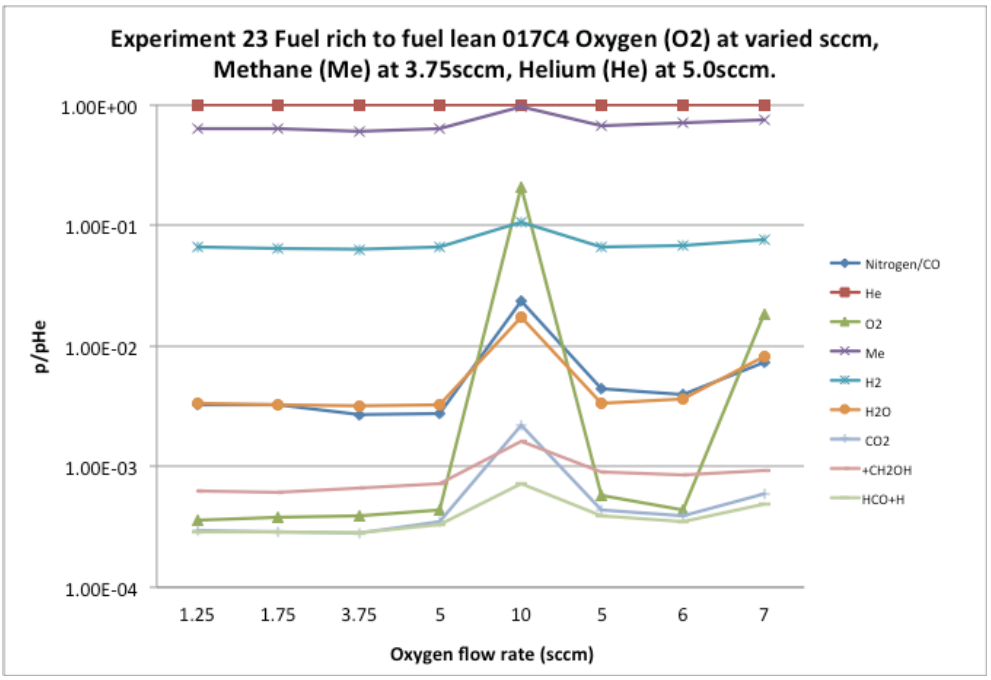

Figure 44 Single gas monitor RGA of sample 017C4 synthesized from cerium nitrate hexahydrate, titanium isopropoxide, CTAB, water, ethanol, and sodium hydroxide

Experiment 24 is sample 017C4 under fuel lean conditions where the overall flow is higher to accommodate for the ratios and flows determined in experiment 23. In figure 45, we see that with 7sccm of oxygen, at room temperature, it shows an initial high level, which quickly decreases (-97.7%) at 373K. Methane shows an increase (26.7%), as does hydrogen (14.3%). There is no discernable oxygen-yielding product. Carbon monoxide (-61.7%), carbon dioxide (-33.3%) and water levels (-51.5%) go down with increasing temperature.

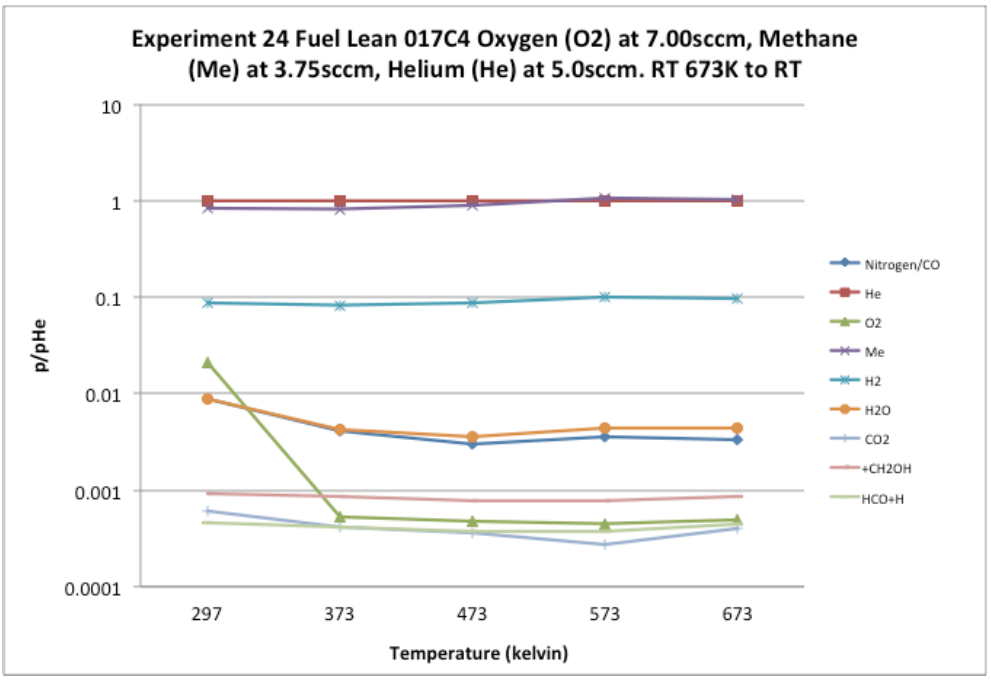

Figure 45 Single gas monitor RGA of sample 017C4 synthesized from cerium nitrate hexahydrate, titanium isopropoxide, CTAB, water, ethanol, and sodium hydroxide

5.2.11 Catalysis 017C4 fuel lean

Experiment 25 is sample 017C4 in fuel lean conditions. Figure 46 shows that methane holds steady with an increase (20.5%) at higher temperature while oxygen holds till it decreases at 473K and continues to do so till 673K (-39.2%). Hydrogen (-36.2%), carbon monoxide (-62.6%), and carbon dioxide (-54.6%) follow a similar path as that of oxygen. Water (6.9%) follows the same path as methane, increasing mostly at the end.

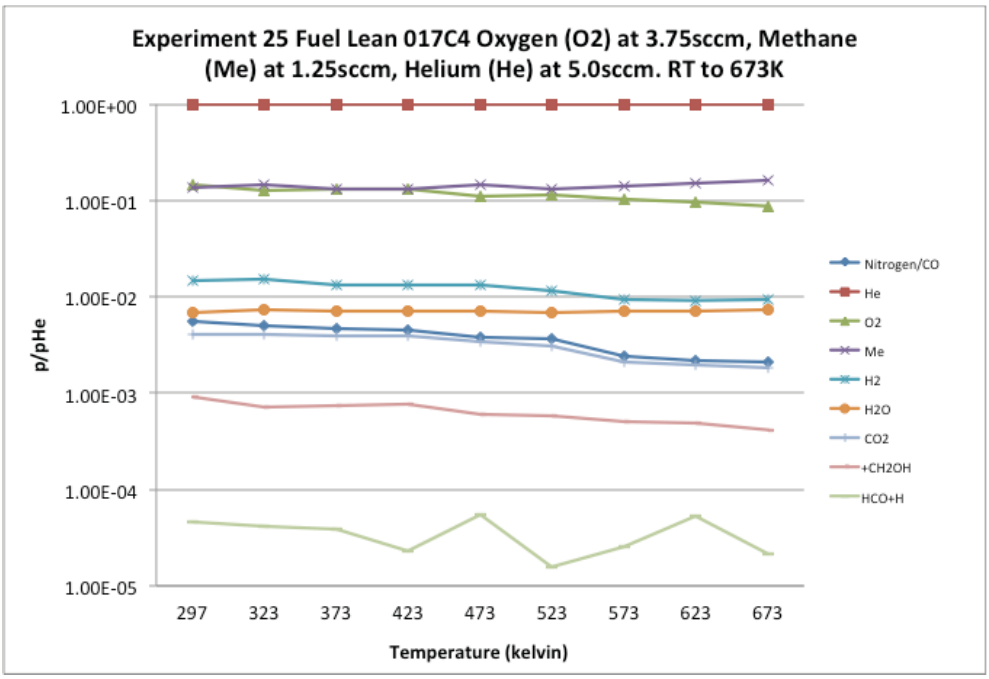

Figure 46 Single gas monitor RGA of sample 017C4 synthesized from cerium nitrate hexahydrate, titanium isopropoxide, CTAB, water, ethanol, and sodium hydroxide

Experiment 23 showed oxygen depletion immediately. The oxygen levels were ramped up to show that between 6 and 7sccm oxygen reappears in the mass spec. This shows there is a limit to the consumption. Further testing shows that with a minor increase in temperature the oxygen depletes again. Experiment 24 displays a 1:2 fuel lean scenario compared to 1:3 fuel lean in experiment 25 and as discussed earlier the larger amount of oxygen present the greater the decrease in the oxygen with a drop of 0.1033sccm for experiment 24 and 0.2813sccm for experiment 25.

Experiment set K

5.2.12 Catalysis 017C6 fuel lean

Experiment 26 sample 017C6 is run under fuel lean conditions from room temperature to 873K. There appears to be some drops and increases in the oxygen levels through the reactor. Experiment 27 investigates at set temperature levels long-term development to see if cycling occurs or if it's a one step process.

For experiment 26, in figure 47, we see methane levels vary slightly with an increase at 873K (26.9%). Oxygen stays fairly constant till 473K decreasing slowly with a further decrease at 873K (-

32.6%). Carbon monoxide (-23.6%) and carbon dioxide (-28.8%) have a steady decline throughout. Water stays consistent throughout (5.5%), as does hydrogen (0.6%).

See figure 42.

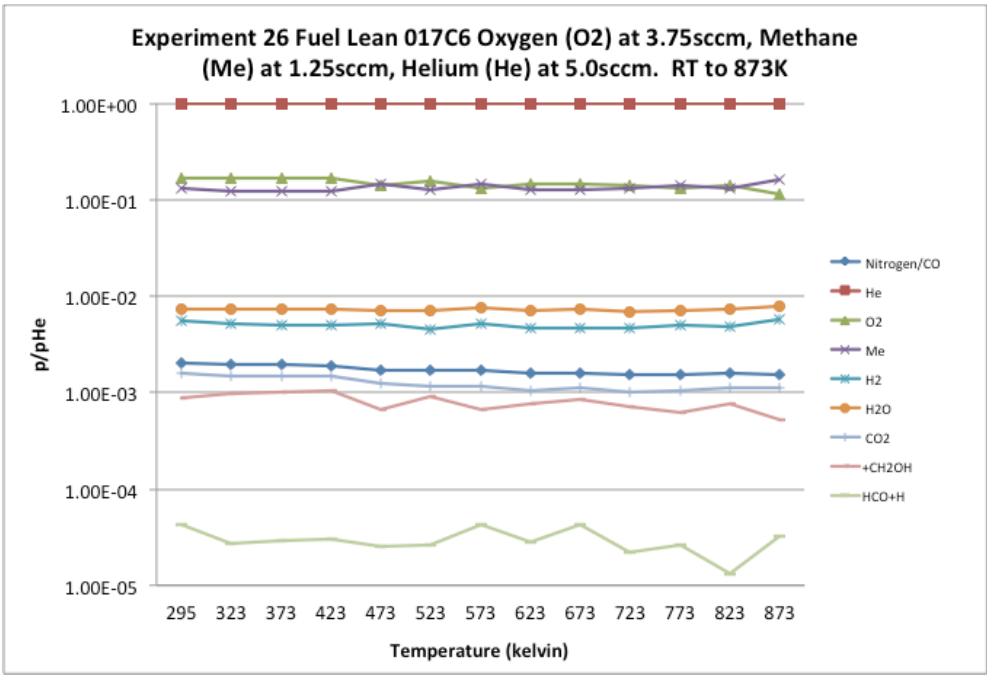

Figure 47 Single gas monitor RGA of sample 017C6 synthesized from cerium nitrate hexahydrate, titanium isopropoxide, CTAB, water, ethanol, and sodium hydroxide

Experiment 27 is sample 017C6 in fuel lean conditions. It is very similar to experiment 26 but left for longer periods of time at 473K and 673K to see if there was a type of cyclization in flow. In figure 48, we see that at 473K the changes are carbon monoxide (1.9%), oxygen (-5.1%), methane (4.2%), hydrogen (7.8%), water (3.5%), carbon dioxide (5.1%). At 673K the changes are carbon monoxide (7.1%), oxygen (-5.5%), methane (4.5%), hydrogen (19.0%), water (4.9%), carbon dioxide (11.9%). There appears to be no significant changes.

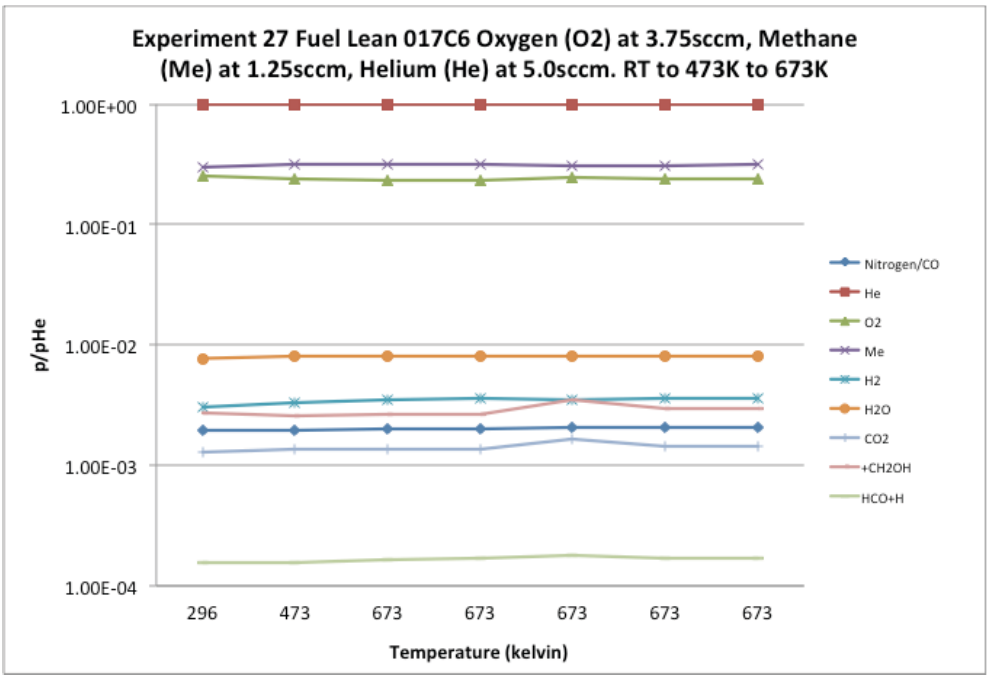

Figure 48 Single gas monitor RGA of sample 017C6 synthesized from cerium nitrate hexahydrate, titanium isopropoxide, CTAB, water, ethanol, and sodium hydroxide

The experiments from the previous set are repeated with a sample that is further calcinated. This sample shows lower reactivity while continuing in the same direction none the less. The idea of periodicity is rejected.

5.3 conclusion

The experiments were mainly run under fuel lean, 1:3 methane to oxygen, and fuel rich, 3:1 methane to oxygen, flows to investigate the conditions that cause partial methane oxidation and full methane oxidation. Some experiments were also run at other ratios for the same purposes. The expectation was that methane and oxygen levels would decrease upon reaction either in the gas phase or on the surface of the catalyst producing water and carbon dioxide or hydrogen and carbon monoxide.

When monitoring for methane oxidation we encountered a significant decrease in oxygen levels for nearly every experiment. This became the norm and not the exception. This effect of oxygen depletion was witnessed with all assayed catalysts. The only discernable significant difference between the catalysts with respect to these experiments was, that the titania doped ceria, sample

017C4 had even greater activity than the other ceria. There didn't appear to be any effects from calcination temperature on the catalyst nor with large difference in surface area.

In experiment set A, experiment 1 with sample 006C6 there is a decrease in oxygen with an increase in hydrogen but also with an increase in methane. There doesn't appear to be any methane oxidation.

When comparing the initial experiments in experiment set B, we investigate different fuel to oxygen ratios with sample 007C6. In experiments 2-5 we have fuel to oxygen ratios of 1:3, 3:1, 1:1, and 2:1. In all of the conditions the oxygen levels drop significantly with varying changes in hydrogen. 1:1 displays the greatest change in oxygen while 1:3 shows the greatest increase in hydrogen and the smallest decrease in oxygen. Unless the reaction happens so fast that the initial values already display that of the products, there is no clear sign of what could be happening. When investigating the change in oxygen and methane ratios, in experiment 6, there appears to be a further loss in oxygen other than that warranted by the change in input flow. When the mass flow of oxygen was decreased by 50% the oxygen level dropped by 88.2%. Oxygen is being consumed. The expected signs of methane oxidation are not seen. Therefore no methane oxidation is occurring.

Experiment set C experiments, 7 and 8, sample 006C4 is run under fuel rich and fuel lean conditions from room temperature to 673K. The comparison of fuel lean and fuel rich conditions for 006C4 both show oxygen decrease and minor increases in hydrogen. These confirm the results that we have seen in the previous set of experiments yet still do not provide a full picture of what is happening in the reaction chamber. Oxygen levels percent decrease is greatest in fuel rich conditions but still decrease in fuel lean conditions yet in converted mass flow values the decrease is greater in fuel lean conditions, with a drop of 0.0461sccm, where there is a greater abundance of oxygen to begin with compared to fuel rich with a drop of 0.0196. The typical methane oxidation products are not being seen; there is no methane oxidation occurring.

Experiment set D In experiment 9 sample 015C4 is run under fuel-less conditions with methane introduction after gas pressure stabilization at 673K. This test shows oxygen depletion after the introduction of methane by 41.6% and hydrogen increases by 56.5%. Comparing the initial levels with 0sccm of methane at RT to those with 0.3sccm of methane at

RT also show that there is a decrease in initial oxygen with the mere presence of methane this effect is further exacerbated by increasing the temperature. Implying that oxygen level decrease is methane dependant.

For experiment set E, in experiment 12, sample 006C4 is run under fuel rich conditions with the mass flow of oxygen and methane while lowering that of the helium to keep total mass flow at 10sccm. This was done to further investigate the oxygen depletion with hopes that any small variations would show up on a bigger scale at these overall ratios while maintaining comparative ratios. The test runs the gas flow in fuel rich conditions until stabilization without a catalyst, then the system is switched to flow through the catalyst. After stabilization oxygen shows depletion and hydrogen shows a large increase. Further demonstrating the previously mentioned possibility that the reaction could be occurring very quickly initially but still does not explain why the oxygen is depleting. Beyond the idea of hydrogen production, which is present in some experiments in certain conditions, there is an overwhelming decrease in oxygen, which is consistently present. As discussed previously, there is an appreciable amount of oxygen level decrease in the presence of methane at RT. This experiment, with a greater quantity of methane and oxygen while preserving the same 3:1 ratio, exhibits a further quantitative decrease of oxygen all the while at RT.

Experiment set F with sample 006C4 (when a catalyst is present), experiments, 13 and 14 cover an extensive set of parameters to see if the overall exhaust flow rate varied throughout the reactions. To investigate the possibility of overall flow change, the execution of the bubble test could rule out any setup issues that could be resulting in oxygen level decrease such as filtering or absorption.

A bubble test was conducted, which measures the exhaust volume for the experiment and conditions. The experiments show that the mass flow through the catalyst does vary but only by 15% at the most, of which the lows account for situations where oxygen wasn't in the conditions, presenting high exhaust flow rates for condition sets that include oxygen. It is expected with the catalyst that overall flow could decrease slightly based on the obstruction it imposes on the system. The largest exhaust flow rates in bubbles come from scenarios where oxygen is involved. There isn't a great flow variation through the catalyst. There is no inhibition of oxygen flow through the catalyst.

Experiment set G experiments, 15, 16 and 17; study the effects of maintaining comparative ratios in fuel rich conditions while changing the overall ratios this time to a further extent. The sample 006C4 is ramped to 673K then back to room temperature as well a more focused run to 423K and back to room temperature. The experiments continue to show oxygen depletion. Reversibility is demonstrated, initially from RT to 423K to RT followed by RT to 673K to RT, both showing similar values in the low points of oxygen levels regardless of the further extent in temperature increase. Experiment 17 looks at a more stepwise approach at the reversibility of the experiment. The results of which shows a fairly symmetric pattern with most gases returning within a 5% change of the initial values with the exception of oxygen, which returns at a 14.7% increase.

In experiment set H, experiment 18 is run with a blank under fuel lean conditions to determine the possibility of thermal reaction in the gas phase or simply in part of the microreactor setup without a catalyst. We see some minor changes as the temperature increases, mainly being an initial increase in levels due to the rise in temperature. The gas levels change as follows, carbon monoxide (4.3%), oxygen (3.2%), methane (1.0%), hydrogen (0.8%), water (3.9%), carbon dioxide (6.2%). We can clearly see that without the catalyst the oxygen levels do not deplete.

In experiment set I with sample 006C4, Experiment 19 is run in a similar fashion as experiment 17 but fuel-less with the reintroduction of methane and reduction of helium to see its effects on oxygen depletion. Experiment 20 follows in the same manner while increasing the oxygen levels to 1.50sccm while keeping the other levels the same. Again we see reduction in oxygen levels, experiment 21 shows a more significant drop at 573K with a simultaneous increase in hydrogen but no decrease in methane, therefore there is no methane oxidation. Experiment 22 shows similar results at lower temperatures. At 373K, oxygen and water begin to decrease while hydrogen and carbon monoxide begin to increase. Under fuel lean conditions there appears to be partial oxidation of methane.

In experiment set J with sample 017C4, experiment 23 showed oxygen depletion immediately. The oxygen levels were ramped up to show that between 6 and 7sccm oxygen reappears in the mass spec. This shows there is a limit to the consumption. Further testing shows that with a minor increase in temperature the oxygen depletes again. Experiment 24 displays a 1:2 fuel lean scenario

compared to 1:3 fuel lean in experiment 25 and as discussed earlier the larger amount of oxygen present the greater the decrease in the oxygen with a drop of 0.1033sccm for experiment 24 and 0.2813sccm for experiment 25.

Experiment set K

Experiment 26 sample 017C6 is run under fuel lean conditions from room temperature to 873K. The experiments from the previous set are repeated with a sample that is further calcinated. This sample shows lower reactivity while continuing in the same direction none the less. The idea of periodicity in oxygen levels from experiment 26 was tested and rejected in experiment 27.

Chapter 6

Conclusion

6.1 Synthesis

A series of mesoporous ceria based materials were synthesized using a range of surfactants, precursors, and solvents. Post-synthesis the samples are were calcinated at different temperatures to test the working conditions under which they would be used. Part of the sample is kept as-synthesized while two other parts are calcinated at 673K and 873K. Ceria doping was performed with samarium, copper, and titanium individually to improve the material's properties including thermal stability and reactivity with methane oxidation.

Analysis of each sample was conducted through characterization techniques, comparing them with XRD and gas adsorption for crystallite size long-range order, pore volume, average pore size, and surface area. XRD and gas adsorption assume spherical shape of particles. SEM and TEM were used to take a closer look at the actual particles and determine shape. Crystallite size varied from 34.0nm to 2.2nm. Typically, larger crystallite sizes are observed at higher temperatures, save for a few samples exhibiting high thermal stability. Pore volume and pore size follow a similar trend, although it should increase initially because of the calcination process, it also increases at higher temperatures because of pore degradation, again except for a few thermally stable sample. Surface area follows an inverted trend of pore size and pore volume since pore degradation decreases the applicable surface of the catalyst.

Displaying higher thermal stability over the other surfactants, the cationic surfactant, CTAB, showed to be the most effective surfactant yielding a high surface area ($90.3 m^2/g$ at 673K). Surfactant concentration effects show that a lower concentration of CTAB has greater thermal stability and surface area at 673K ($90.3 m^2/g$). Cerium nitrate hexahydrate produces the most thermally stable product out the four precursors, yielding the highest surface area at 673K ($97.7 m^2/g$). Doping ceria with titanium provides the most stability to give great thermal stability and high surface area at 673K ($114.9 m^2/g$).

Solvent system effects show that using hexane with NaOH yields a high surface area at 393K ($78.8m^2/g$), with very poor thermal stability. Water/ethanol with NaOH yields the highest surface area at 673K ($90.3m^2/g$) while using toluene and pyridine yields the highest surface area at 873K ($47.2m^2/g$) and demonstrating the greater thermal stability. Since the target temperature is 673K water/ethanol with NaOH is considered to be the best-suited solvent system.

The ideal synthesis method that was understood to be the most thermally stable was low concentration CTAB as a surfactant, cerium nitrate hexahydrate as a precursor, and water/ethanol with NaOH as the solvent system. Individually these factors provide the building blocks for thermally stable ceria. Coincidently; sample 006 shows to be the most thermally stable version of non-doped ceria yielding a high surface area of $97.7m^2/g$. This method was then applied to the synthesis of doped ceria. At 693K the surface area is greatest with sample 017 ($114.9m^2/g$); the titanium doping increases thermal stability. Pore volume (0.613cc/g) and pore size (21.4nm) also were among the highest with 017 at 673K.

6.2 Catalysis

From the synthesis we selected pure ceria samples 006C4, 007C6, 015C4, as well as titania doped ceria 017C4, 017C6 to test the material characteristics with methane oxidation. The experiments were mainly run under fuel lean, 1:3 methane to oxygen, and fuel rich, 3:1 methane to oxygen, flows to investigate the conditions that cause partial methane oxidation and full methane oxidation. Some experiments were also run at other ratios for the same purposes.

When monitoring for methane oxidation we encountered a significant decrease in oxygen levels for nearly every experiment. This became the norm and not the exception. This effect of oxygen depletion was witnessed with all assayed catalysts. The only discernable significant difference between the catalysts with respect to these experiments was, that the titania doped ceria, sample 017C4 had even greater activity than the other ceria when it came to oxygen depletion. Most of the time the only other gases increasing are methane and hydrogen. There didn't appear to be any effects from calcination temperature on the catalyst nor with large difference in surface area. A blank was run with no discernible changes in oxygen and methane levels. The catalyst was also run with only oxygen and helium as well as with only methane and helium, both scenarios showing no changes in oxygen and/or methane until the introduction of the missing component. This showed

that all the components; ceria, methane, and oxygen, were necessary for oxygen depletion. Even the idea of adsorption into the ceria was thought to be a possibility. When run for several days, even weeks there was no sign of saturation.

This oxygen loss was more prevalent with titania doped ceria. On the other and there was no observable methane oxidation. The method of catalysis is not understood and has yet to be explained. There are no identified side products that could be coming from oxygen.

References

1) Yu, G. et al, Fuel, 2010, 89, 1070–1076
2) Liu, Q. et al, J. Phys. Chem. C 2009, 113, 17262–17267
3) Inaba, H.; Tagawa, H., Solid State Ionics, 1996, 83, 1
4) Xu, X. Y.; Xia, C. R.; Mao, G. L.; Peng, D. Solid State Ionics, 2005, 176, 1513.
5) Tjandra, W., Yao, J., Tam, K.C., Langmuir, 2006, 22, 1493-1499
6) Nagarajan, R. et al, J. Chem. Phys., 1989, 90, 5843
7) Southall et al., J. Phys. Chem. B, 2002, 106, 521.
8) Keith R. Williams, Brian D. McNicol, Encyclopedia of Catalysis, 2002
9) Cox, D., Nanostructure Science and Technology: R & D Status and Trends in Nanoparticles, Nanostructured Materials and Nanodevices, 1999, 49-66
10) Quantachrome instruments, Autosorb-1 operating manual, 2004
11) Pavia et al, Introduction to spectroscopy (third edition), 2001, 579 pages
12) Knapp, D., J. Phys. Chem. C 2008, 112, 17311–17318
13) Chang, R., Chemistry (7th edition), 2002, 1001pages
14) Younes-Metzler et al, Journal of Catalysis, 2006, 241, 74-82
15) Lyons, D., Ryan K., Morris, M., J. Materials Chemistry, 2002, 12, 1207-1212
16) Tompsett, G. A., Langmuir 2005, 21, 8214-8225
17) Choi, M., Cho, H. S., nature materials, 2006, 5, 718-723
18) Kuni, M. F. Shchekin, A. K., Langmuir 2006, 22, 1534-1543
19) Lu, C., et al, Journal of the Electrochemical Society, 2003,150, 3 A354-A358
20) Mamak, M., et al Chem Materials 2001, 13, 3564-3570
21) Sinha, A. K., Suzuki, K. J. Phys. Chem. B 2005, 109, 1708-1714
22) Deshpande, A. S., Pinna, N., Small 2005, 1, No.3, 313-316
23) Zhang, G., Shen, Z., J Phys. Chem.. B 2006, 110, 25782-25790
24) Sun, C., Sun, J., Xiao, G., J. Phys. Chem. B 2006, 110, 13445-13452
25) Williamson G. K., Hall, H., Acta Metallurgica, 1953, 1, 22-31
26) Yue, L., Zhang, X.M., Ceramics international, 2009, 35, 847-853
27) Calles, J.A., et al, Microporous and mesoporous materials, 2009, 119, 200-207
28) Bricker, L. M., North American Catalysis society, 20th NAM, 2007 “Characterization of catalyst intermediates in Methane Oxidation”
29) Fu, G., Xu, X., Catalysis Today, 2006, 117, 133-137

30) Idriss, H., Platinum Metals Rev, 2004, 48, 3, 105-115
31) M. D. MDI Jade 6.1 Inc.; Material Data Inc., 2002.
32) Brunauer, S.; Emmett, P.; Teller, E. J. Am Chem. Soc. 1938, 60, 309
33) Dudek, M., J. European Ceramic Society, 2008, 28, 965-971
34) Zhang, J. H., Journal of Molecular Catalysis A: Chemical 237 (2005) 182–190
35) Lyons D., J. Mater. Chem., 2004, 14, 1976–1981
36) Rumruangwong, M., Appl. Organometal. Chem. 2008, 22, 167–170
37) Shishkin, M., J. Phys. Chem. C 2009, 113, 21667–21678
38) Ksapabutr, B., Materials Chemistry and Physics, 2004, 83, 34–42
39) Reichinger, M., Journal of Catalysis, 2010, 269, 367–375
40) EG&G Technical Services, Inc, Fuel Cell Handbook, 2004, 427 pages
41) Luo, J. -Y., Journal of Catalysis, 2008, 254, 310–324
42) Khalil, K.M.S., Microporous and Mesoporous Materials, 2005, 269, 83–89
43) K.S.W. Sing and R.T. Williams, Adsorption Science & Technology, 2004, 22, 10
44) Rouquerol, J. Pure Appl. Chem., 1994, 66, 8, 1739-1758
45) de Boer, J. H., Journal of colloid and interface science, 1966, 21, 405-414
46) Stanford research systems, gas correction factors for ionization gauges
47) MKS RGA Application Bulletin #208, Note #03/02

Appendices

Appendix A

Powder x-ray diffractograms

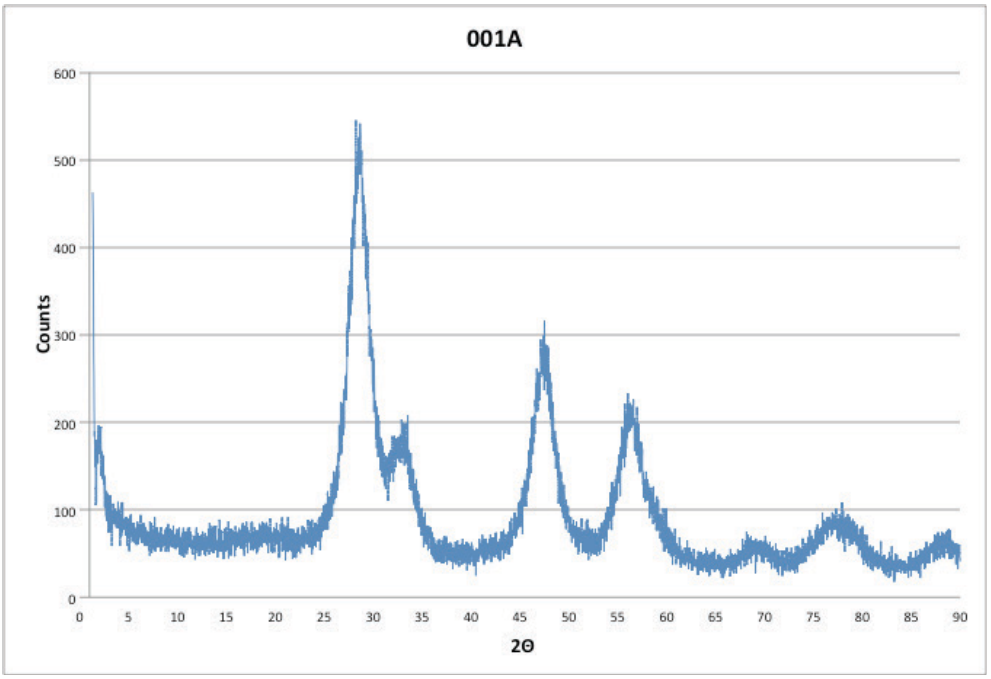

Figure 49 pXRD of sample 001A, synthesized from cerium (IV) hydroxide, CTAB, water, ethanol, and sodium hydroxide, uncalcinated

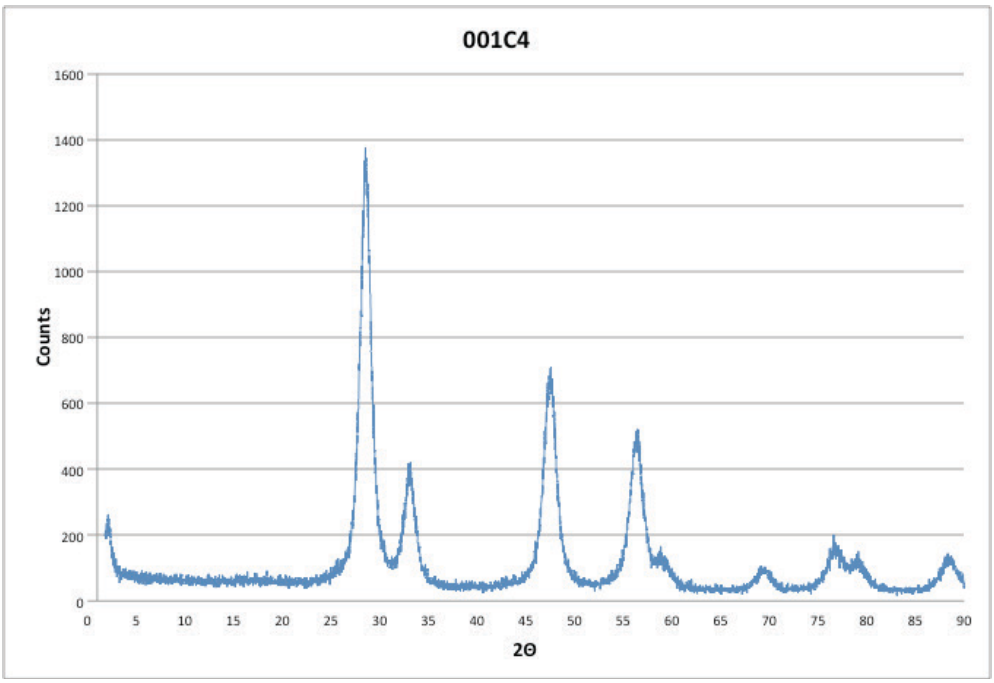

Figure 50 pXRD of sample 001C4, synthesized from cerium (IV) hydroxide, CTAB, water, ethanol, and sodium hydroxide, calcinated at 673K

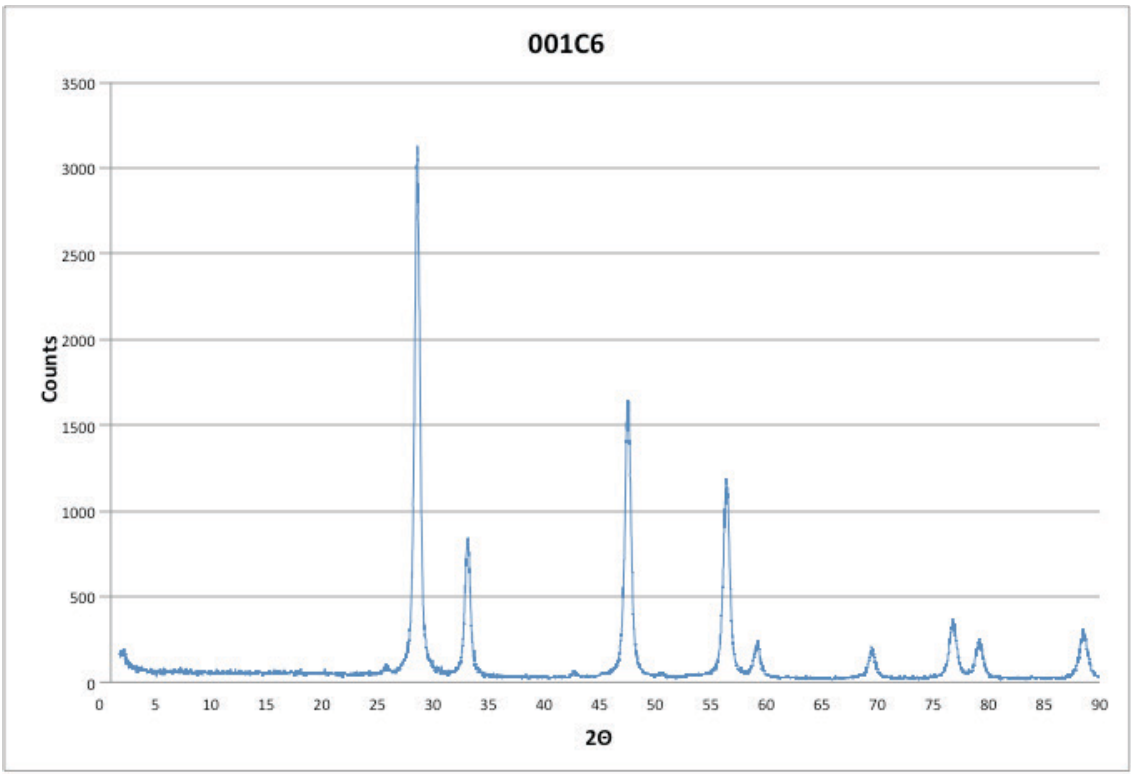

Figure 51 pXRD of sample 001C6 synthesized from cerium (IV) hydroxide, CTAB, water, ethanol, and sodium hydroxide, calcinated at 873K

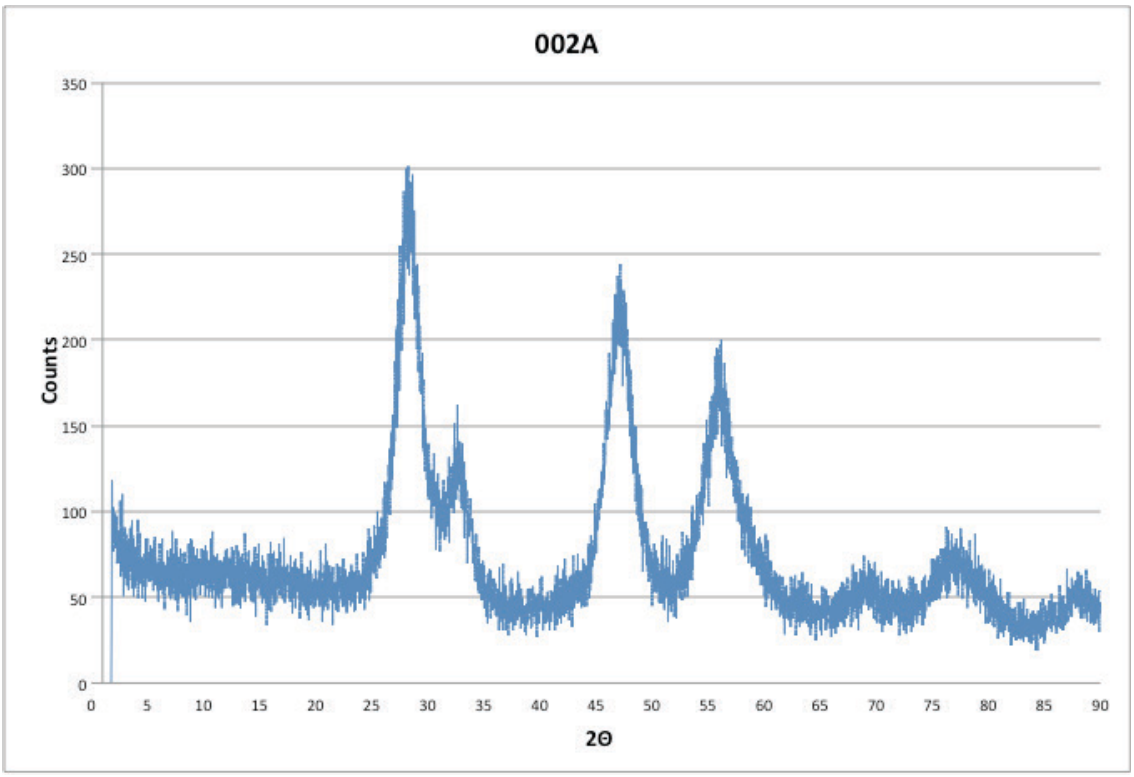

Figure 52 pXRD of sample 002A synthesized from cerium (IV) hydroxide, myristyl trimethylammonium bromide, water, ethanol, and sodium hydroxide, uncalcinated

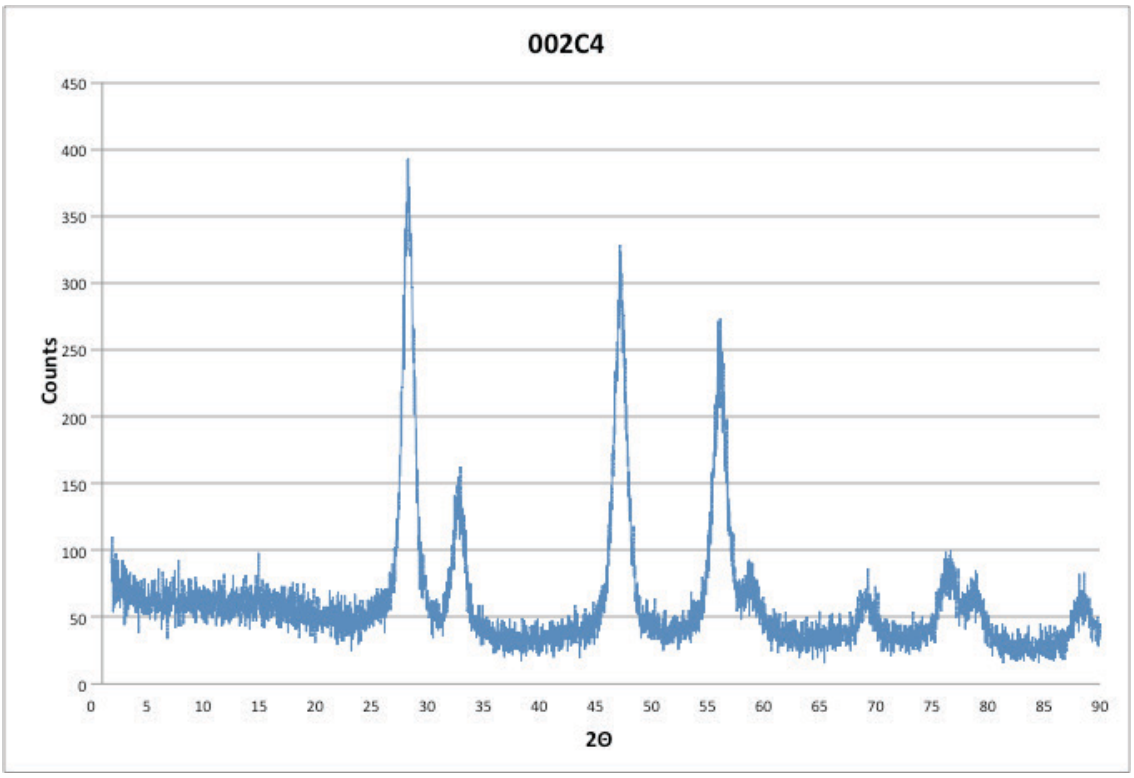

Figure 53 pXRD of sample 002C4, synthesized from cerium (IV) hydroxide, myristyl trimethylammonium bromide, water, ethanol, and sodium hydroxide, calcinated at 673K

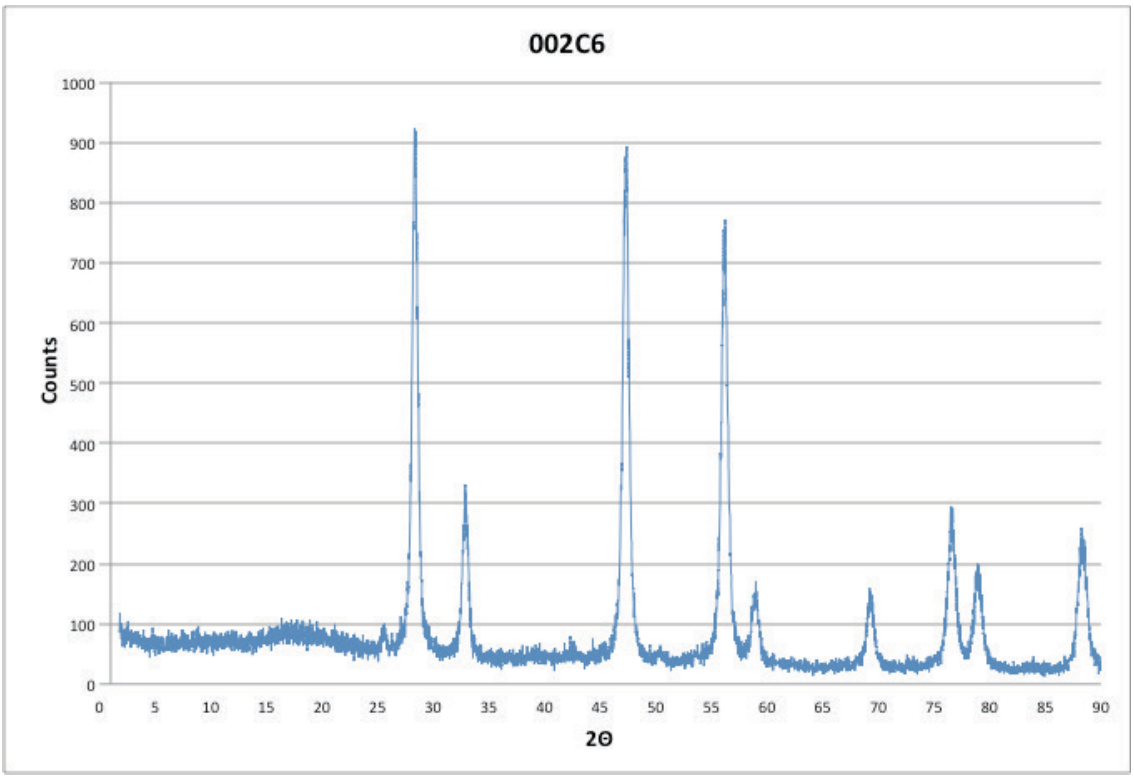

Figure 54 pXRD of sample 002C6, synthesized from cerium (IV) hydroxide, myristyl trimethylammonium bromide, water, ethanol, and sodium hydroxide, calcinated at 873K

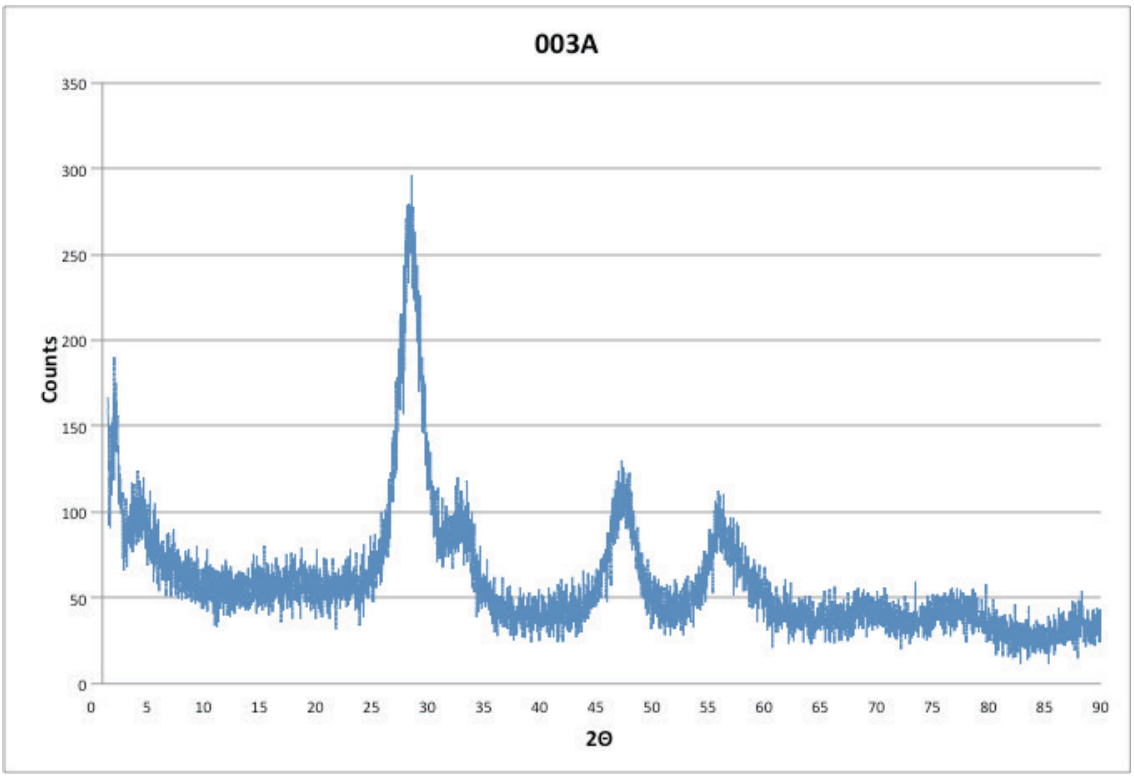

Figure 55 pXRD of sample 003A synthesized from cerium (IV) hydroxide, CTAB, hexane, ethanol, and sodium hydroxide, uncalcinated

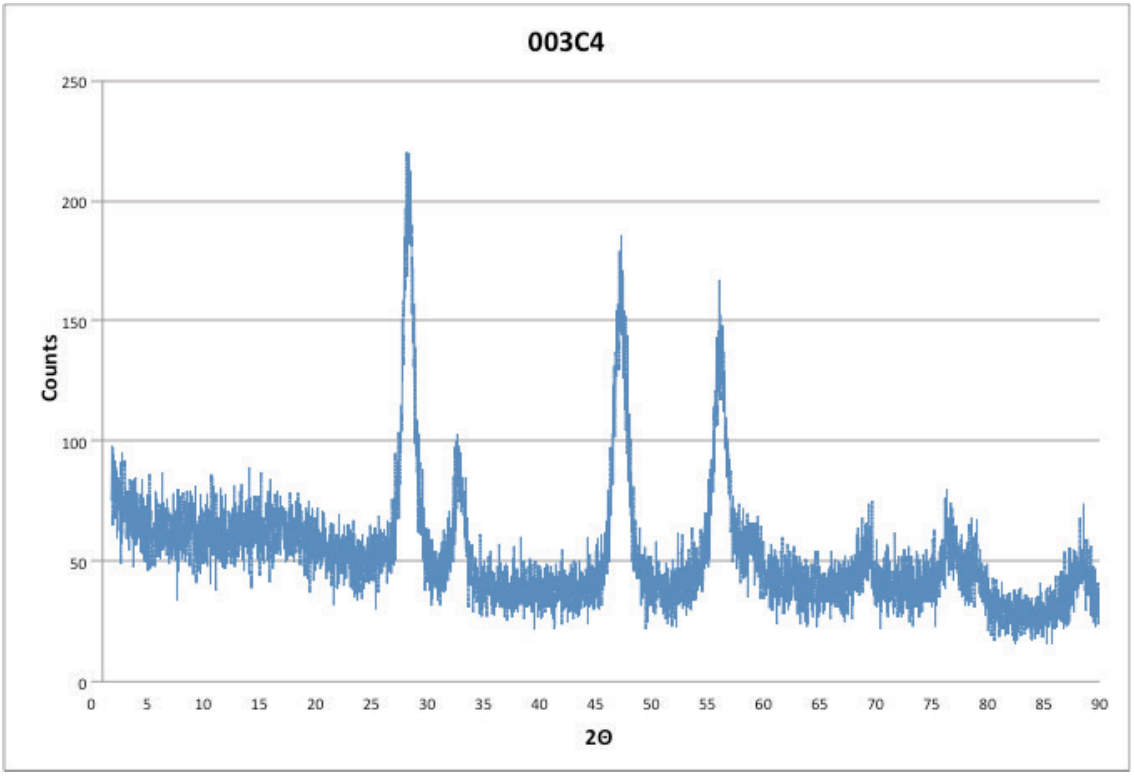

Figure 56 pXRD of sample 003C4 synthesized from cerium (IV) hydroxide, CTAB, hexane, ethanol, and sodium hydroxide, calcinated at 673K

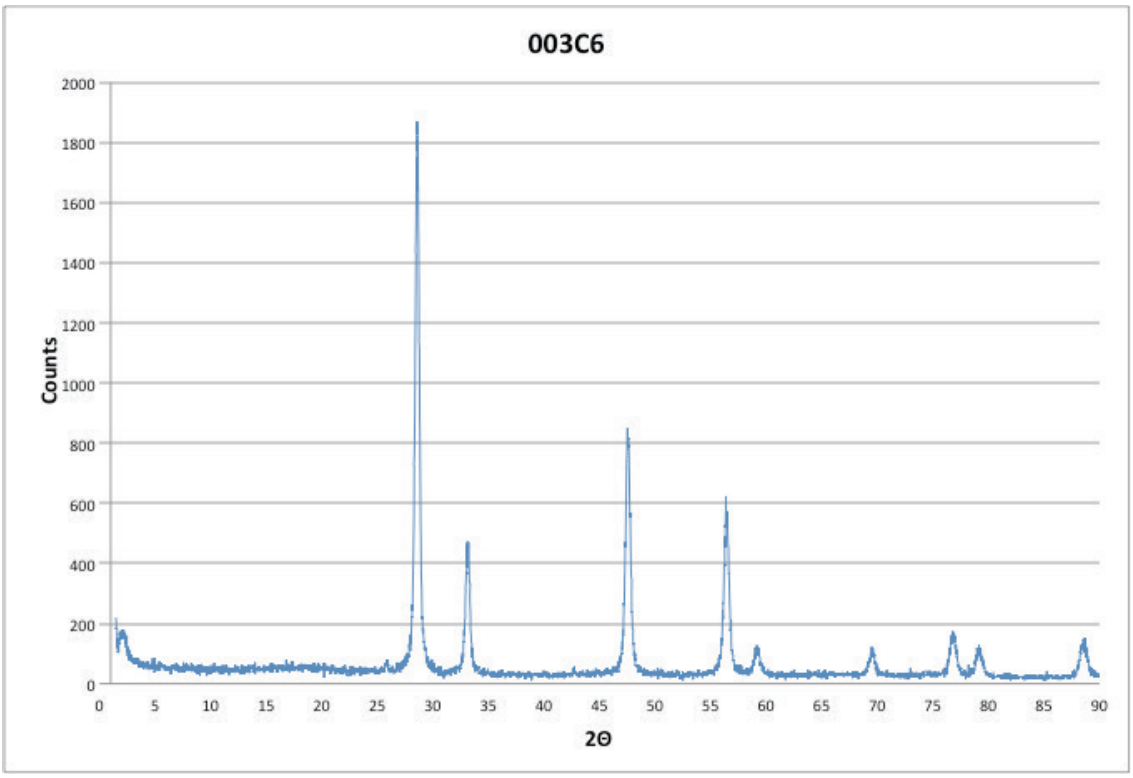

Figure 57 pXRD of sample 003C6 synthesized from cerium (IV) hydroxide, CTAB, hexane, ethanol, and sodium hydroxide, calcinated at 873K

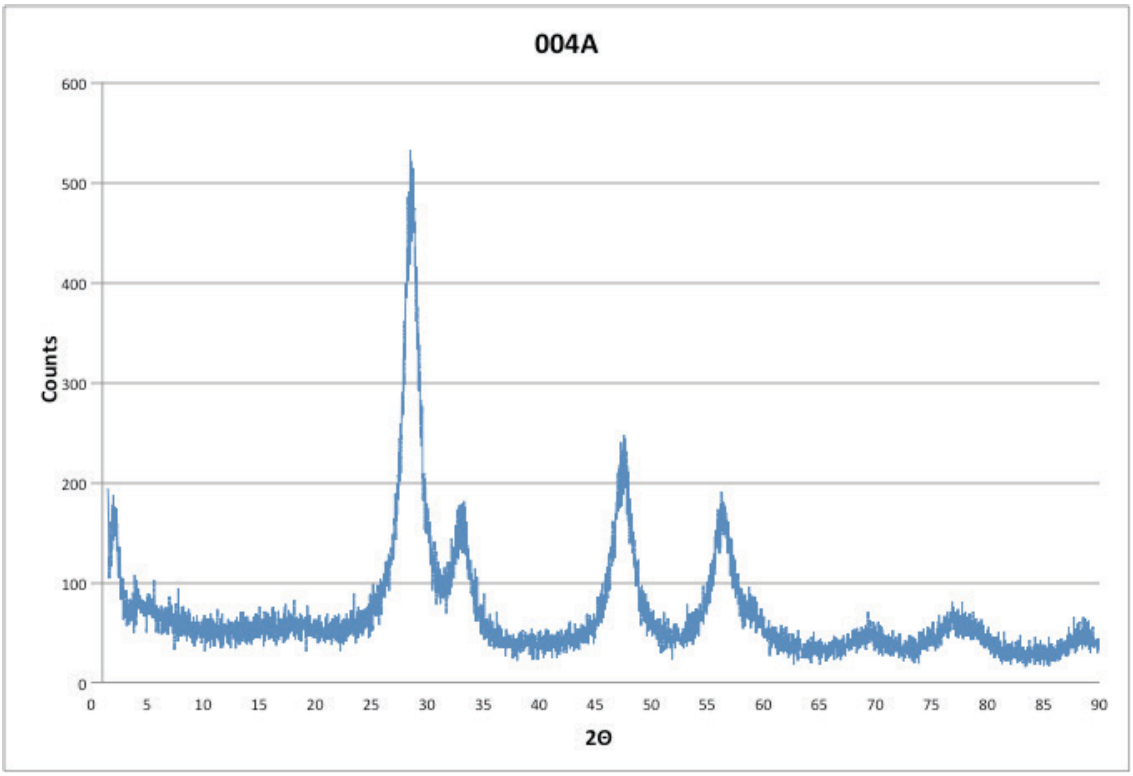

Figure 58 pXRD of sample 004A synthesized from cerium glycolate, CTAB, water, ethanol, and sodium hydroxide, uncalcinated

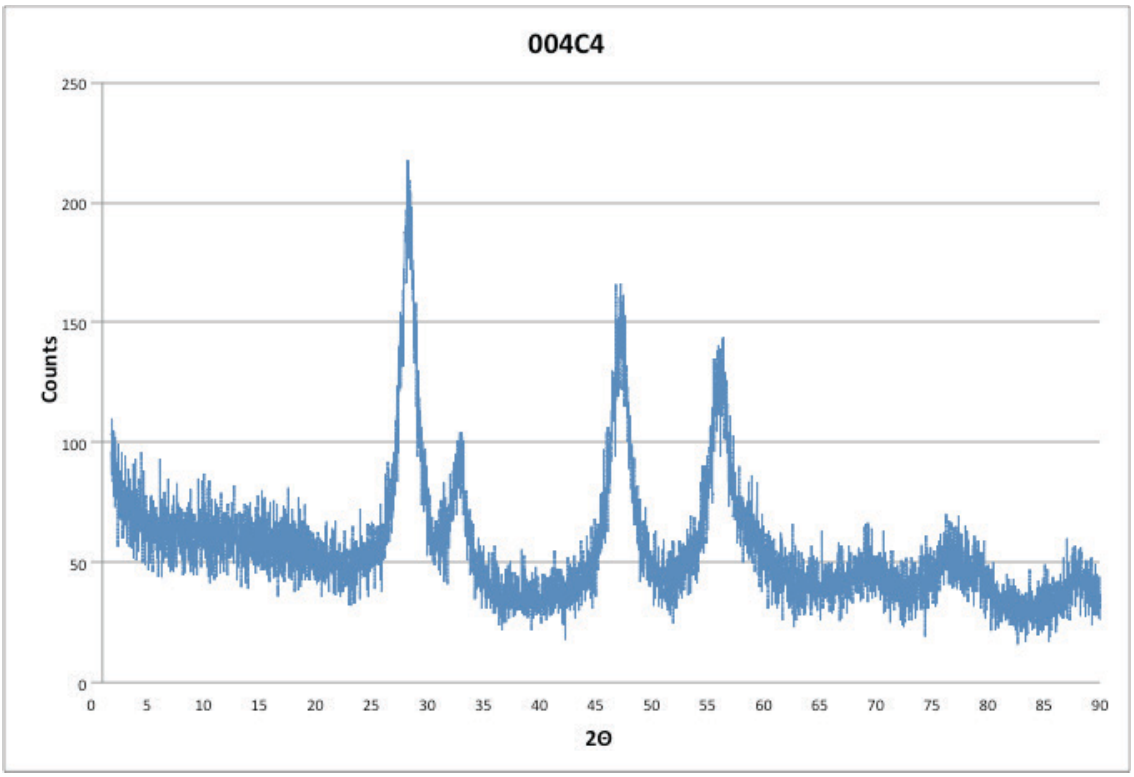

Figure 59 pXRD of sample 004C4 synthesized from cerium glycolate, CTAB, water, ethanol, and sodium hydroxide, calcinated at 673K

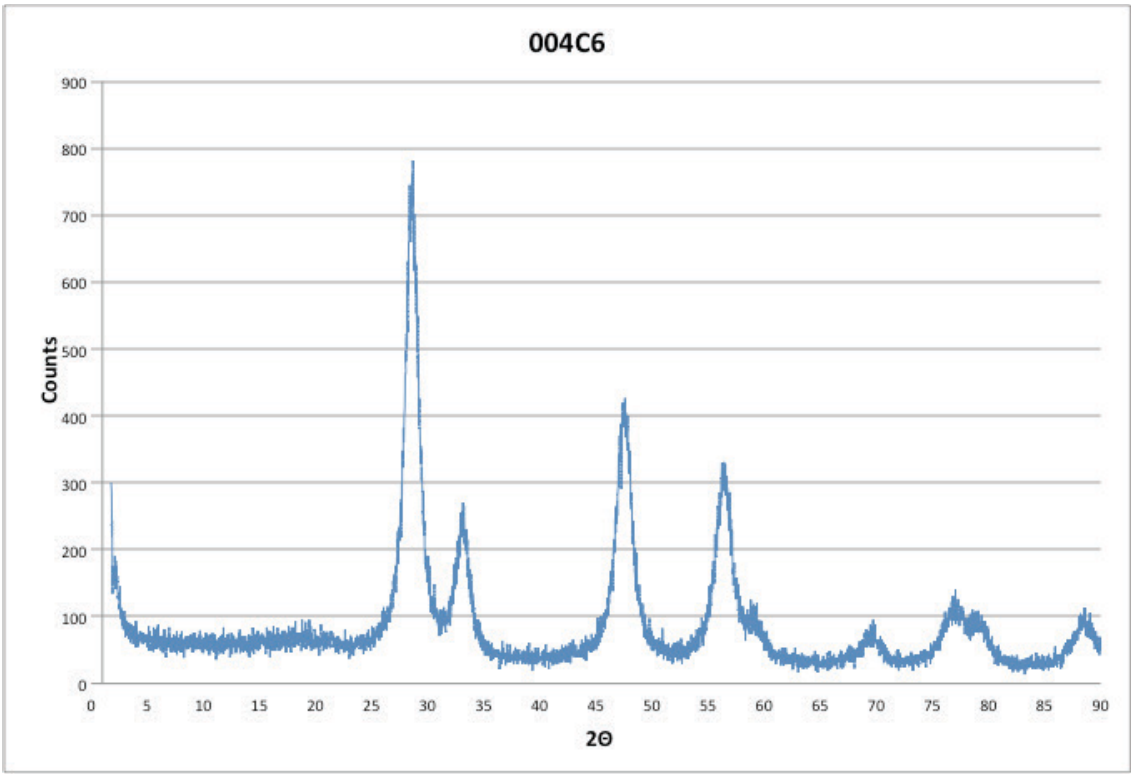

Figure 60 pXRD of sample 004C6 synthesized from cerium glycolate, CTAB, water, ethanol, and sodium hydroxide, calcinated at 873K

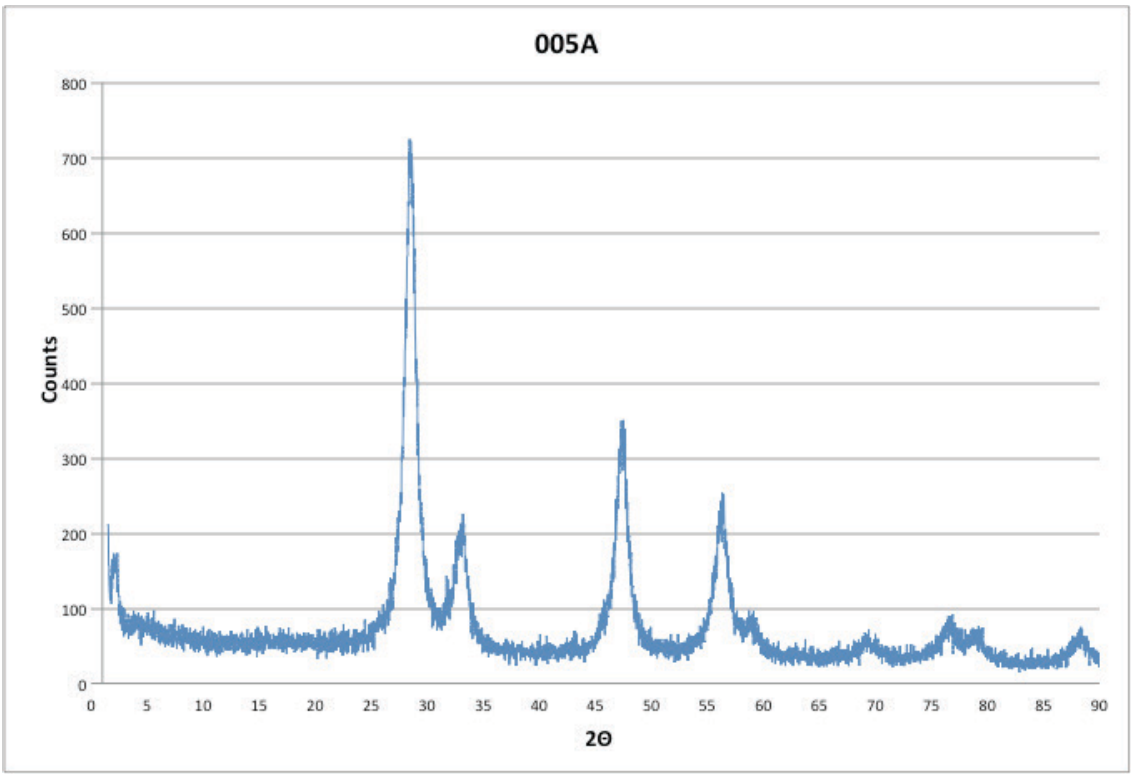

Figure 61 pXRD of sample 005A synthesized from cerium (III) chloride heptahydrate, CTAB, water, ethanol, and sodium hydroxide, uncalcinated

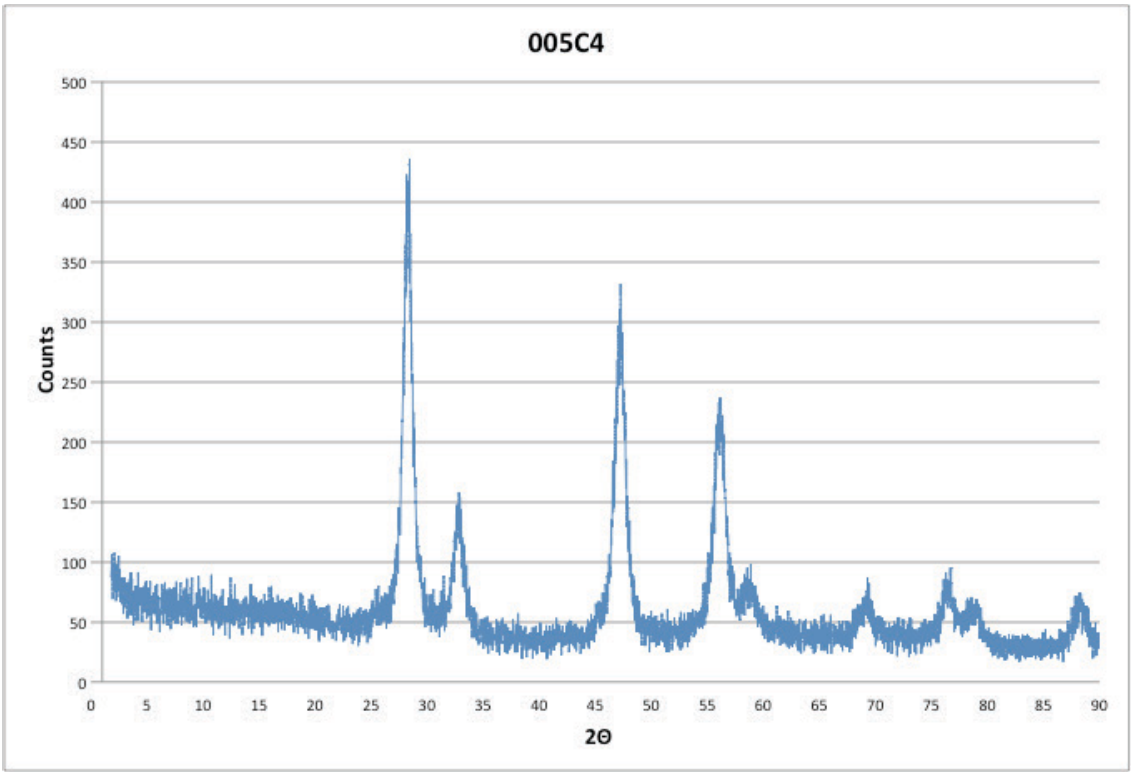

Figure 62 pXRD of sample 005C4 synthesized from cerium (III) chloride heptahydrate, CTAB, water, ethanol, and sodium hydroxide, calcinated at 673K

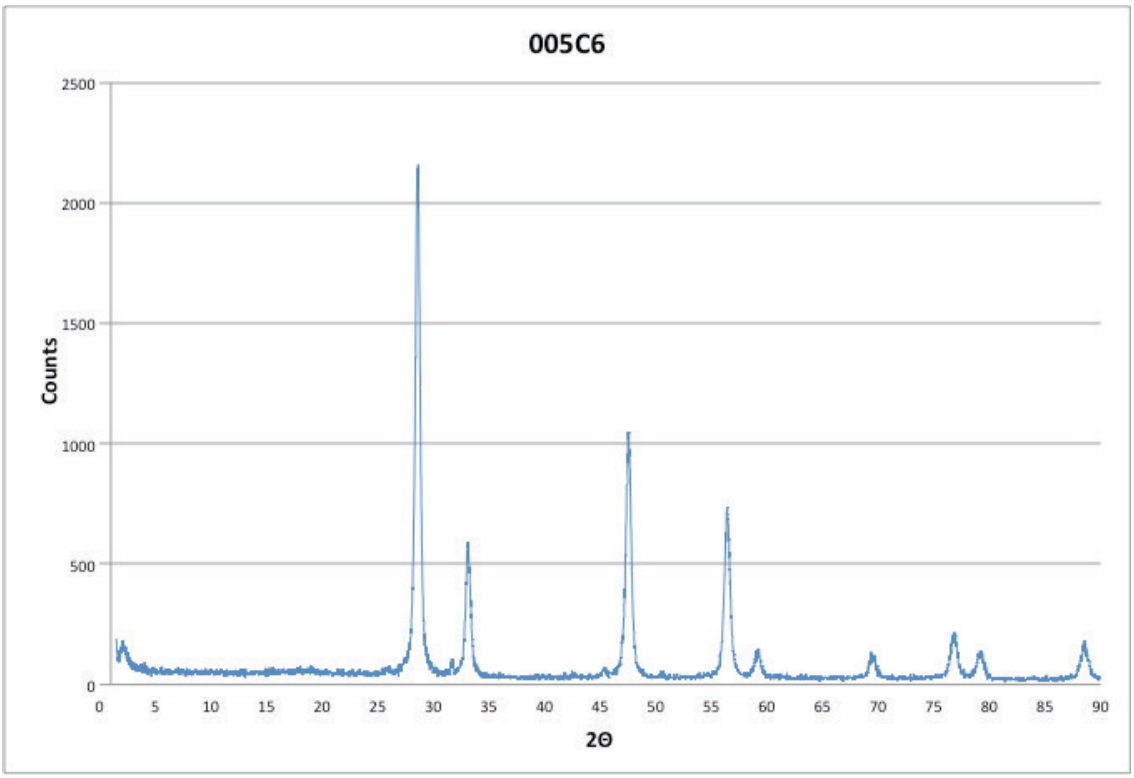

Figure 63 pXRD of sample 005C6 synthesized from cerium (III) chloride heptahydrate, CTAB, water, ethanol, and sodium hydroxide, calcinated at 873K

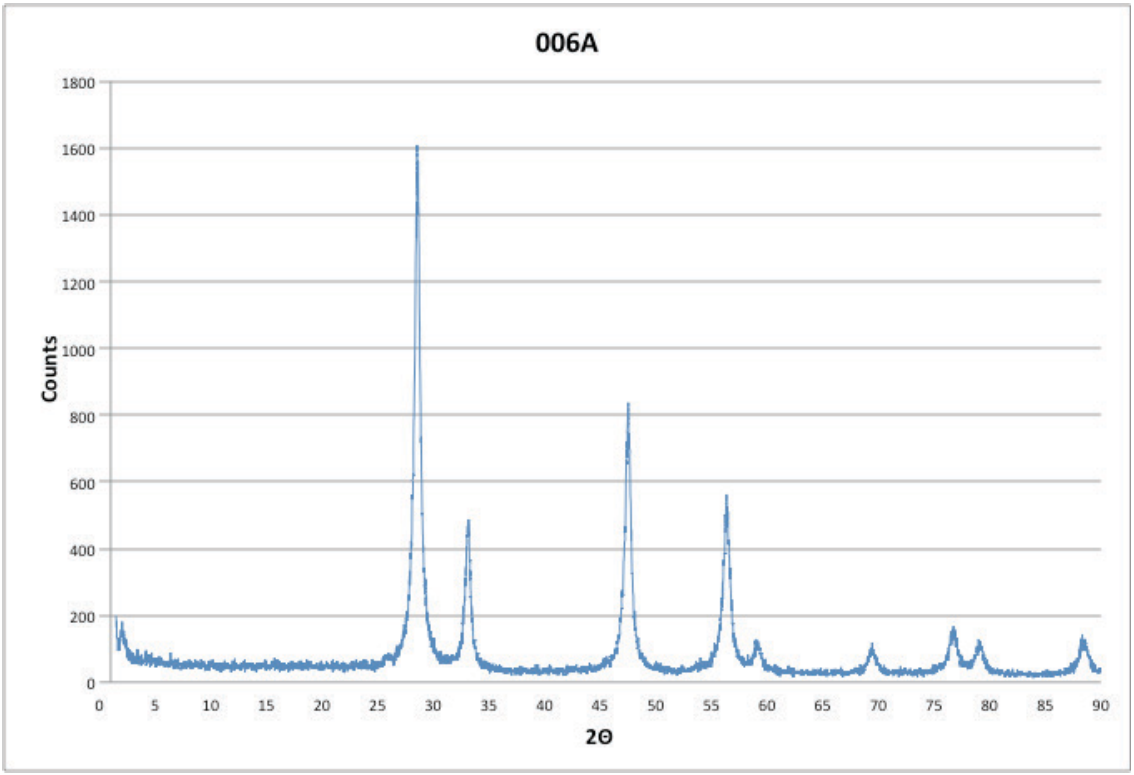

Figure 64 pXRD of sample 006A synthesized from cerium (III) nitrate hexahydrate, CTAB, water, ethanol, and sodium hydroxide, uncalcinated

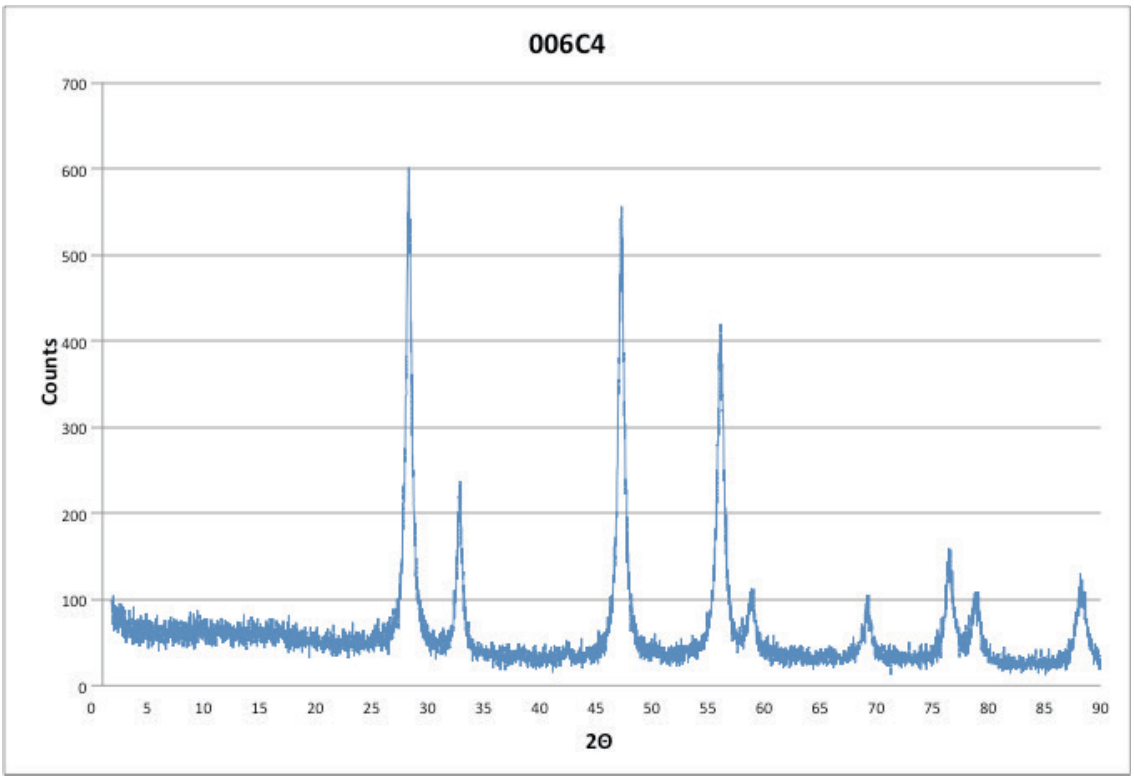

Figure 65 pXRD of sample 006C4 synthesized from cerium (III) nitrate hexahydrate, CTAB, water, ethanol, and sodium hydroxide, calcinated at 673K

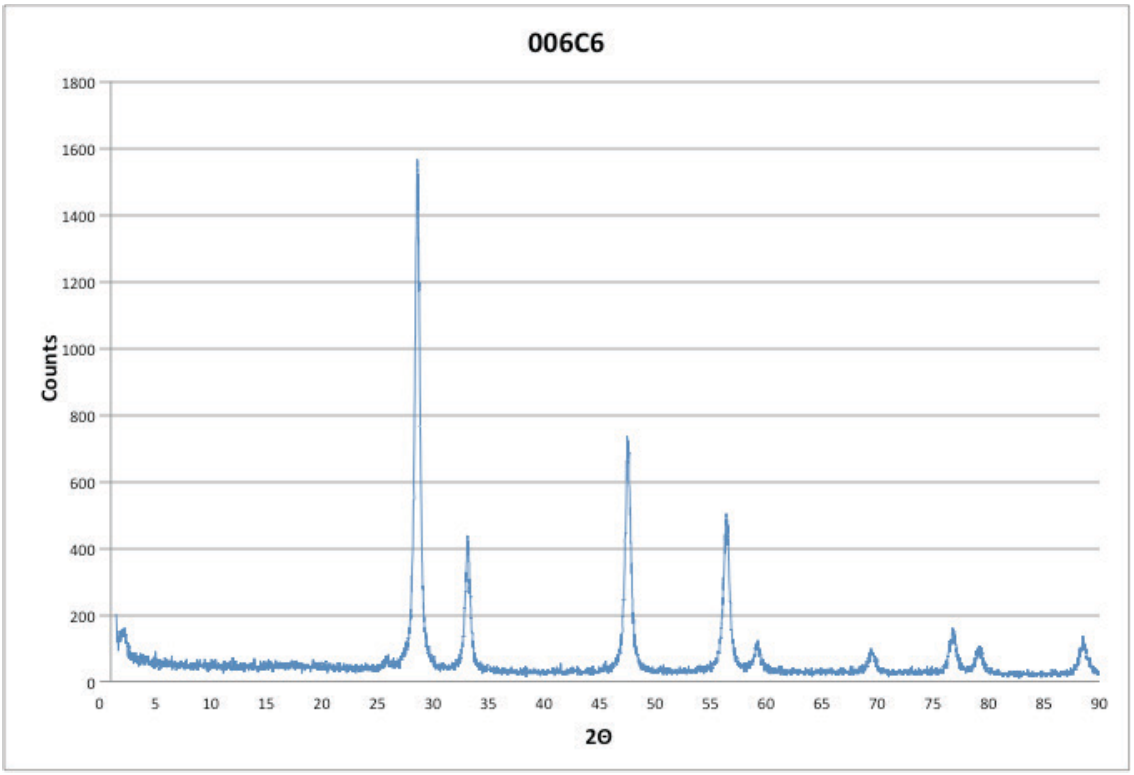

Figure 66 pXRD of sample 006C6 synthesized from cerium (III) nitrate hexahydrate, CTAB, water, ethanol, and sodium hydroxide, calcinated at 873K

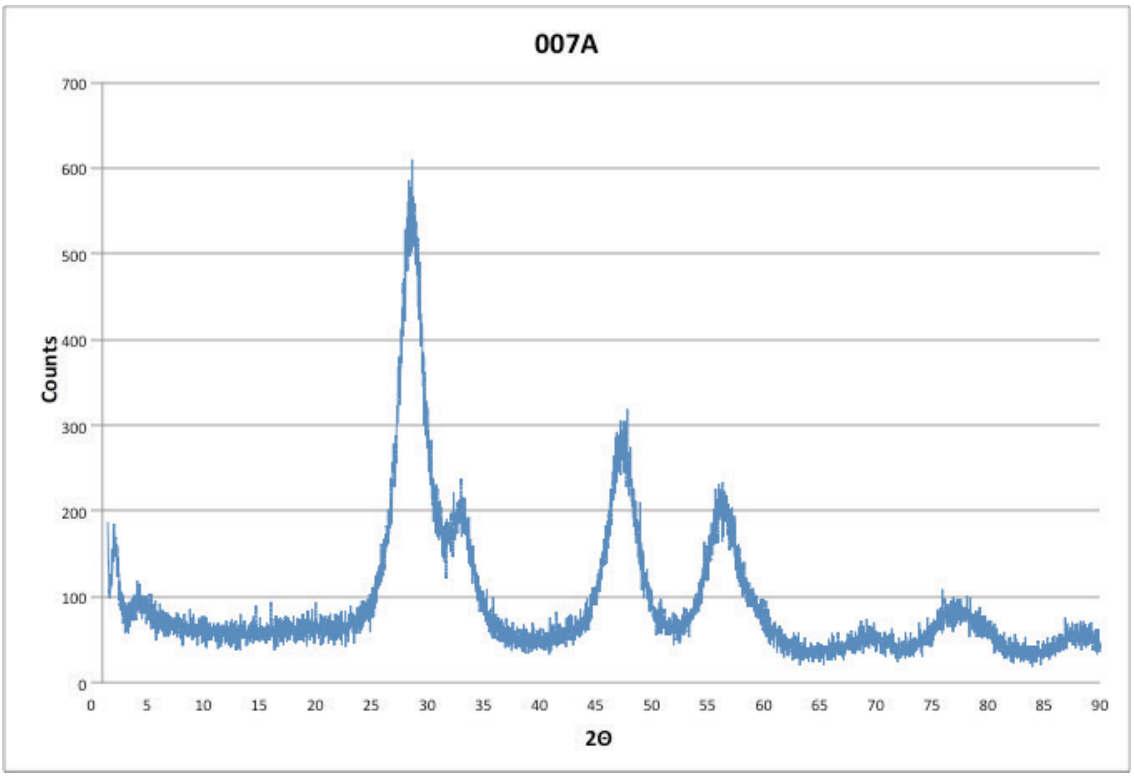

Figure 67 pXRD of sample 007A synthesized from cerium hydroxide, CTAB, paraffin, water, ethanol, dichloromethane, and sodium hydroxide, uncalcinated

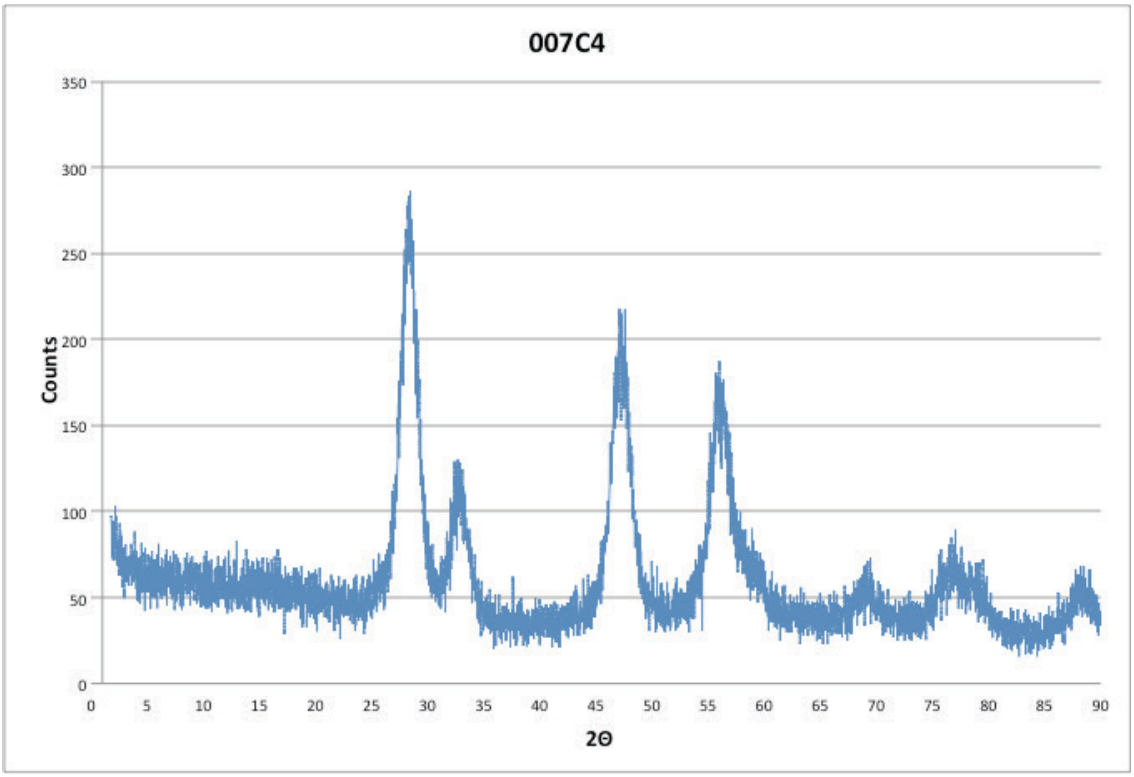

Figure 68 pXRD of sample 007C4 synthesized from cerium hydroxide, CTAB, paraffin, water, ethanol, dichloromethane, and sodium hydroxide, calcinated at 673K

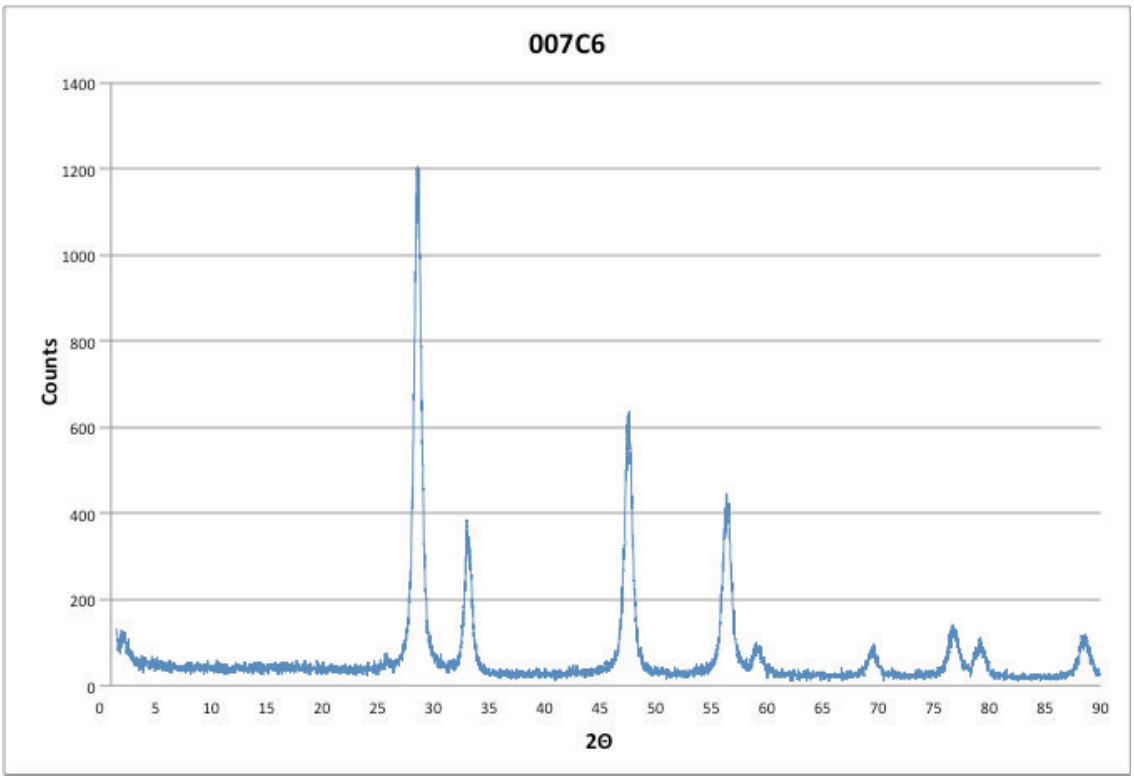

Figure 69 pXRD of sample 007C6 synthesized from cerium hydroxide, CTAB, paraffin, water, ethanol, dichloromethane, and sodium hydroxide, calcinated at 873K

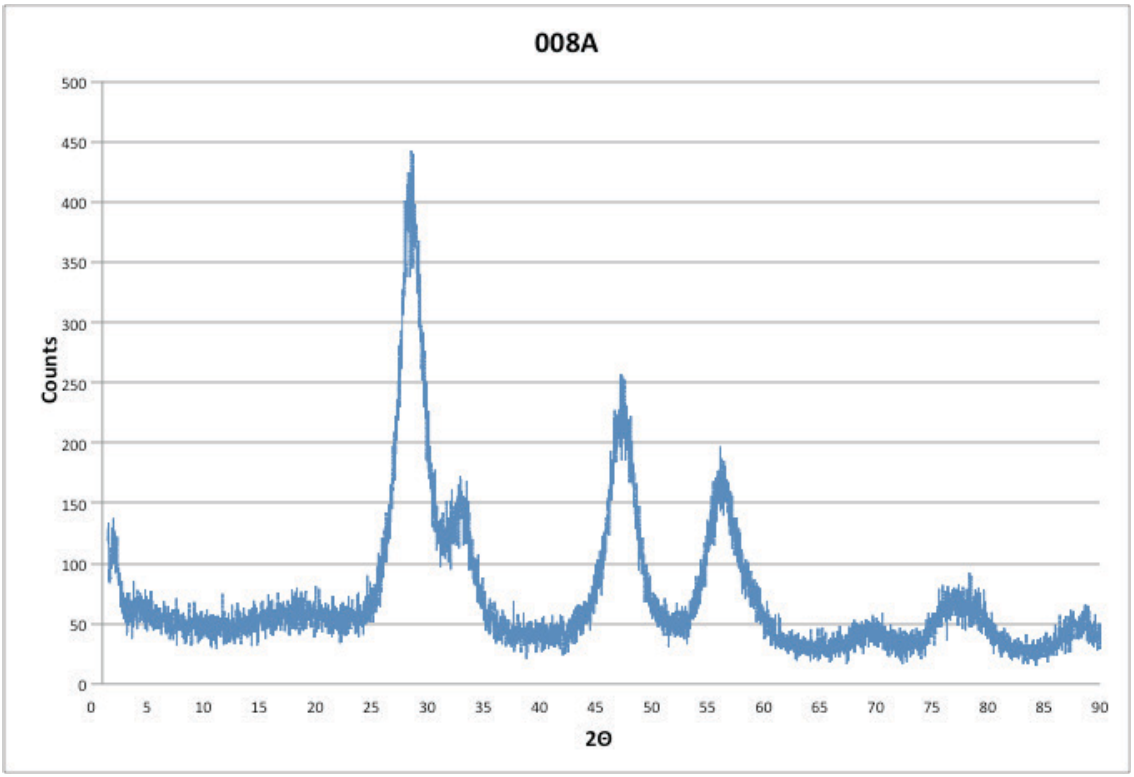

Figure 70 pXRD of sample 008A synthesized from cerium hydroxide, CTAB, paraffin, water, ethanol, and sodium hydroxide, uncalcinated

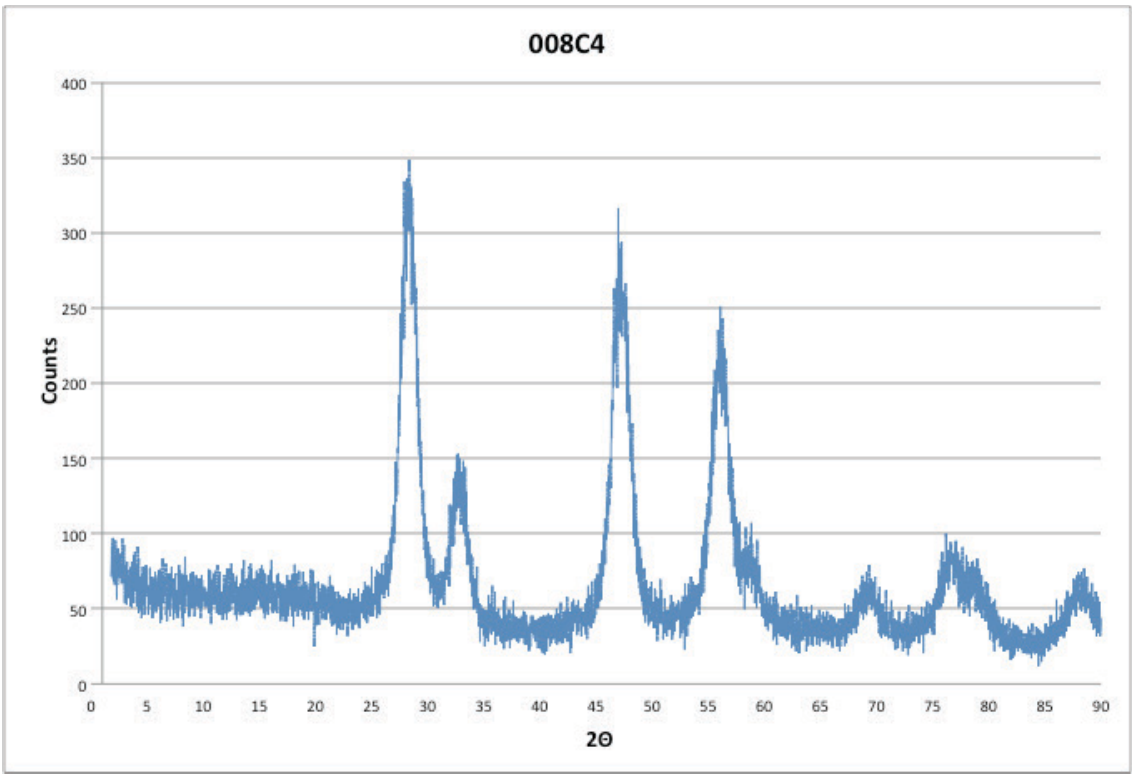

Figure 71 pXRD of sample 008C4 synthesized from cerium hydroxide, CTAB, paraffin, water, ethanol, and sodium hydroxide, calcinated at 673K

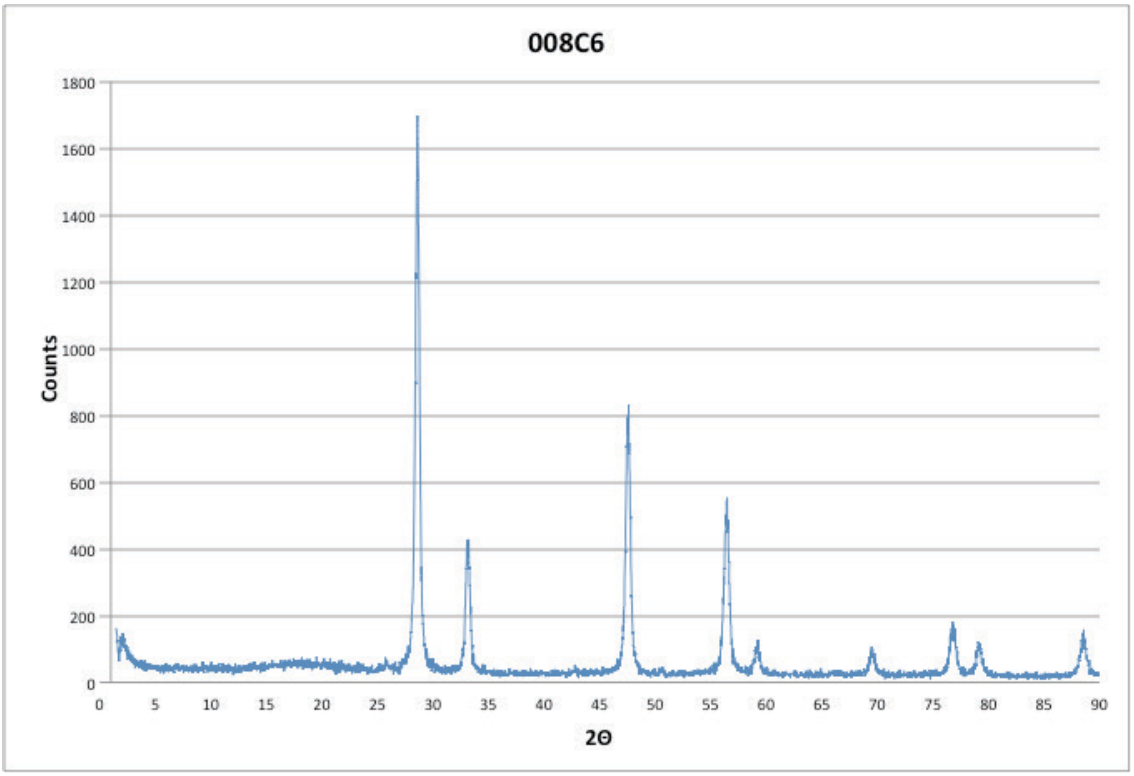

Figure 72 pXRD of sample 008C6 synthesized from cerium hydroxide, CTAB, paraffin, water, ethanol, and sodium hydroxide, calcinated at 873K

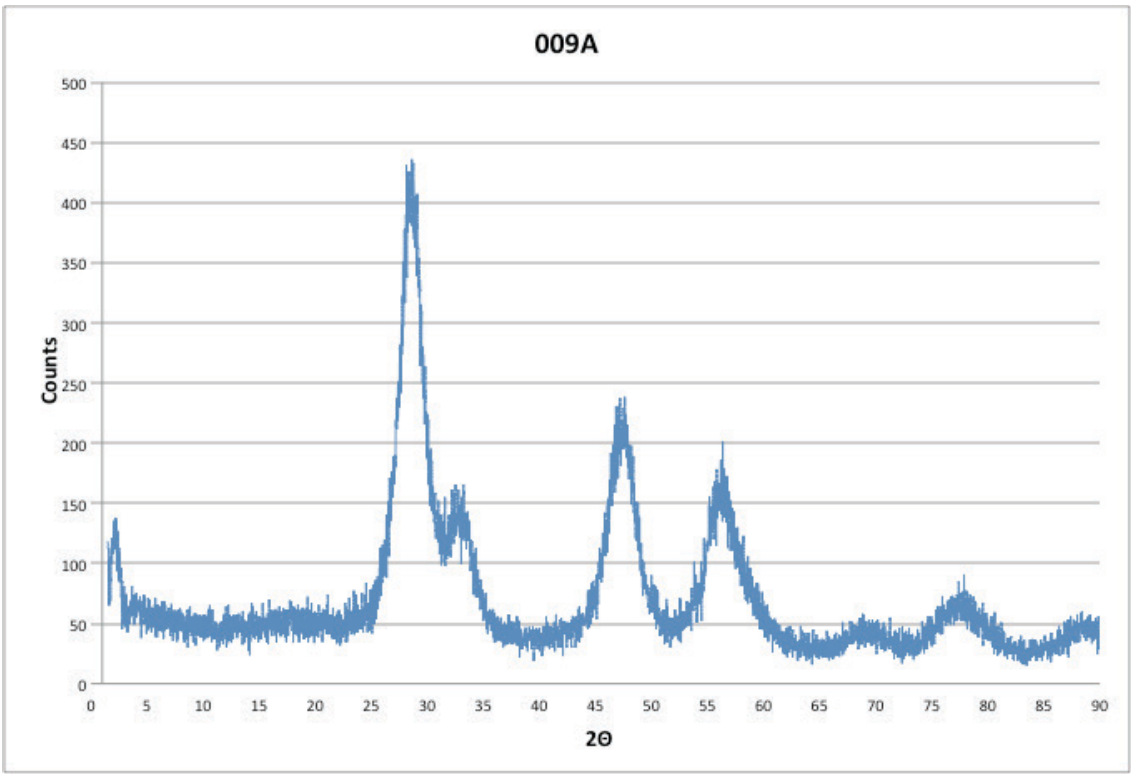

Figure 73 pXRD of sample 009A synthesized from cerium hydroxide, SDS, water, ethanol, and sodium hydroxide, uncalcinated

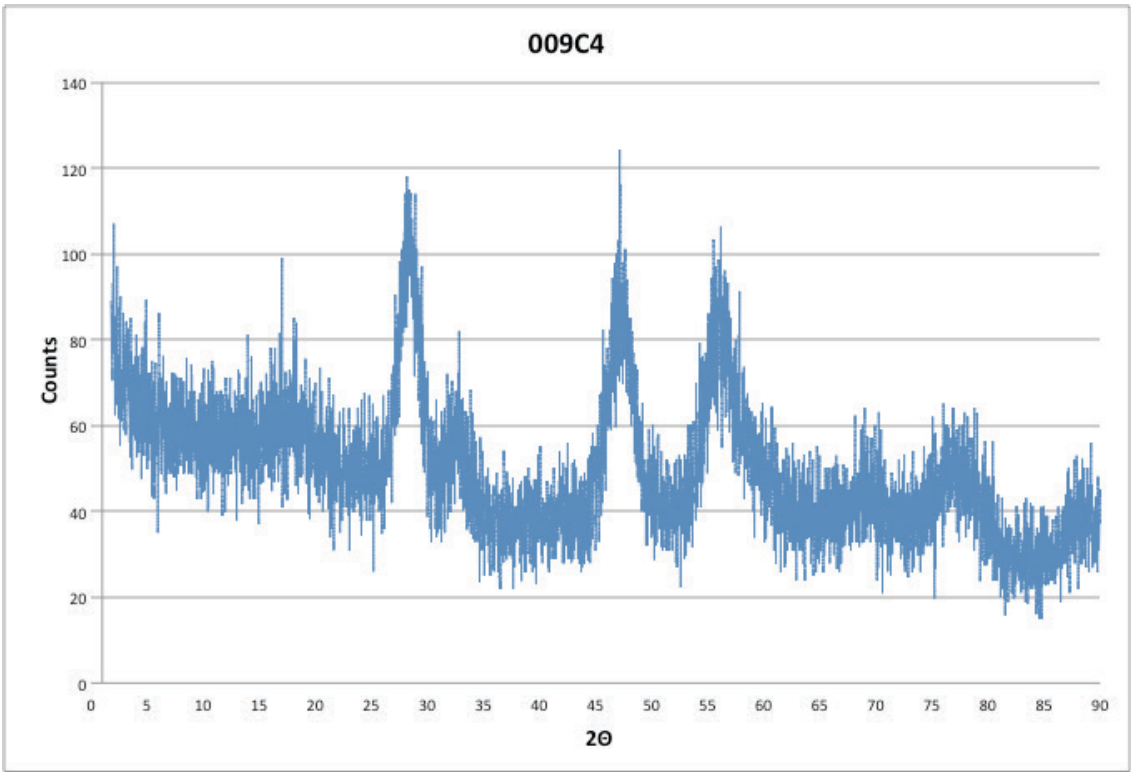

Figure 74 pXRD of sample 009C4 synthesized from cerium hydroxide, SDS, water, ethanol, and sodium hydroxide, calcinated at 673K

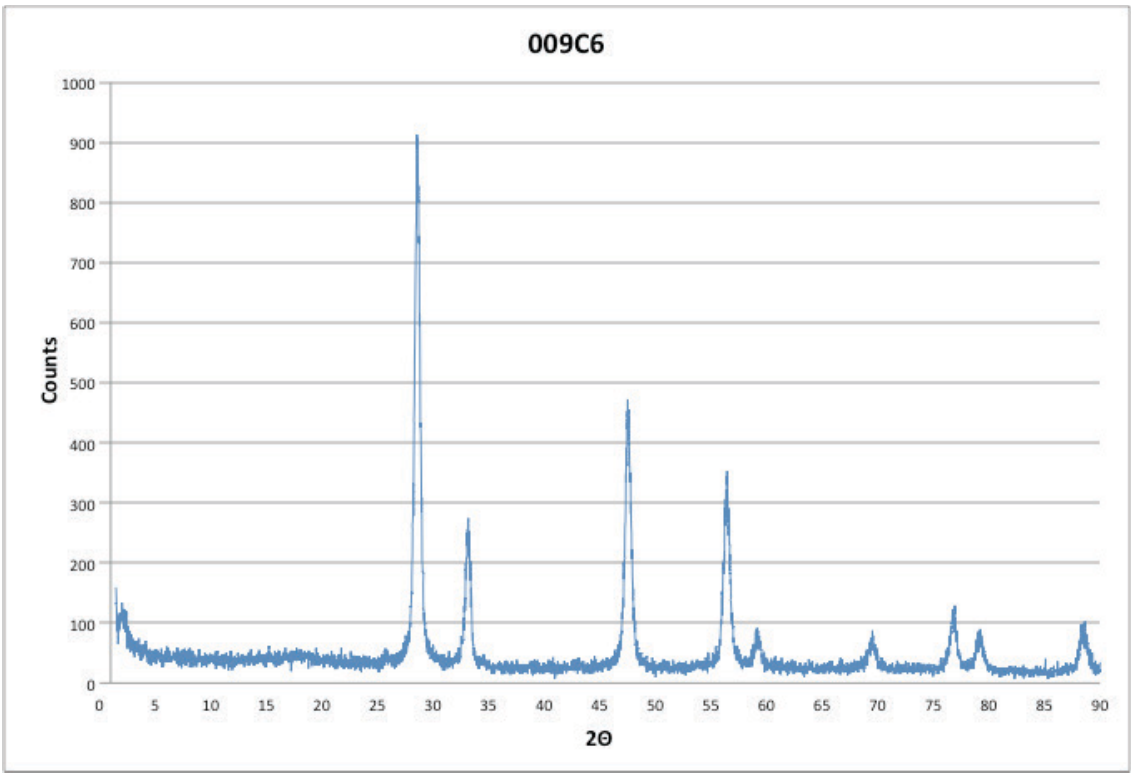

Figure 75 pXRD of sample 009C6 synthesized from cerium hydroxide, SDS, water, ethanol, and sodium hydroxide, calcinated at 873K

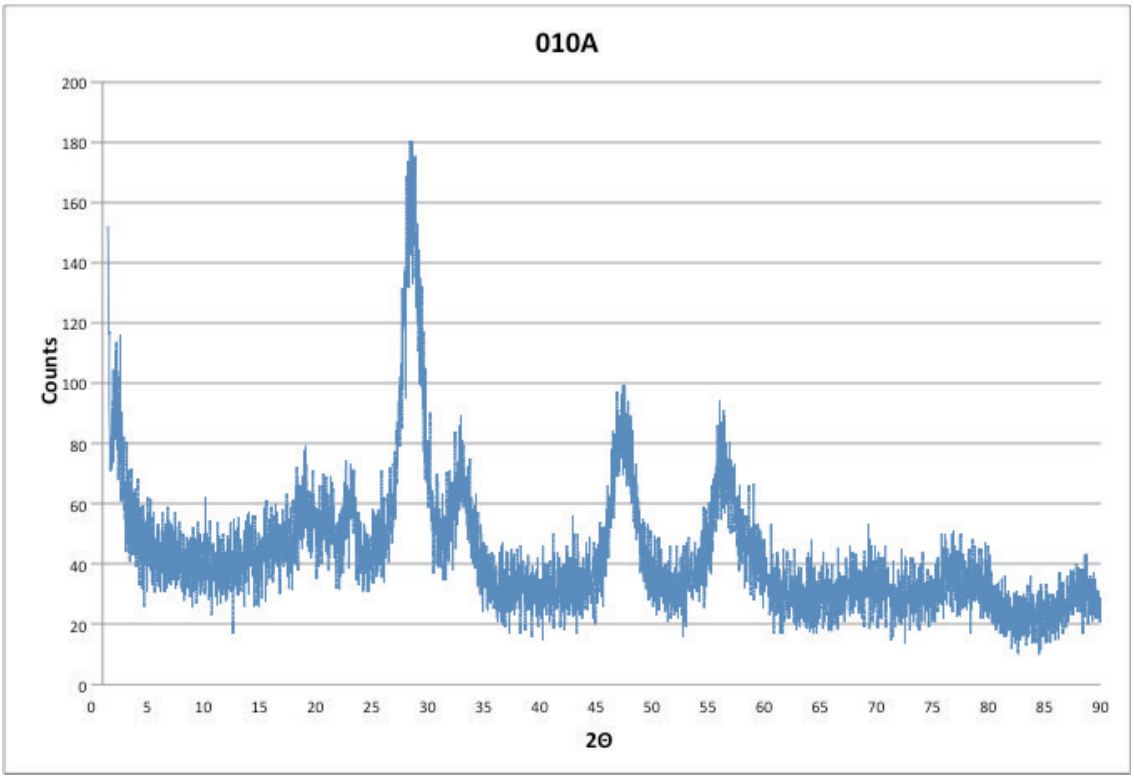

Figure 76 pXRD of sample 010A synthesized from cerium hydroxide, CTAB/SDS, water, ethanol, and sodium hydroxide, uncalcinated

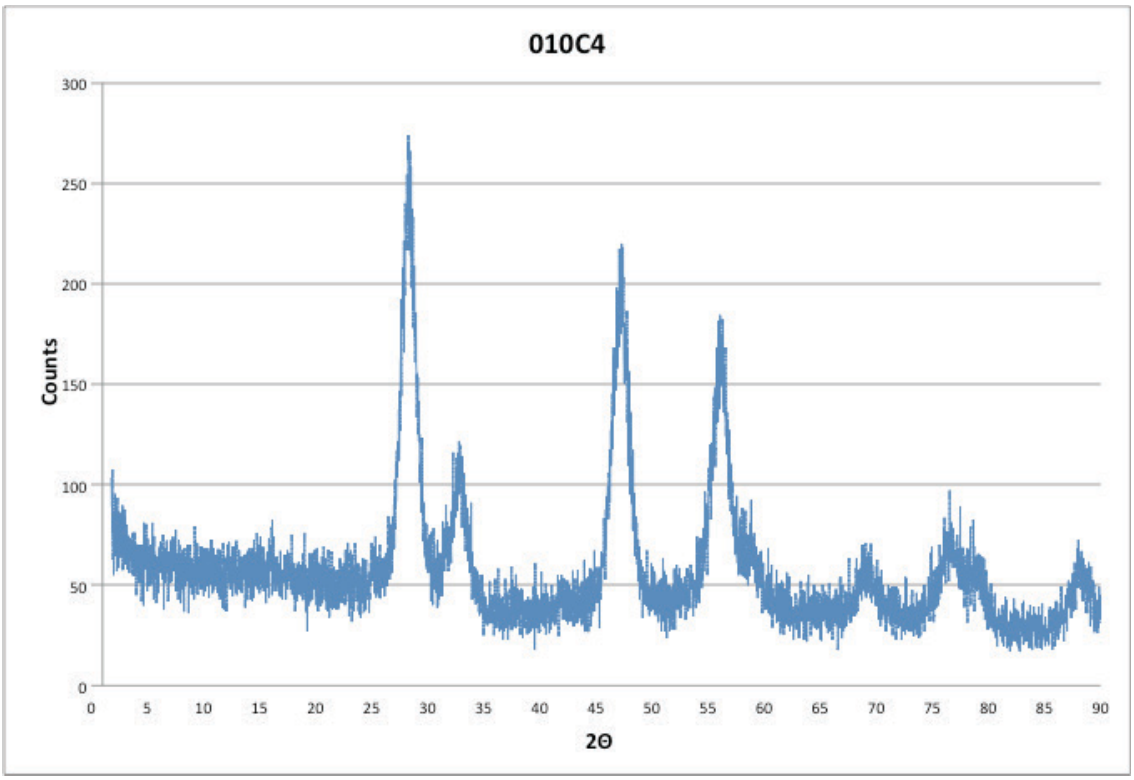

Figure 77 pXRD of sample 010C4 synthesized from cerium hydroxide, CTAB/SDS, water, ethanol, and sodium hydroxide, calcinated at 673K

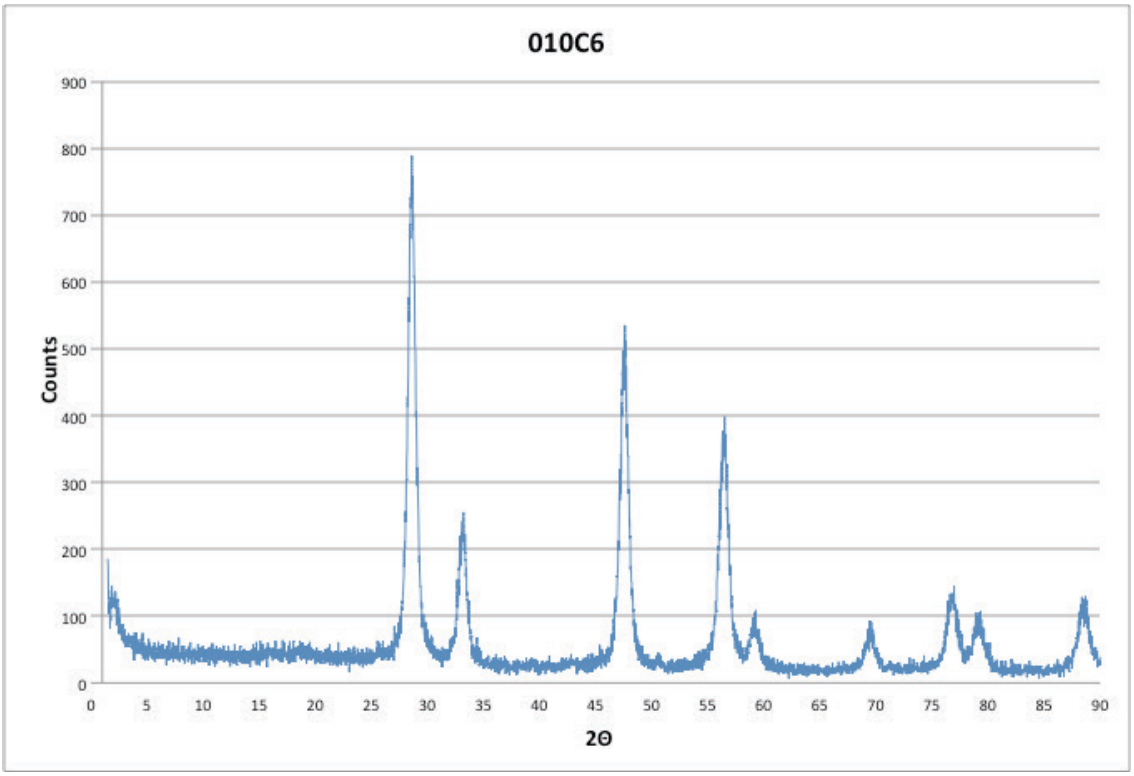

Figure 78 pXRD of sample 010C6 synthesized from cerium hydroxide, CTAB/SDS, water, ethanol, and sodium hydroxide, calcinated at 873K

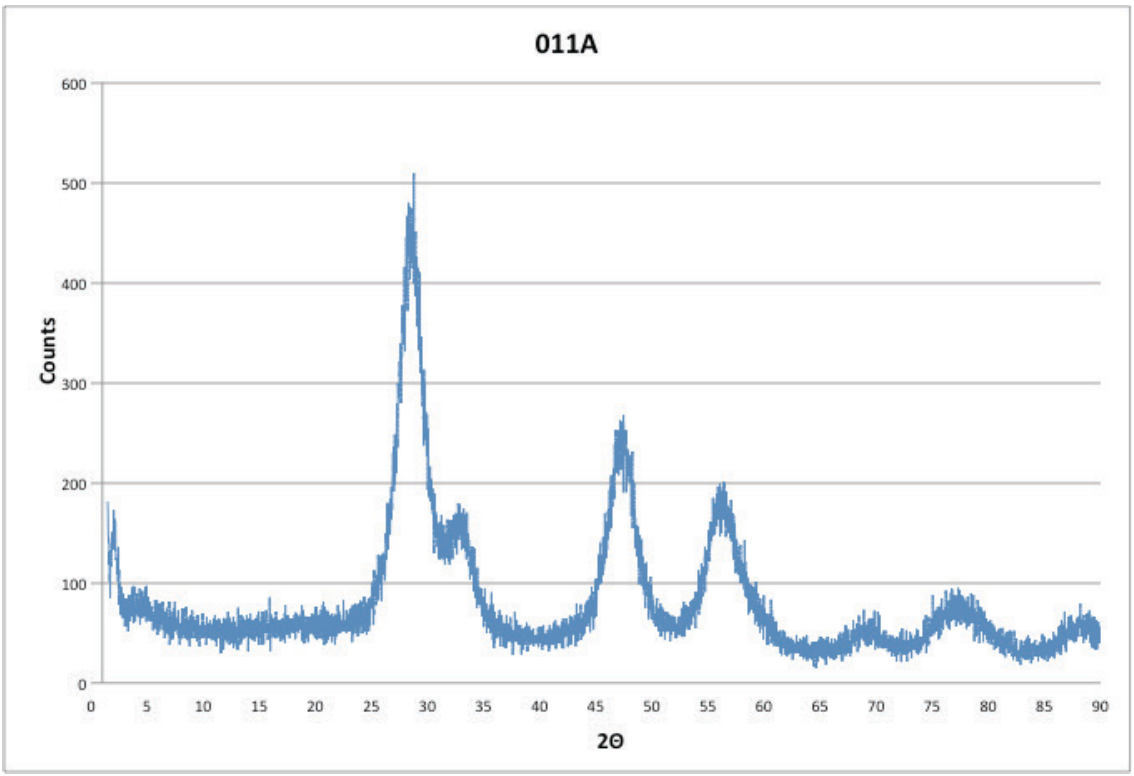

Figure 79 pXRD of sample 011A synthesized from cerium hydroxide, CTAB, toluene, pyridine, uncalcinated

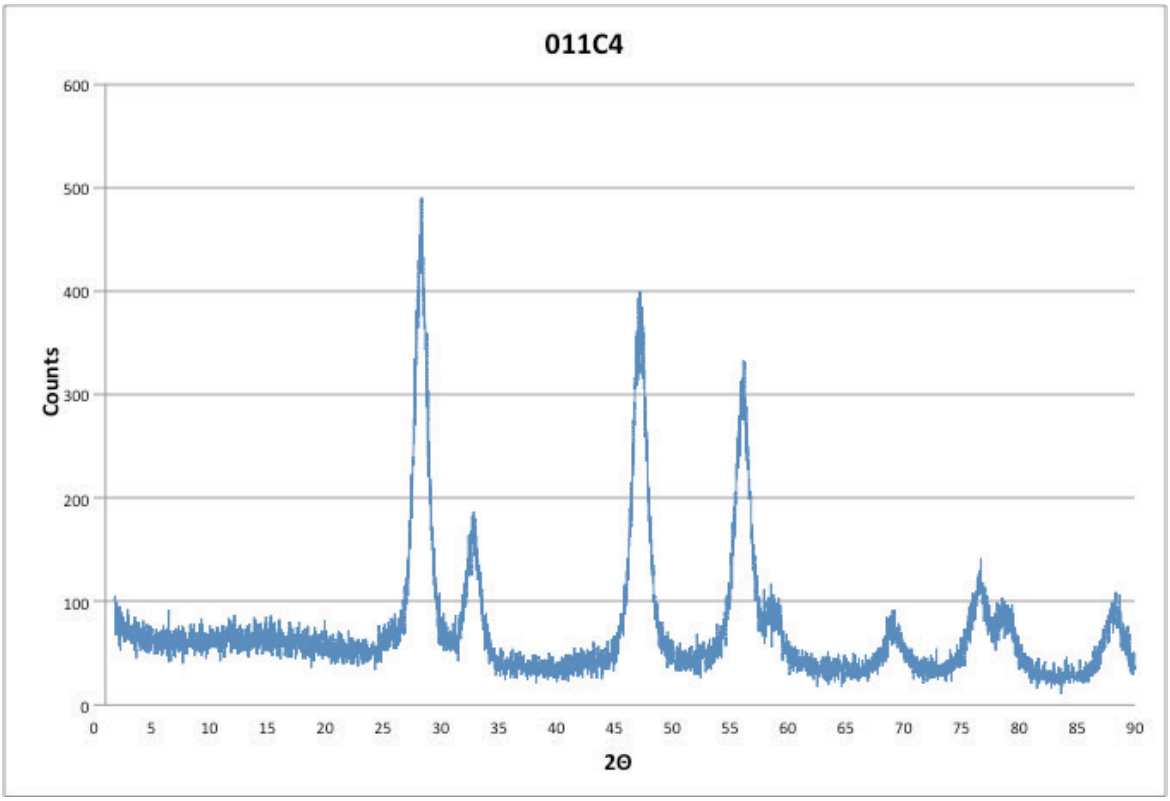

Figure 80 pXRD of sample 011C4 synthesized from cerium hydroxide, CTAB, toluene, pyridine, calcinated at 673K

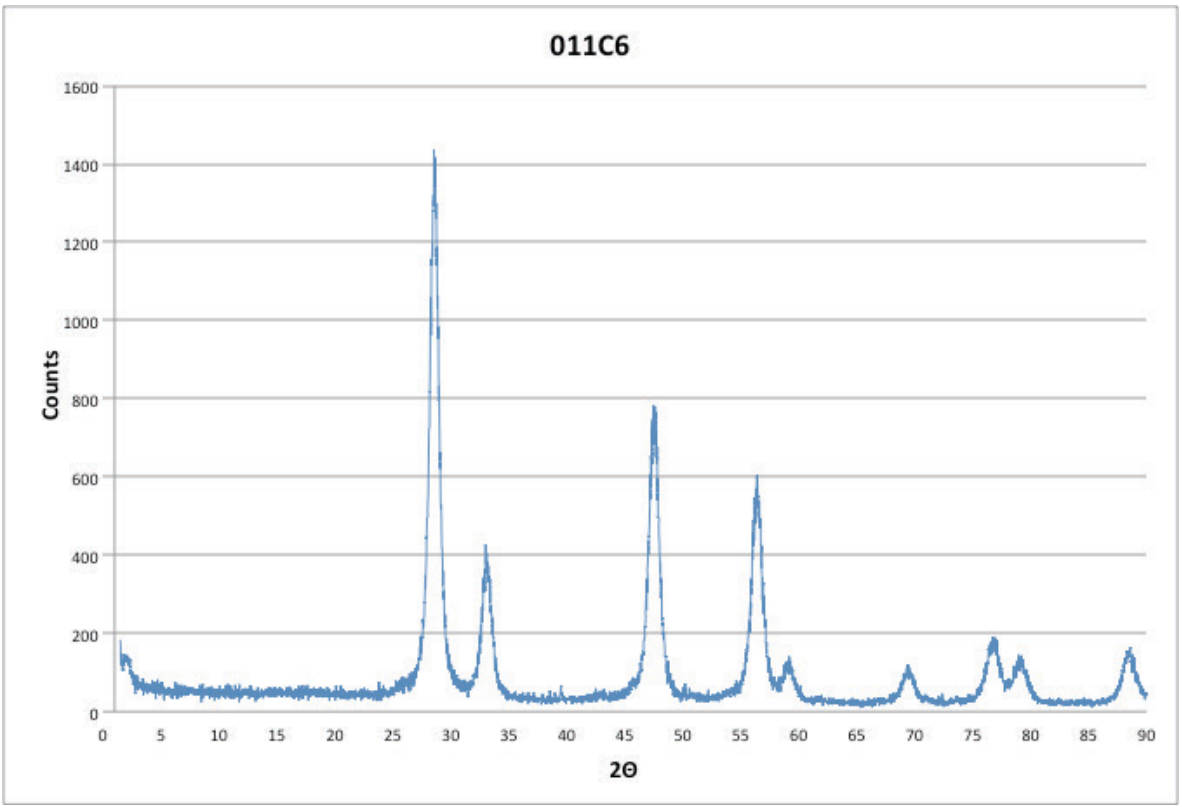

Figure 81 pXRD of sample 011C6 synthesized from cerium hydroxide, CTAB, toluene, pyridine, calcinated at 873K

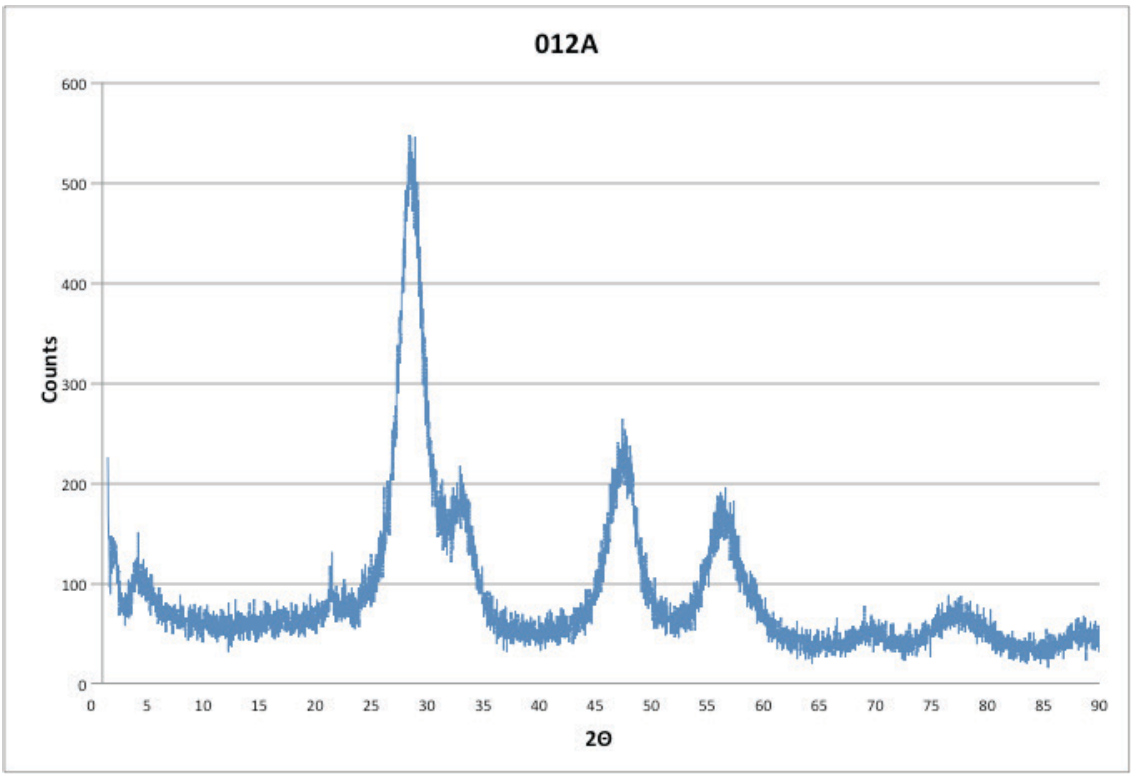

Figure 82 pXRD of sample 012A synthesized from cerium hydroxide, CTAB (300mM), water, ethanol, and sodium hydroxide, uncalcinated

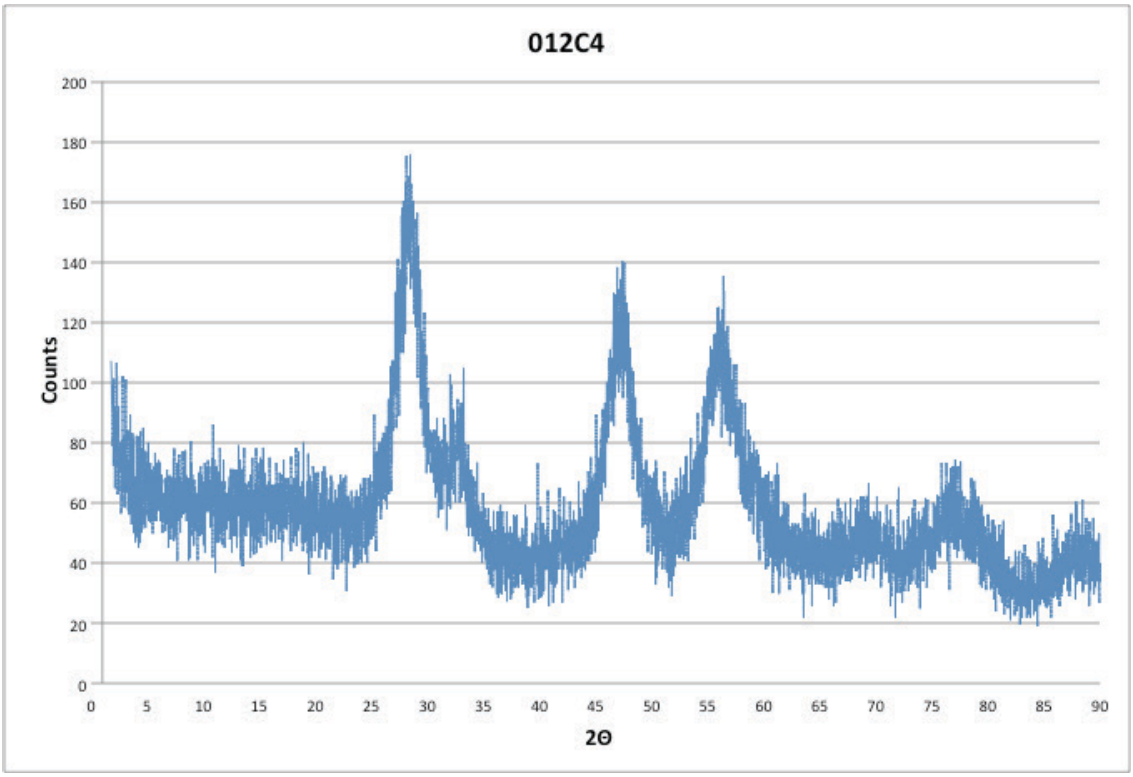

Figure 83 pXRD of sample 012C4 synthesized from cerium hydroxide, CTAB (300mM), water, ethanol, and sodium hydroxide, calcinated at 673K

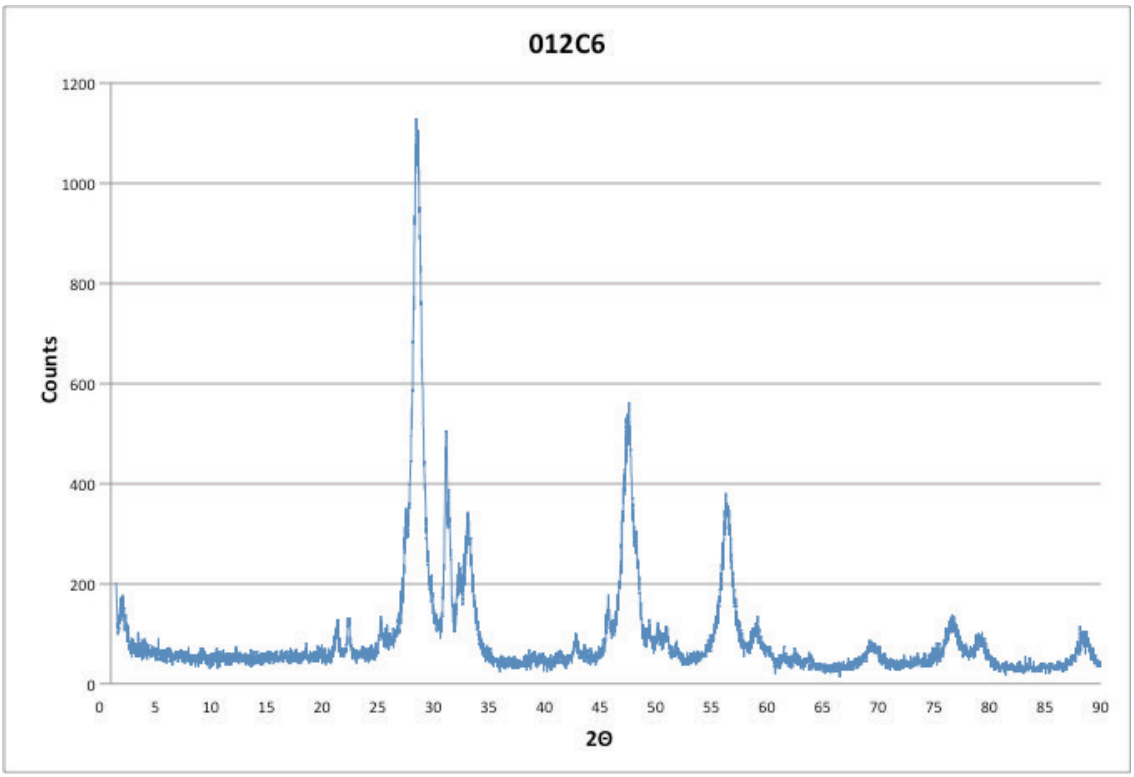

Figure 84 pXRD of sample 012C6 synthesized from cerium hydroxide, CTAB (300mM), water, ethanol, and sodium hydroxide, calcinated at 873K

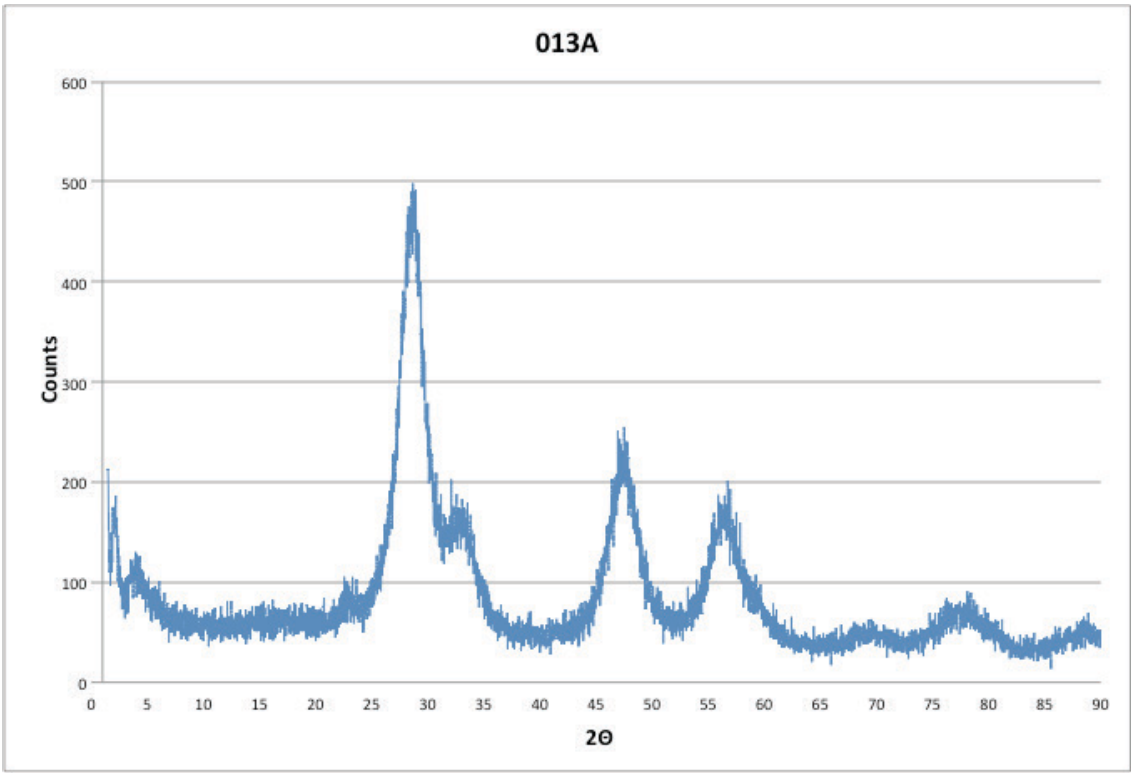

Figure 85 pXRD of sample 013A synthesized from cerium hydroxide, SDS (300mM), water, ethanol, and sodium hydroxide, uncalcinated

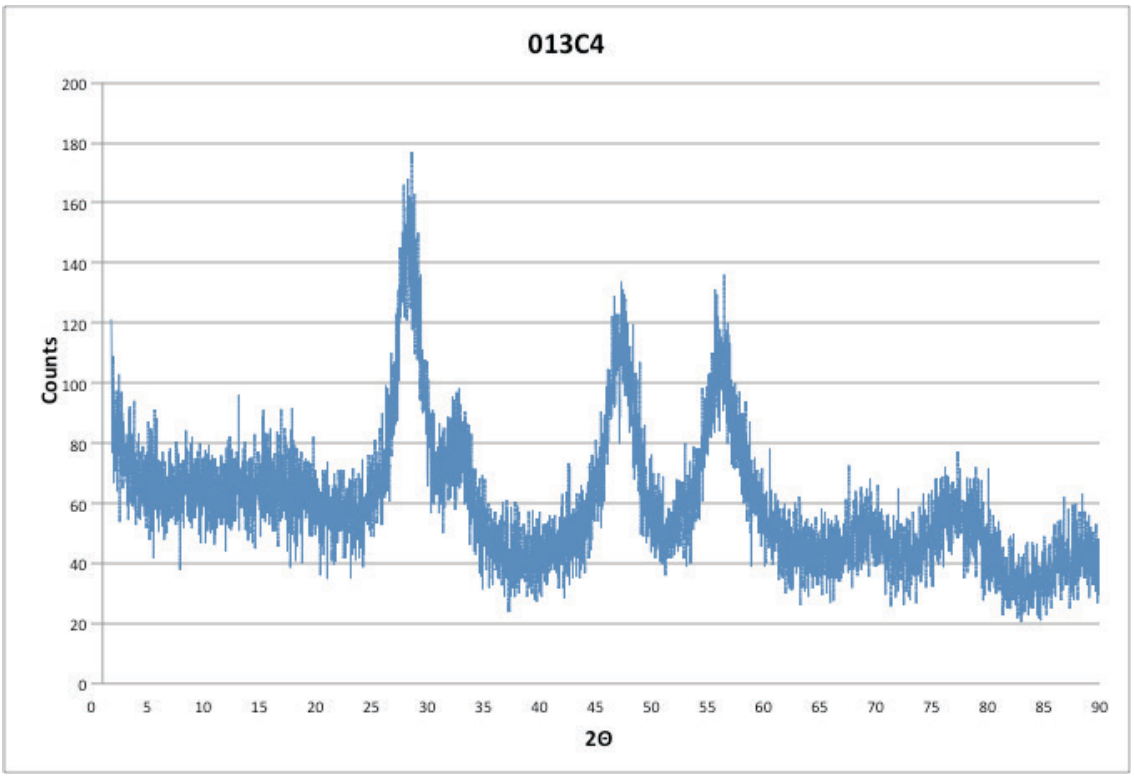

Figure 86 pXRD of sample 013C4 synthesized from cerium hydroxide, SDS (300mM), water, ethanol, and sodium hydroxide, calcinated at 673K

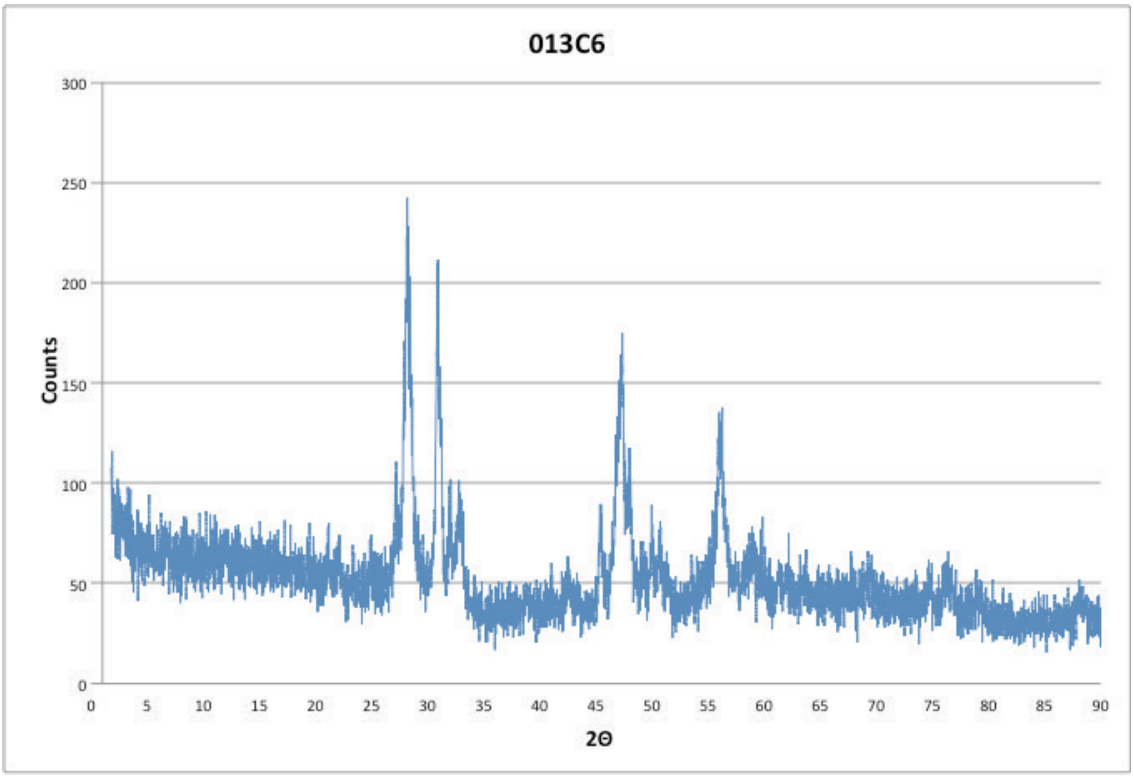

Figure 87 pXRD of sample 013C6 synthesized from cerium hydroxide, SDS (300mM), water, ethanol, and sodium hydroxide, calcinated at 873K

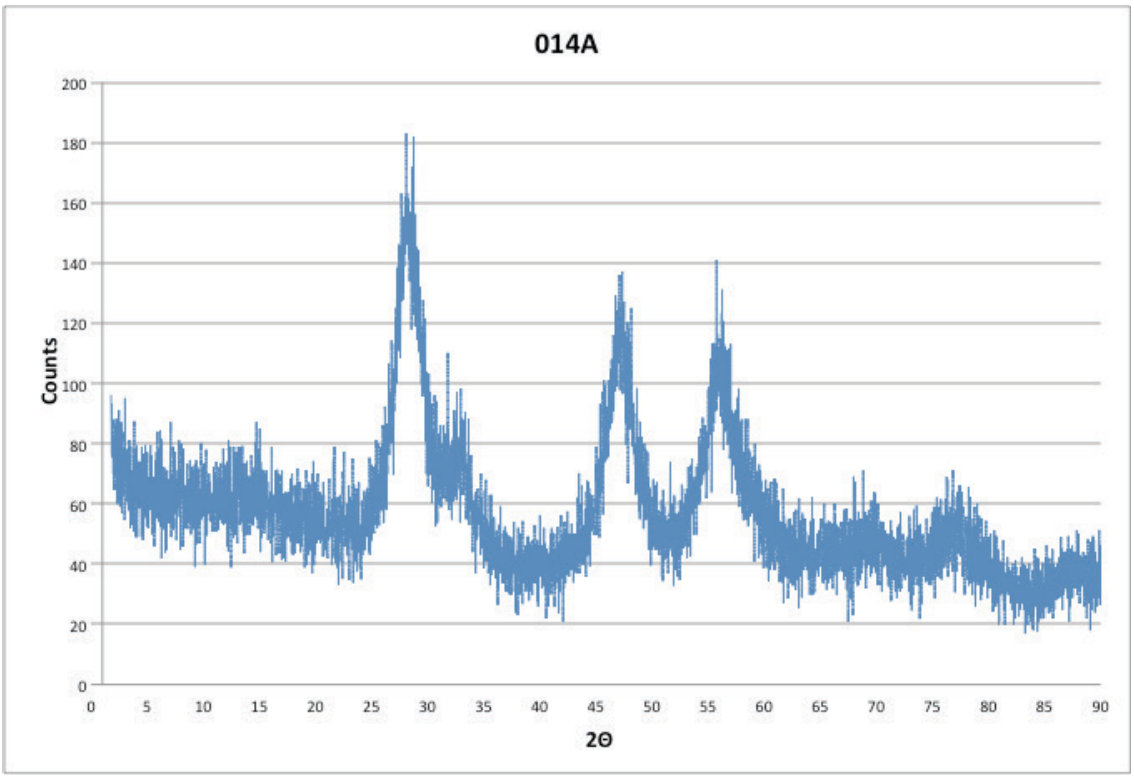

Figure 88 pXRD of sample 014A synthesized from cerium hydroxide, triton-X, water, ethanol, and sodium hydroxide, uncalcinated

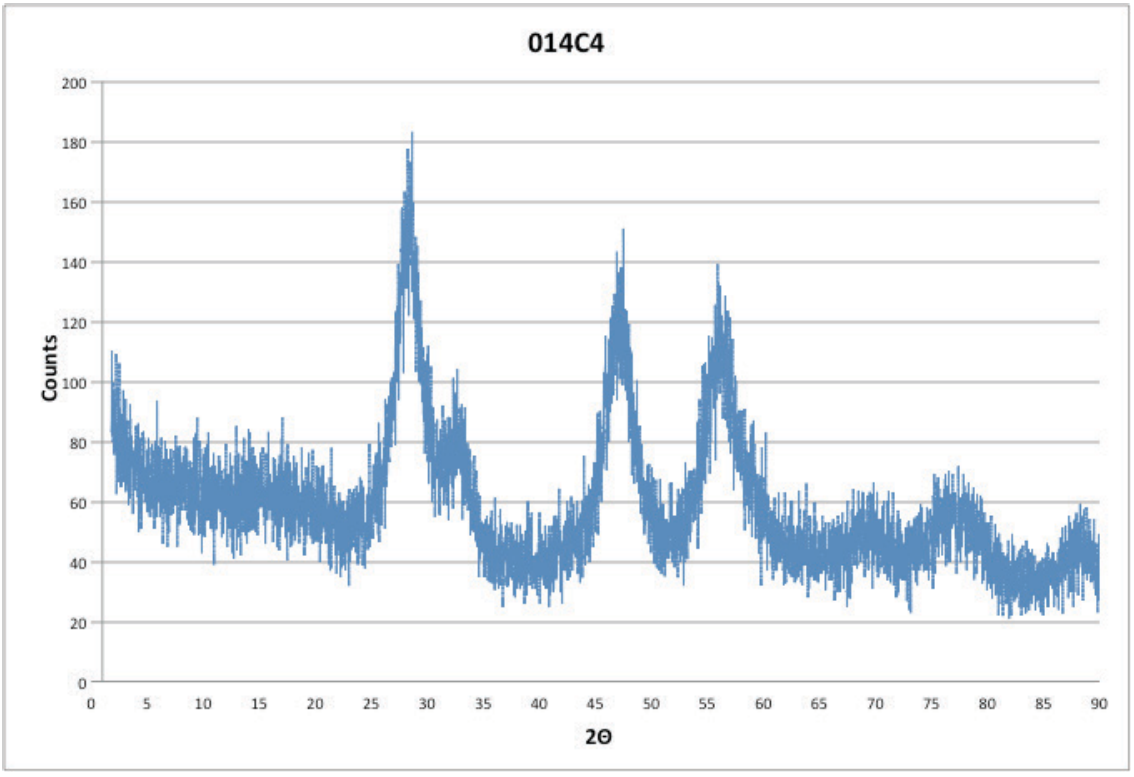

Figure 89 pXRD of sample 014C4 synthesized from cerium hydroxide, triton-X, water, ethanol, and sodium hydroxide, calcinated at 673K

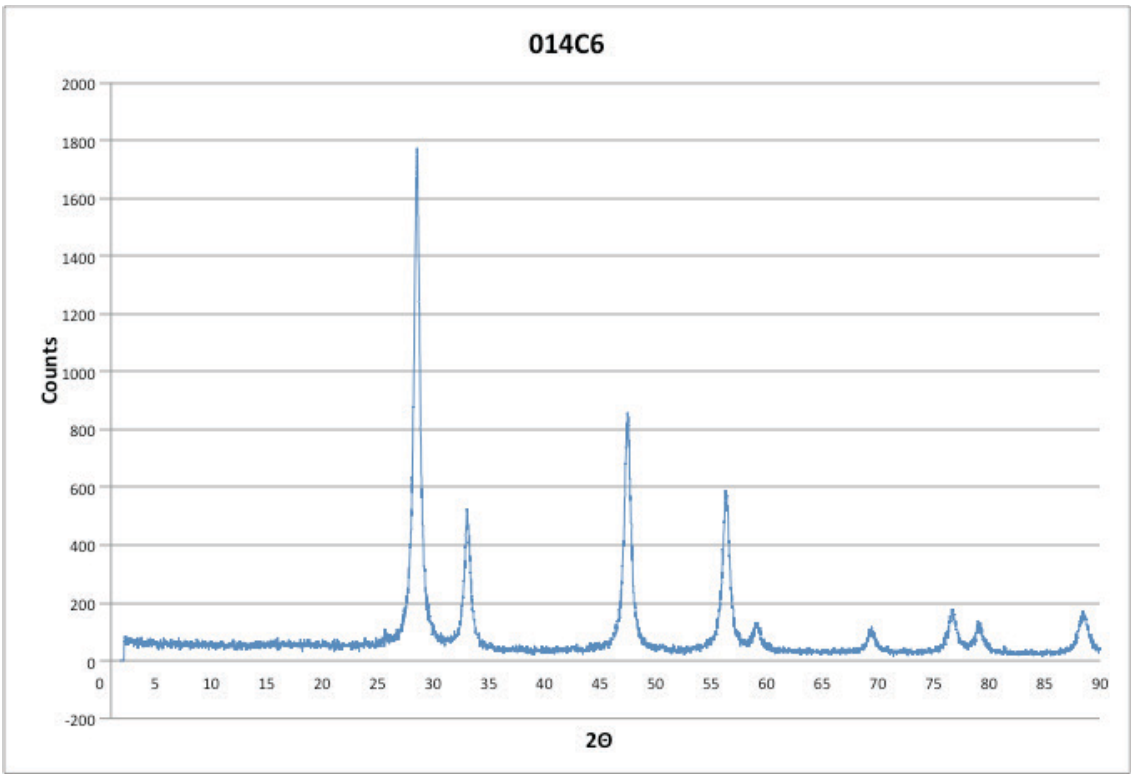

Figure 90 pXRD of sample 014C6 synthesized from cerium hydroxide, triton-X, water, ethanol, and sodium hydroxide, calcinated at 873K

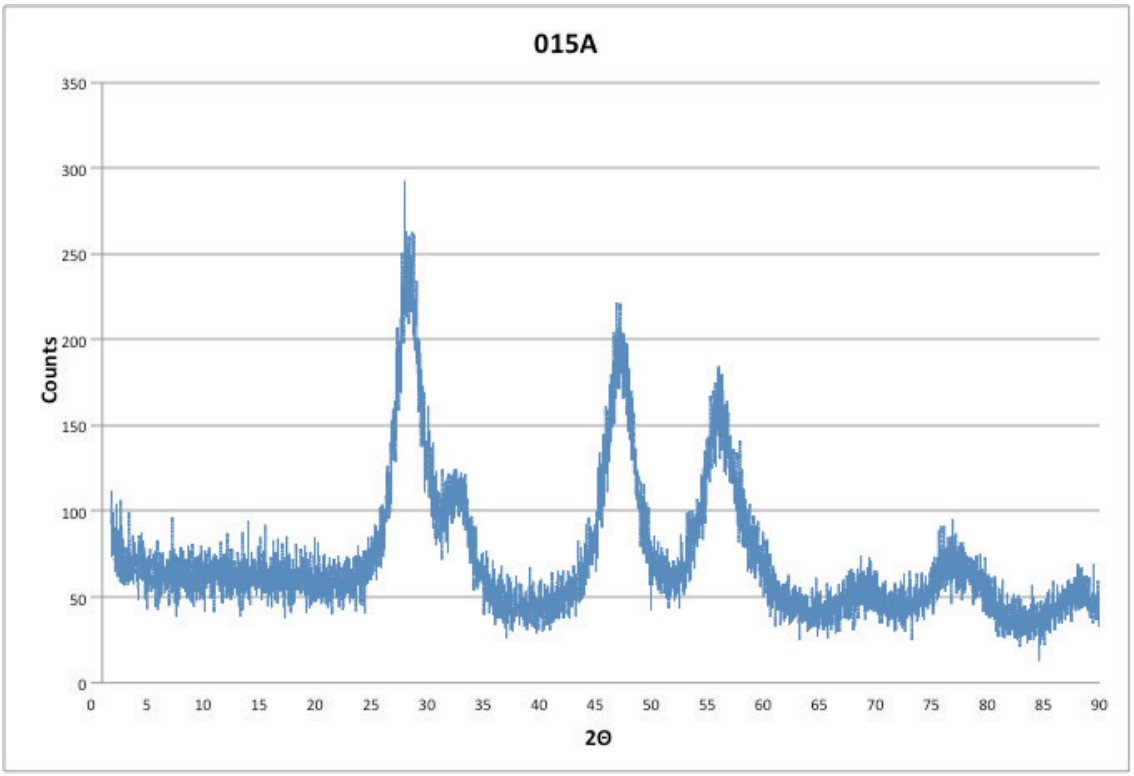

Figure 91 pXRD of sample 015A synthesized from cerium hydroxide, n-hexadecylamine, water, ethanol, and sodium hydroxide, uncalcinated

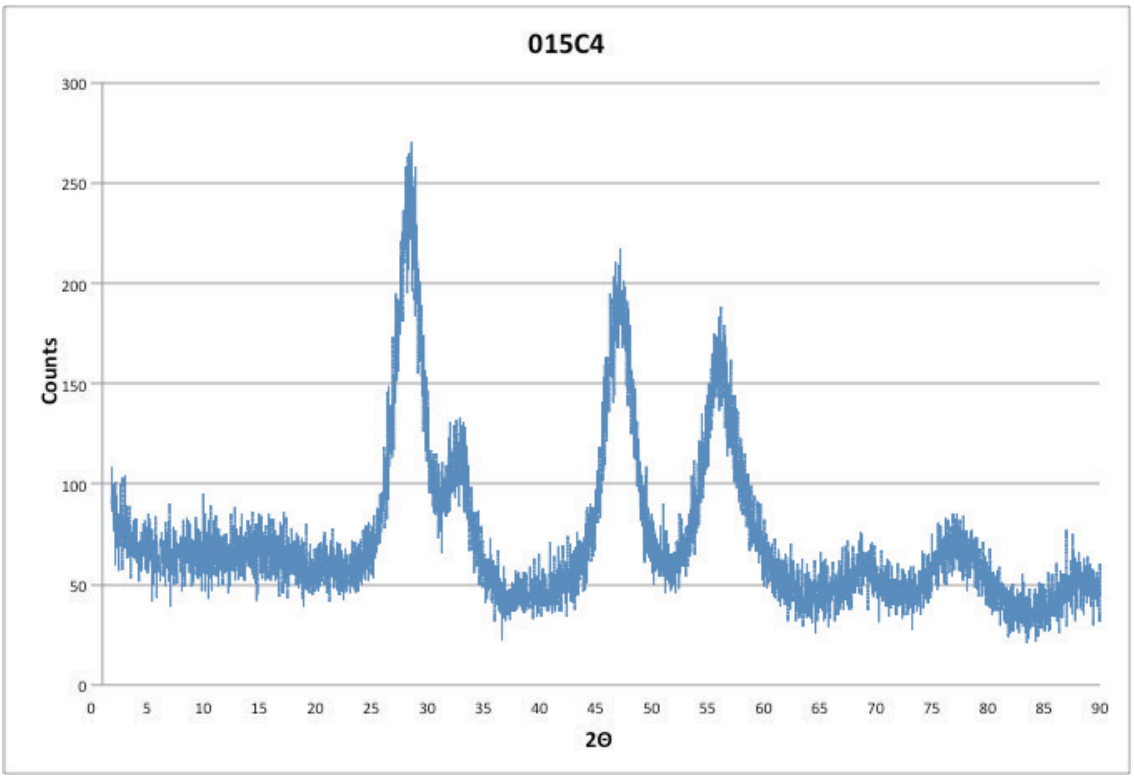

Figure 92 pXRD of sample 015C4 synthesized from cerium hydroxide, n-hexadecylamine, water, ethanol, and sodium hydroxide, calcinated at 673K

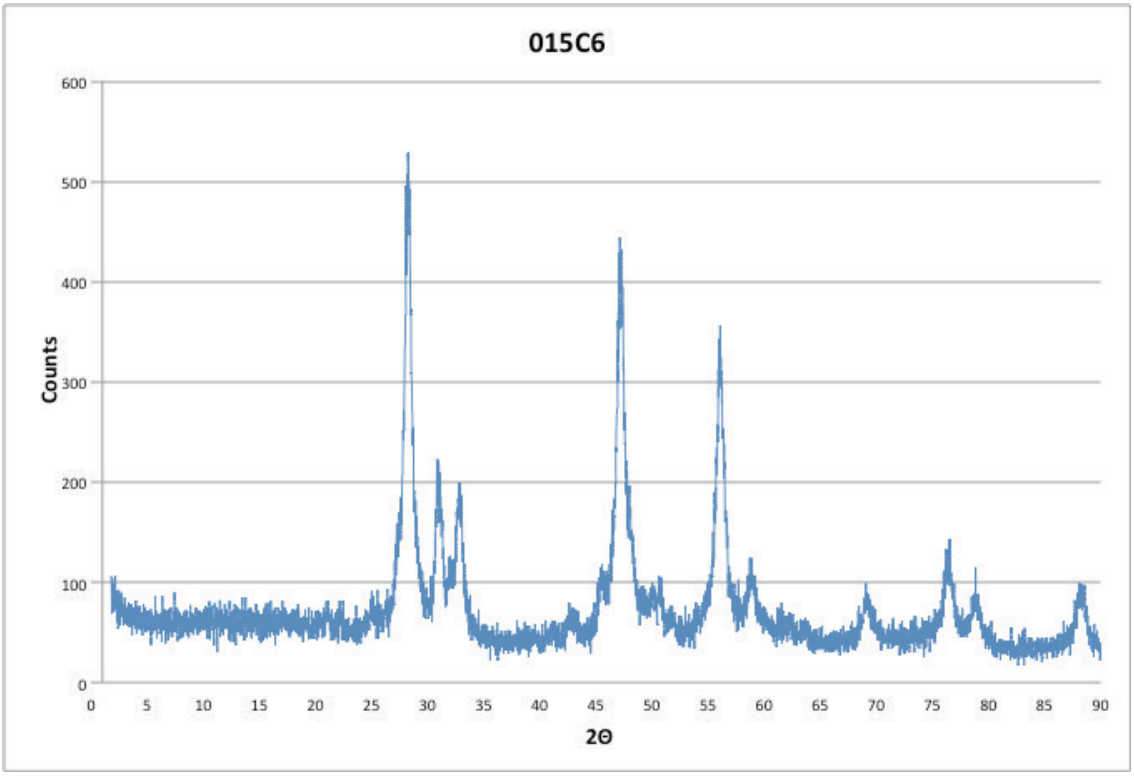

Figure 93 pXRD of sample 015C6 synthesized from cerium hydroxide, n-hexadecylamine, water, ethanol, and sodium hydroxide, calcinated at 873K

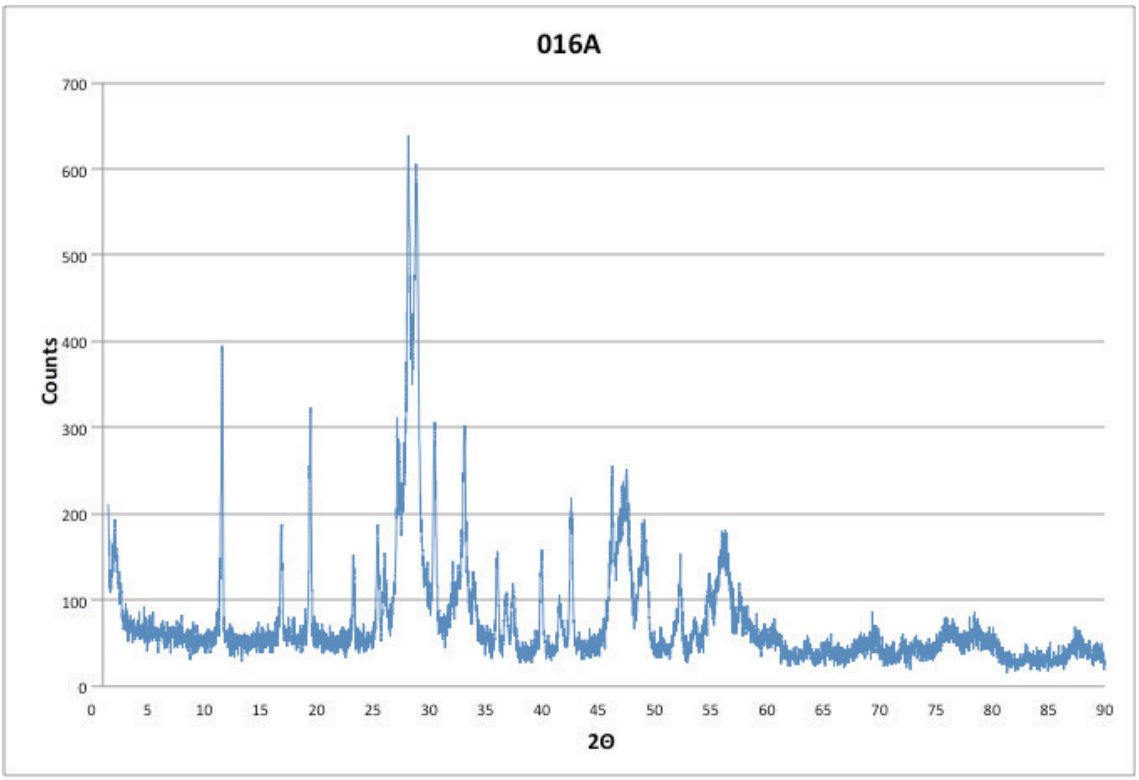

Figure 94 pXRD of sample 016A synthesized from cerium (III) nitrate hexahydrate, samarium (III) nitrate hexahydrate, CTAB, water, ethanol, and sodium hydroxide, uncalcinated

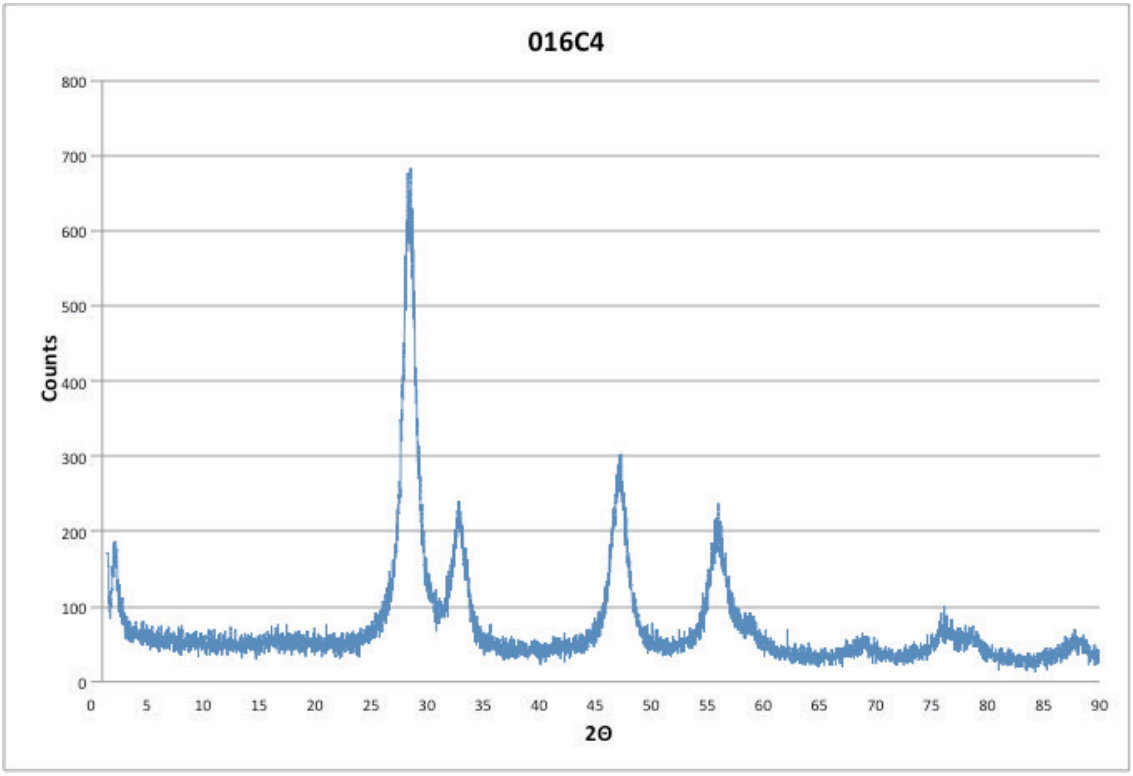

Figure 95 pXRD of sample 016C4 synthesized from cerium (III) nitrate hexahydrate, samarium (III) nitrate hexahydrate, CTAB, water, ethanol, and sodium hydroxide, calcinated at 673K

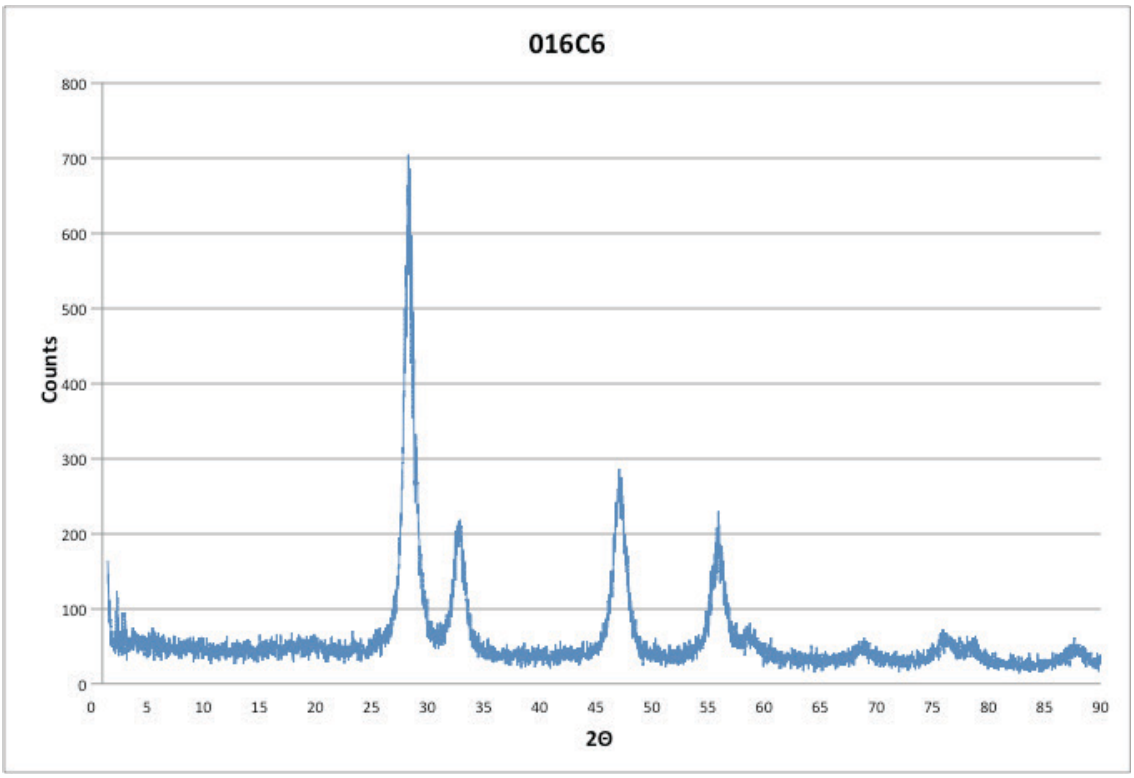

Figure 96 pXRD of sample 016C6 synthesized from cerium (III) nitrate hexahydrate, samarium (III) nitrate hexahydrate, CTAB, water, ethanol, and sodium hydroxide, calcinated at 873K

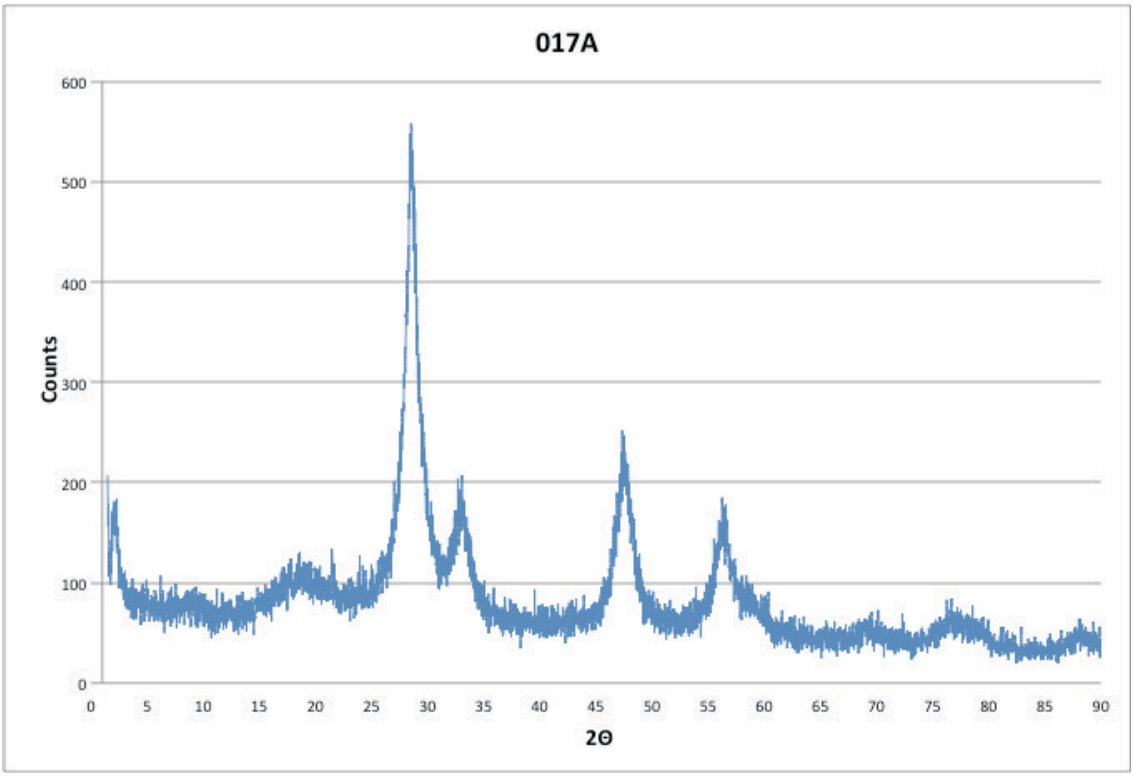

Figure 97 pXRD of sample 017A synthesized from cerium (III) nitrate hexahydrate, titanium isopropoxide, CTAB, water, ethanol, and sodium hydroxide, uncalcinated

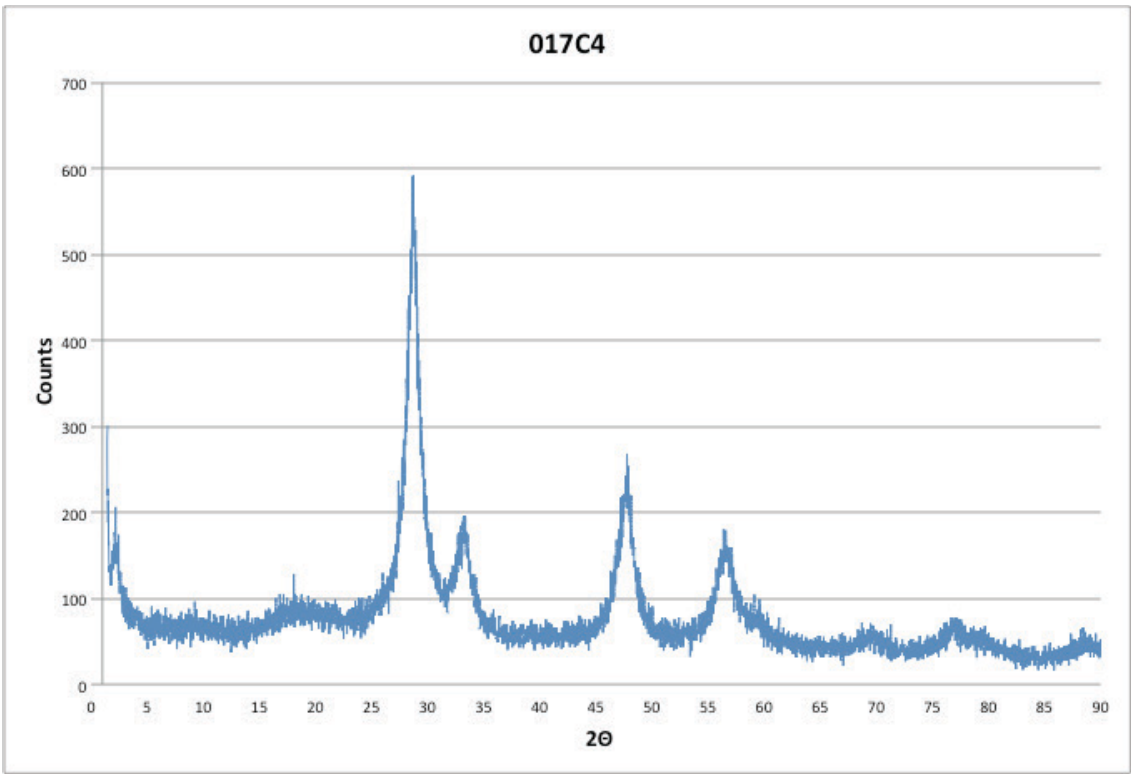

Figure 98 pXRD of sample 017C4 synthesized from cerium (III) nitrate hexahydrate, titanium isopropoxide, CTAB, water, ethanol, and sodium hydroxide, calcinated at 673K

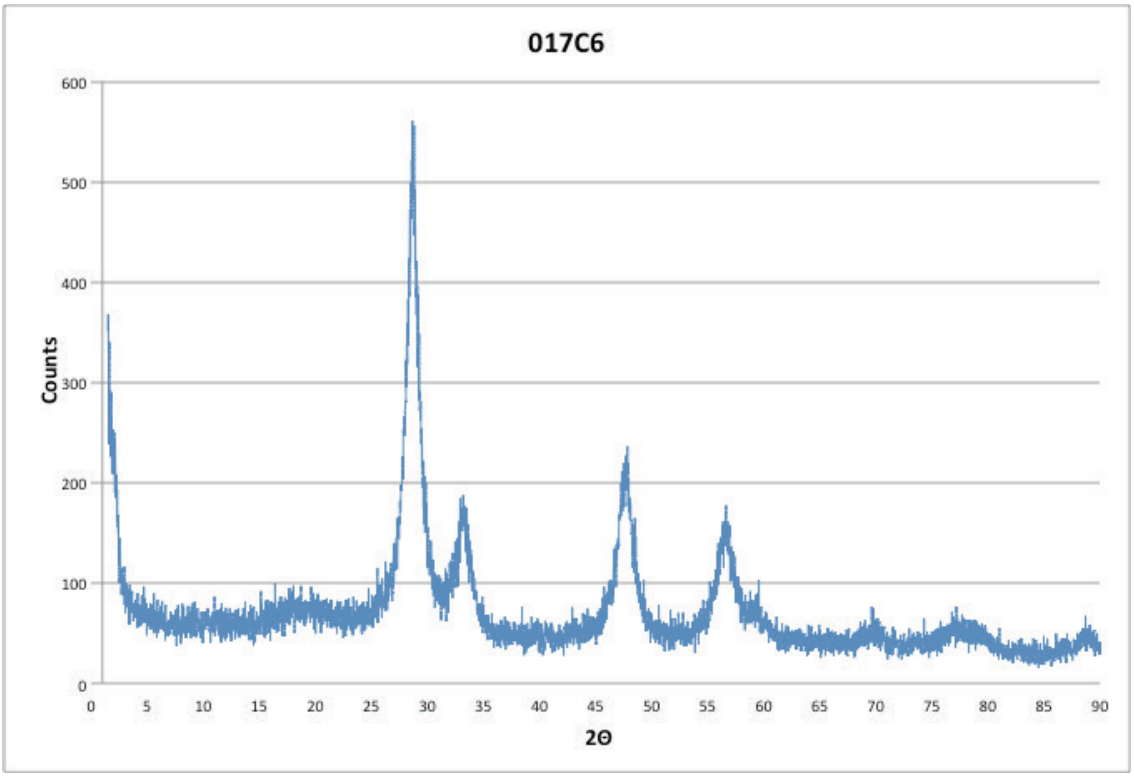

Figure 99 pXRD of sample 017C6 synthesized from cerium (III) nitrate hexahydrate, titanium isopropoxide, CTAB, water, ethanol, and sodium hydroxide, calcinated at 873K

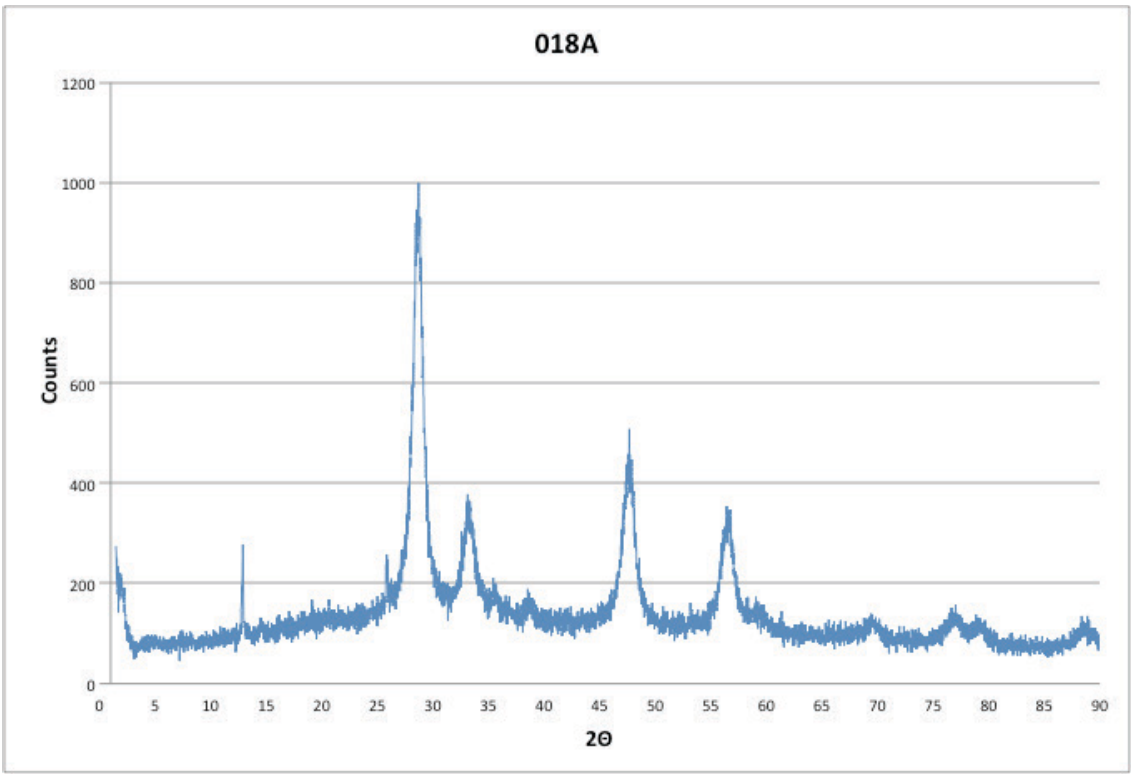

Figure 100 pXRD of sample 018A synthesized from cerium (III) nitrate hexahydrate, copper (III) hemi pentahydrate, CTAB, water, ethanol, and sodium hydroxide, uncalcinated

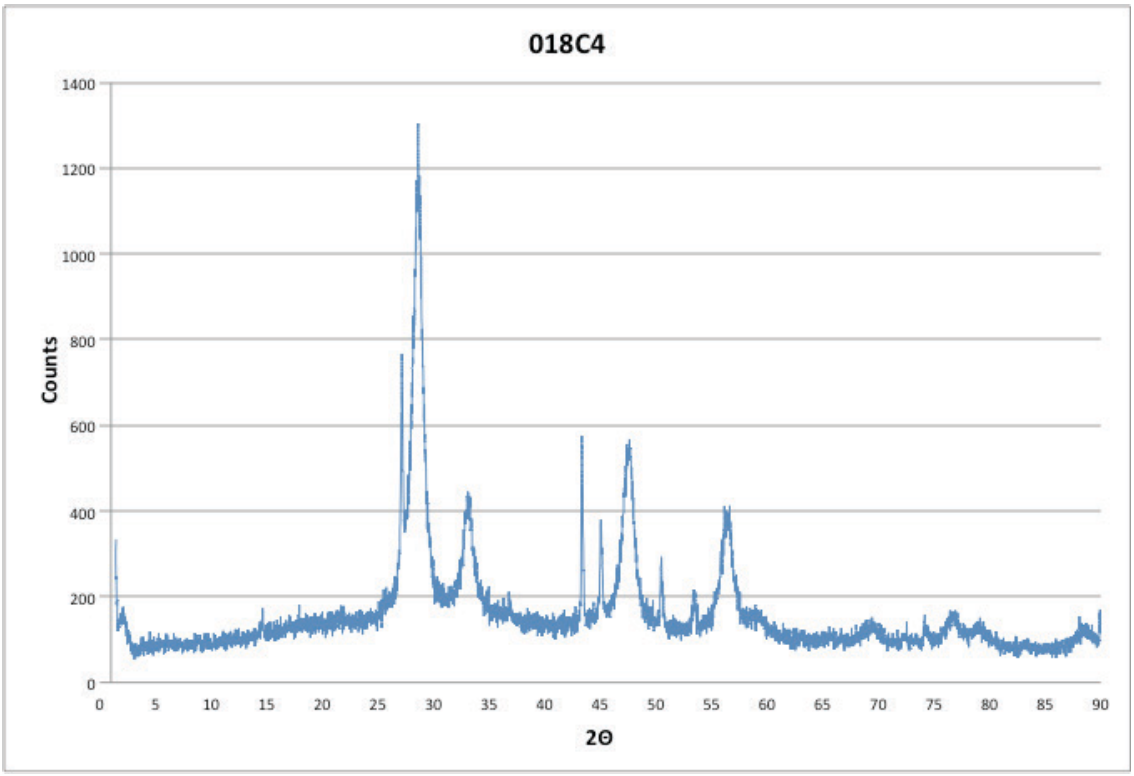

Figure 101 pXRD of sample 018C4 synthesized from cerium (III) nitrate hexahydrate, copper (III) hemi pentahydrate, CTAB, water, ethanol, and sodium hydroxide, calcinated at 673K

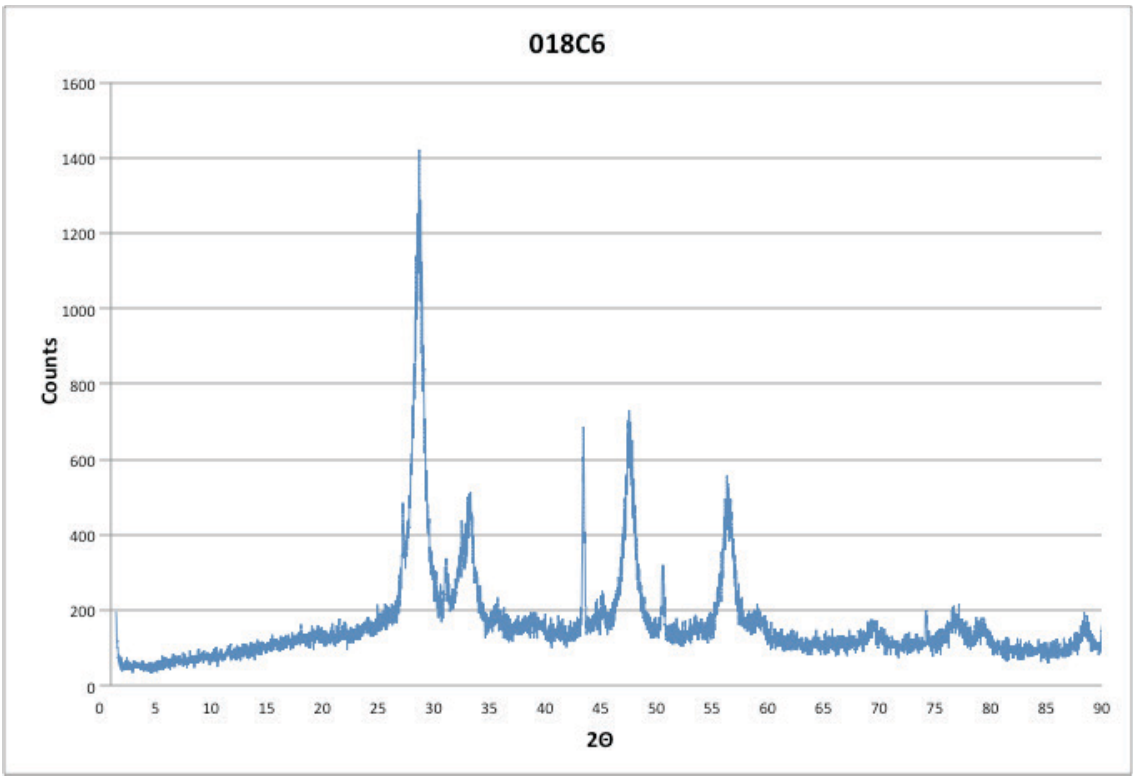

Figure 102 pXRD of sample 018C6 synthesized from cerium (III) nitrate hexahydrate, copper (III) hemi pentahydrate, CTAB, water, ethanol, and sodium hydroxide, calcinated at 873K

Appendices B

Isotherms and pore size distribution

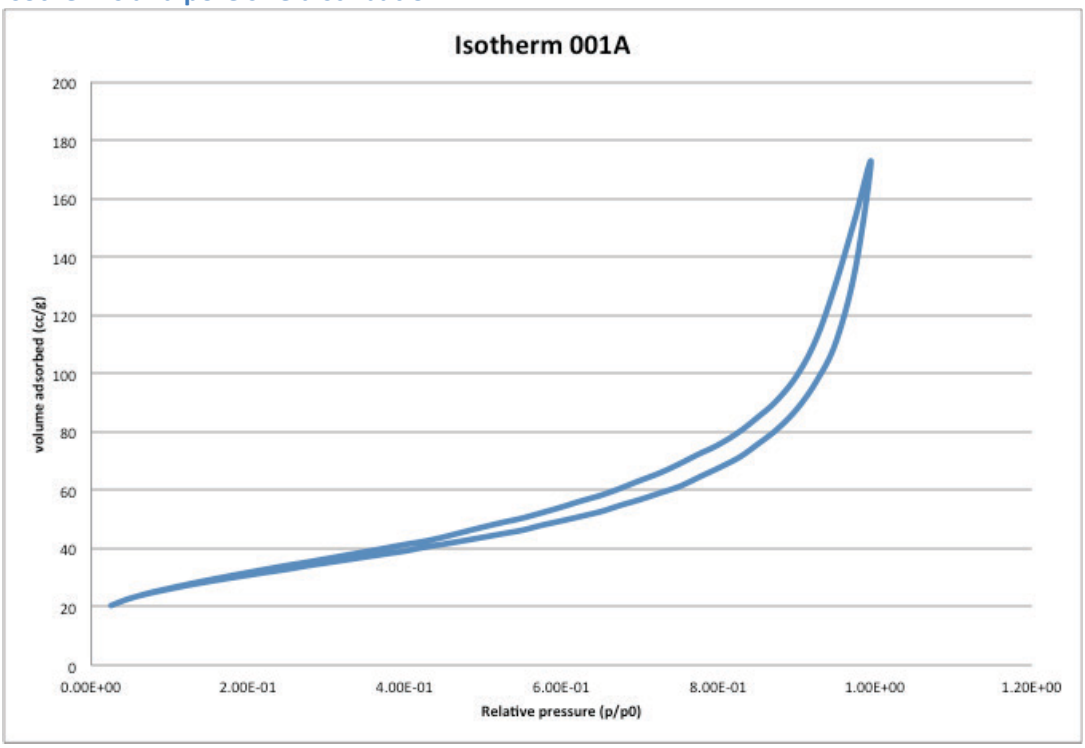

Figure 103 isotherm of sample 001A, synthesized from cerium (IV) hydroxide, CTAB, water, ethanol, and sodium hydroxide, uncalcinated

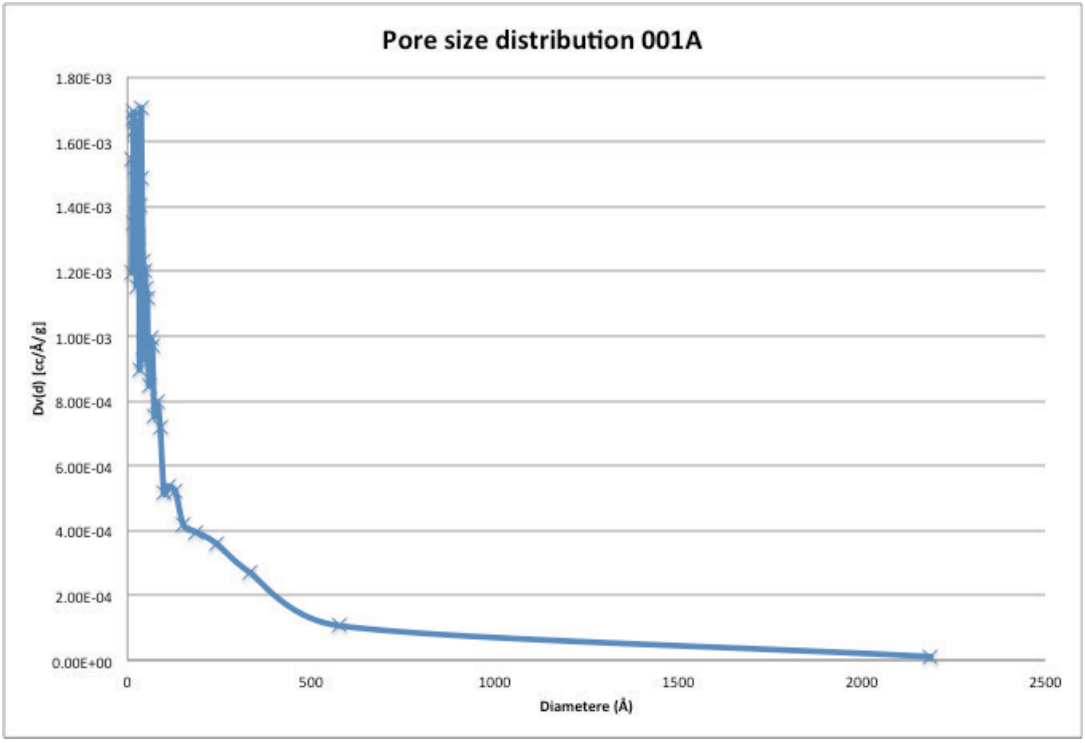

Figure 104 pore size distribution of sample 001A, synthesized from cerium (IV) hydroxide, CTAB, water, ethanol, and sodium hydroxide, uncalcinated

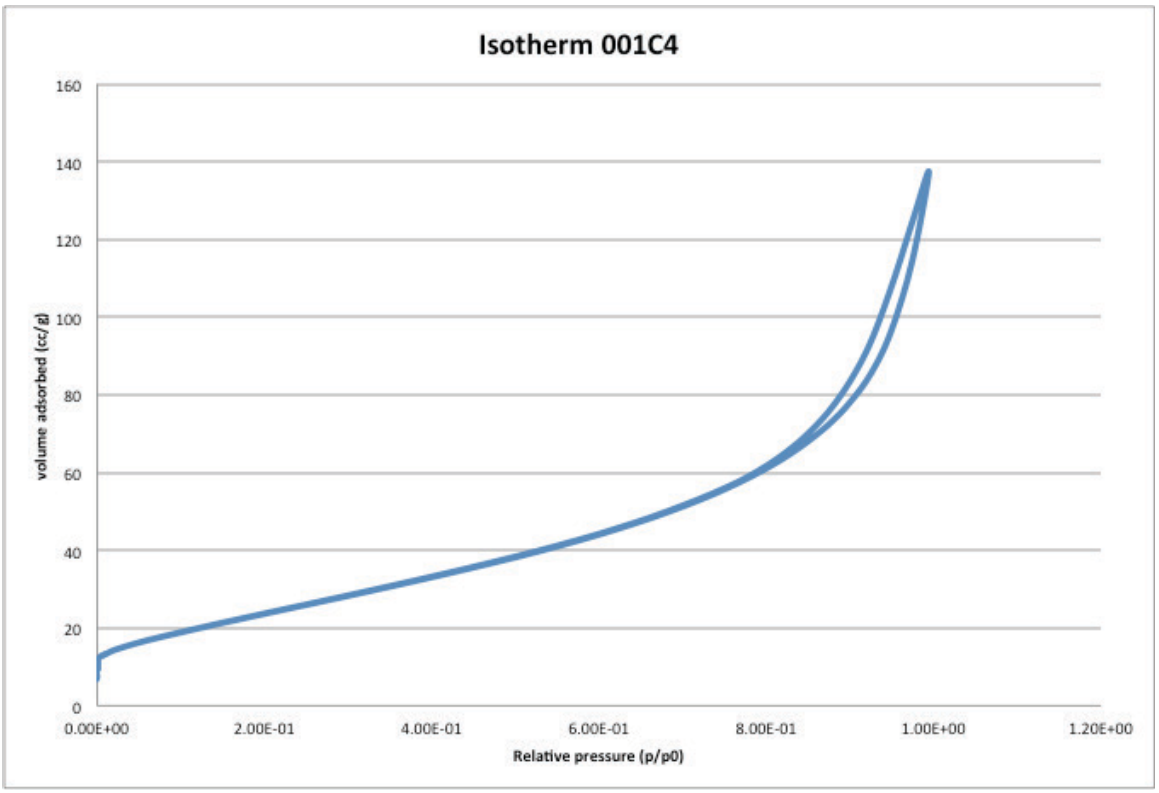

Figure 105 isotherm of sample 001C4, synthesized from cerium (IV) hydroxide, CTAB, water, ethanol, and sodium hydroxide, calcinated at 673K

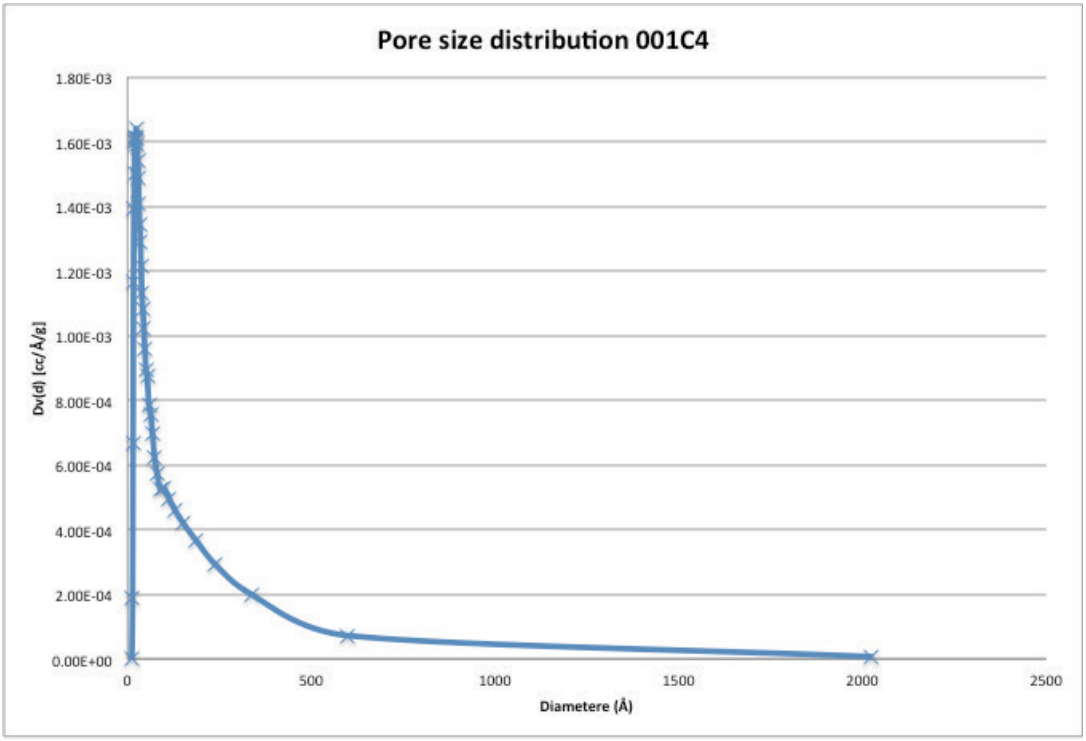

Figure 106 pore size distribution of sample 001C4, synthesized from cerium (IV) hydroxide, CTAB, water, ethanol, and sodium hydroxide, calcinated at 673K

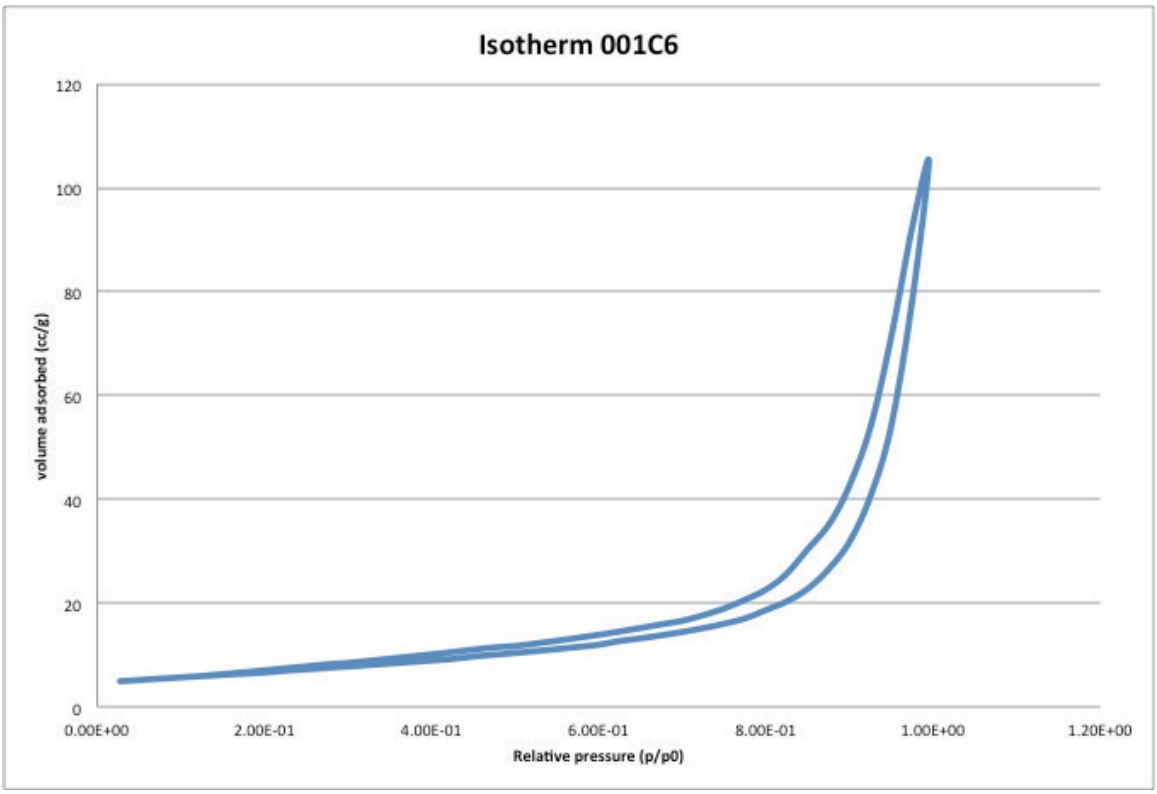

Figure 107 isotherm of sample 001C6 synthesized from cerium (IV) hydroxide, CTAB, water, ethanol, and sodium hydroxide, calcinated at 873K

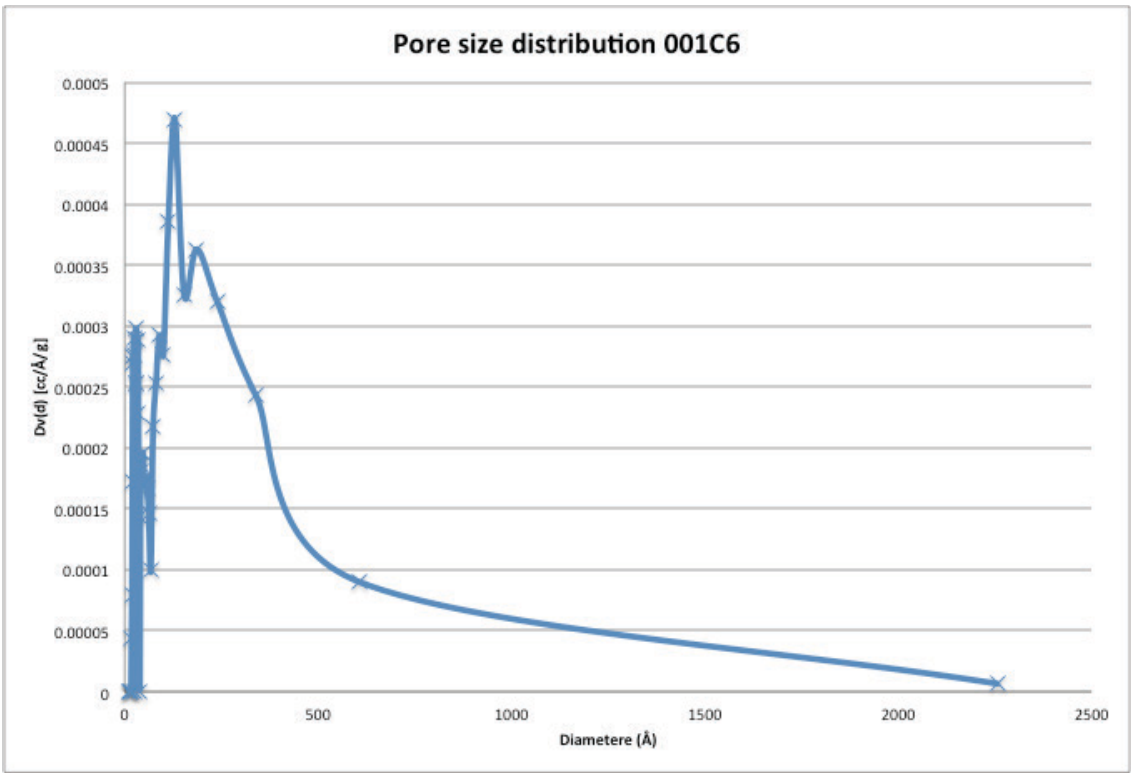

Figure 108 pore size distribution of sample 001C6 synthesized from cerium (IV) hydroxide, CTAB, water, ethanol, and sodium hydroxide, calcinated at 873K

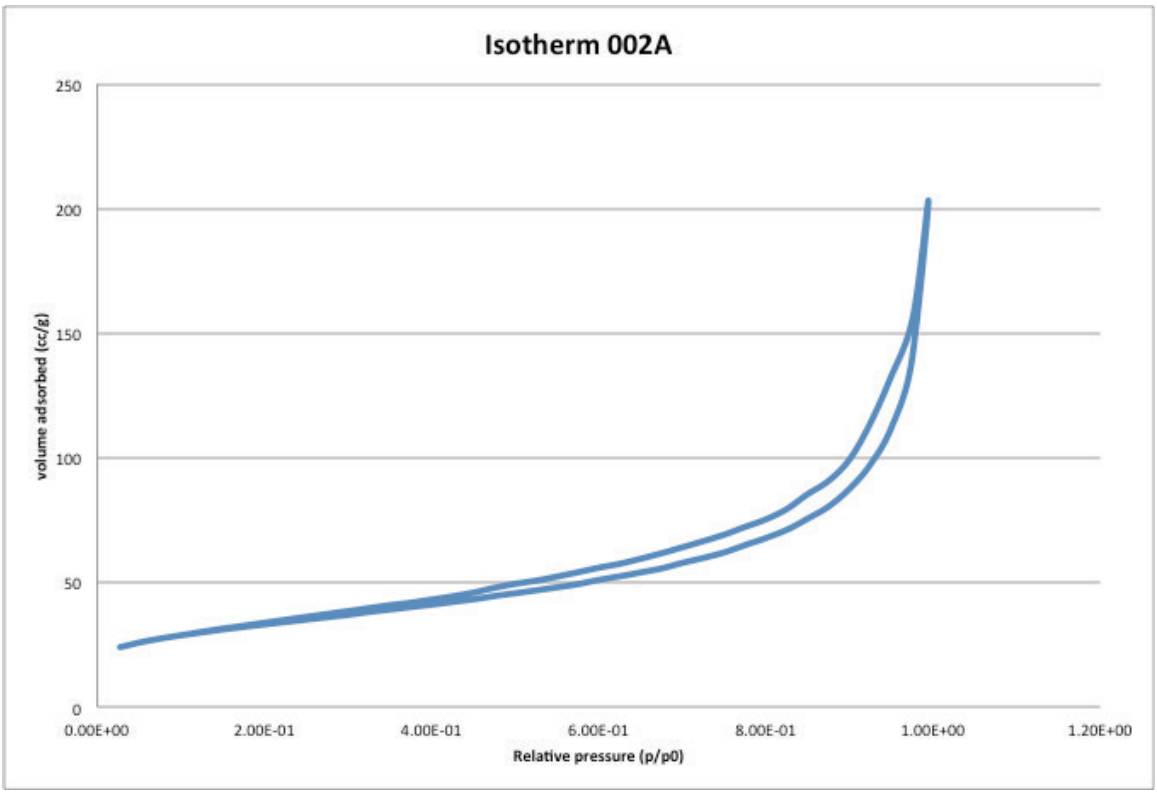

Figure 109 isotherm of sample 002A synthesized from cerium (IV) hydroxide, myristyl trimethylammonium bromide, water, ethanol, and sodium hydroxide, uncalcinated

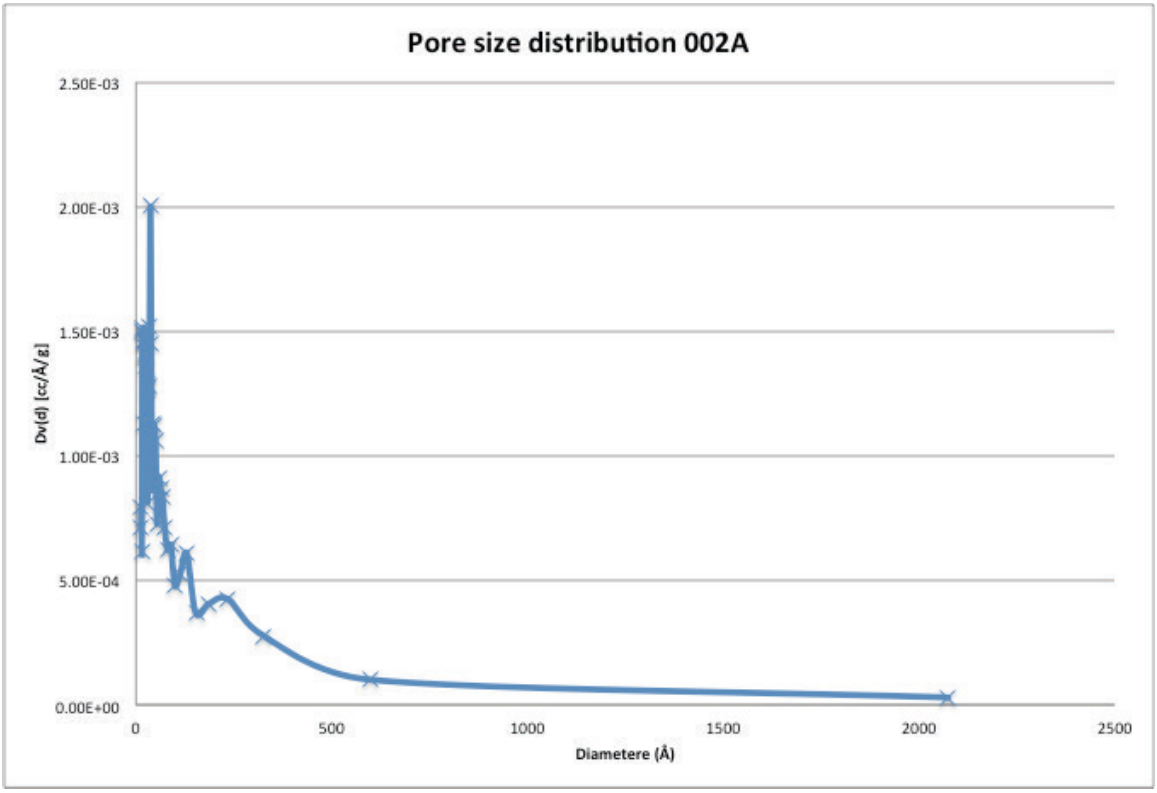

Figure 110 pore size distribution of sample 002A synthesized from cerium (IV) hydroxide, myristyl trimethylammonium bromide, water, ethanol, and sodium hydroxide, uncalcinated

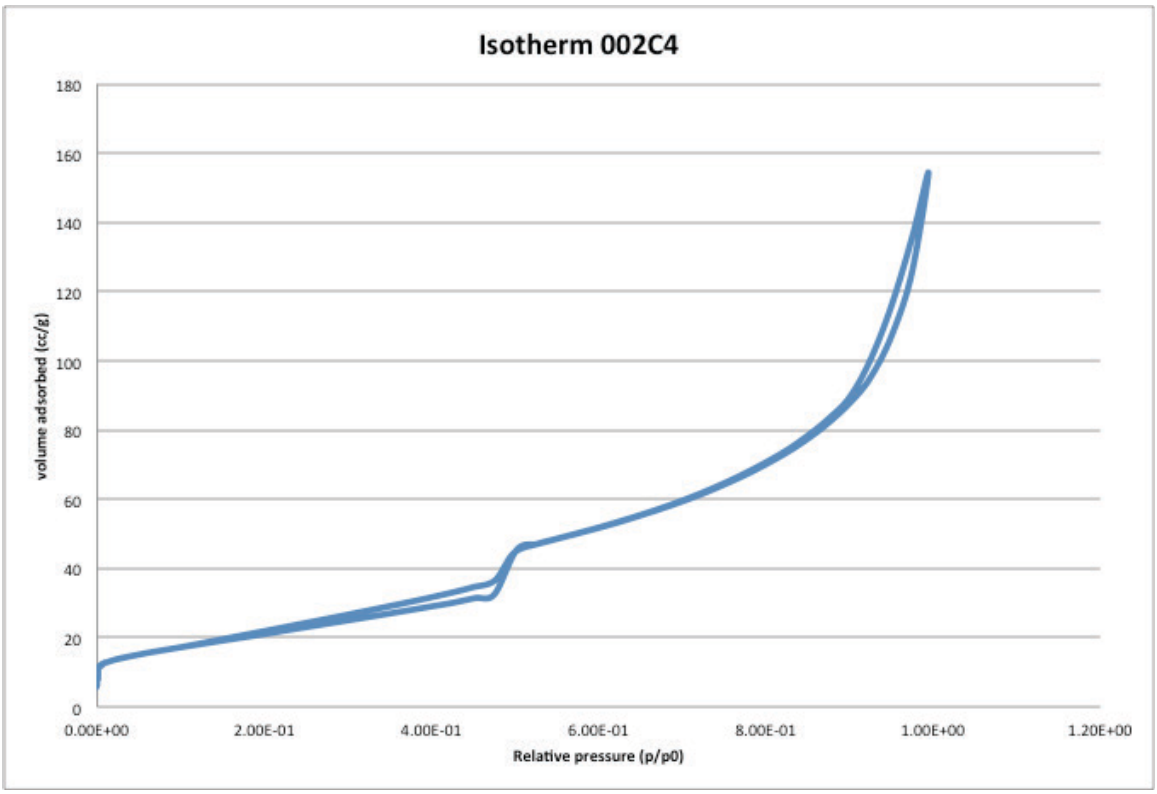

Figure 111 isotherm of sample 002C4, synthesized from cerium (IV) hydroxide, myristyl trimethylammonium bromide, water, ethanol, and sodium hydroxide, calcinated at 673K

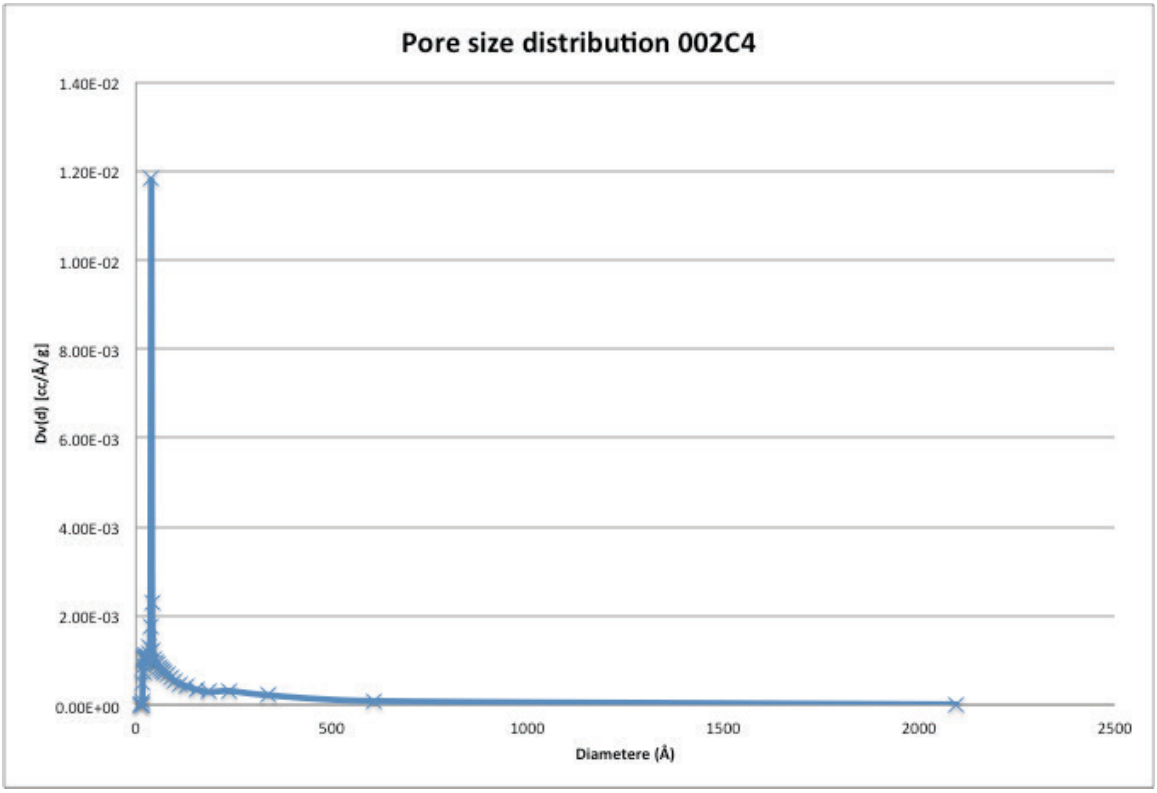

Figure 112 pore size distribution of sample 002C4, synthesized from cerium (IV) hydroxide, myristyl trimethylammonium bromide, water, ethanol, and sodium hydroxide, calcinated at 673K

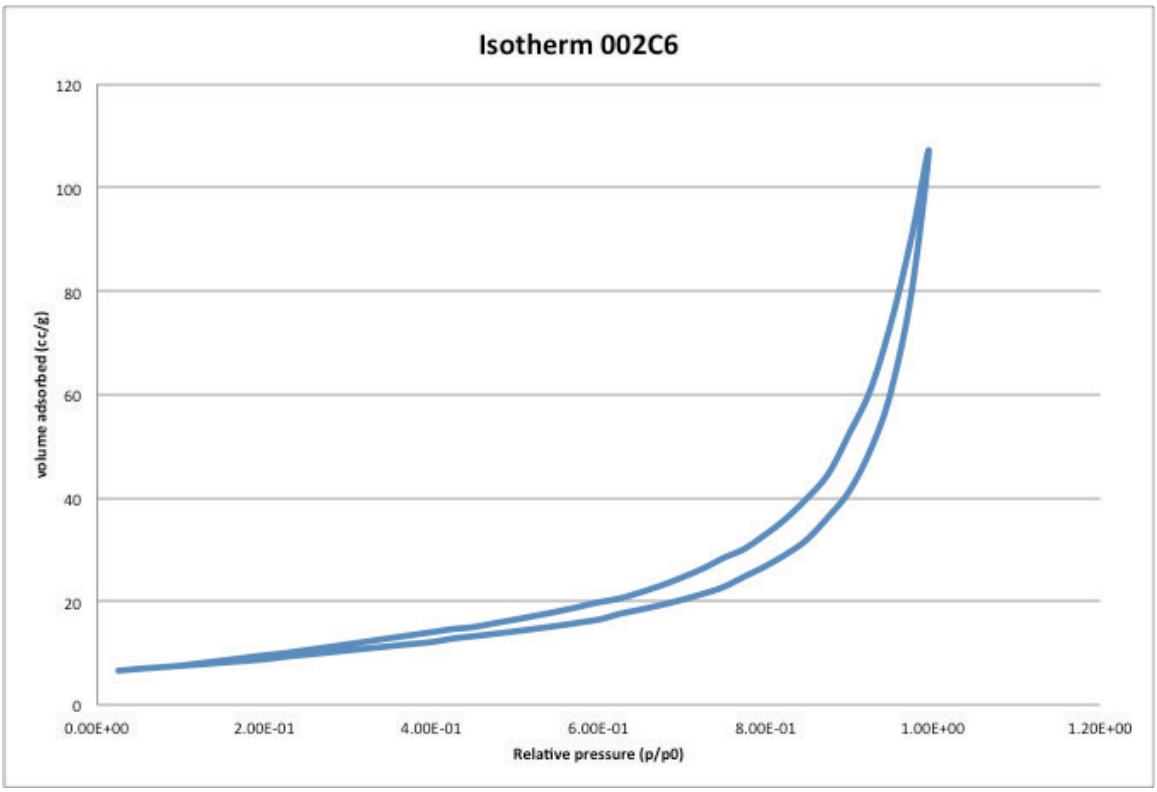

Figure 113 isotherm of sample 002C6, synthesized from cerium (IV) hydroxide, myristyl trimethylammonium bromide, water, ethanol, and sodium hydroxide, calcinated at 873K

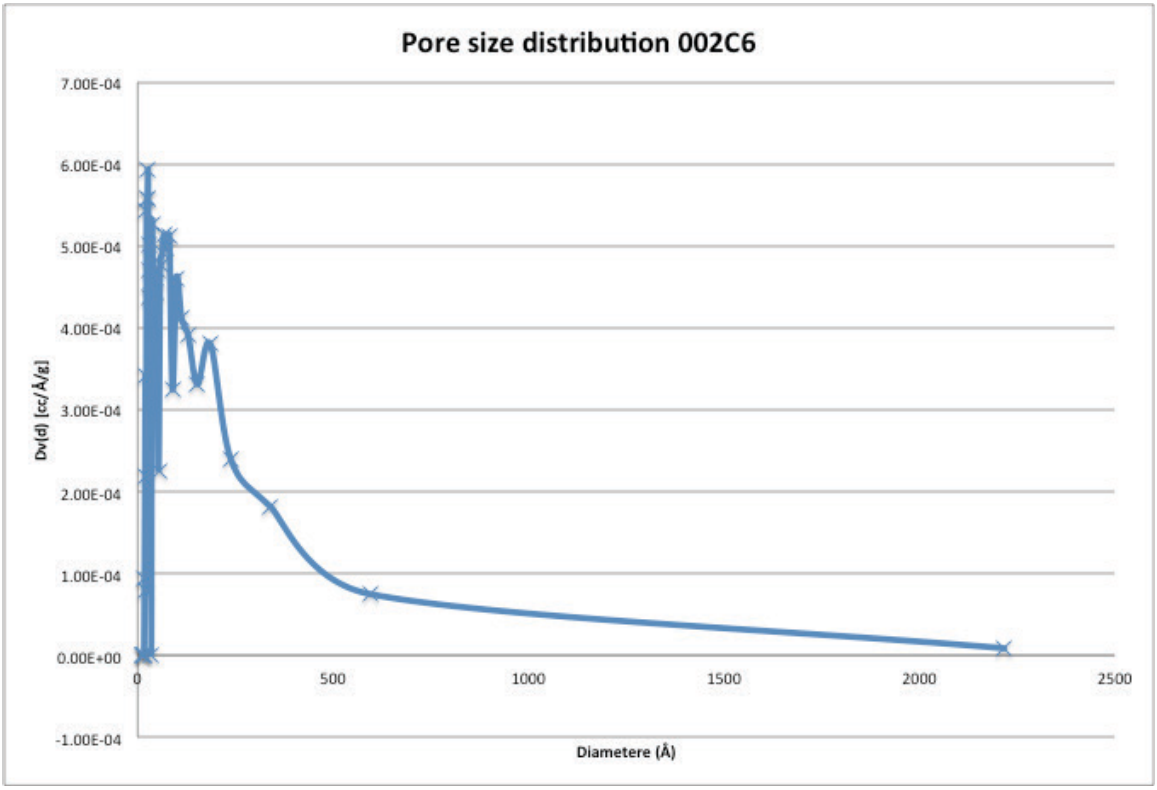

Figure 114 pore size distribution of sample 002C6, synthesized from cerium (IV) hydroxide, myristyl trimethylammonium bromide, water, ethanol, and sodium hydroxide, calcinated at 873K

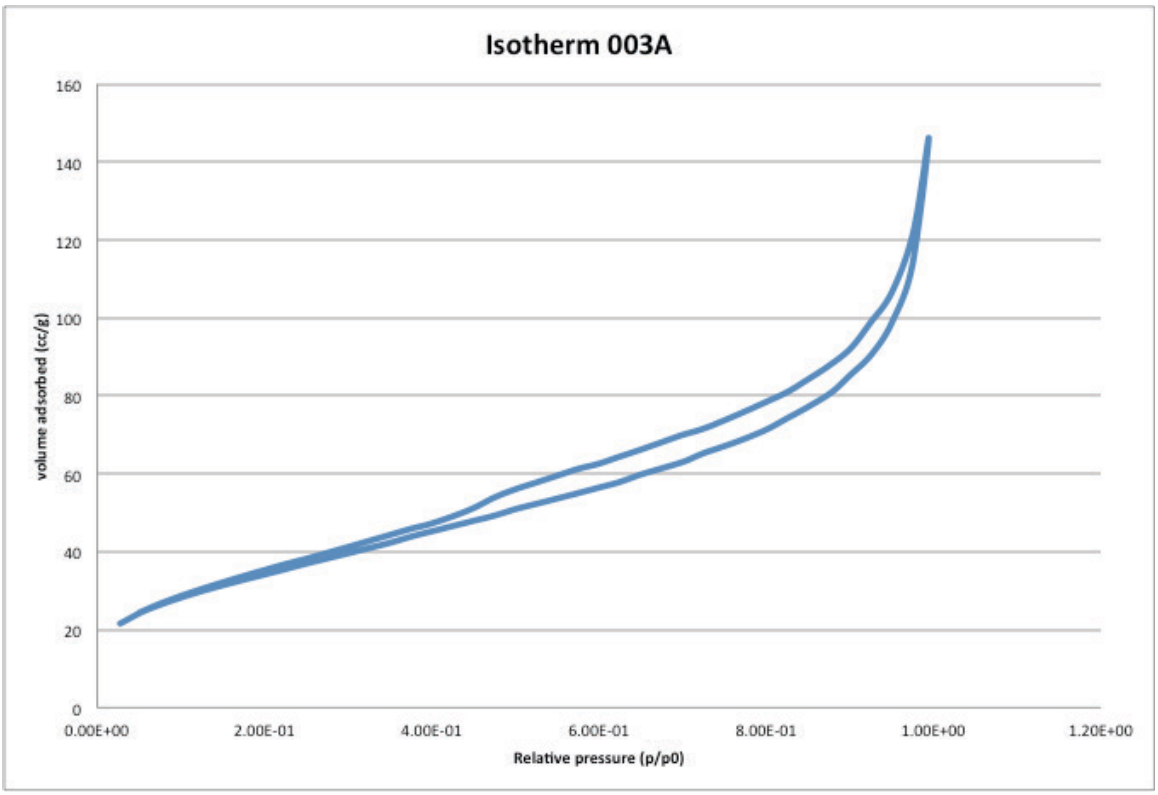

Figure 115 isotherm of sample 003A synthesized from cerium (IV) hydroxide, CTAB, hexane, ethanol, and sodium hydroxide, uncalcinated

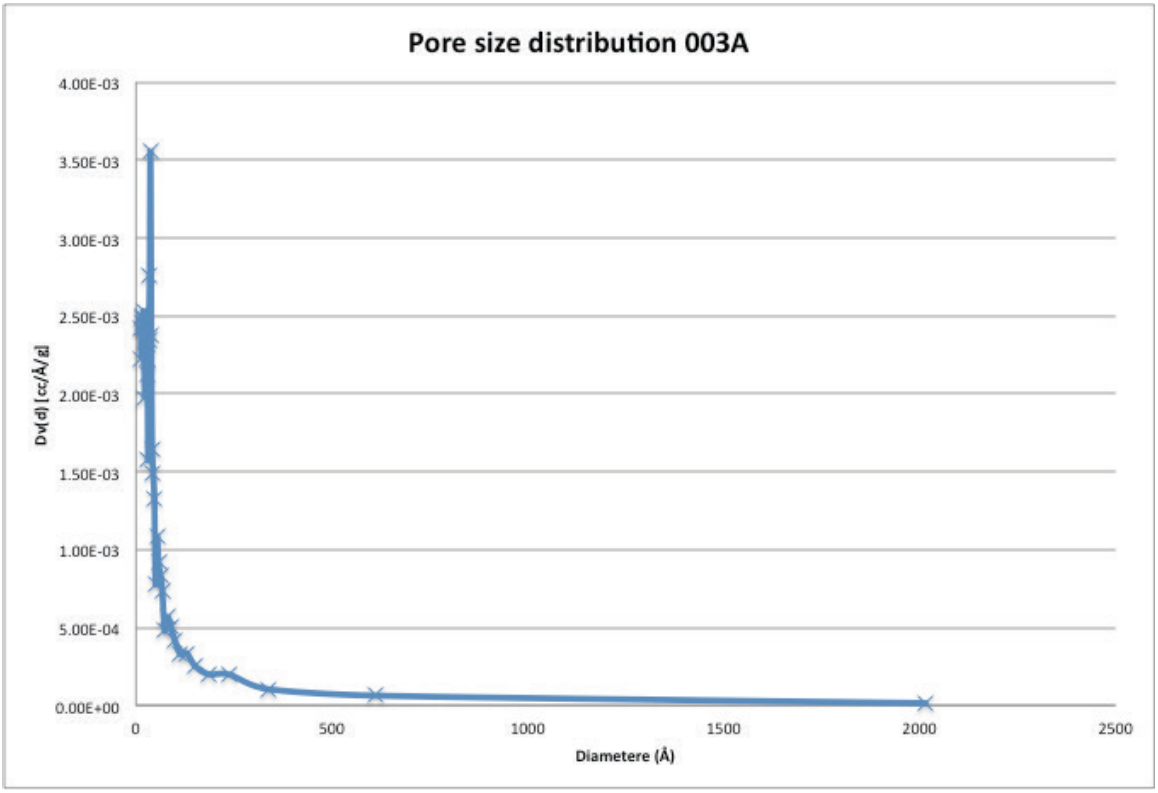

Figure 116 pore size distribution of sample 003A synthesized from cerium (IV) hydroxide, CTAB, hexane, ethanol, and sodium hydroxide, uncalcinated

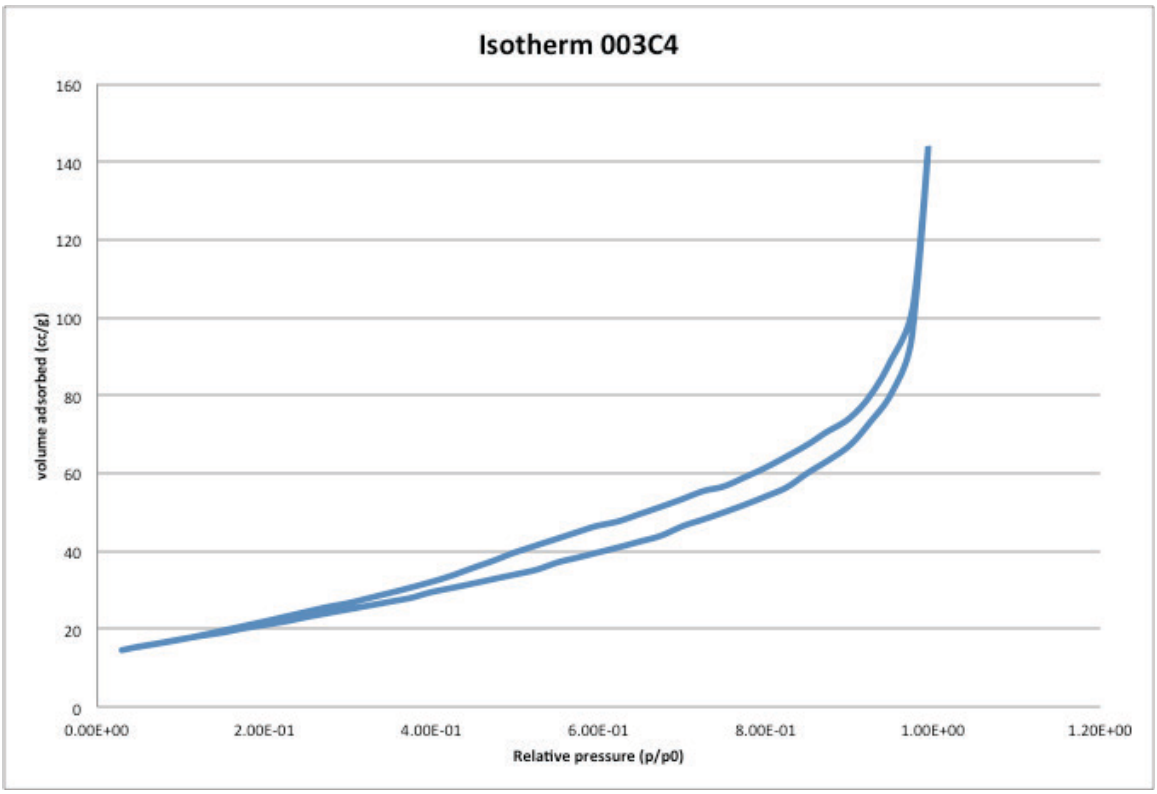

Figure 117 isotherm of sample 003C4 synthesized from cerium (IV) hydroxide, CTAB, hexane, ethanol, and sodium hydroxide, calcinated at 673K

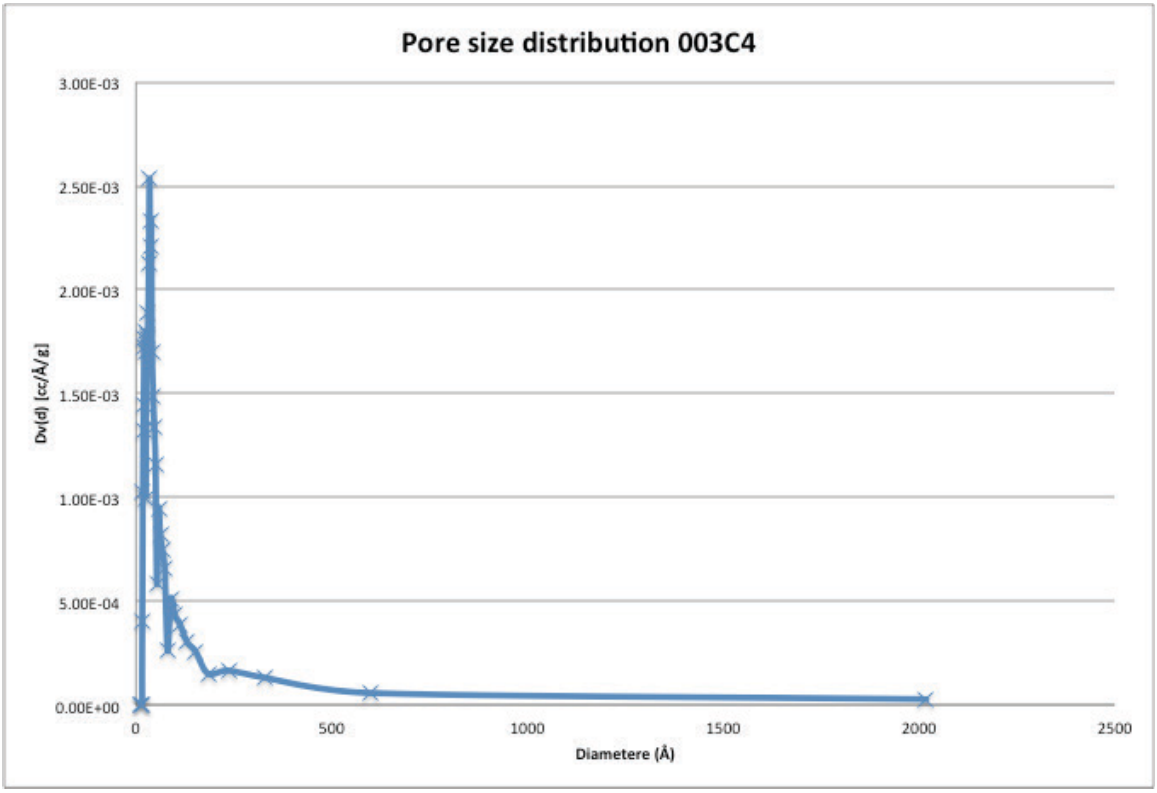

Figure 118 pore size distribution of sample 003C4 synthesized from cerium (IV) hydroxide, CTAB, hexane, ethanol, and sodium hydroxide, calcinated at 673K

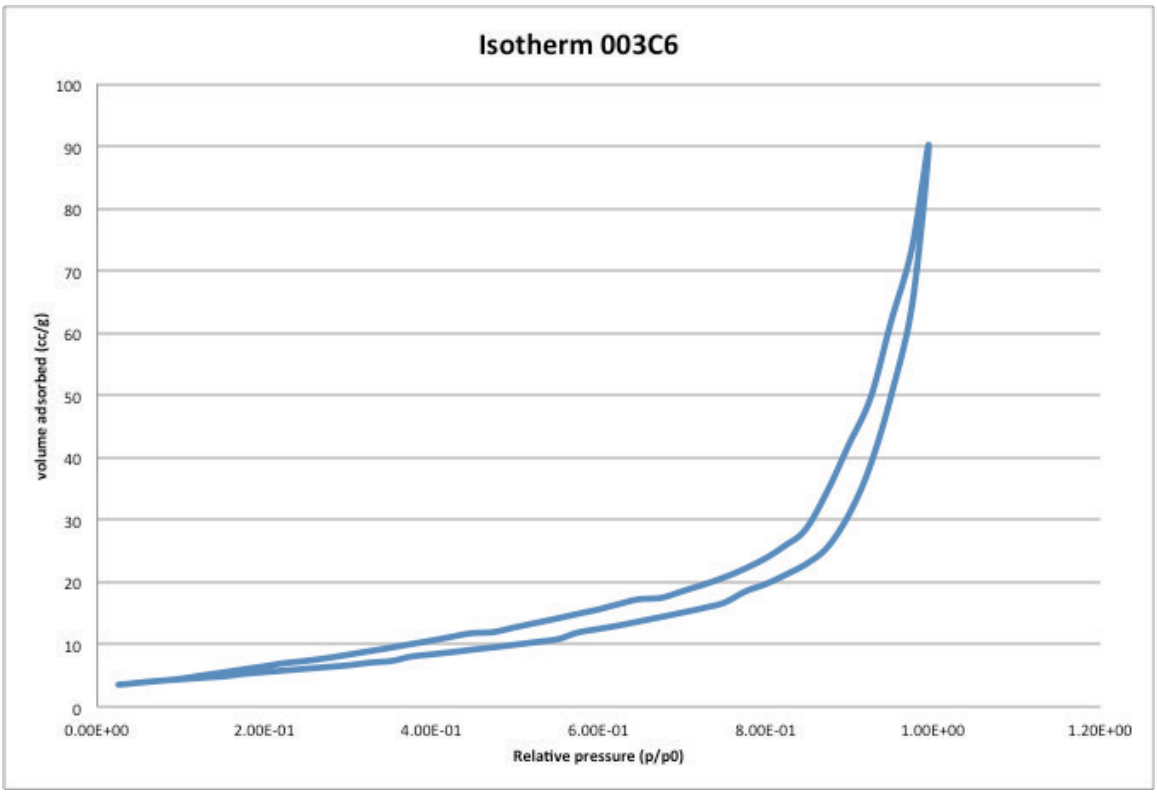

Figure 119 isotherm of sample 003C6 synthesized from cerium (IV) hydroxide, CTAB, hexane, ethanol, and sodium hydroxide, calcinated at 873K

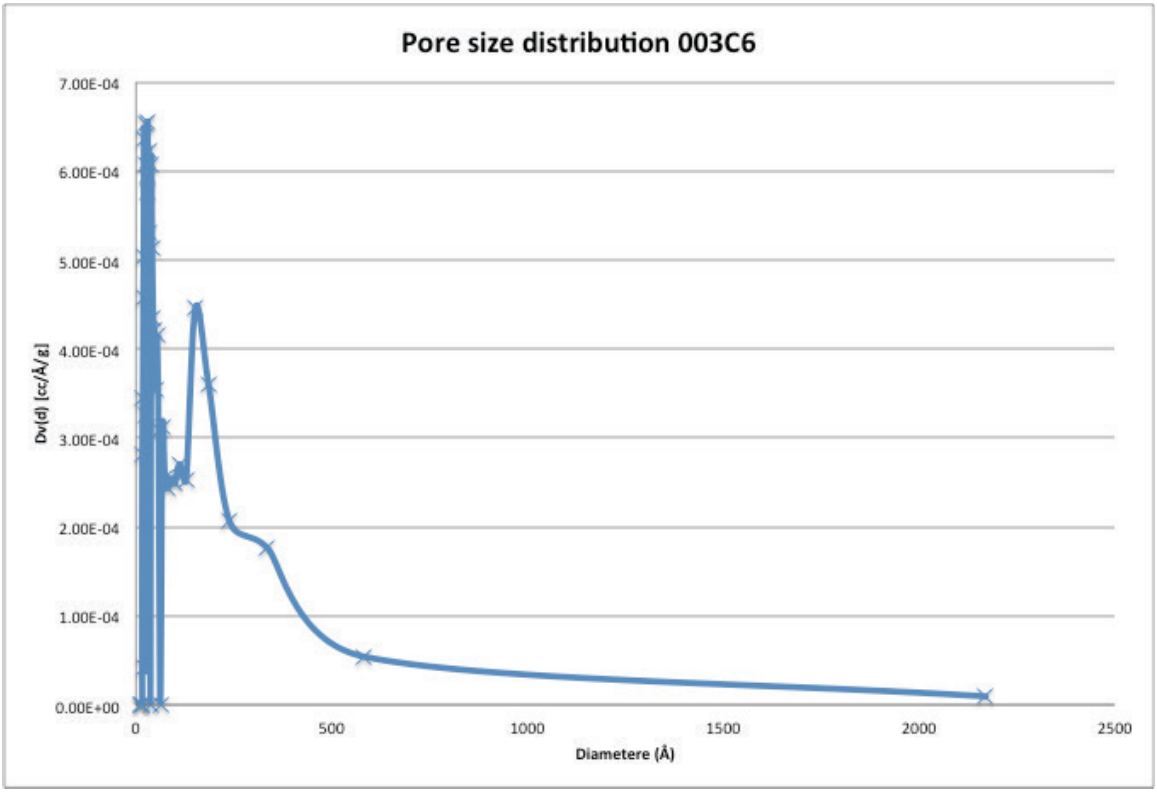

Figure 120 pore size distribution of sample 003C6 synthesized from cerium (IV) hydroxide, CTAB, hexane, ethanol, and sodium hydroxide, calcinated at 873K

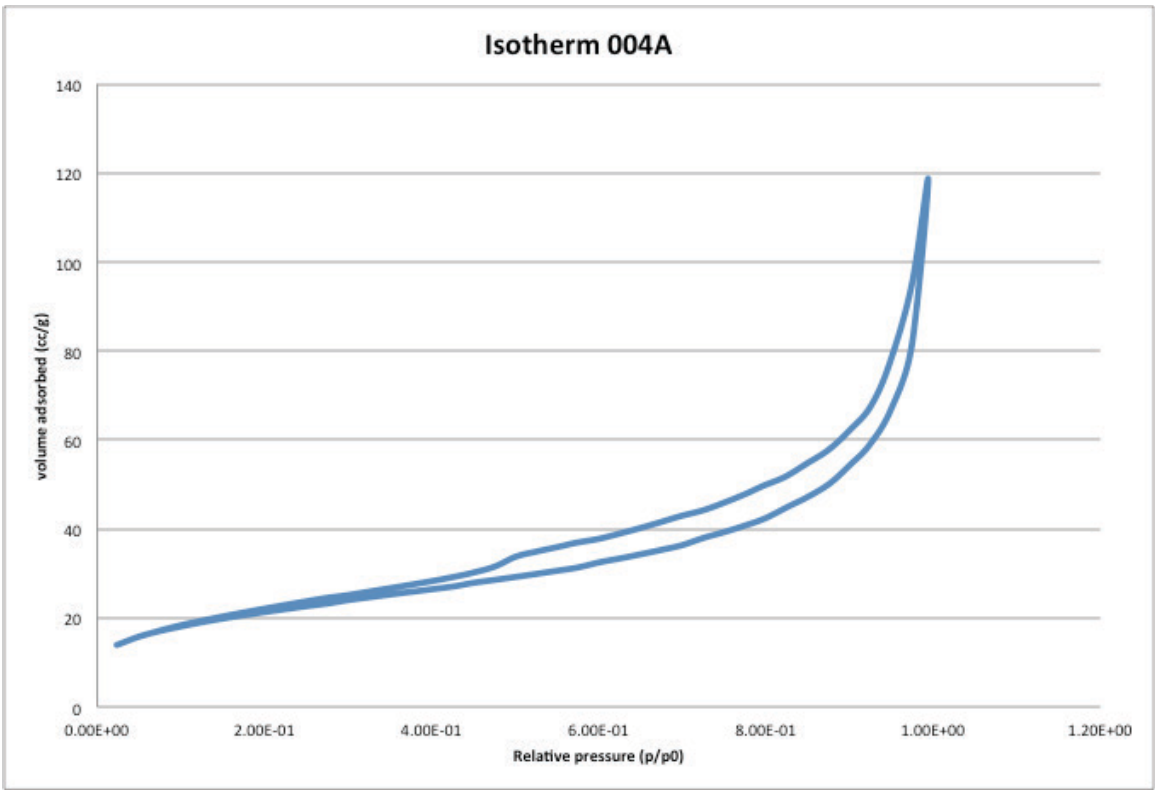

Figure 121 isotherm of sample 004A synthesized from cerium glycolate, CTAB, water, ethanol, and sodium hydroxide, uncalcinated

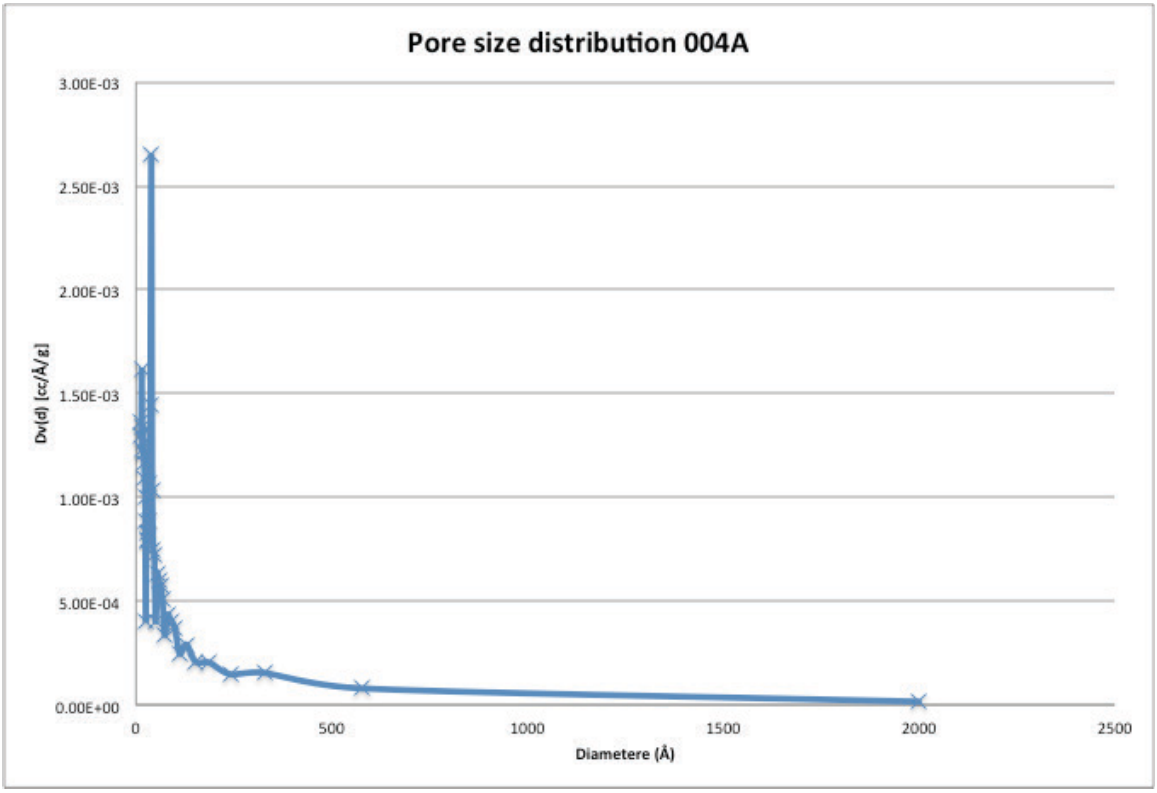

Figure 122 pore size distribution of sample 004A synthesized from cerium glycolate, CTAB, water, ethanol, and sodium hydroxide, uncalcinated

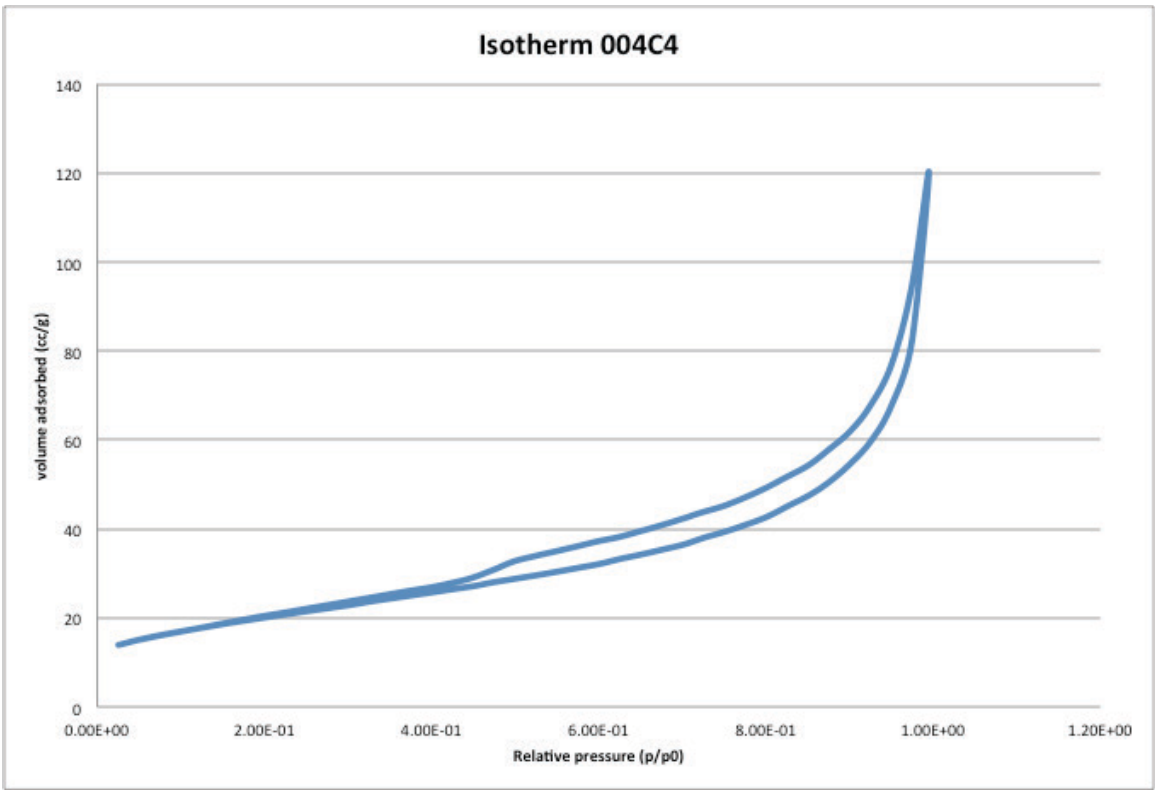

Figure 123 isotherm of sample 004C4 synthesized from cerium glycolate, CTAB, water, ethanol, and sodium hydroxide, calcinated at 673K

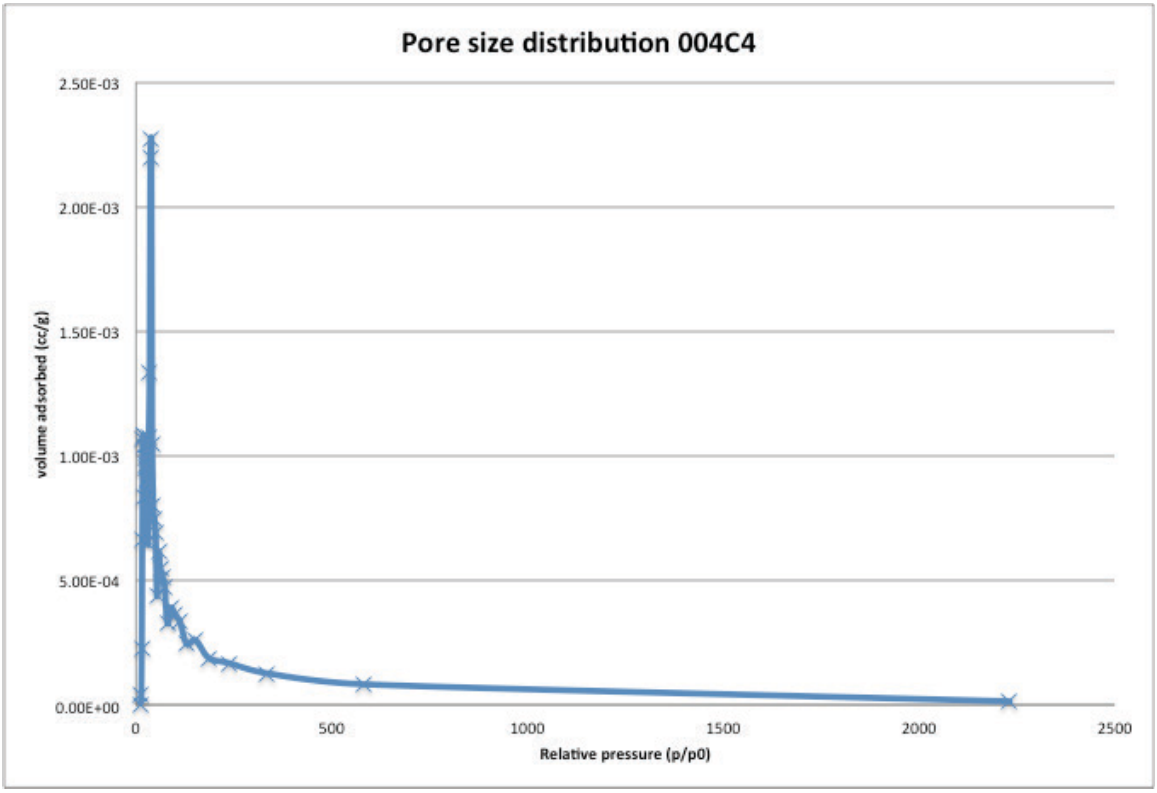

Figure 124 pore size distribution of sample 004C4 synthesized from cerium glycolate, CTAB, water, ethanol, and sodium hydroxide, calcinated at 673K

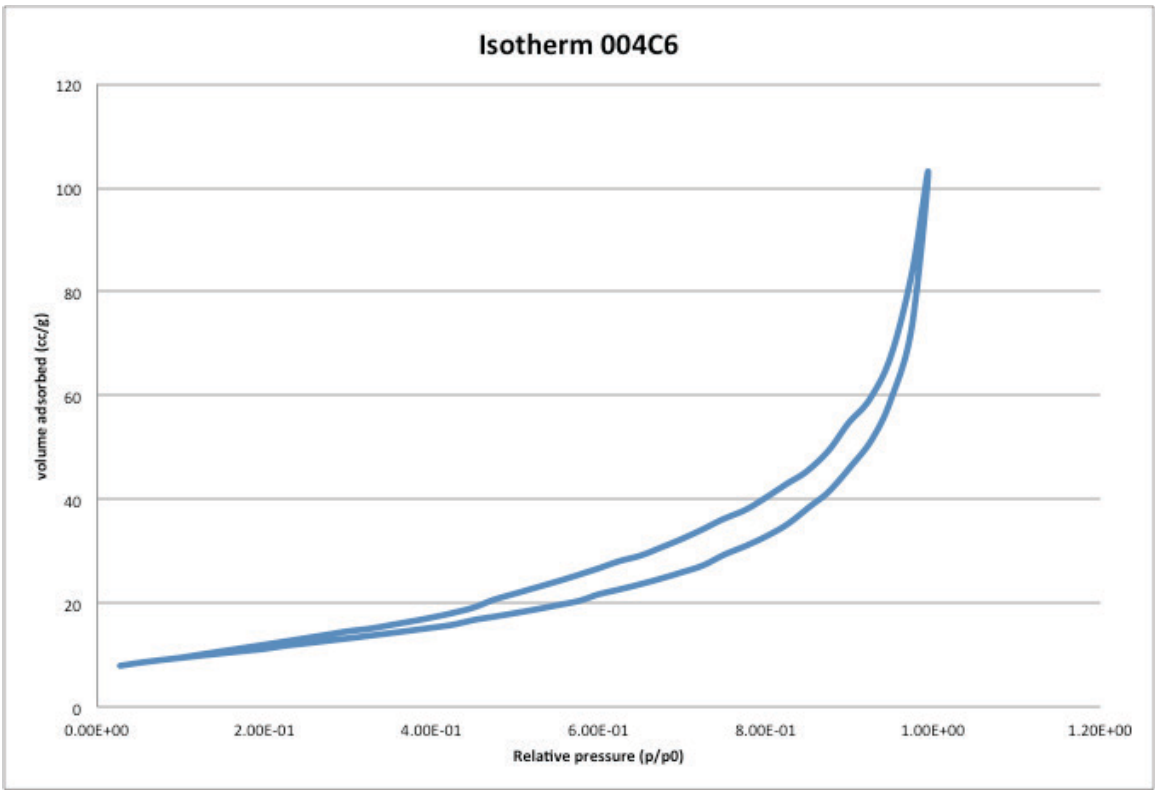

Figure 125 isotherm of sample 004C6 synthesized from cerium glycolate, CTAB, water, ethanol, and sodium hydroxide, calcinated at 873K

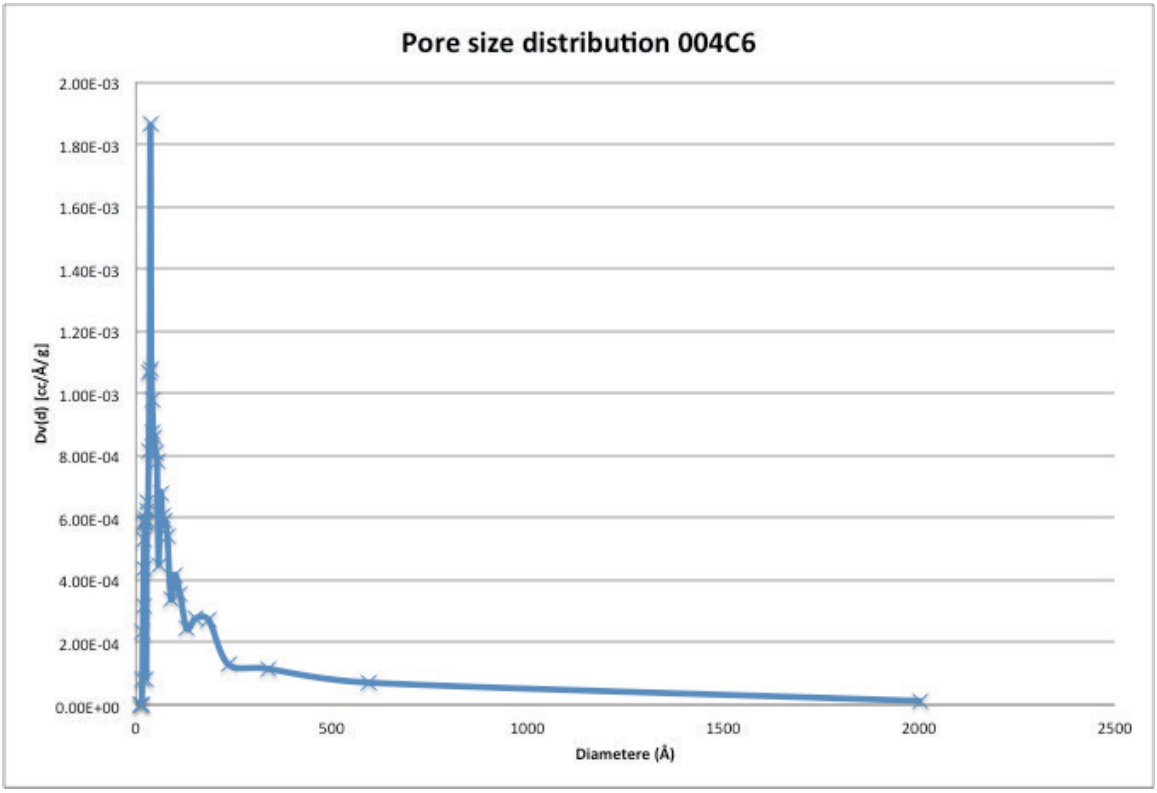

Figure 126 pore size distribution of sample 004C6 synthesized from cerium glycolate, CTAB, water, ethanol, and sodium hydroxide, calcinated at 873K

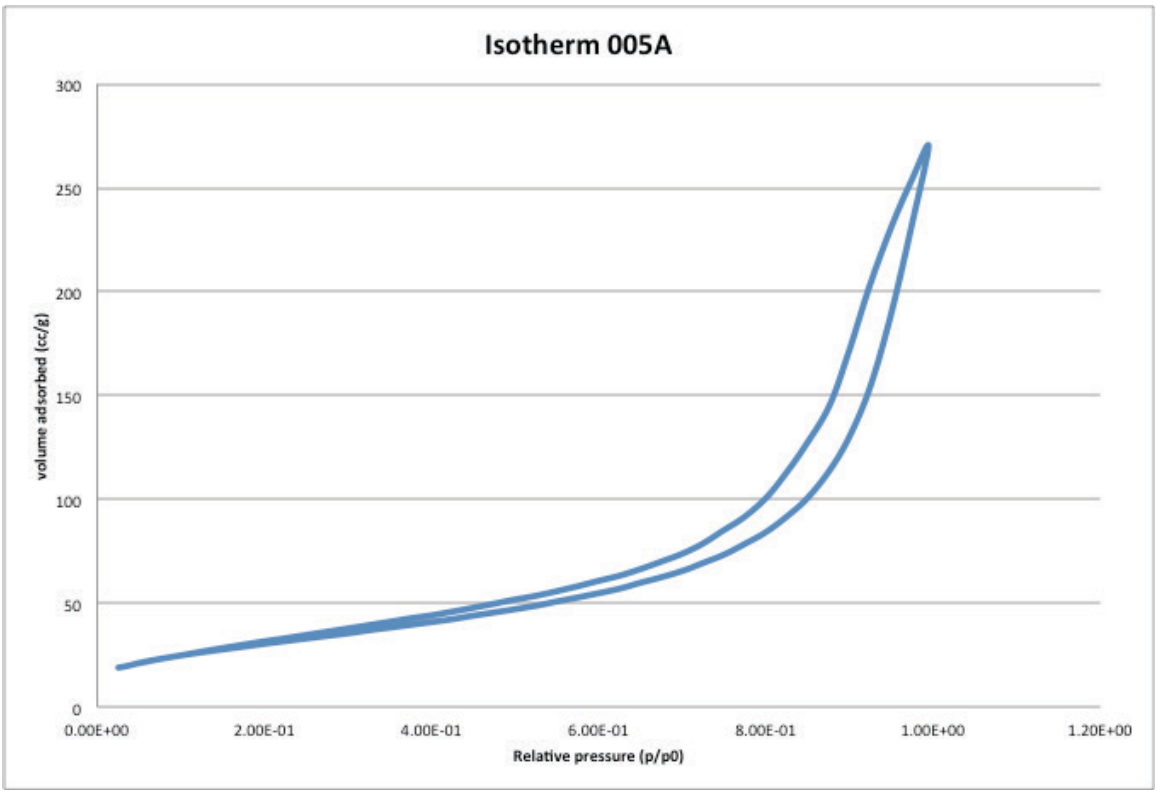

Figure 127 isotherm of sample 005A synthesized from cerium (III) chloride heptahydrate, CTAB, water, ethanol, and sodium hydroxide, uncalcinated

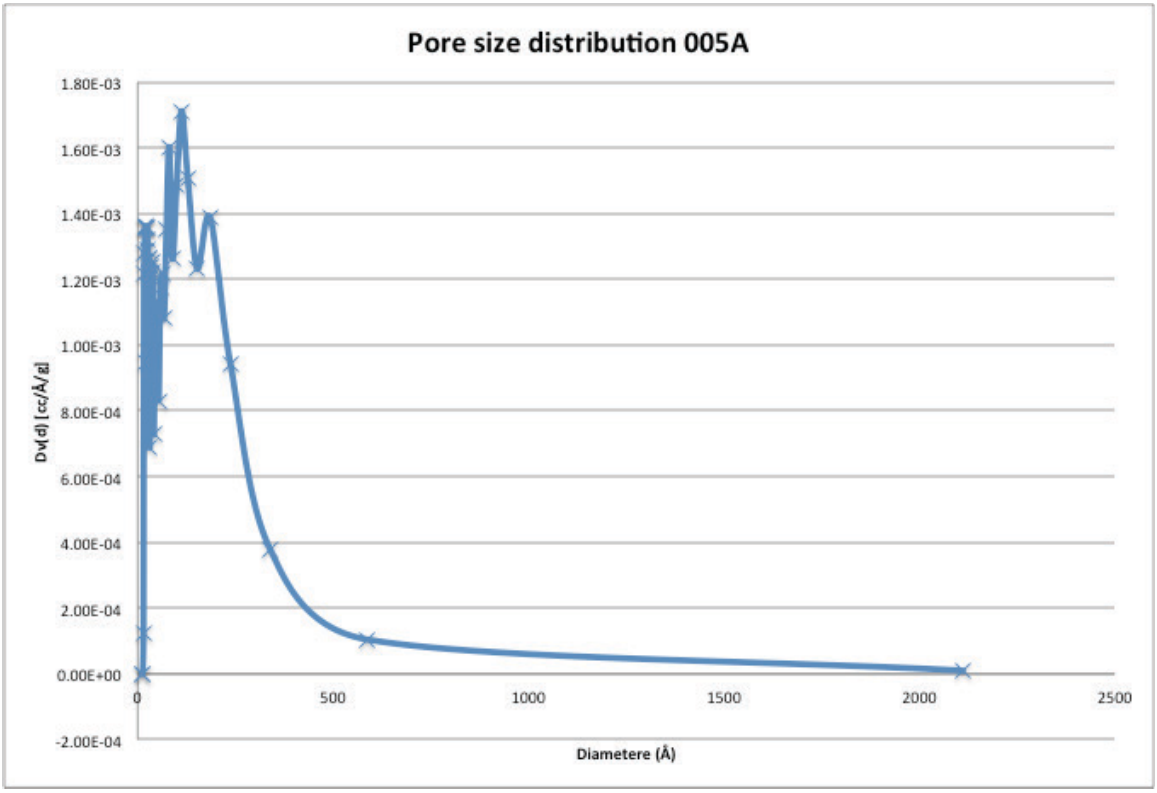

Figure 128 pore size distribution of sample 005A synthesized from cerium (III) chloride heptahydrate, CTAB, water, ethanol, and sodium hydroxide, uncalcinated

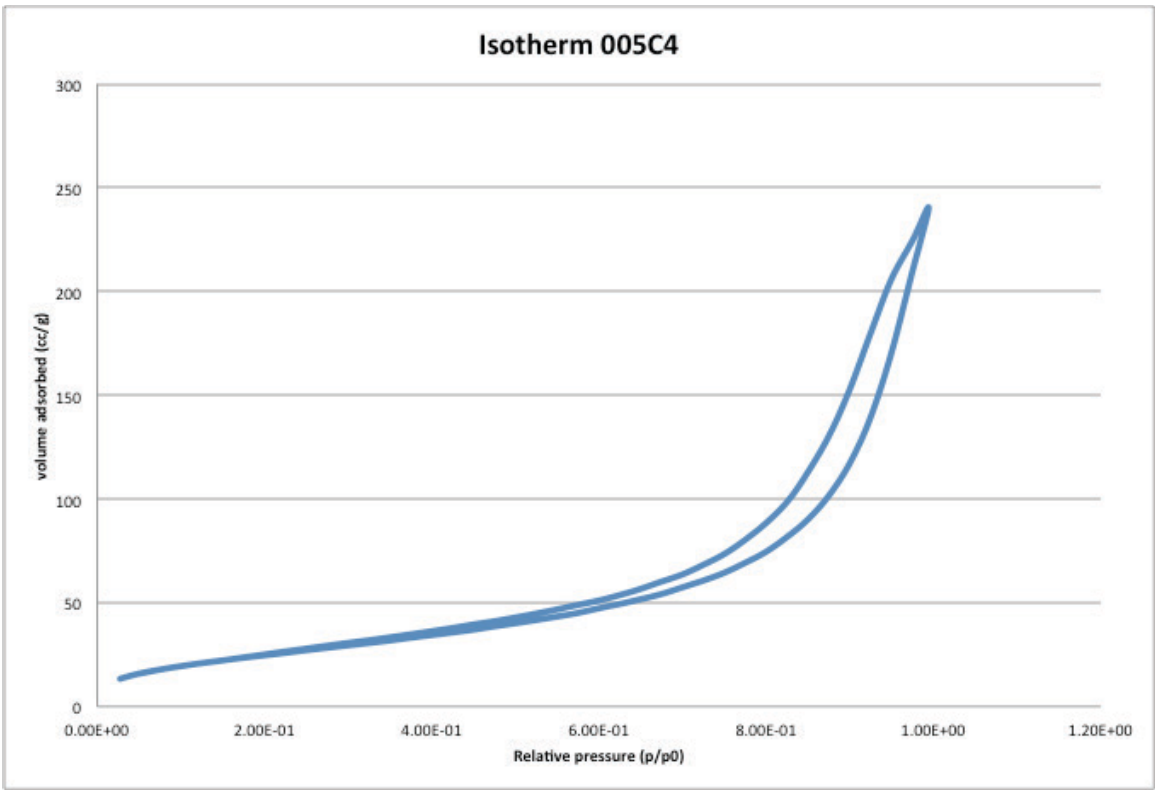

Figure 129 isotherm of sample 005C4 synthesized from cerium (III) chloride heptahydrate, CTAB, water, ethanol, and sodium hydroxide, calcinated at 673K

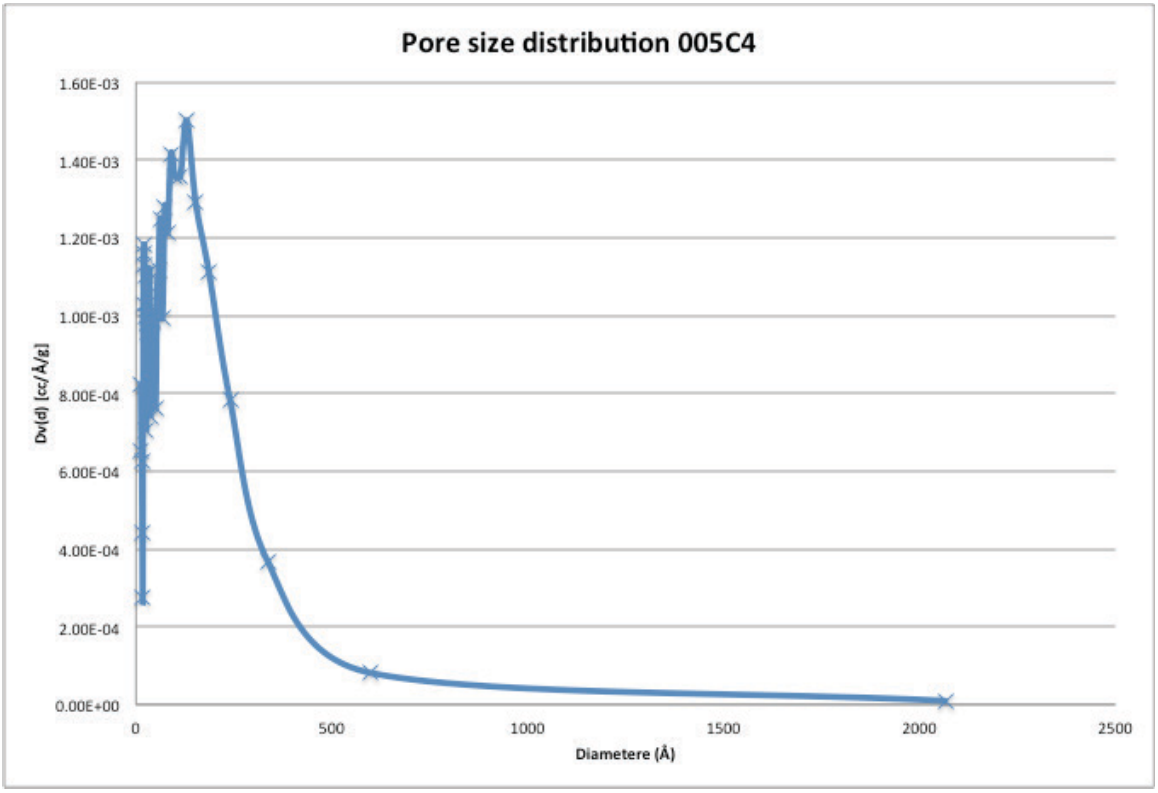

Figure 130 pore size distribution of sample 005C4 synthesized from cerium (III) chloride heptahydrate, CTAB, water, ethanol, and sodium hydroxide, calcinated at 673K

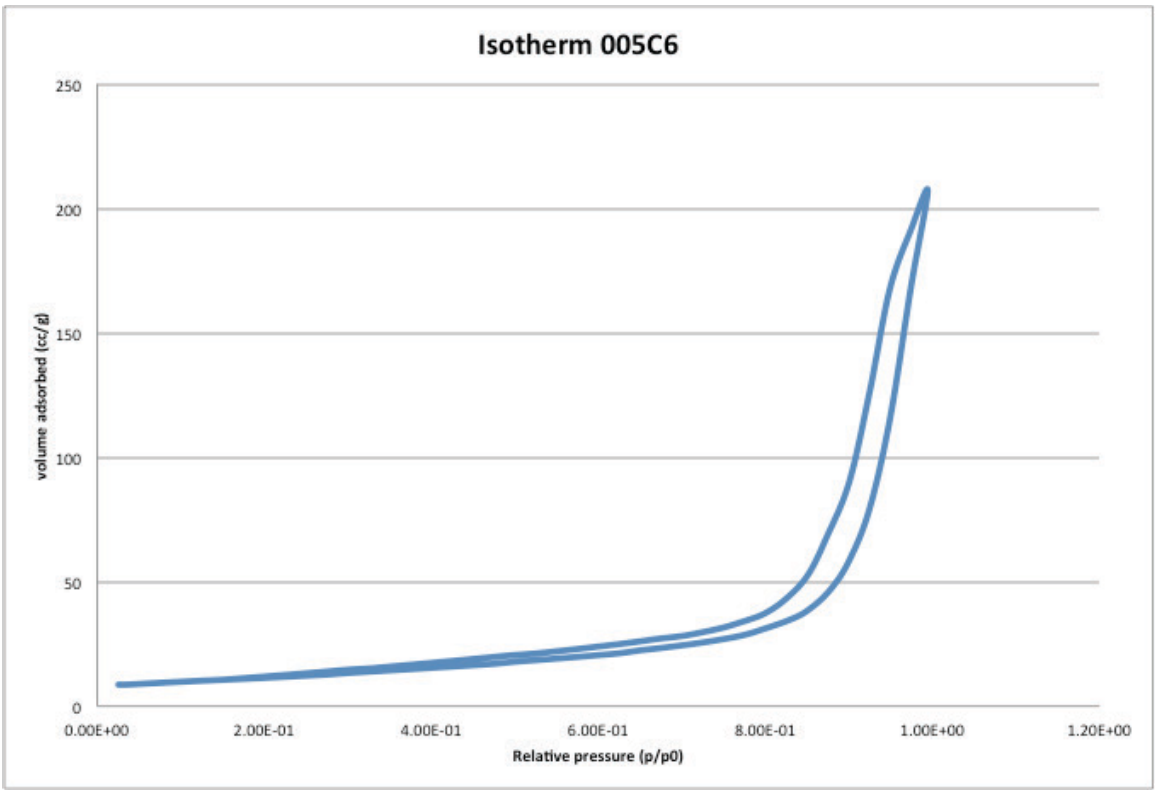

Figure 131 isotherm of sample 005C6 synthesized from cerium (III) chloride heptahydrate, CTAB, water, ethanol, and sodium hydroxide, calcinated at 873K

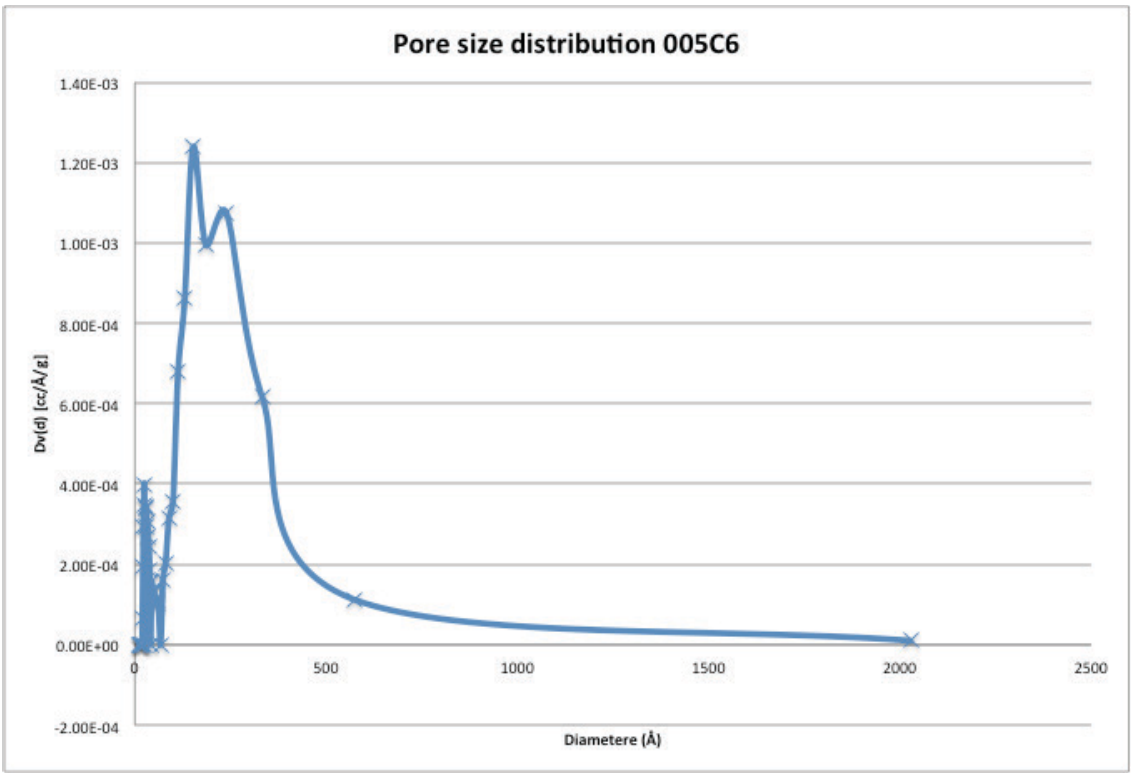

Figure 132 pore size distribution of sample 005C6 synthesized from cerium (III) chloride heptahydrate, CTAB, water, ethanol, and sodium hydroxide, calcinated at 873K

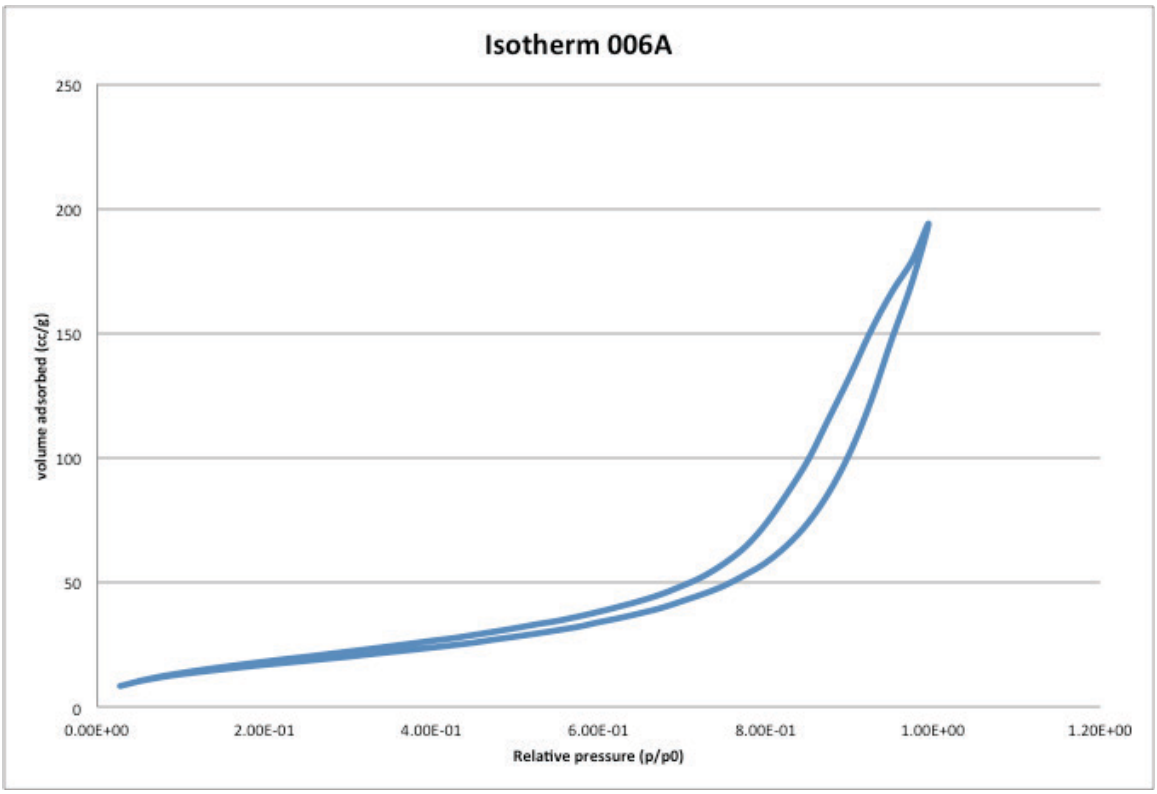

Figure 133 isotherm of sample 006A synthesized from cerium (III) nitrate hexahydrate, CTAB, water, ethanol, and sodium hydroxide, uncalcinated

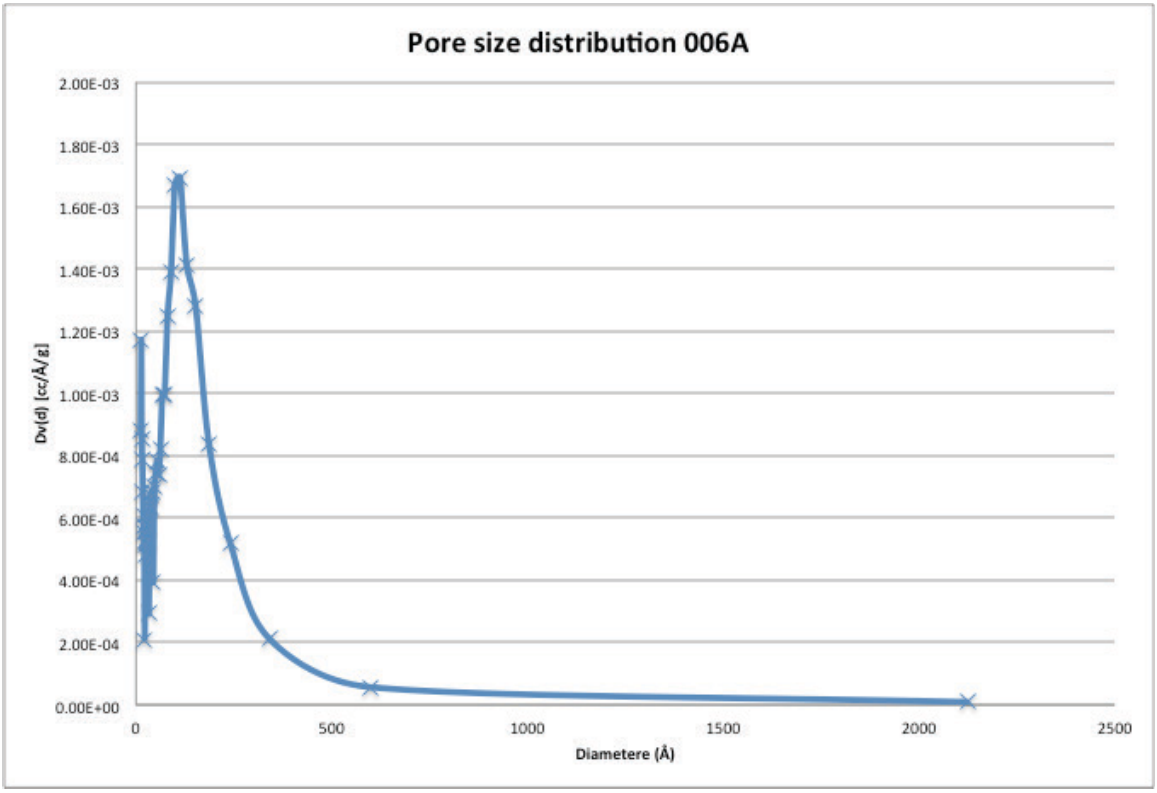

Figure 134 pore size distribution of sample 006A synthesized from cerium (III) nitrate hexahydrate, CTAB, water, ethanol, and sodium hydroxide, uncalcinated

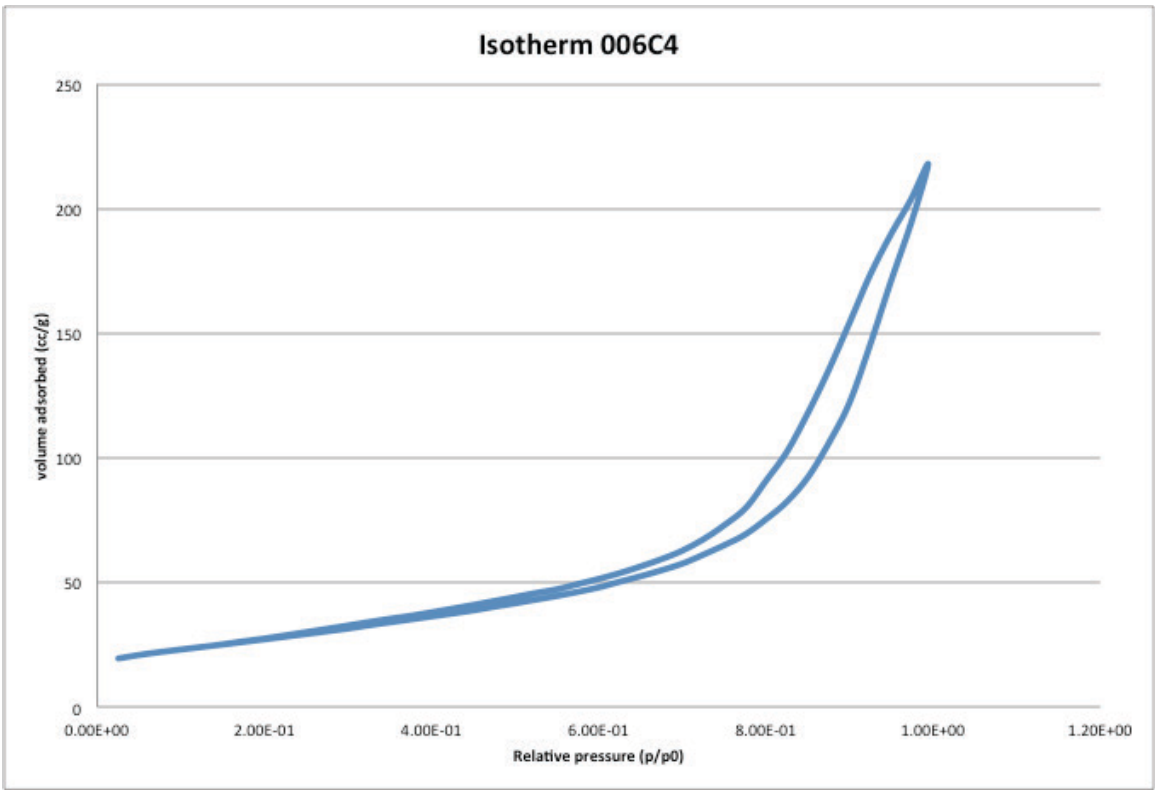

Figure 135 isotherm of sample 006C4 synthesized from cerium (III) nitrate hexahydrate, CTAB, water, ethanol, and sodium hydroxide, calcinated at 673K

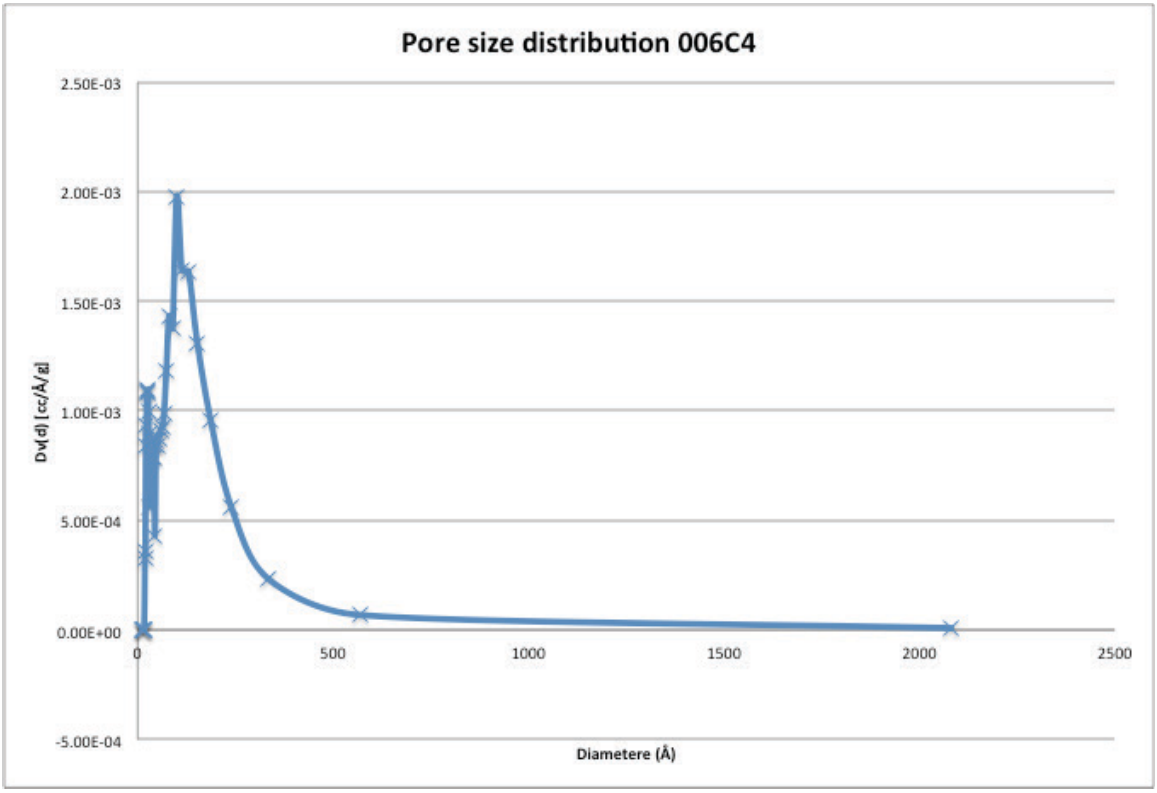

Figure 136 pore size distribution of sample 006C4 synthesized from cerium (III) nitrate hexahydrate, CTAB, water, ethanol, and sodium hydroxide, calcinated at 673K

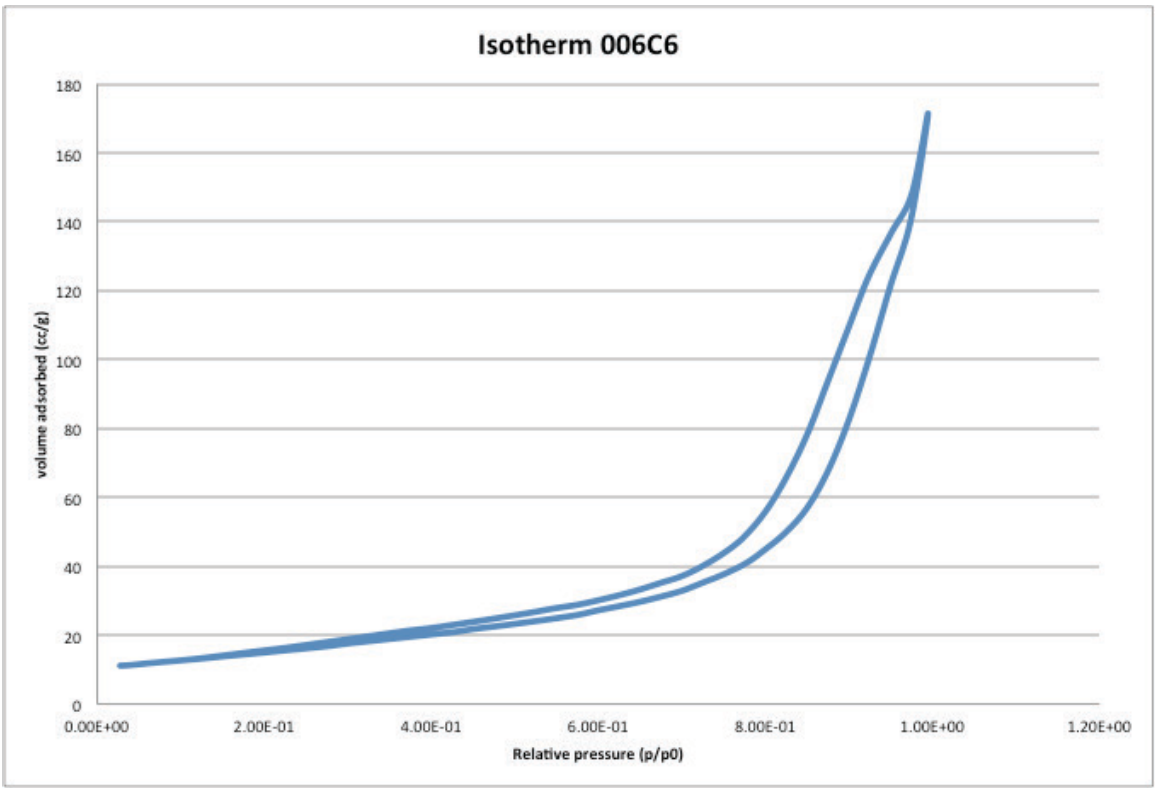

Figure 137 isotherm of sample 006C6 synthesized from cerium (III) nitrate hexahydrate, CTAB, water, ethanol, and sodium hydroxide, calcinated at 873K

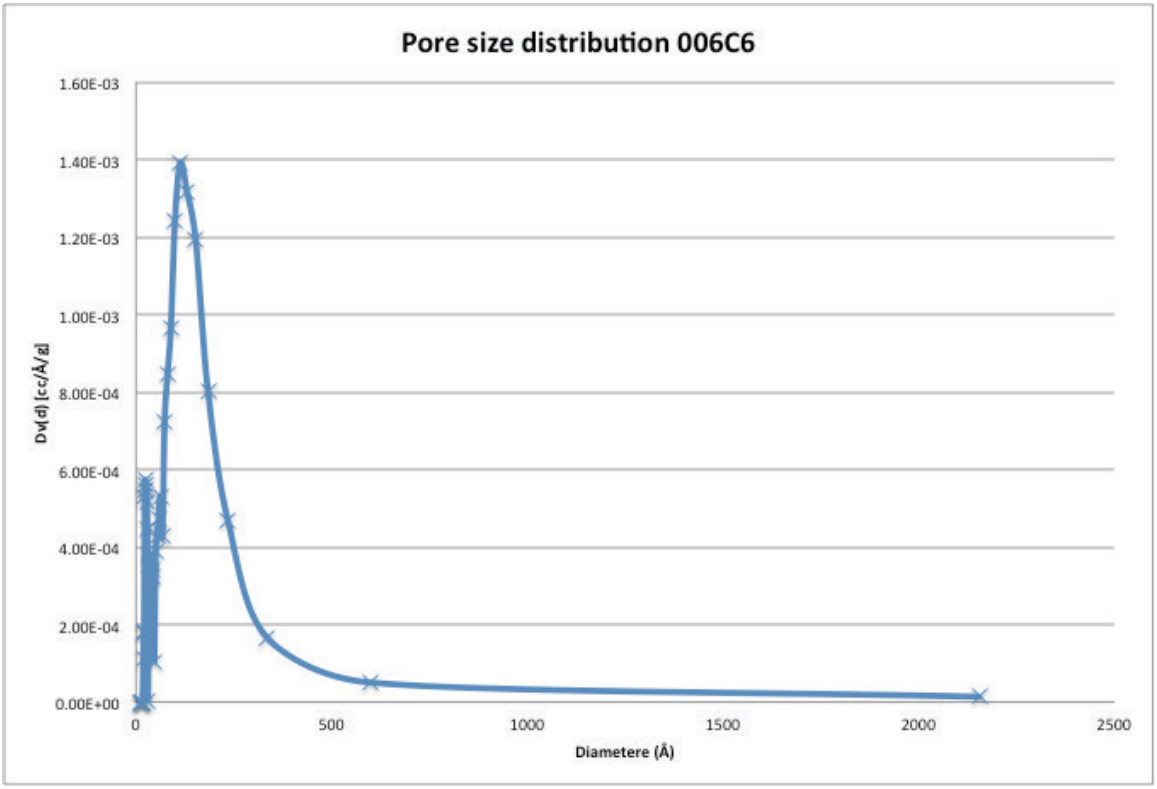

Figure 138 pore size distribution of sample 006C6 synthesized from cerium (III) nitrate hexahydrate, CTAB, water, ethanol, and sodium hydroxide, calcinated at 873K

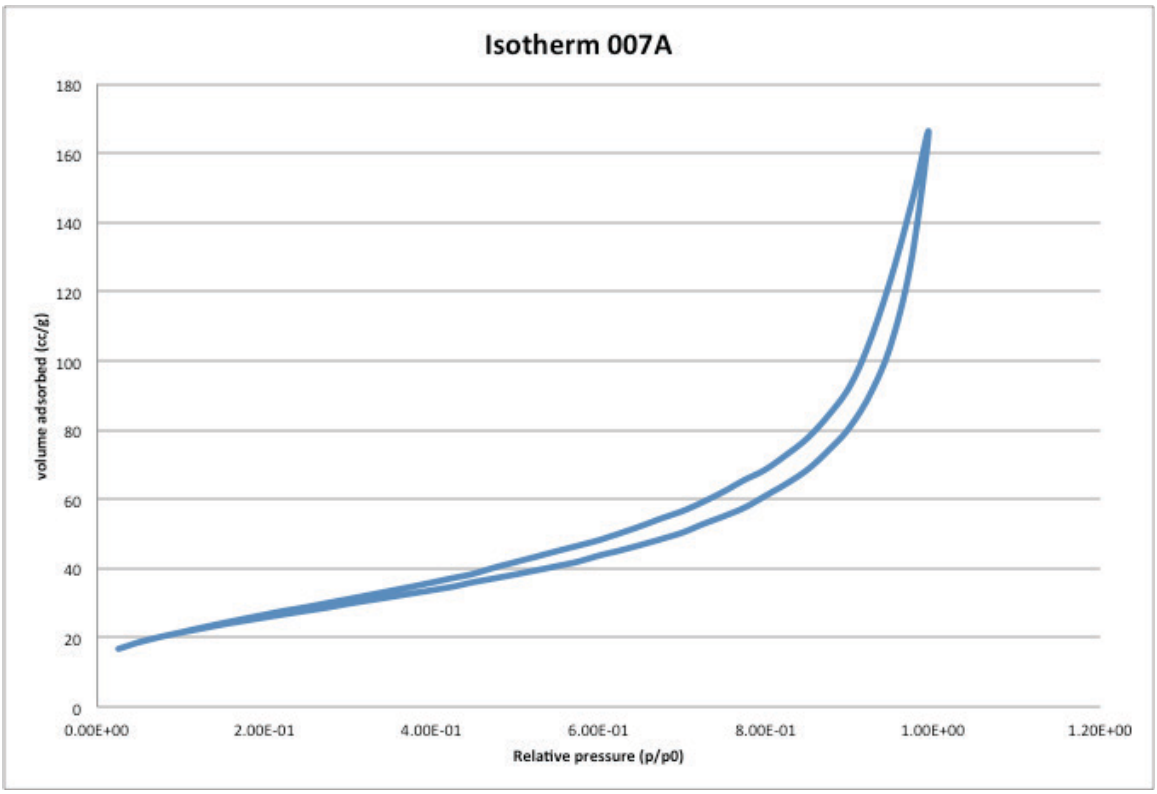

Figure 139 isotherm of sample 007A synthesized from cerium hydroxide, CTAB, paraffin, water, ethanol, dichloromethane, and sodium hydroxide, uncalcinated

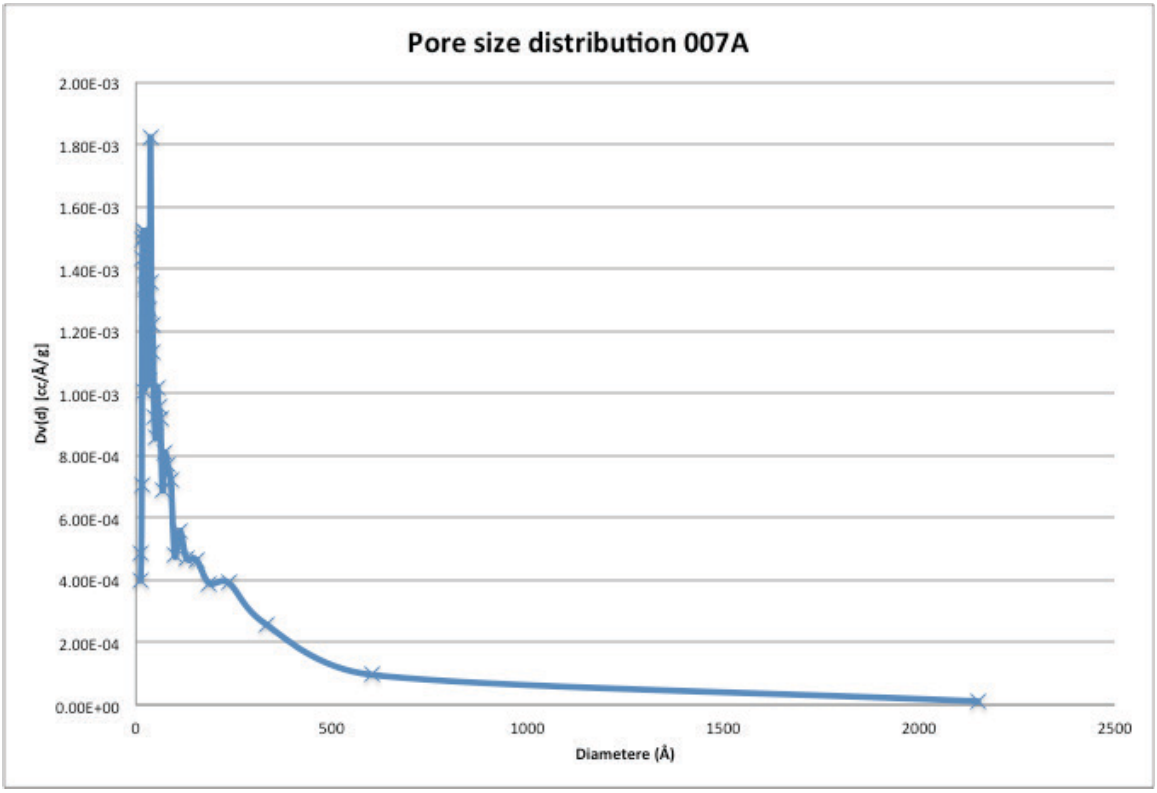

Figure 140 pore size distribution of sample 007A synthesized from cerium hydroxide, CTAB, paraffin, water, ethanol, dichloromethane, and sodium hydroxide, uncalcinated

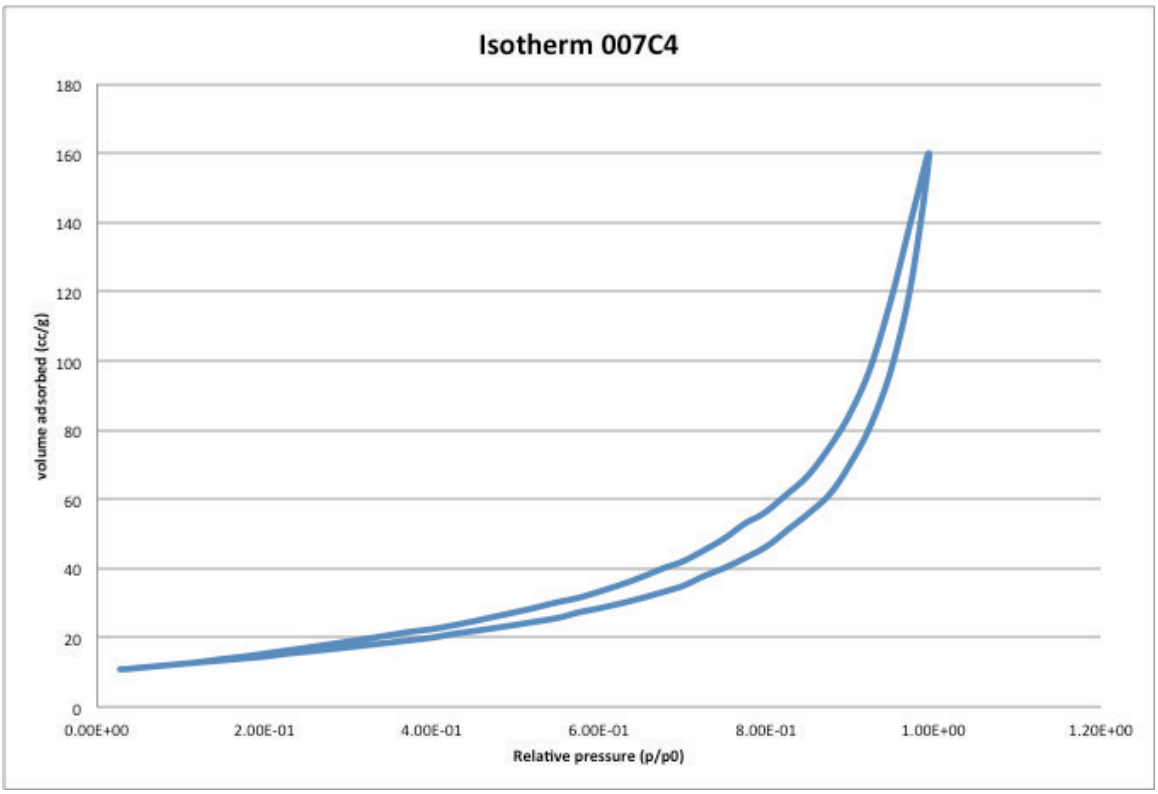

Figure 141 isotherm of sample 007C4 synthesized from cerium hydroxide, CTAB, paraffin, water, ethanol, dichloromethane, and sodium hydroxide, calcinated at 673K

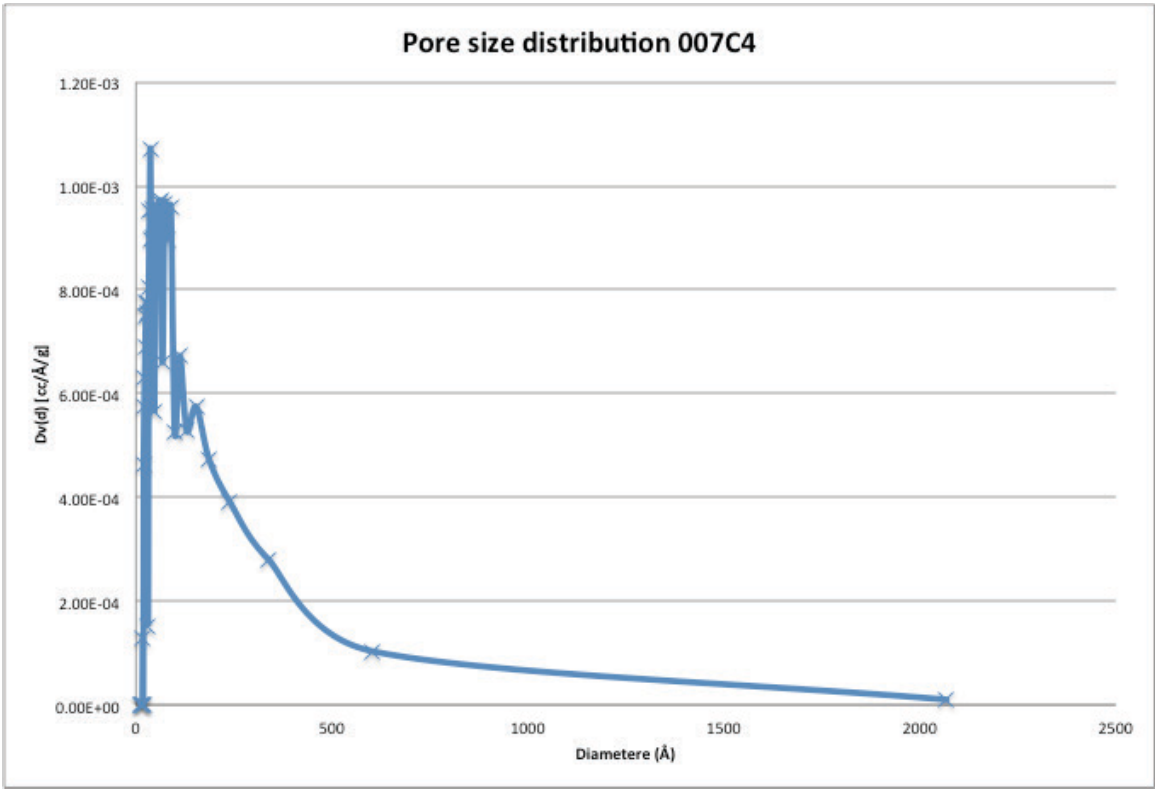

Figure 142 pore size distribution of sample 007C4 synthesized from cerium hydroxide, CTAB, paraffin, water, ethanol, dichloromethane, and sodium hydroxide, calcinated at 673K

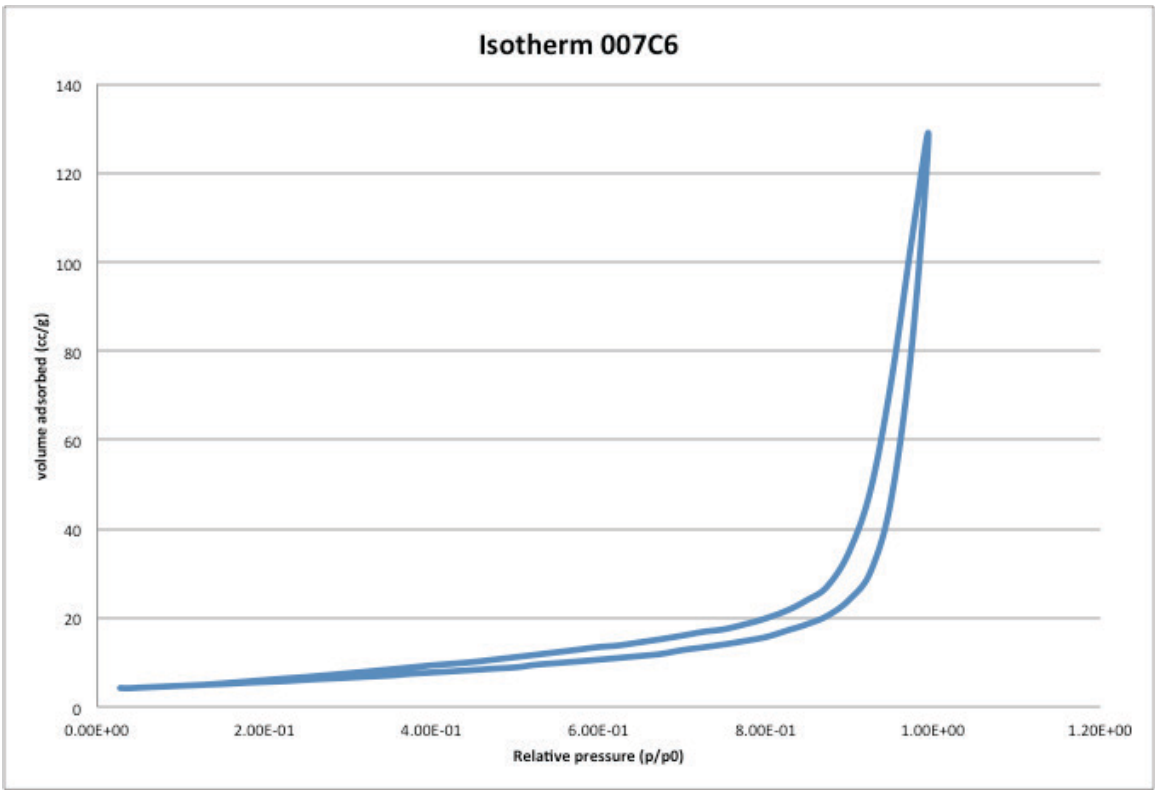

Figure 143 isotherm of sample 007C6 synthesized from cerium hydroxide, CTAB, paraffin, water, ethanol, dichloromethane, and sodium hydroxide, calcinated at 873K

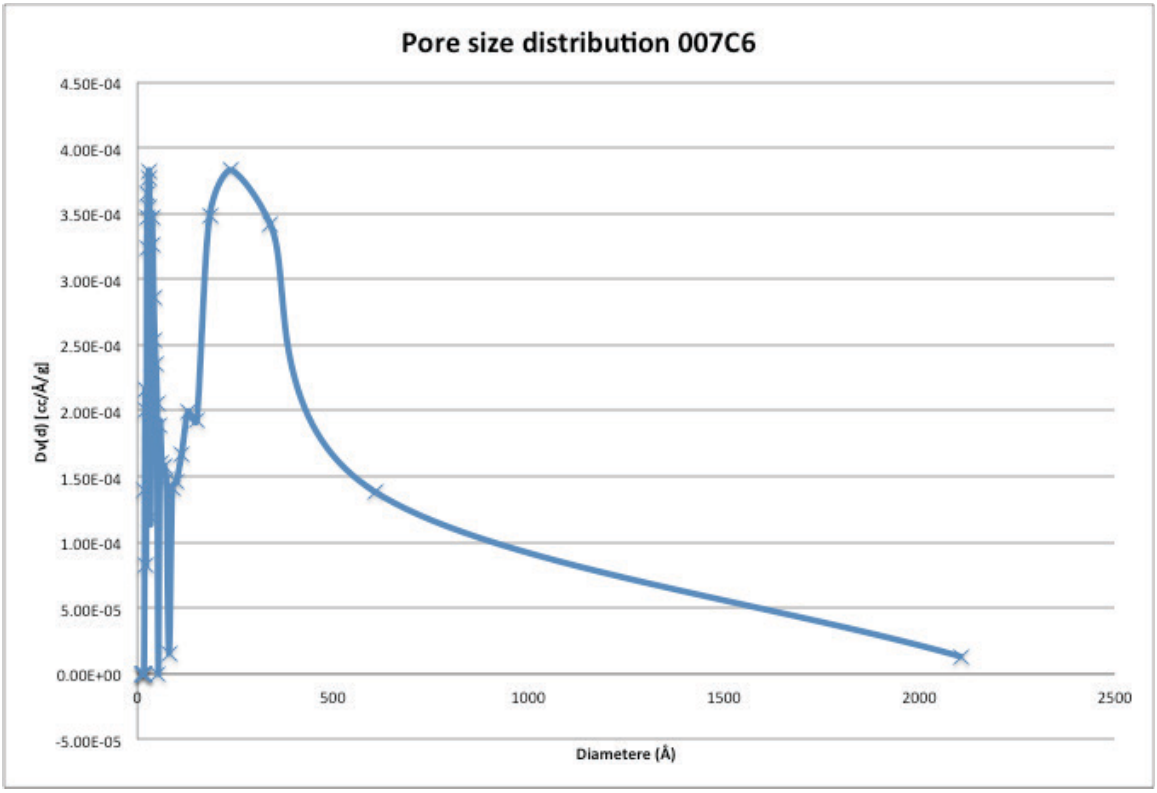

Figure 144 pore size distribution of sample 007C6 synthesized from cerium hydroxide, CTAB, paraffin, water, ethanol, dichloromethane, and sodium hydroxide, calcinated at 873K

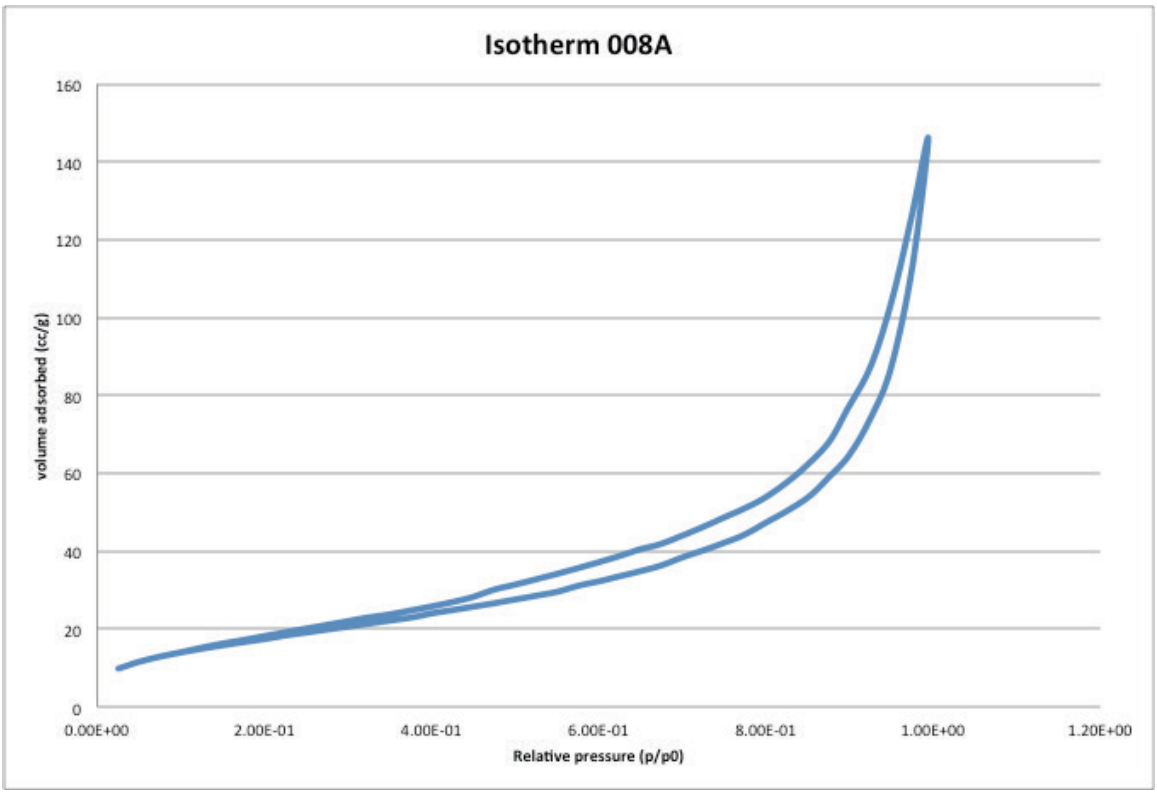

Figure 145 isotherm of sample 008A synthesized from cerium hydroxide, CTAB, paraffin, water, ethanol, and sodium hydroxide, uncalcinated

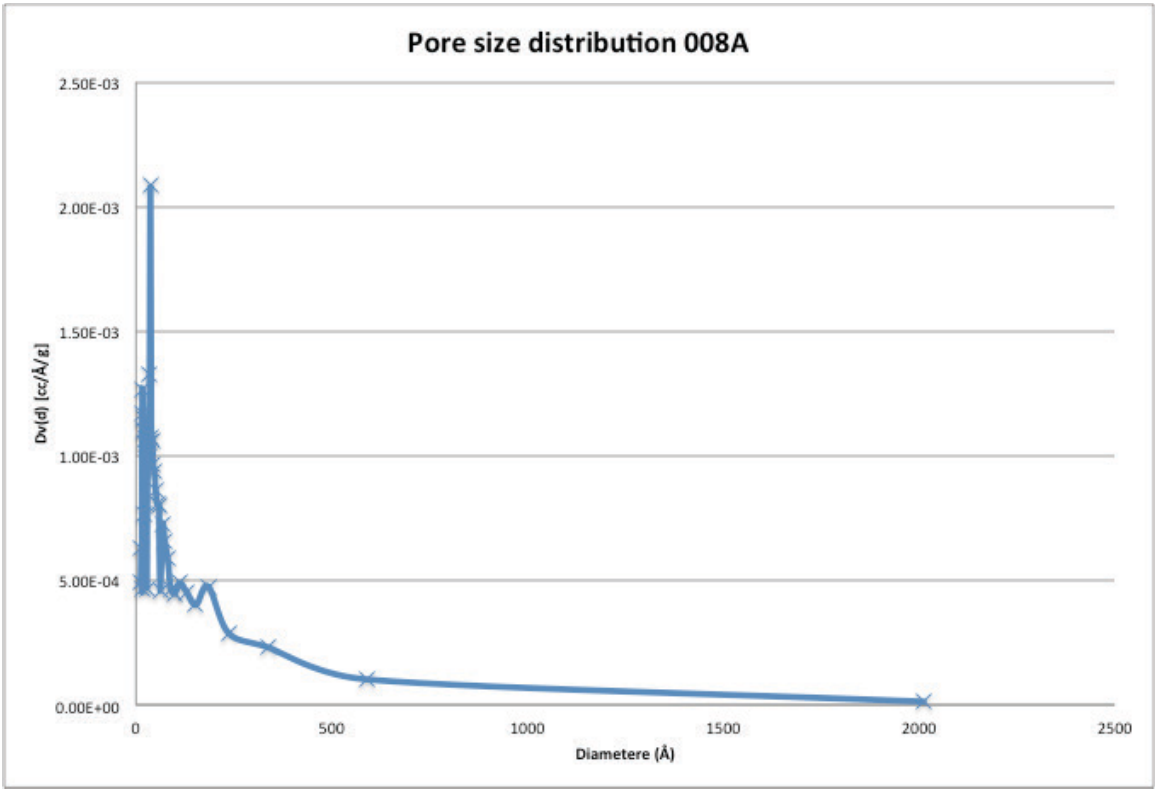

Figure 146 pore size distribution of sample 008A synthesized from cerium hydroxide, CTAB, paraffin, water, ethanol, and sodium hydroxide, uncalcinated

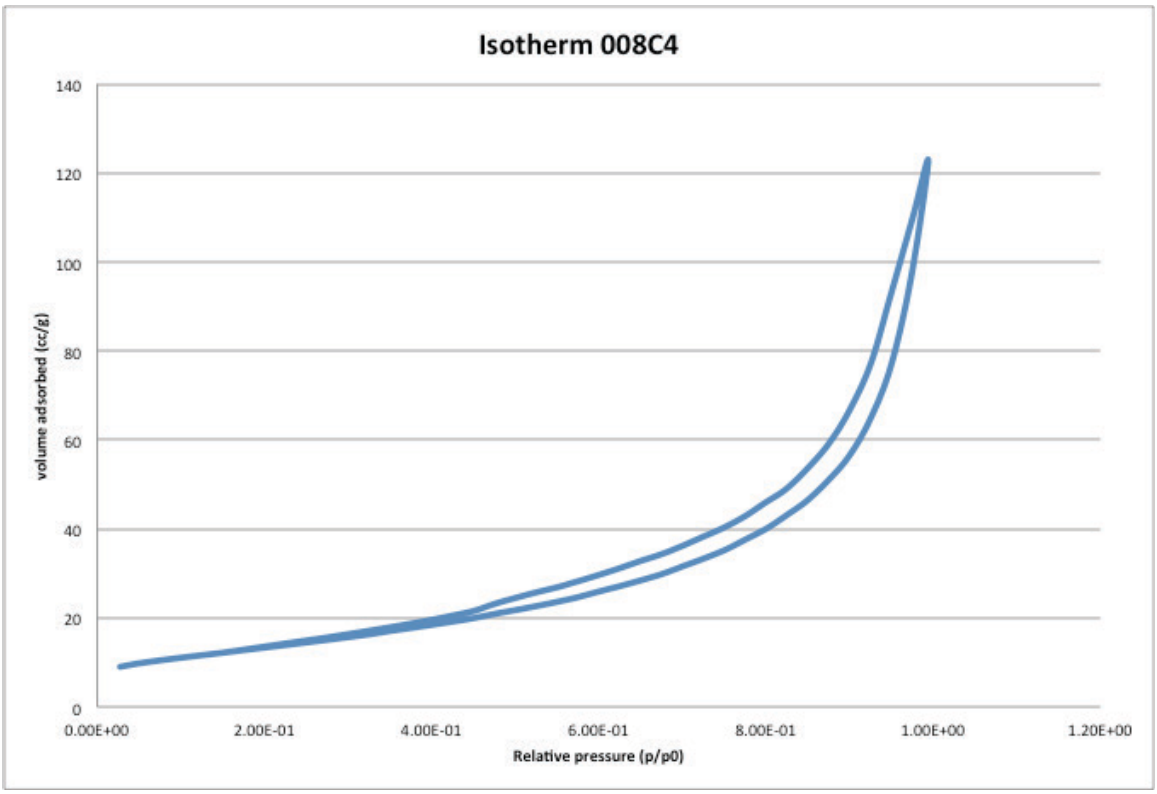

Figure 147 isotherm of sample 008C4 synthesized from cerium hydroxide, CTAB, paraffin, water, ethanol, and sodium hydroxide, calcinated at 673K

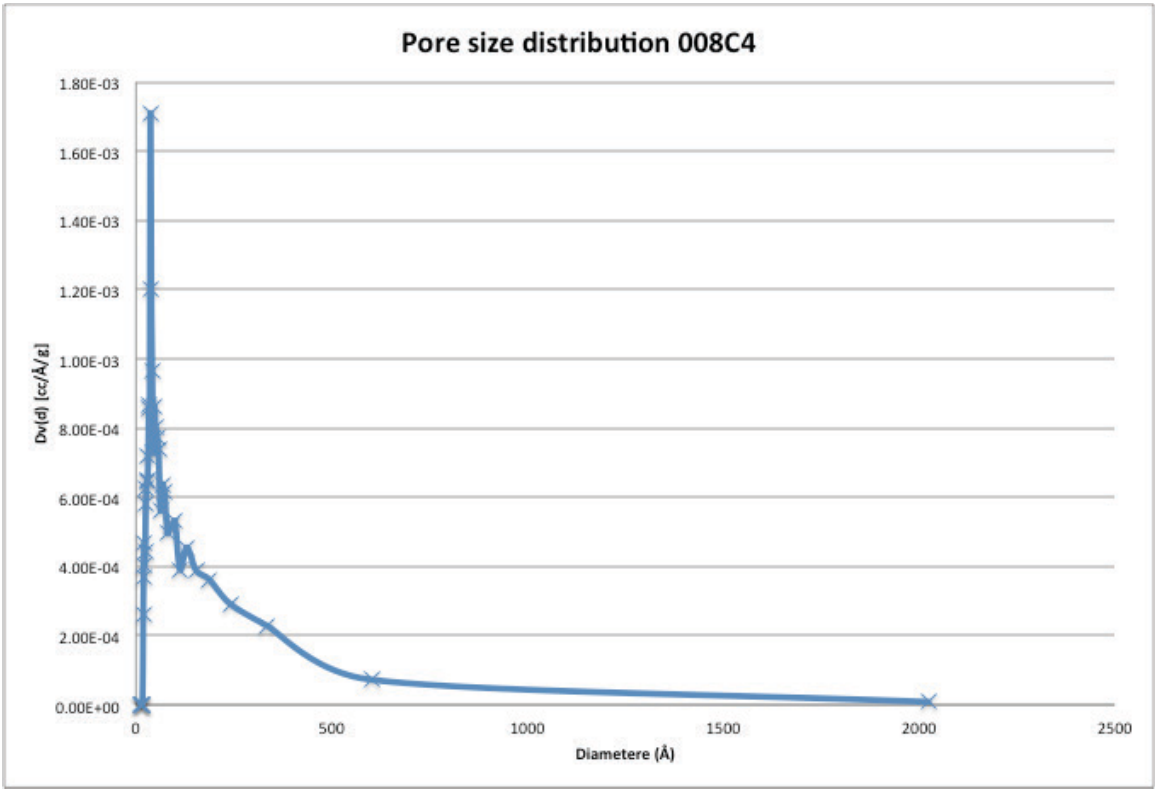

Figure 148 pore size distribution of sample 008C4 synthesized from cerium hydroxide, CTAB, paraffin, water, ethanol, and sodium hydroxide, calcinated at 673K

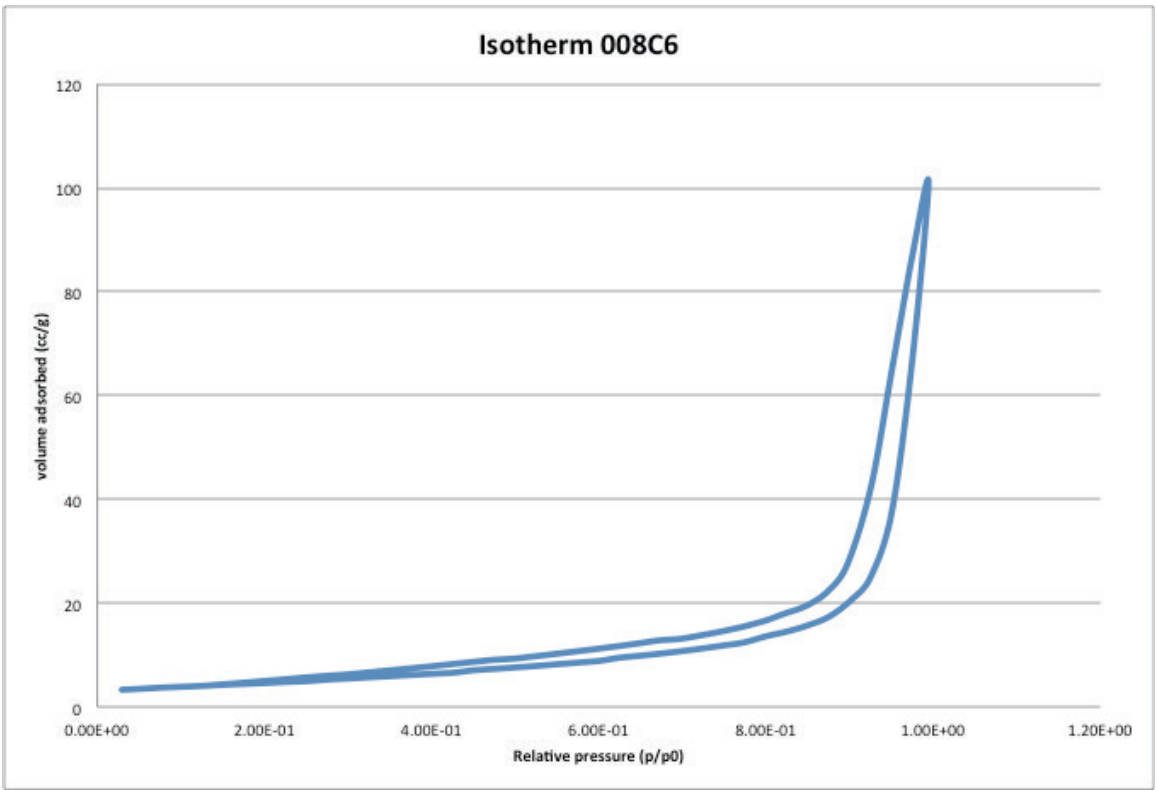

Figure 149 isotherm of sample 008C6 synthesized from cerium hydroxide, CTAB, paraffin, water, ethanol, and sodium hydroxide, calcinated at 873K

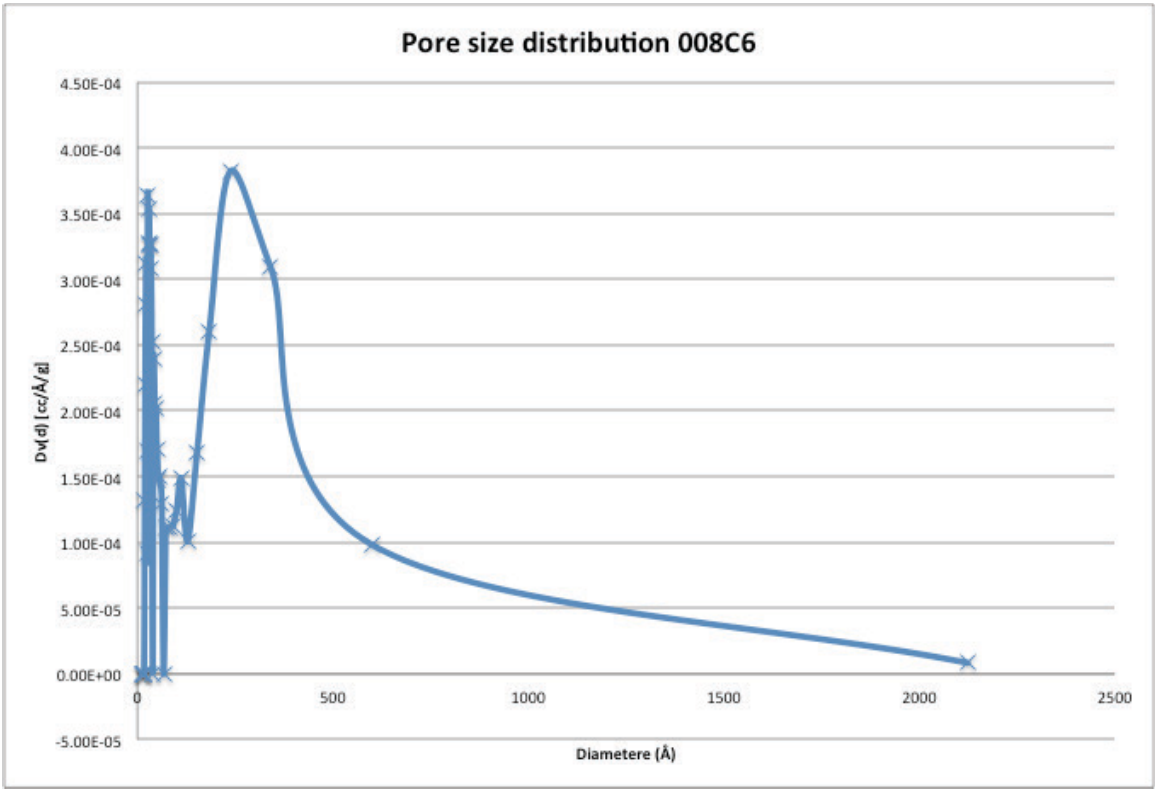

Figure 150 pore size distribution of sample 008C6 synthesized from cerium hydroxide, CTAB, paraffin, water, ethanol, and sodium hydroxide, calcinated at 873K

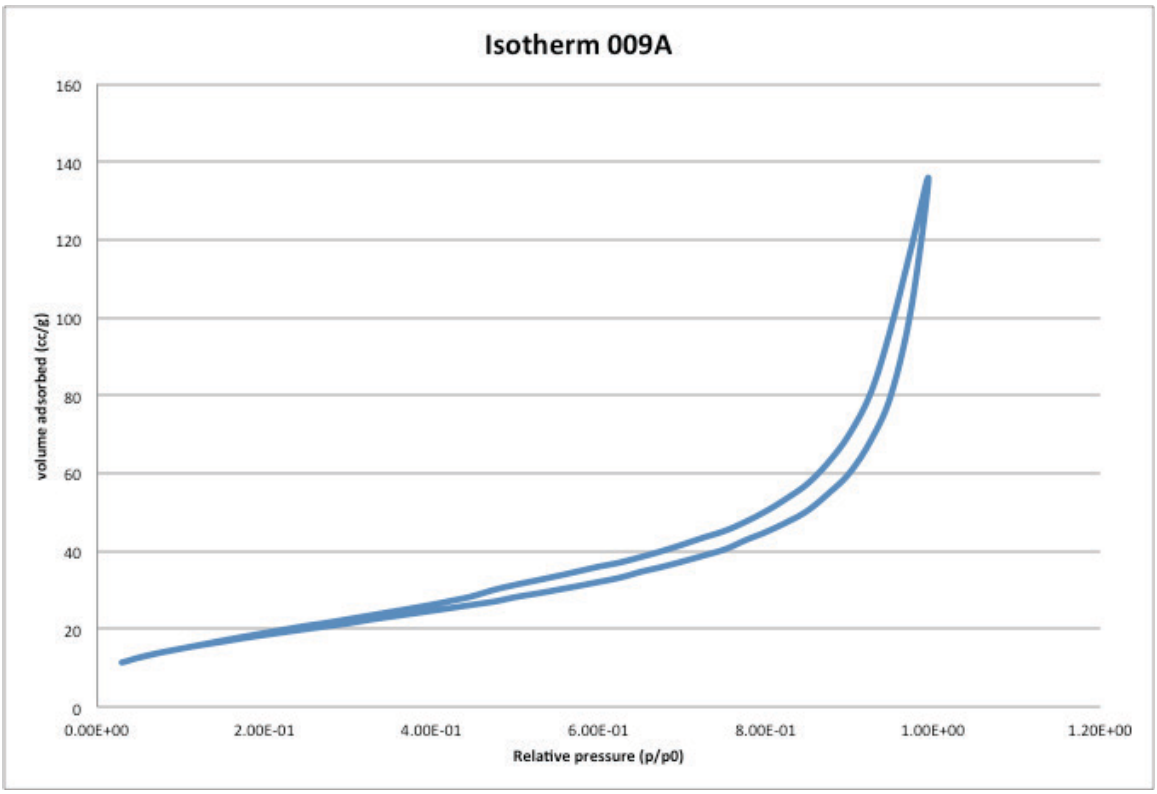

Figure 151 isotherm of sample 009A synthesized from cerium hydroxide, SDS, water, ethanol, and sodium hydroxide, uncalcinated

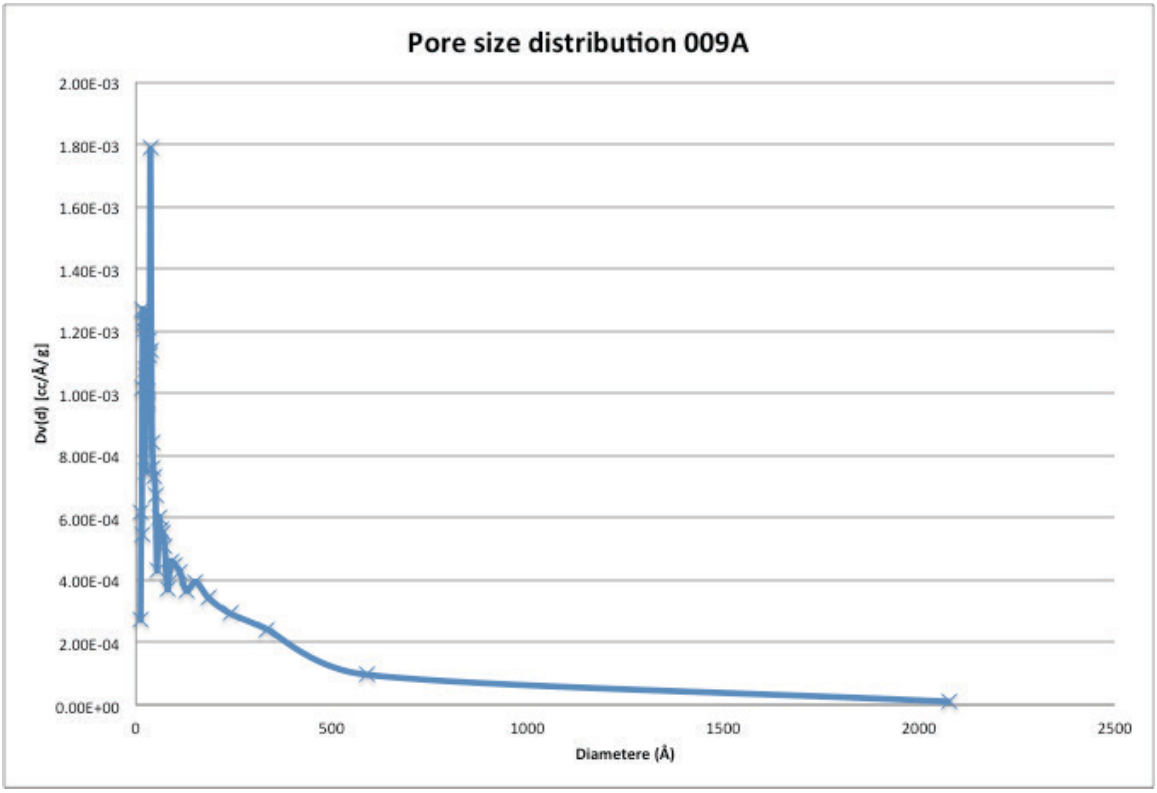

Figure 152 pore size distribution of sample 009A synthesized from cerium hydroxide, SDS, water, ethanol, and sodium hydroxide, uncalcinated

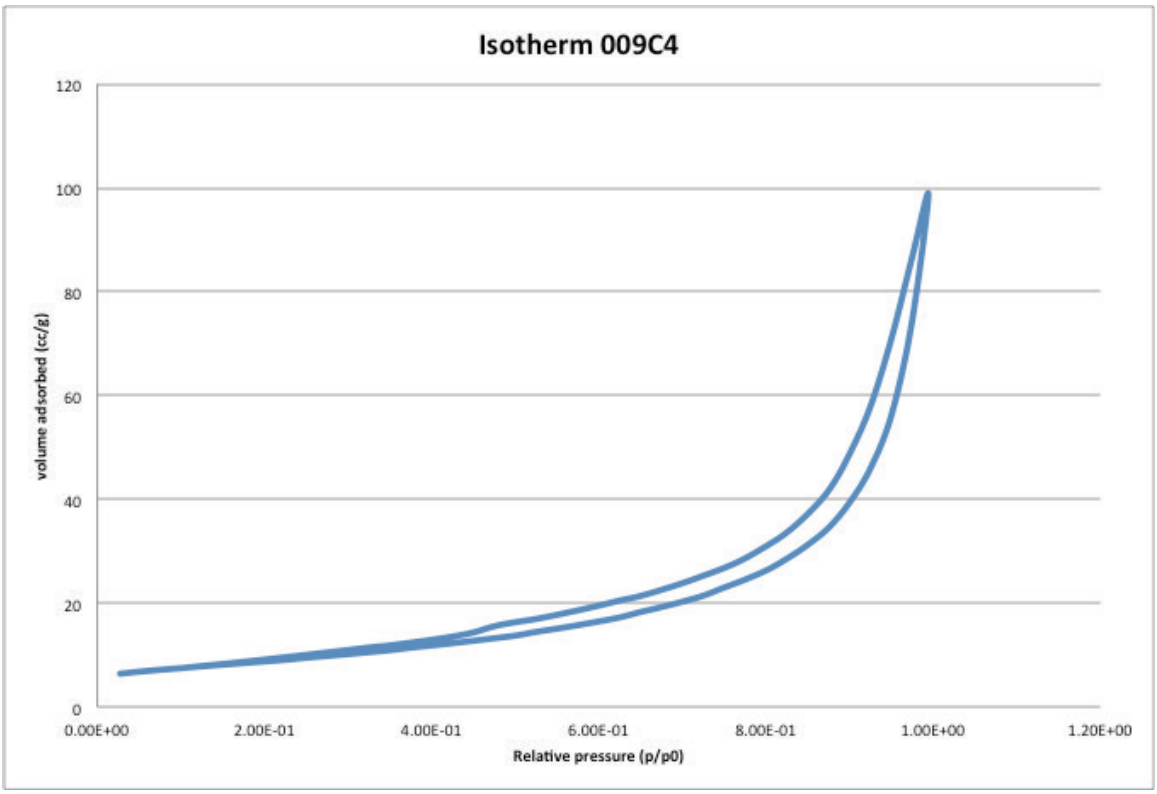

Figure 153 isotherm of sample 009C4 synthesized from cerium hydroxide, SDS, water, ethanol, and sodium hydroxide, calcinated at 673K

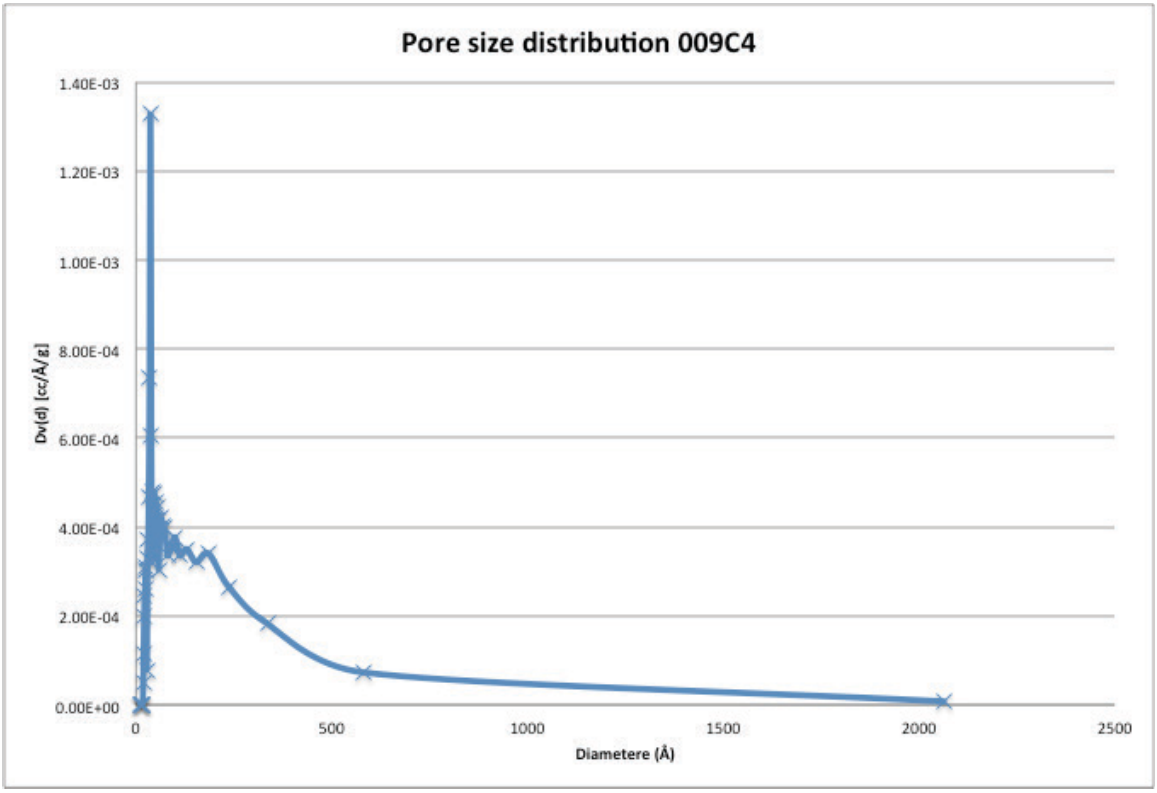

Figure 154 pore size distribution of sample 009C4 synthesized from cerium hydroxide, SDS, water, ethanol, and sodium hydroxide, calcinated at 673K

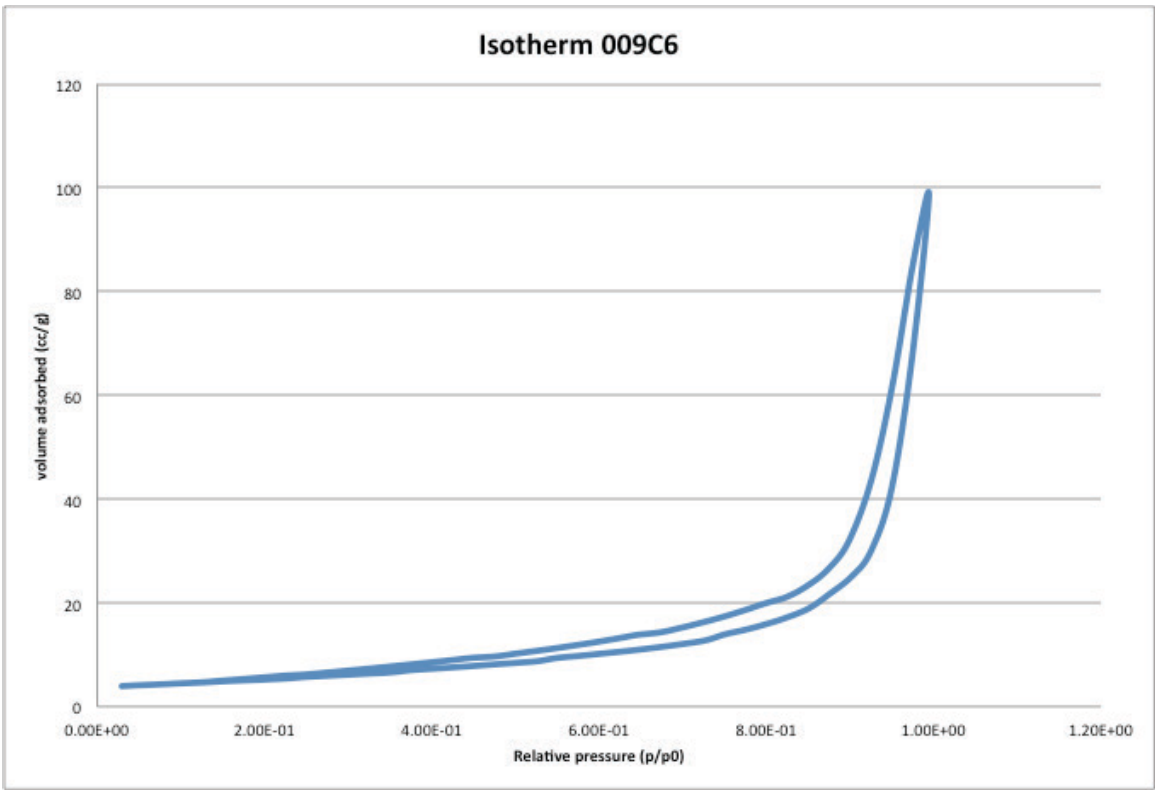

Figure 155 isotherm of sample 009C6 synthesized from cerium hydroxide, SDS, water, ethanol, and sodium hydroxide, calcinated at 873K

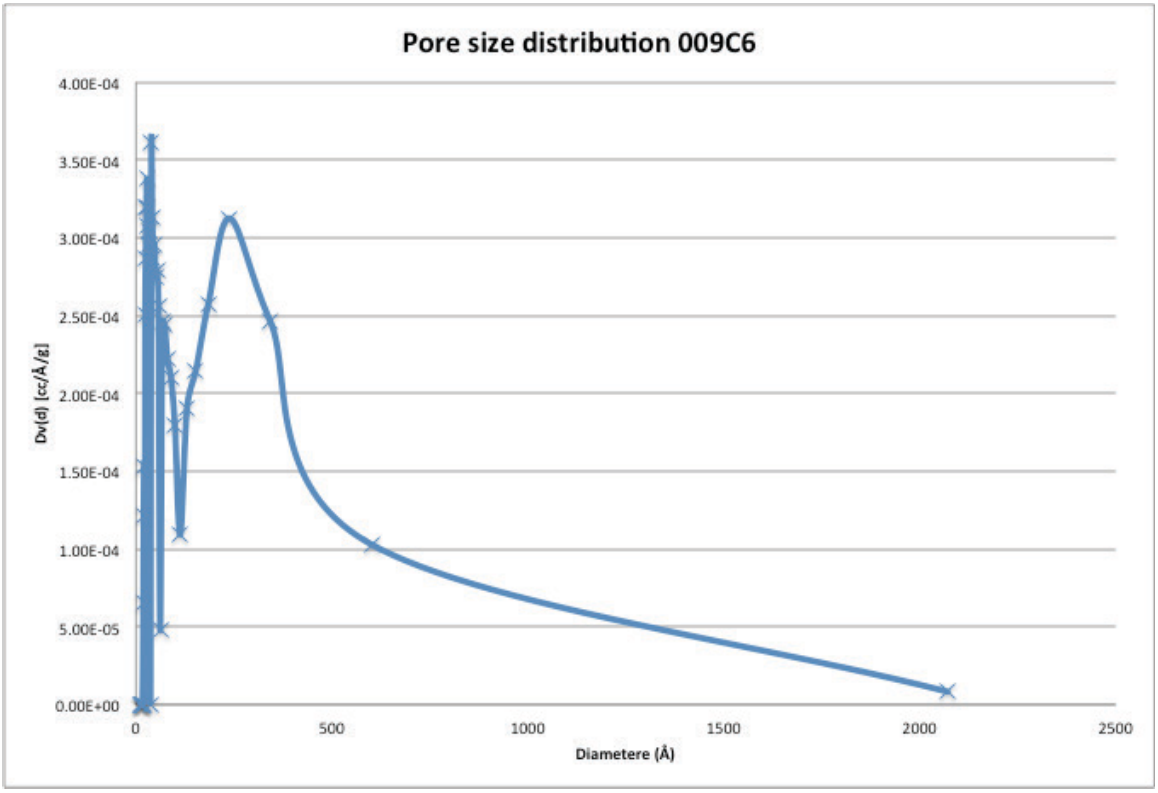

Figure 156 pore size distribution of sample 009C6 synthesized from cerium hydroxide, SDS, water, ethanol, and sodium hydroxide, calcinated at 873K

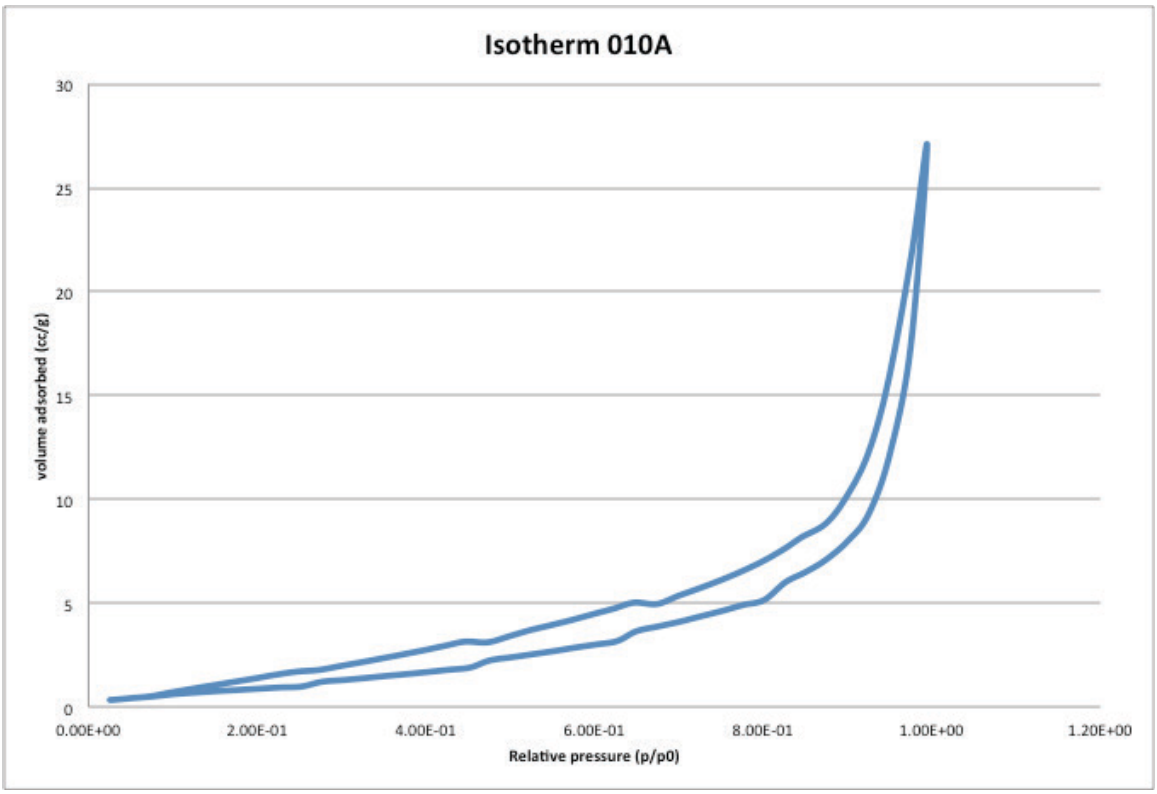

Figure 157 isotherm of sample 010A synthesized from cerium hydroxide, CTAB/SDS, water, ethanol, and sodium hydroxide, uncalcinated

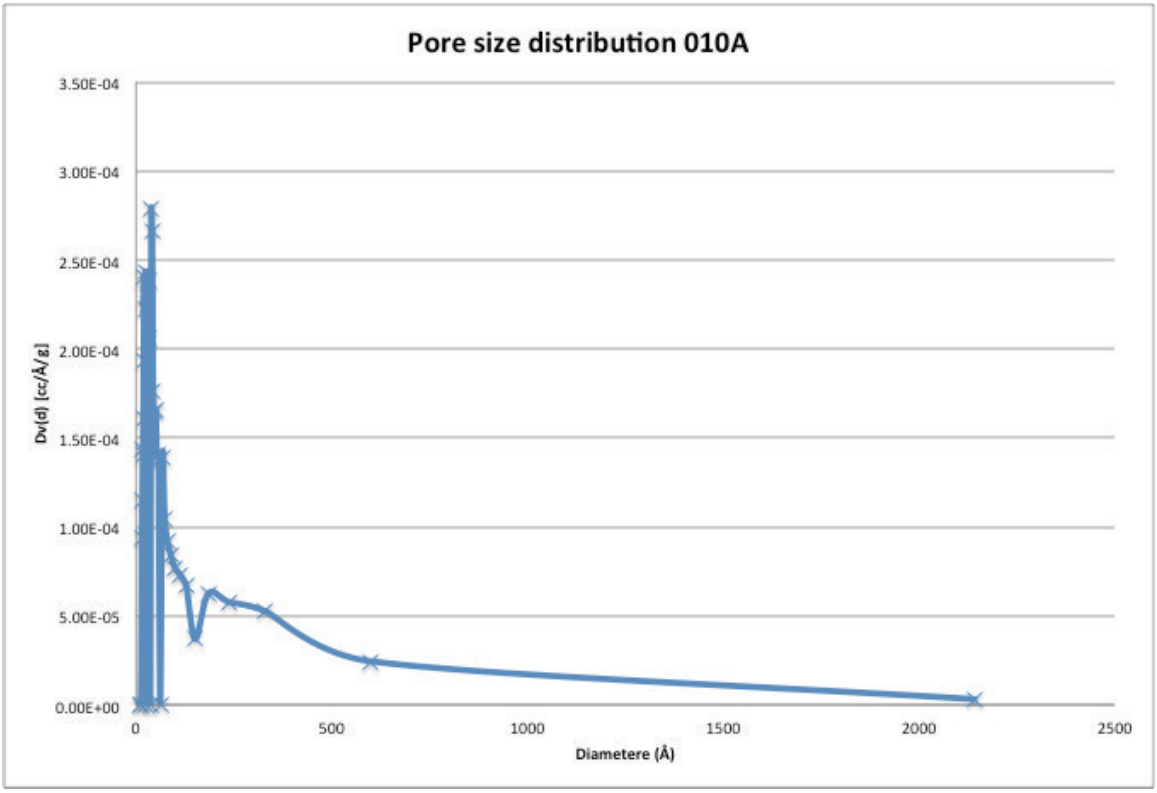

Figure 158 pore size distribution of sample 010A synthesized from cerium hydroxide, CTAB/SDS, water, ethanol, and sodium hydroxide, uncalcinated

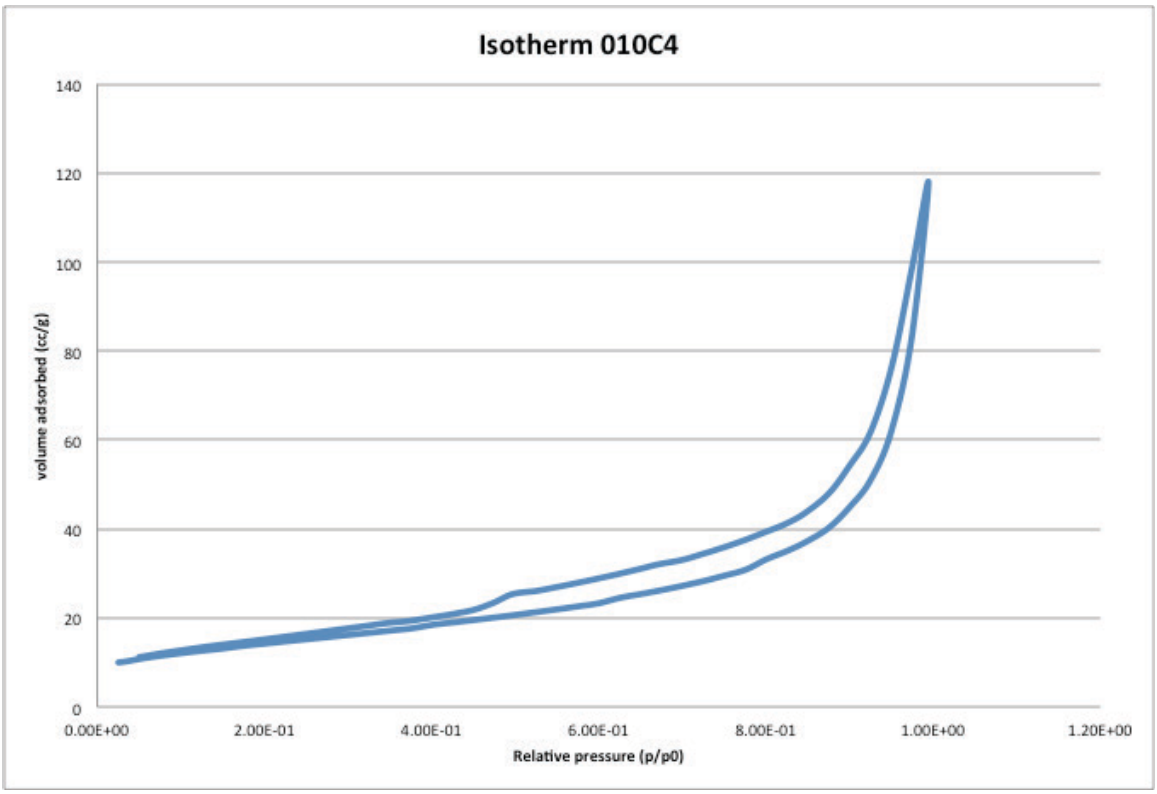

Figure 159 isotherm of sample 010C4 synthesized from cerium hydroxide, CTAB/SDS, water, ethanol, and sodium hydroxide, calcinated at 673K

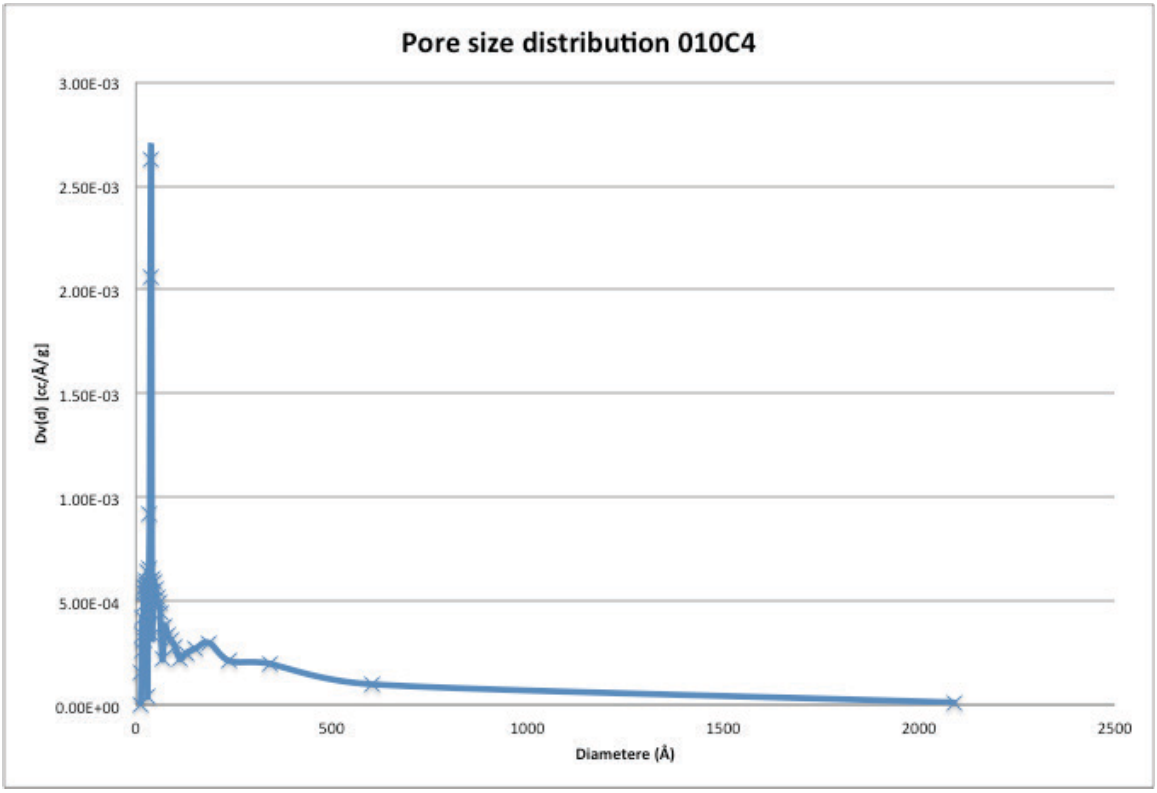

Figure 160 pore size distribution of sample 010C4 synthesized from cerium hydroxide, CTAB/SDS, water, ethanol, and sodium hydroxide, calcinated at 673K

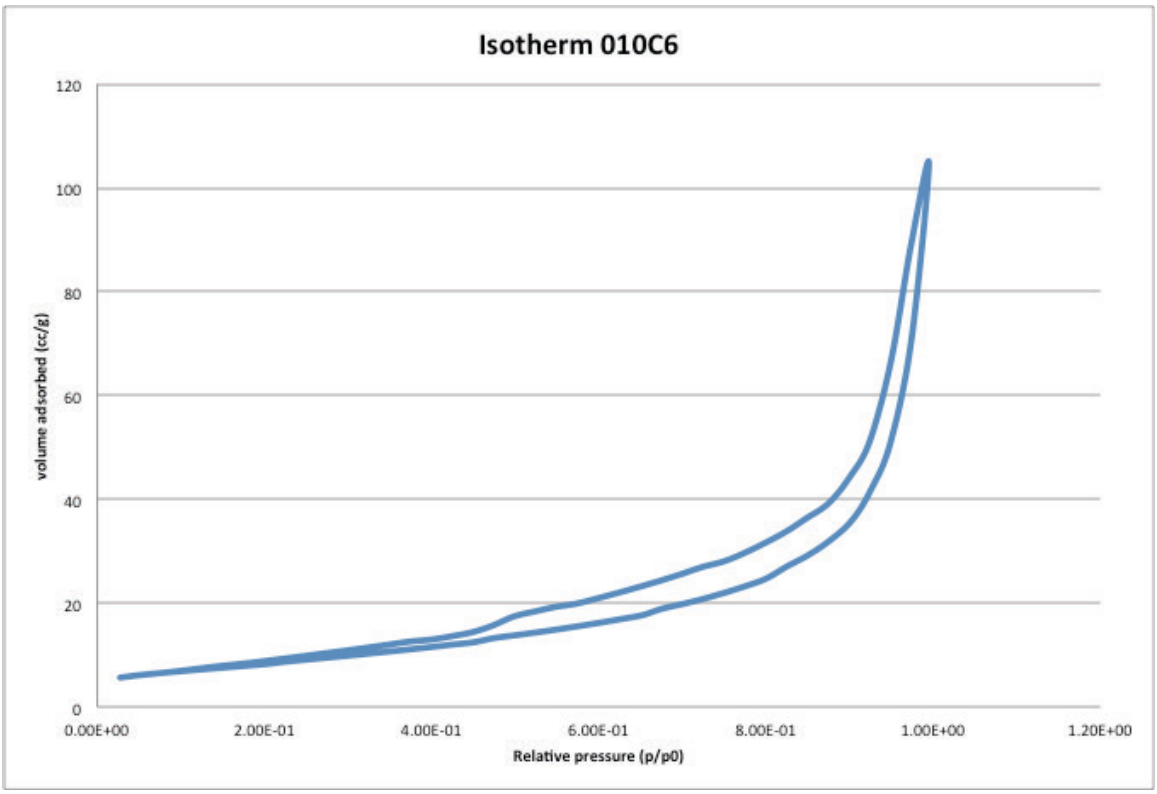

Figure 161 isotherm of sample 010C6 synthesized from cerium hydroxide, CTAB/SDS, water, ethanol, and sodium hydroxide, calcinated at 873K

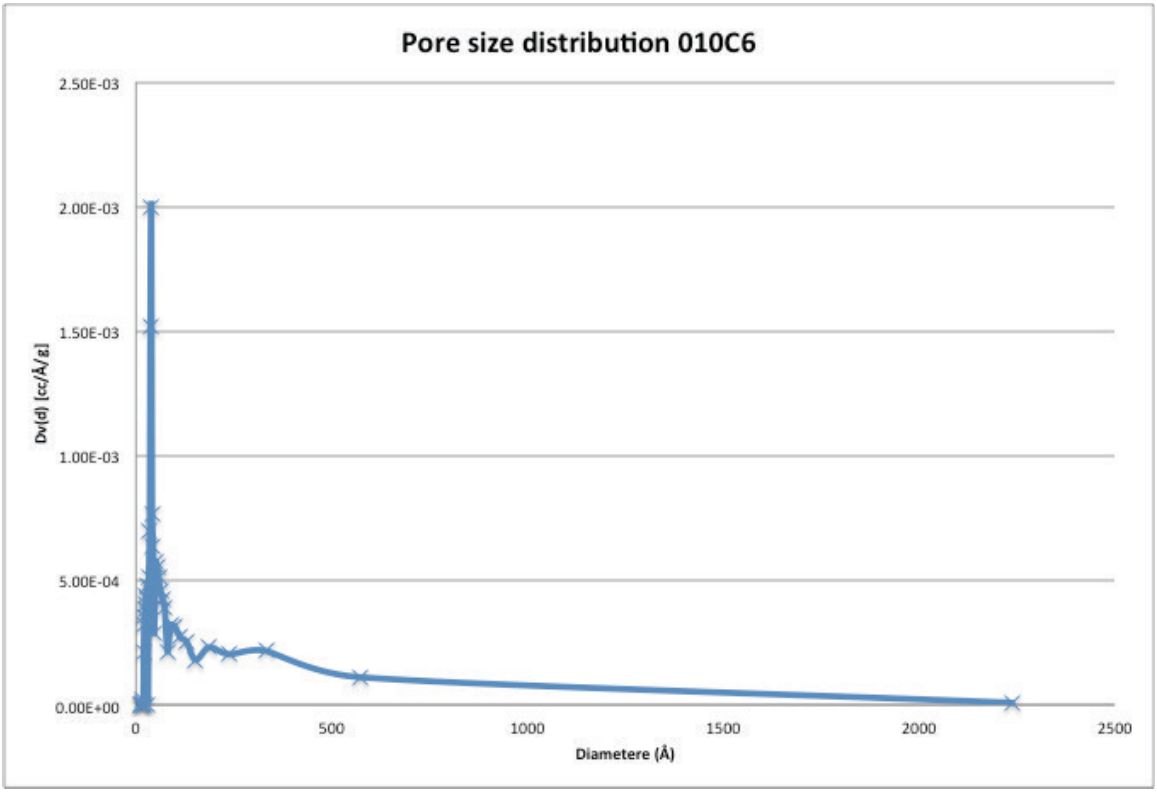

Figure 162 pore size distribution of sample 010C6 synthesized from cerium hydroxide, CTAB/SDS, water, ethanol, and sodium hydroxide, calcinated at 873K

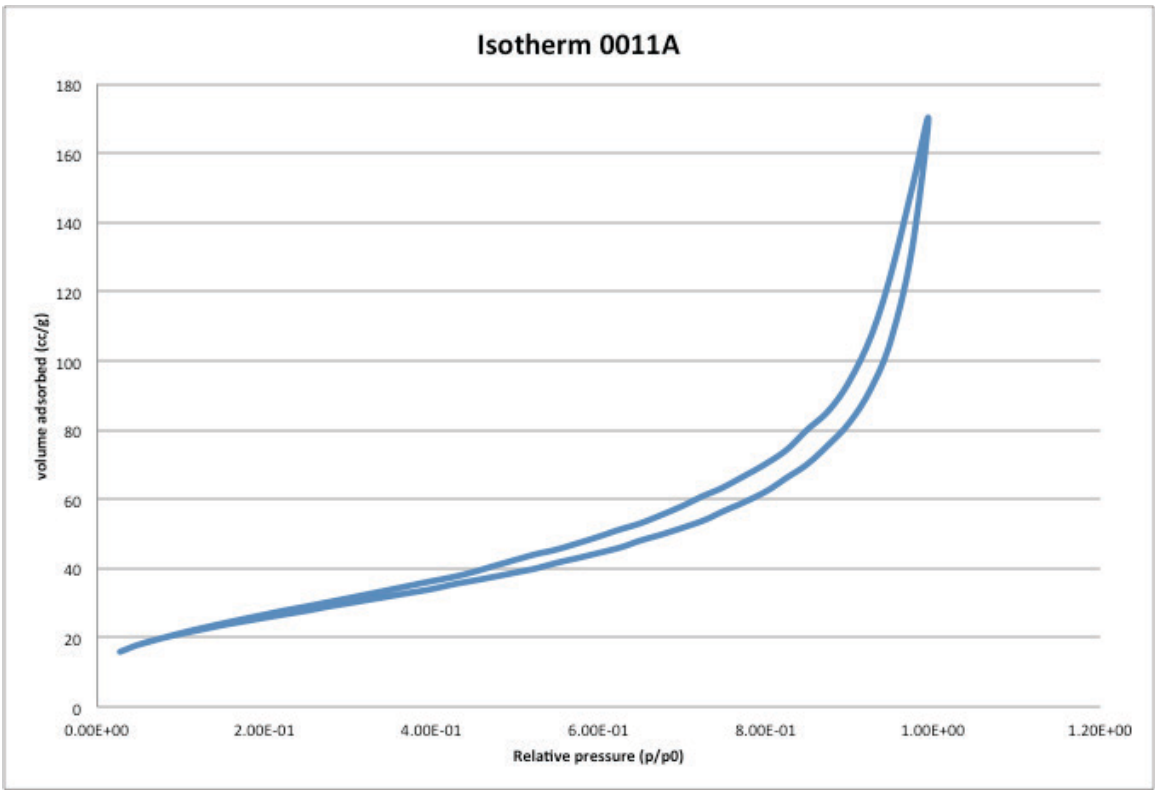

Figure 163 isotherm of sample 011A synthesized from cerium hydroxide, CTAB, toluene, pyridine, uncalcinated

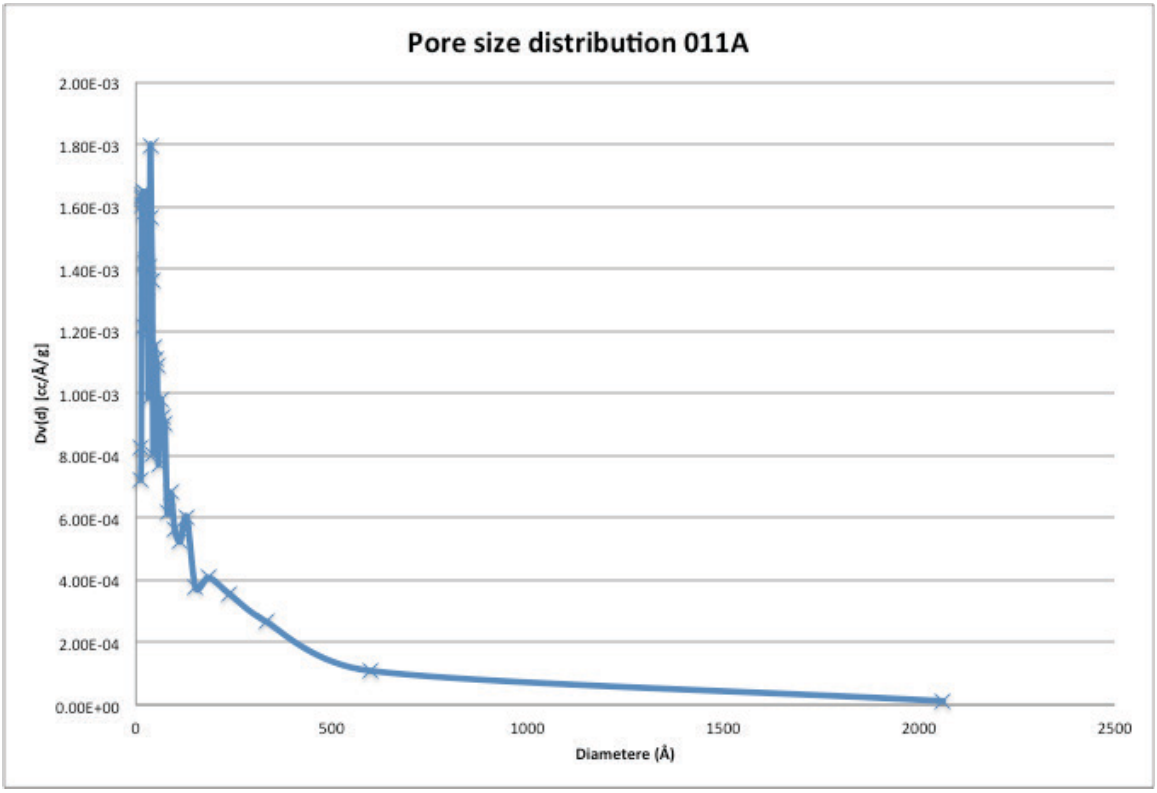

Figure 164 pore size distribution of sample 011A synthesized from cerium hydroxide, CTAB, toluene, pyridine, uncalcinated

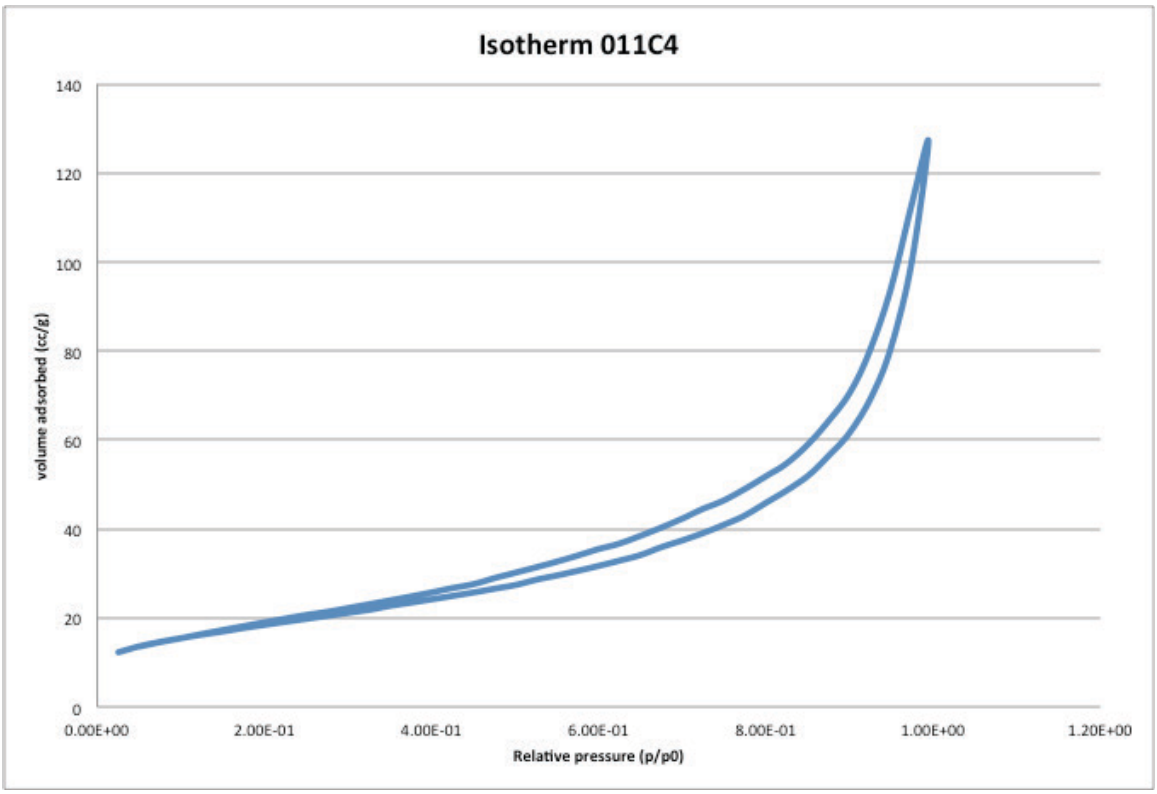

Figure 165 isotherm of sample 011C4 synthesized from cerium hydroxide, CTAB, toluene, pyridine, calcinated at 673K

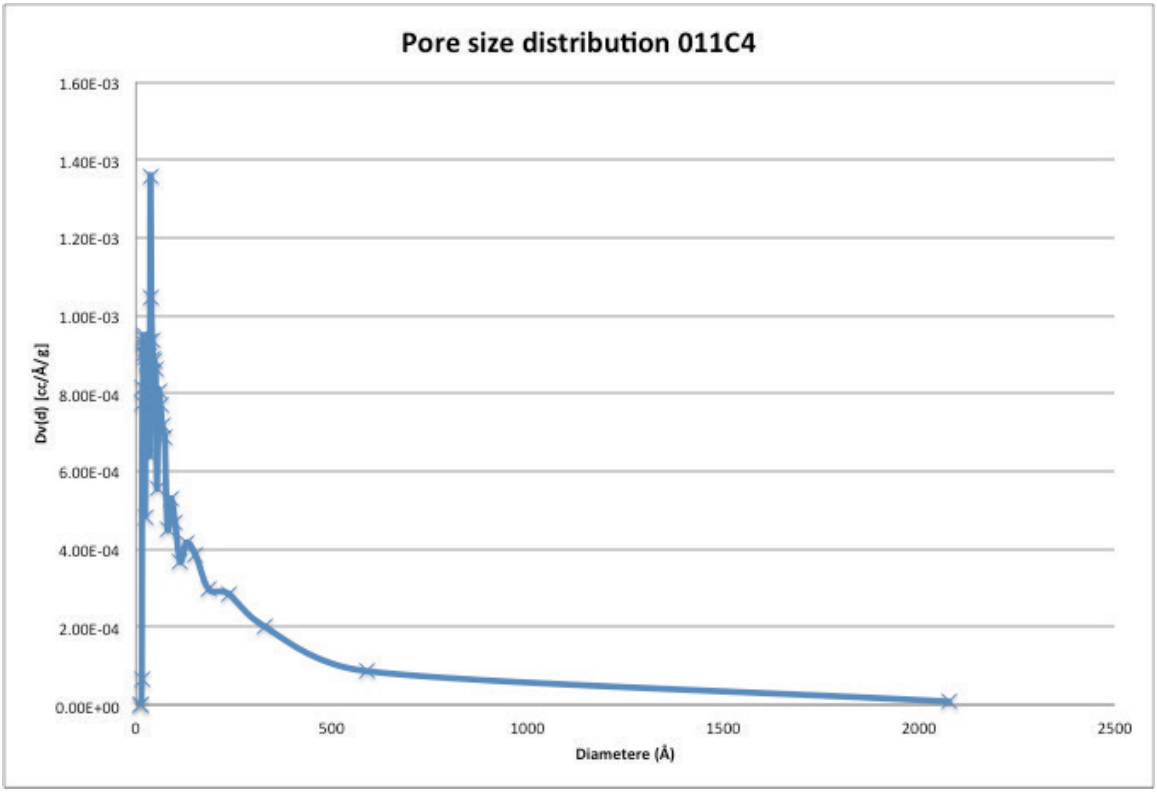

Figure 166 pore size distribution of sample 011C4 synthesized from cerium hydroxide, CTAB, toluene, pyridine, calcinated at 673K

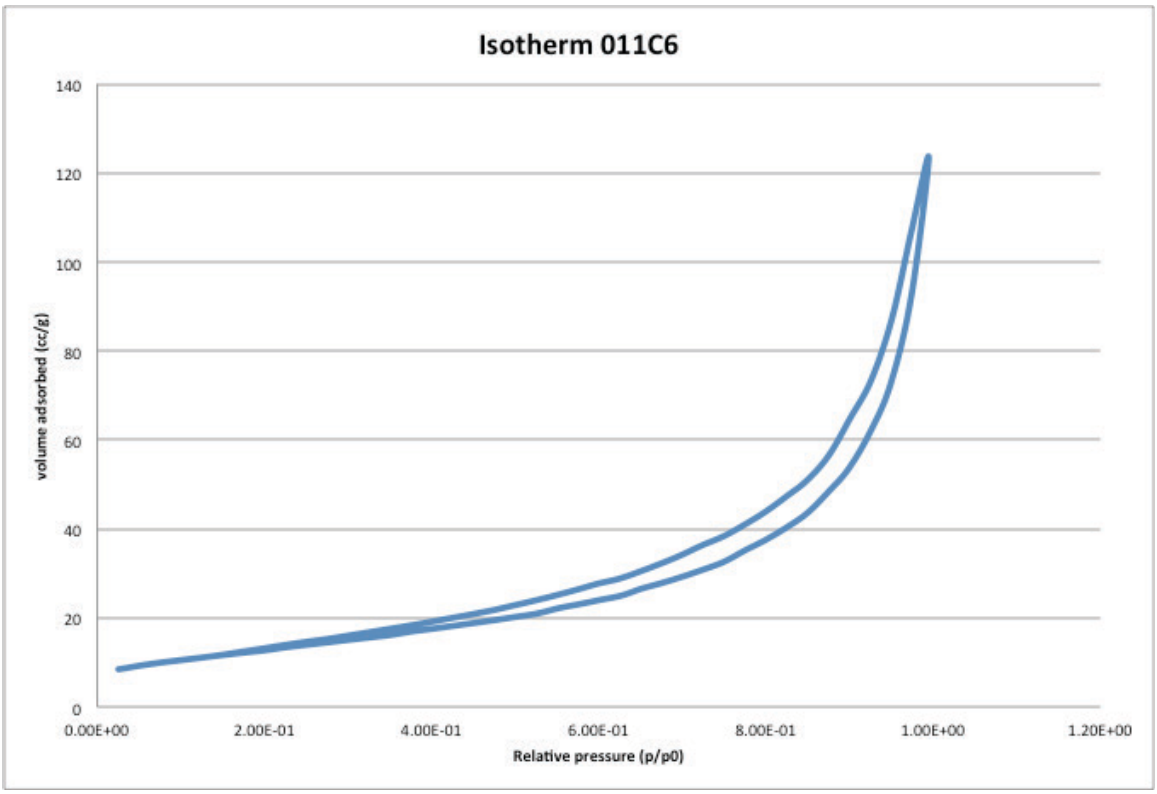

Figure 167 isotherm of sample 011C6 synthesized from cerium hydroxide, CTAB, toluene, pyridine, calcinated at 873K

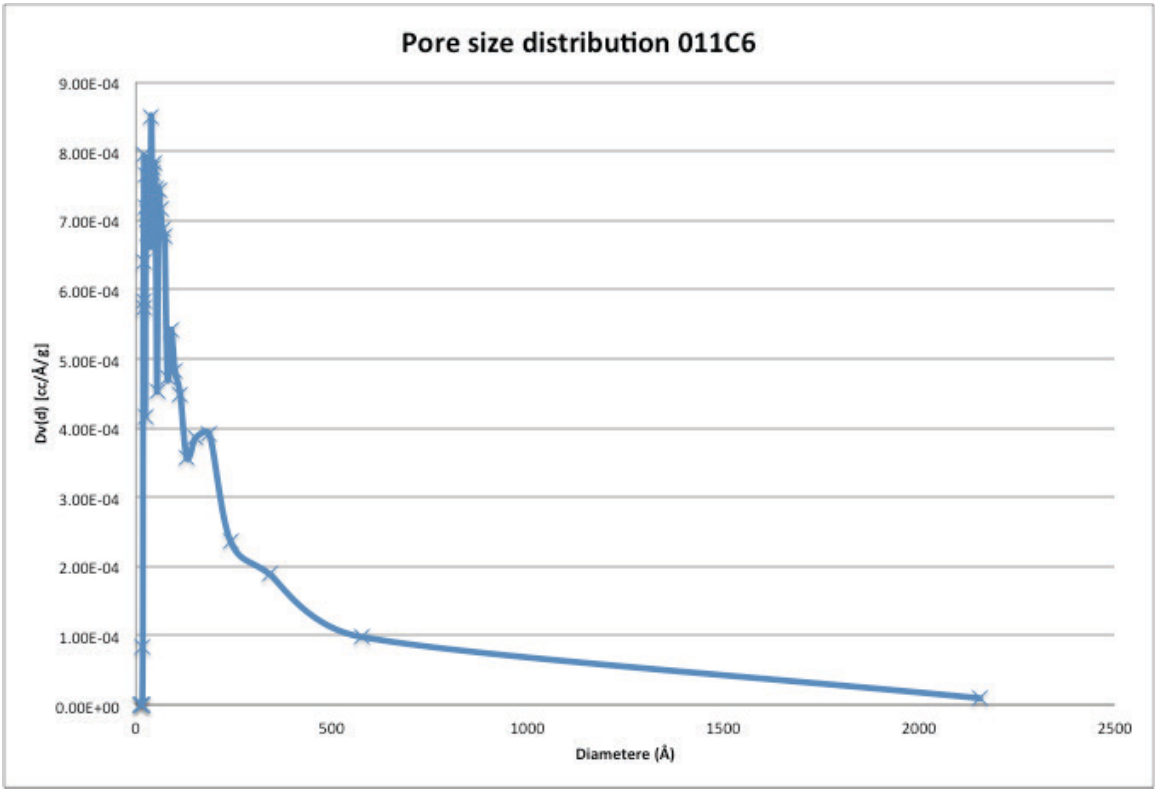

Figure 168 pore size distribution of sample 011C6 synthesized from cerium hydroxide, CTAB, toluene, pyridine, calcinated at 873K

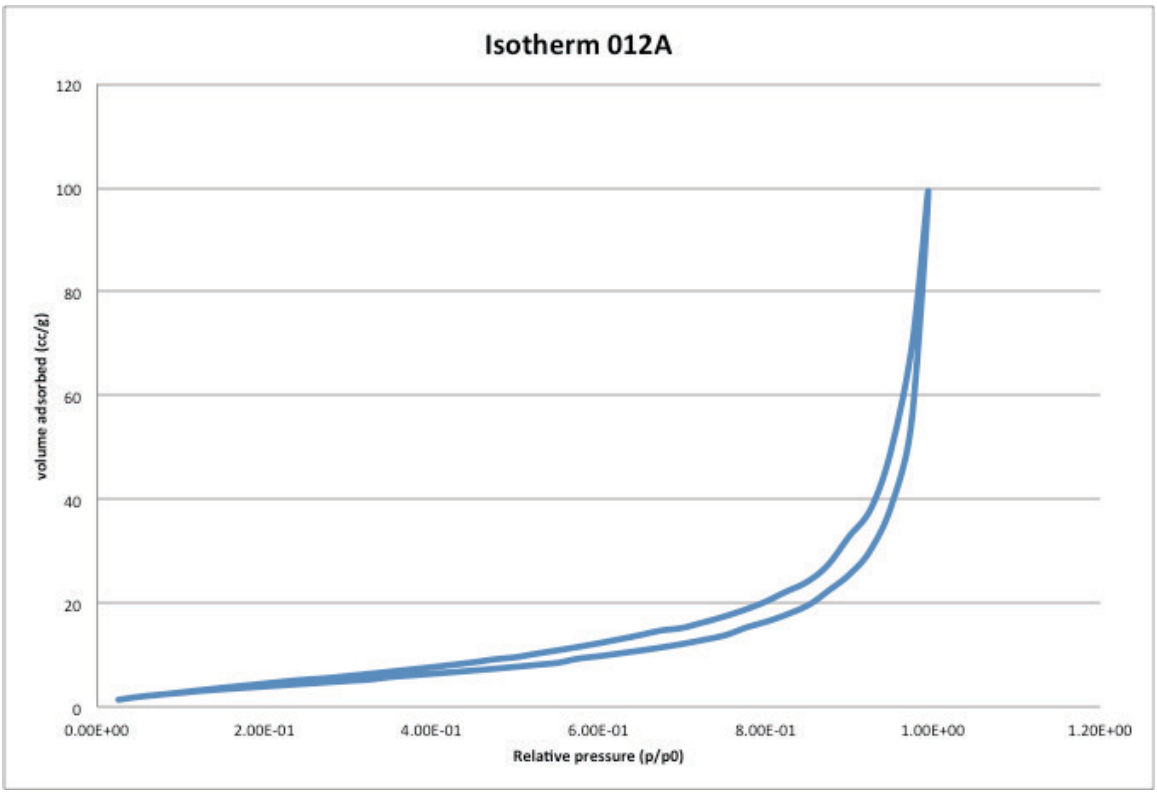

Figure 169 isotherm of sample 012A synthesized from cerium hydroxide, CTAB (300mM), water, ethanol, and sodium hydroxide, uncalcinated

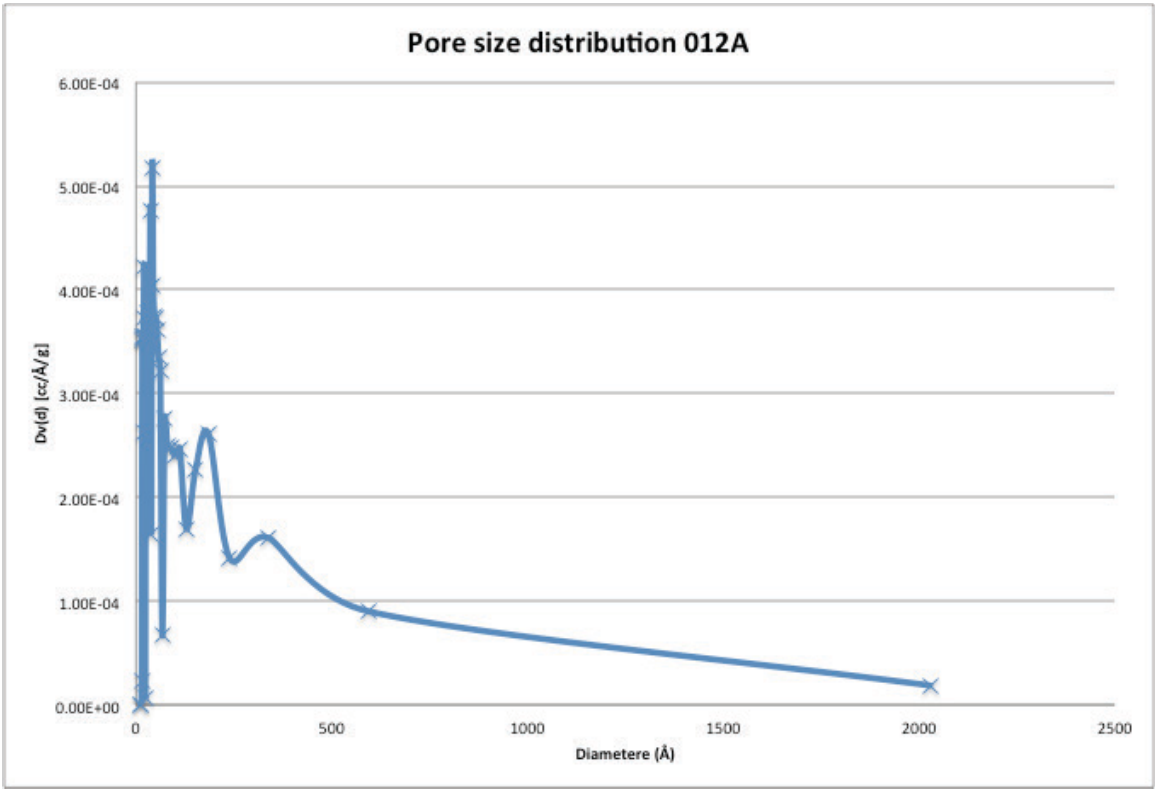

Figure 170 pore size distribution of sample 012A synthesized from cerium hydroxide, CTAB (300mM), water, ethanol, and sodium hydroxide, uncalcinated

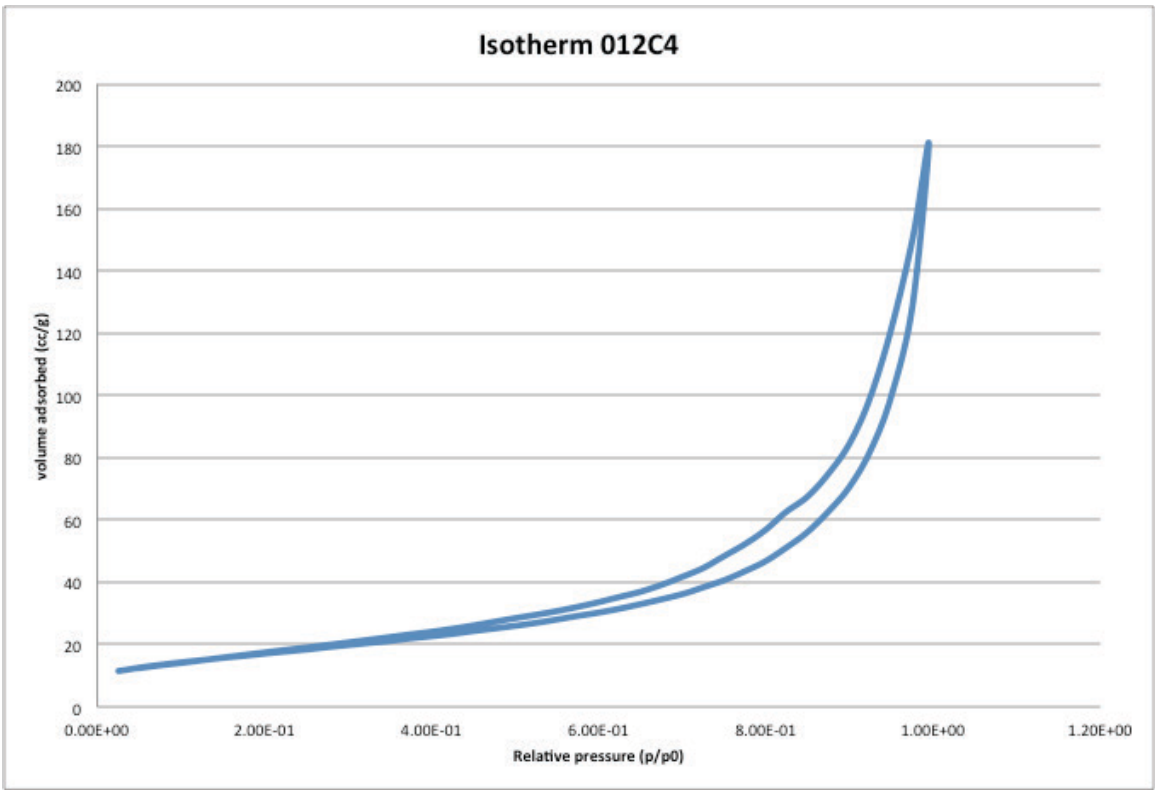

Figure 171 isotherm of sample 012C4 synthesized from cerium hydroxide, CTAB (300mM), water, ethanol, and sodium hydroxide, calcinated at 673K

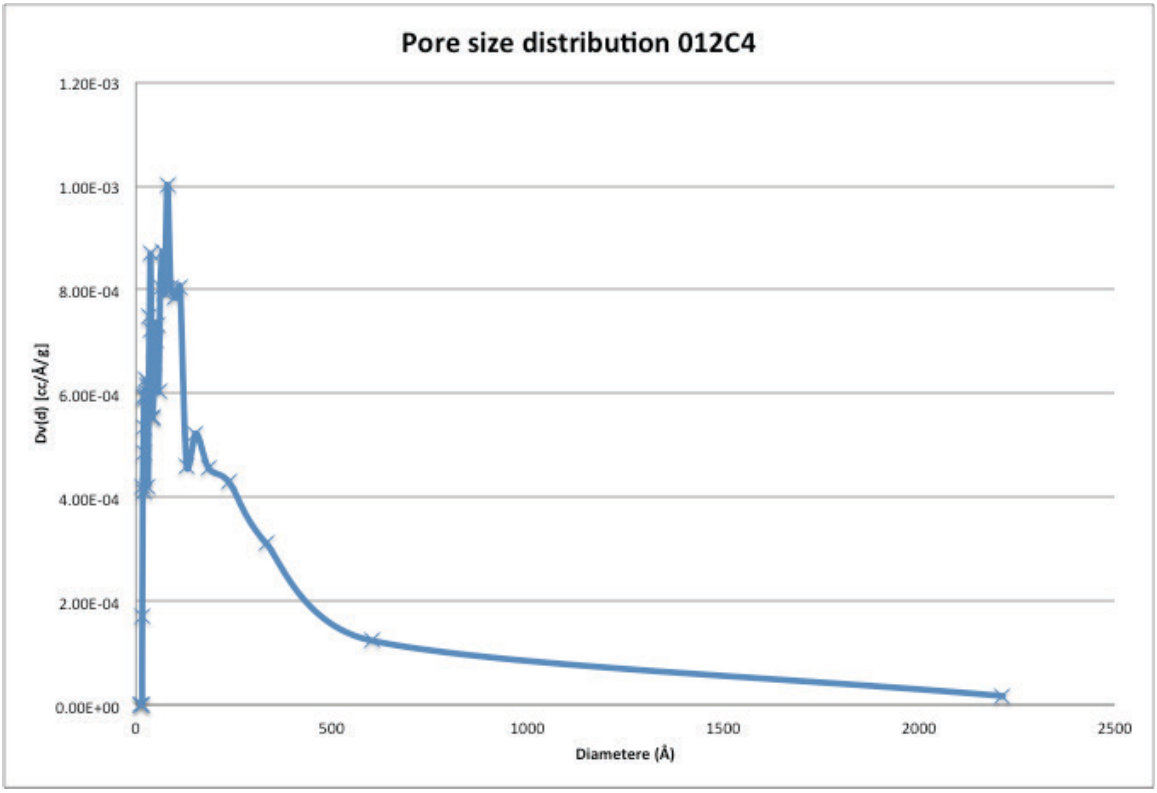

Figure 172 pore size distribution of sample 012C4 synthesized from cerium hydroxide, CTAB (300mM), water, ethanol, and sodium hydroxide, calcinated at 673K

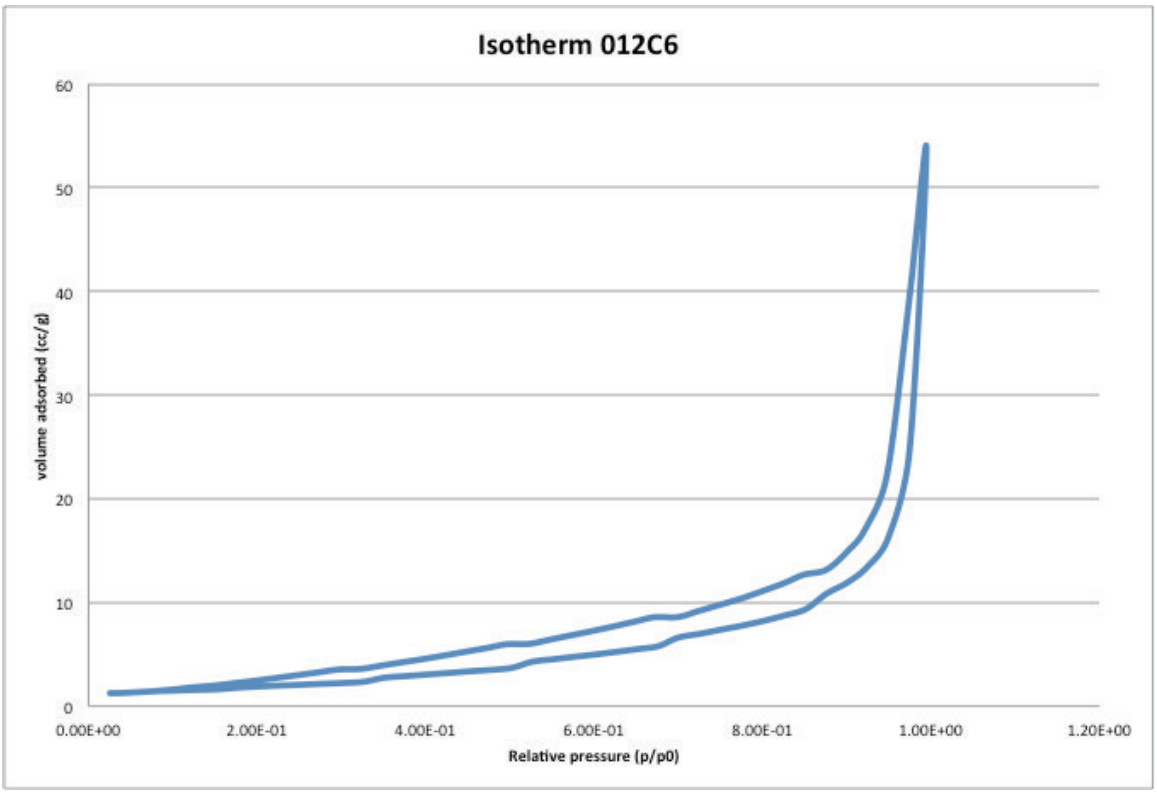

Figure 173 isotherm of sample 012C6 synthesized from cerium hydroxide, CTAB (300mM), water, ethanol, and sodium hydroxide, calcinated at 873K

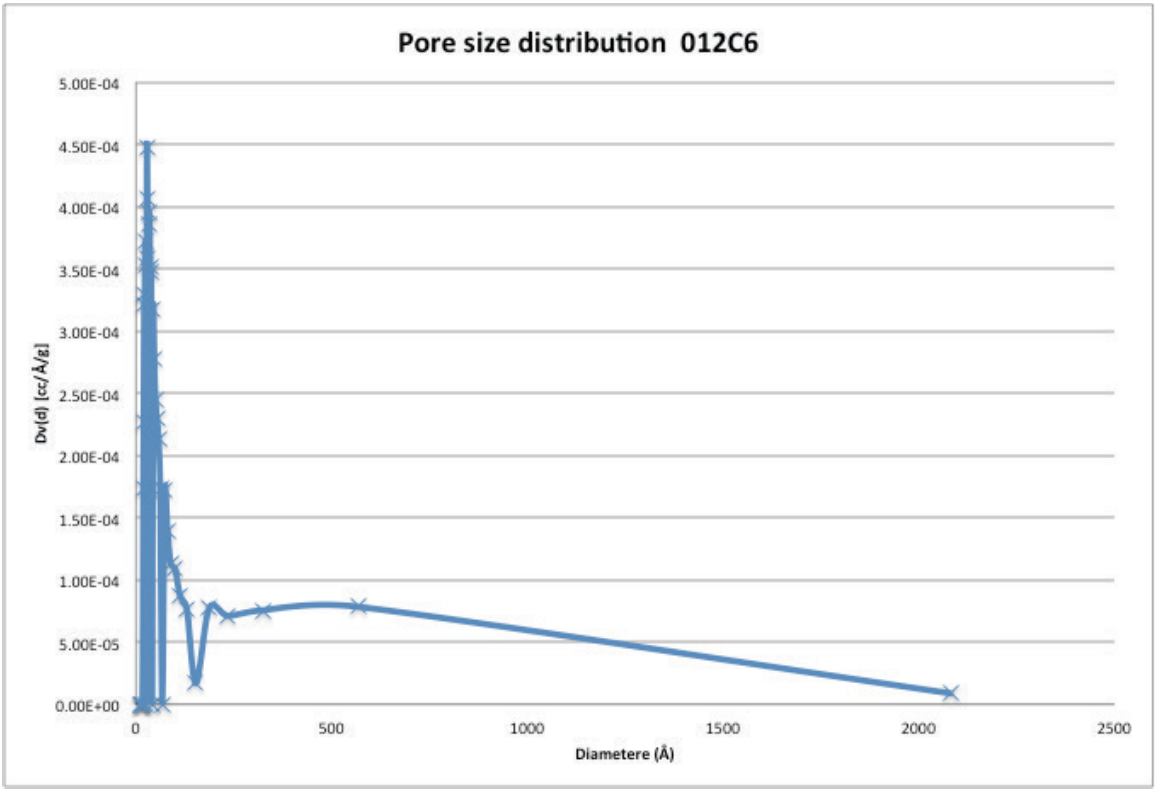

Figure 174 pore size distribution of sample 012C6 synthesized from cerium hydroxide, CTAB (300mM), water, ethanol, and sodium hydroxide, calcinated at 873K

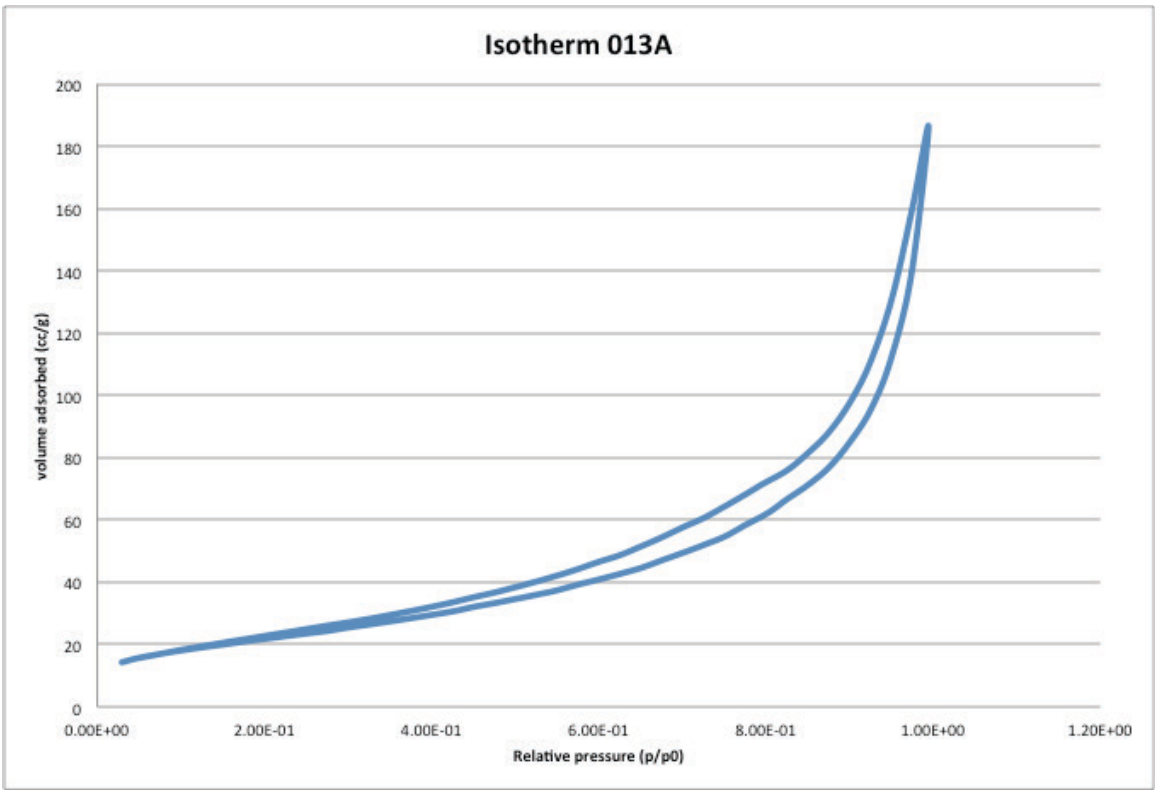

Figure 175 isotherm of sample 013A synthesized from cerium hydroxide, SDS (300mM), water, ethanol, and sodium hydroxide, uncalcinated

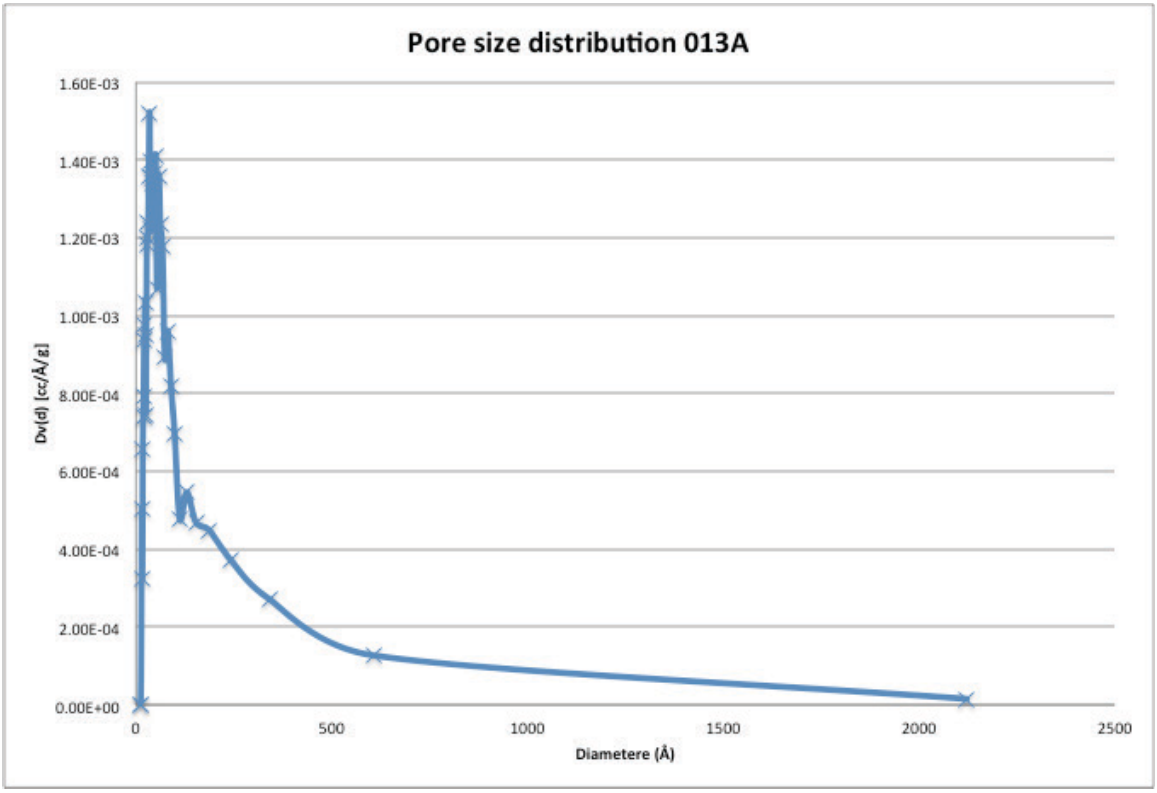

Figure 176 pore size distribution of sample 013A synthesized from cerium hydroxide, SDS (300mM), water, ethanol, and sodium hydroxide, uncalcinated

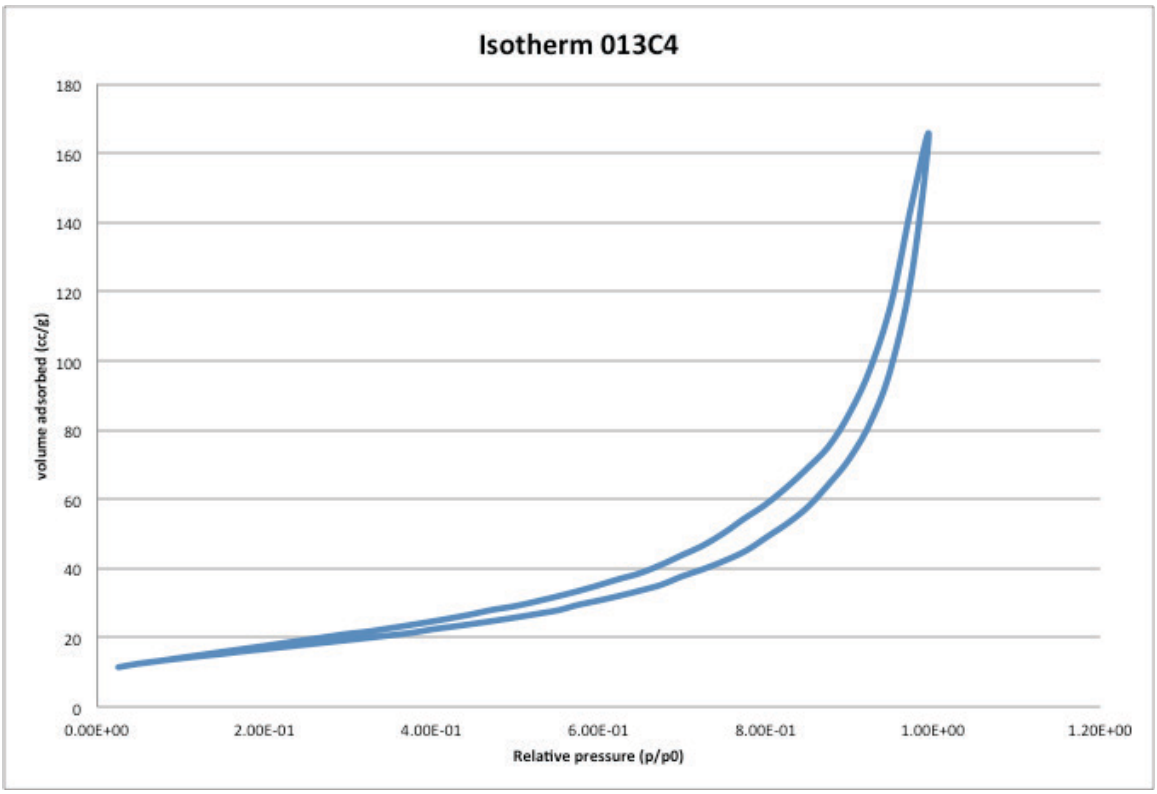

Figure 177 isotherm of sample 013C4 synthesized from cerium hydroxide, SDS (300mM), water, ethanol, and sodium hydroxide, calcinated at 673K

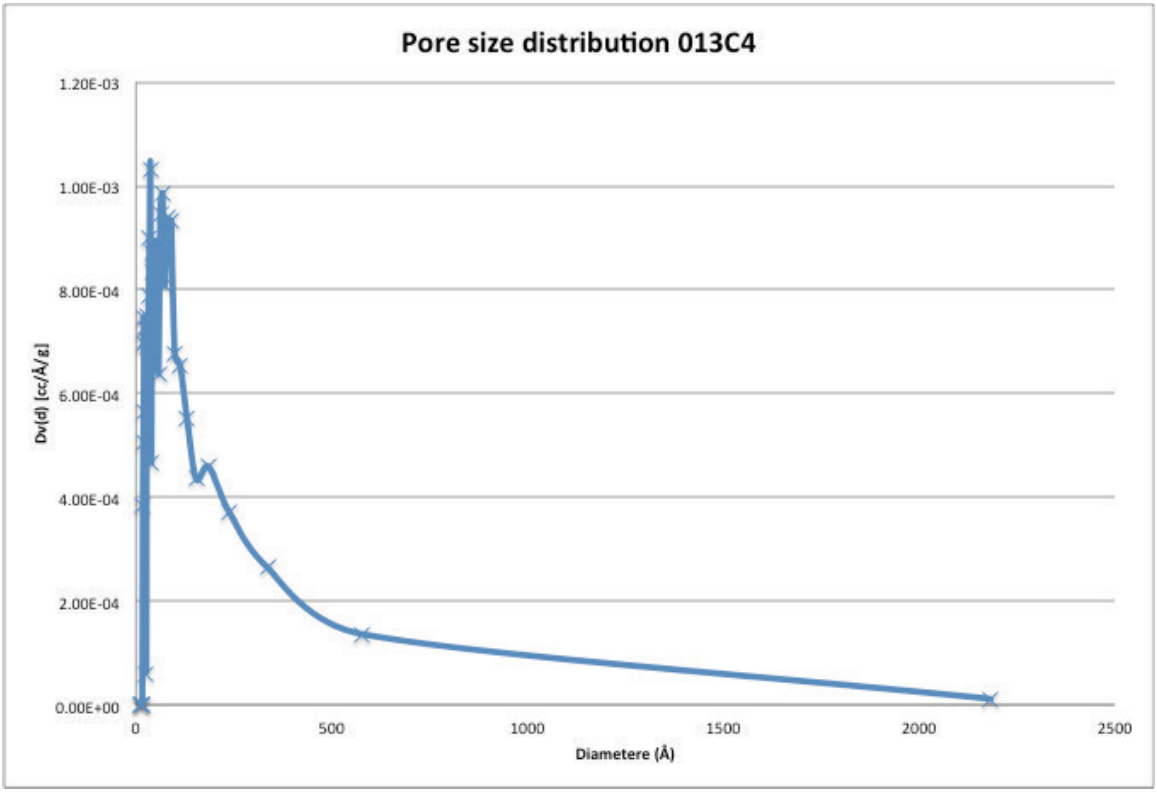

Figure 178 pore size distribution of sample 013C4 synthesized from cerium hydroxide, SDS (300mM), water, ethanol, and sodium hydroxide, calcinated at 673K

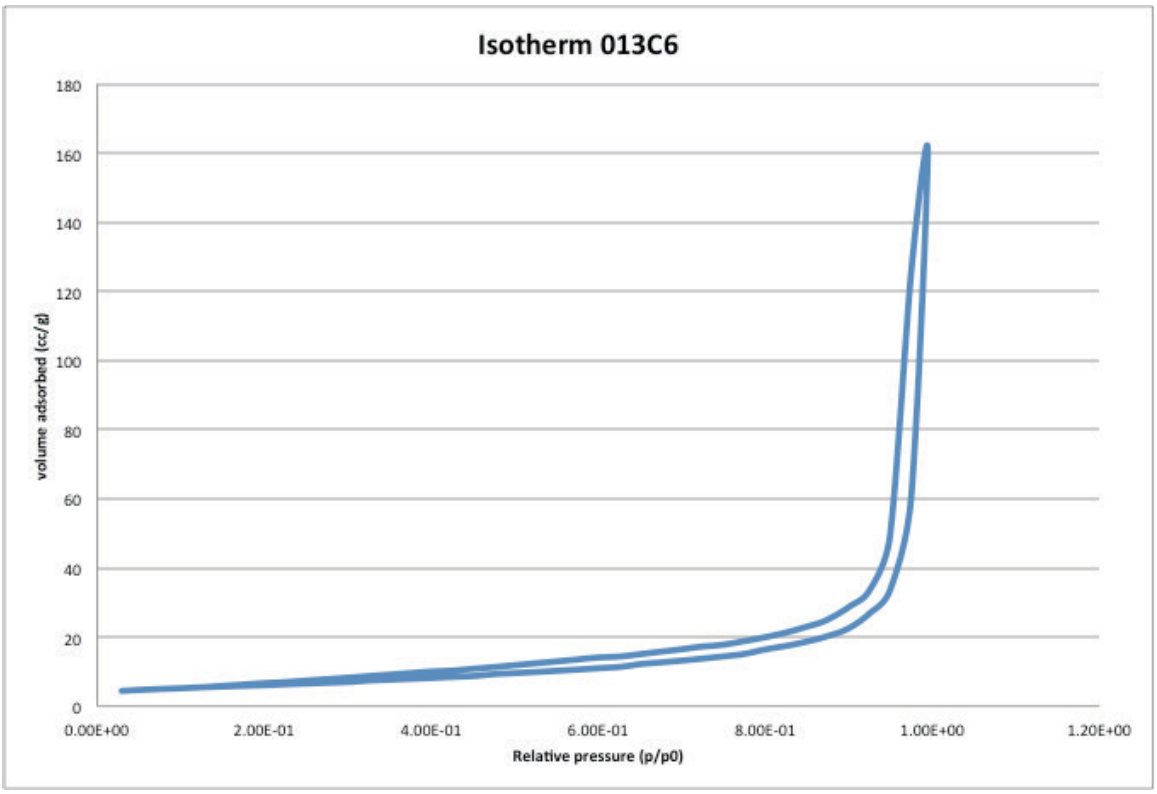

Figure 179 isotherm of sample 013C6 synthesized from cerium hydroxide, SDS (300mM), water, ethanol, and sodium hydroxide, calcinated at 873K

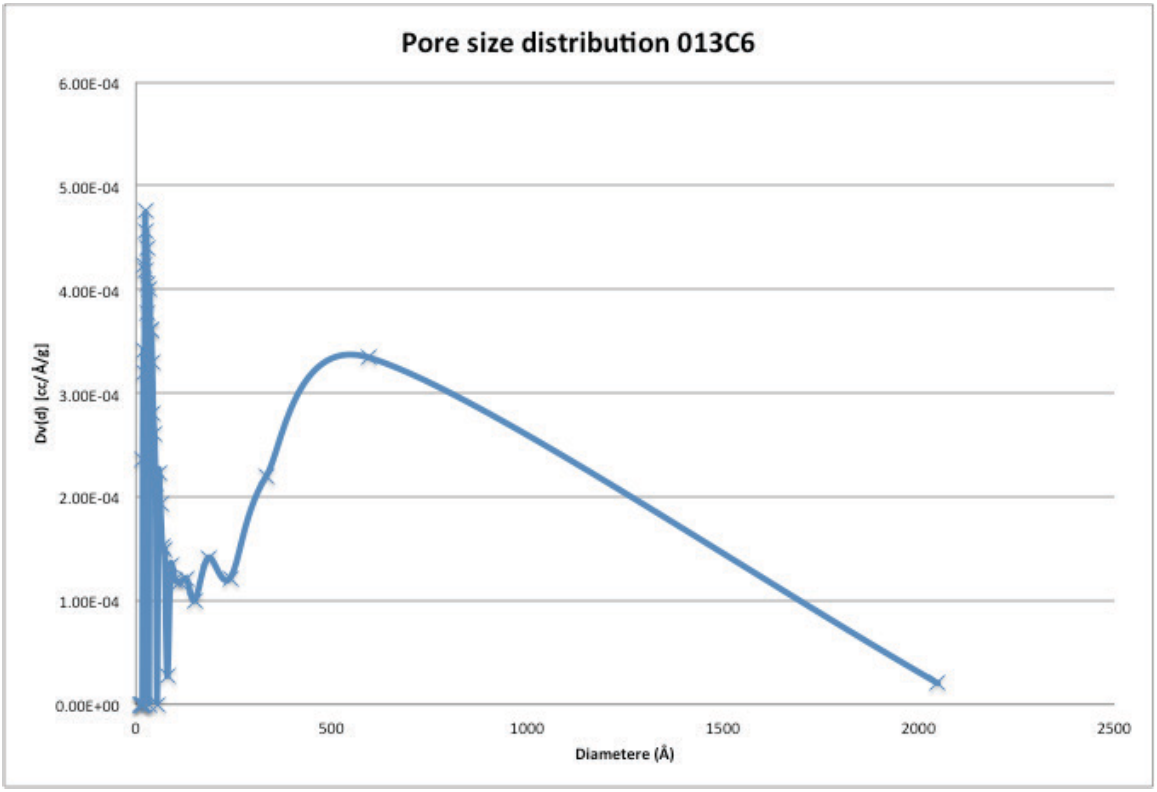

Figure 180 pore size distribution of sample 013C6 synthesized from cerium hydroxide, SDS (300mM), water, ethanol, and sodium hydroxide, calcinated at 873K

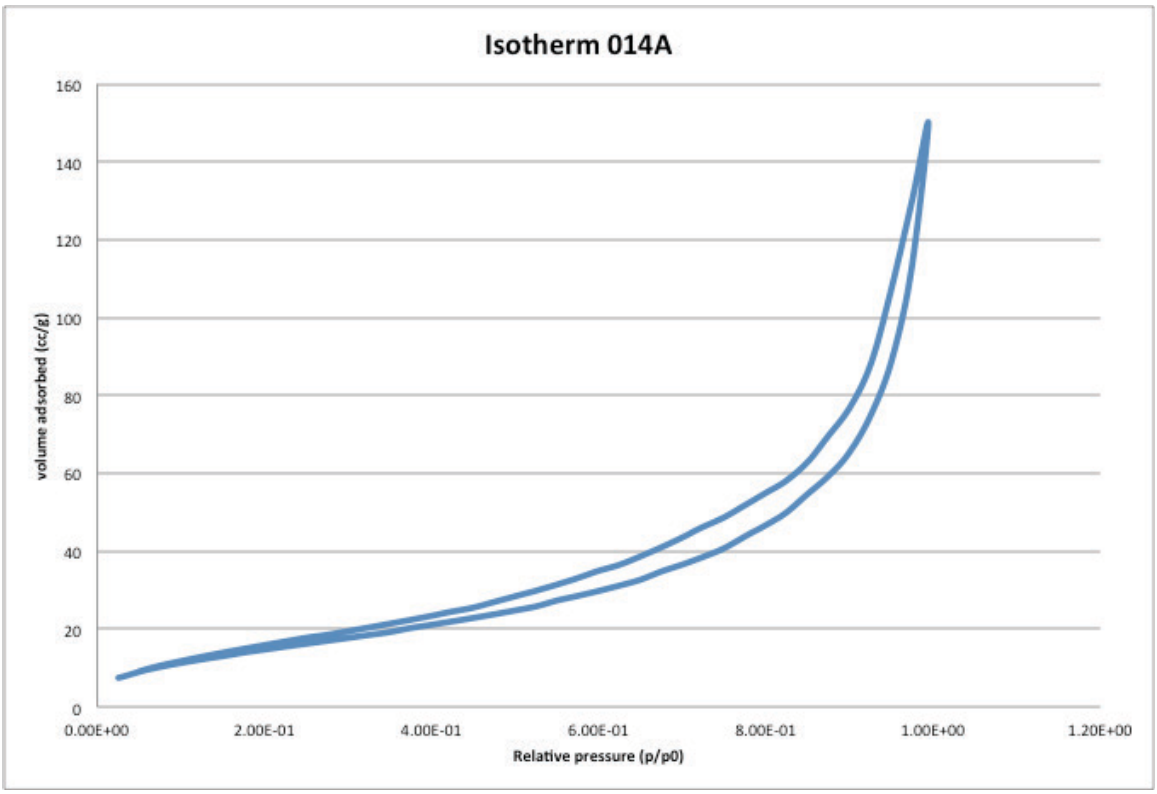

Figure 181 isotherm of sample 014A synthesized from cerium hydroxide, triton-X, water, ethanol, and sodium hydroxide, uncalcinated

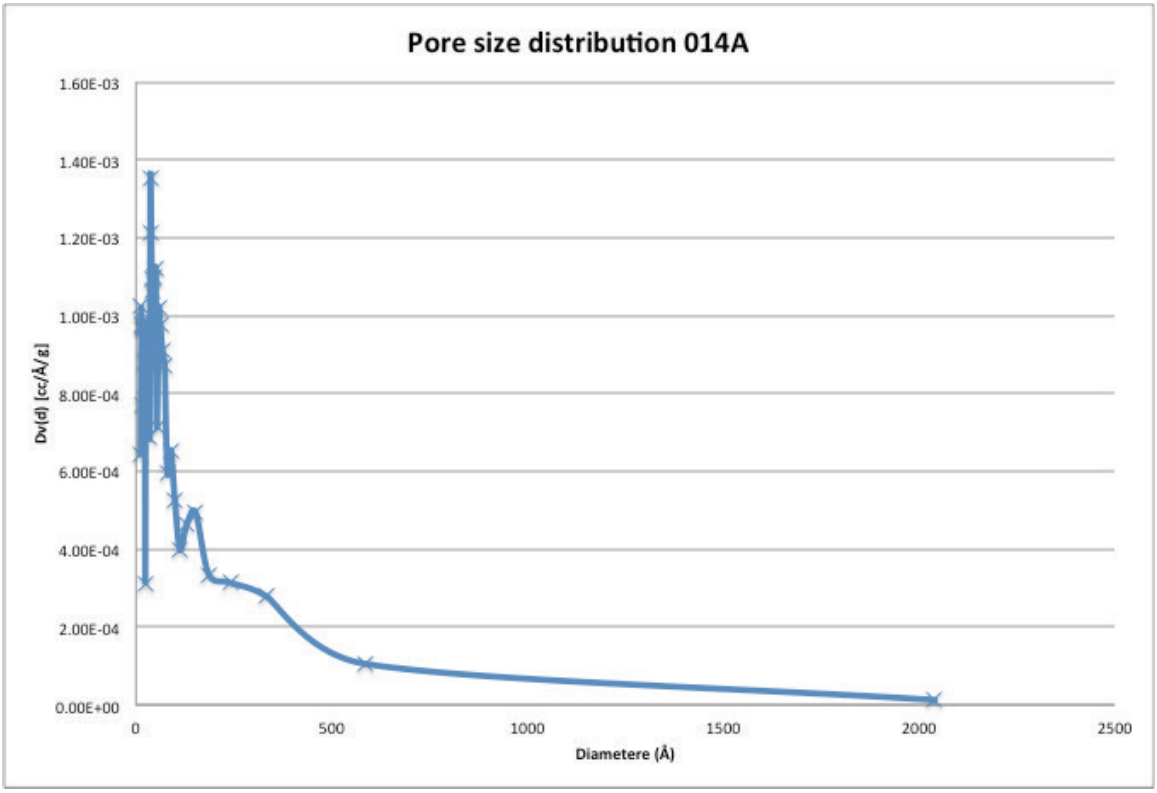

Figure 182 pore size distribution of sample 014A synthesized from cerium hydroxide, triton-X, water, ethanol, and sodium hydroxide, uncalcinated

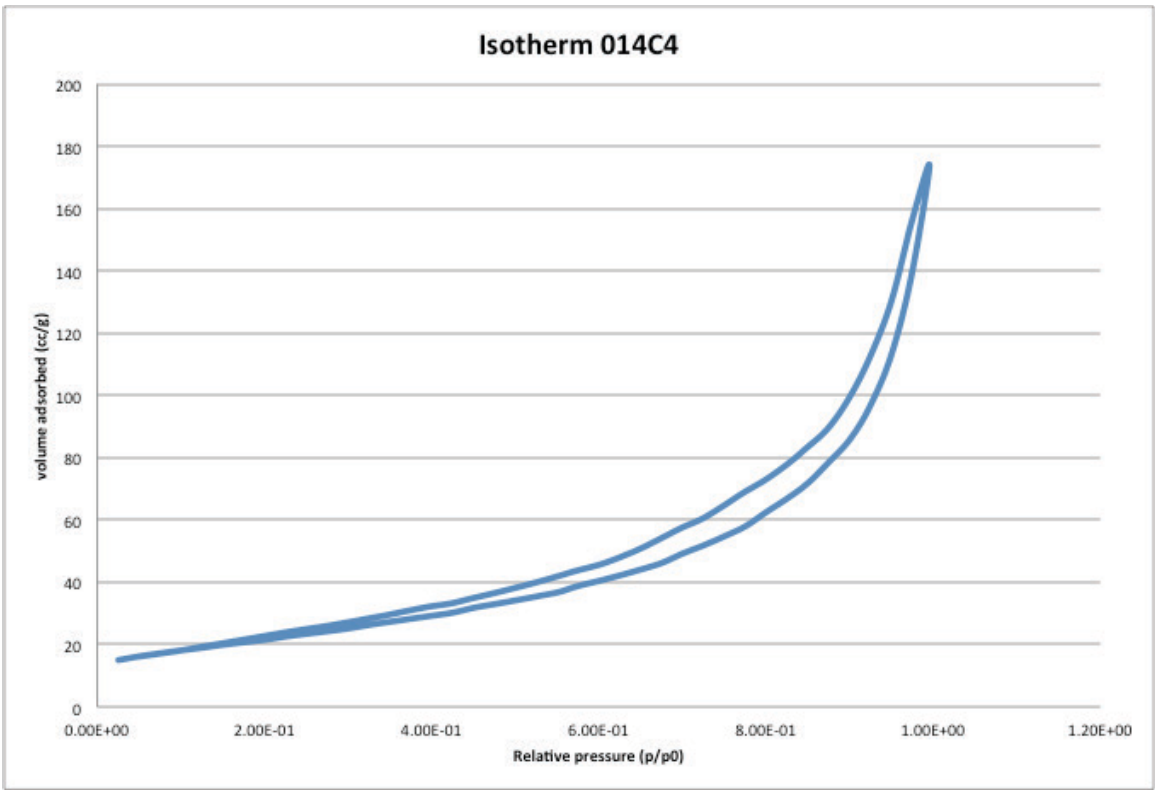

Figure 183 isotherm of sample 014C4 synthesized from cerium hydroxide, triton-X, water, ethanol, and sodium hydroxide, calcinated at 673K

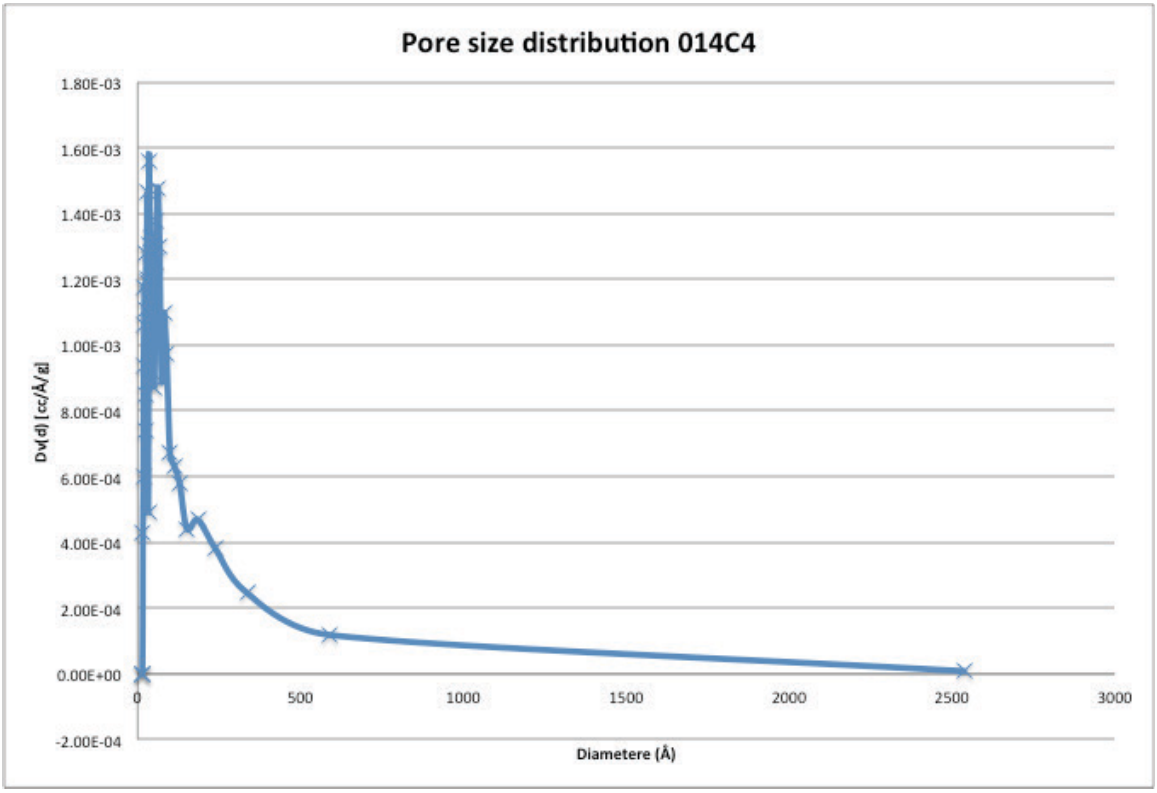

Figure 184 pore size distribution of sample 014C4 synthesized from cerium hydroxide, triton-X, water, ethanol, and sodium hydroxide, calcinated at 673K

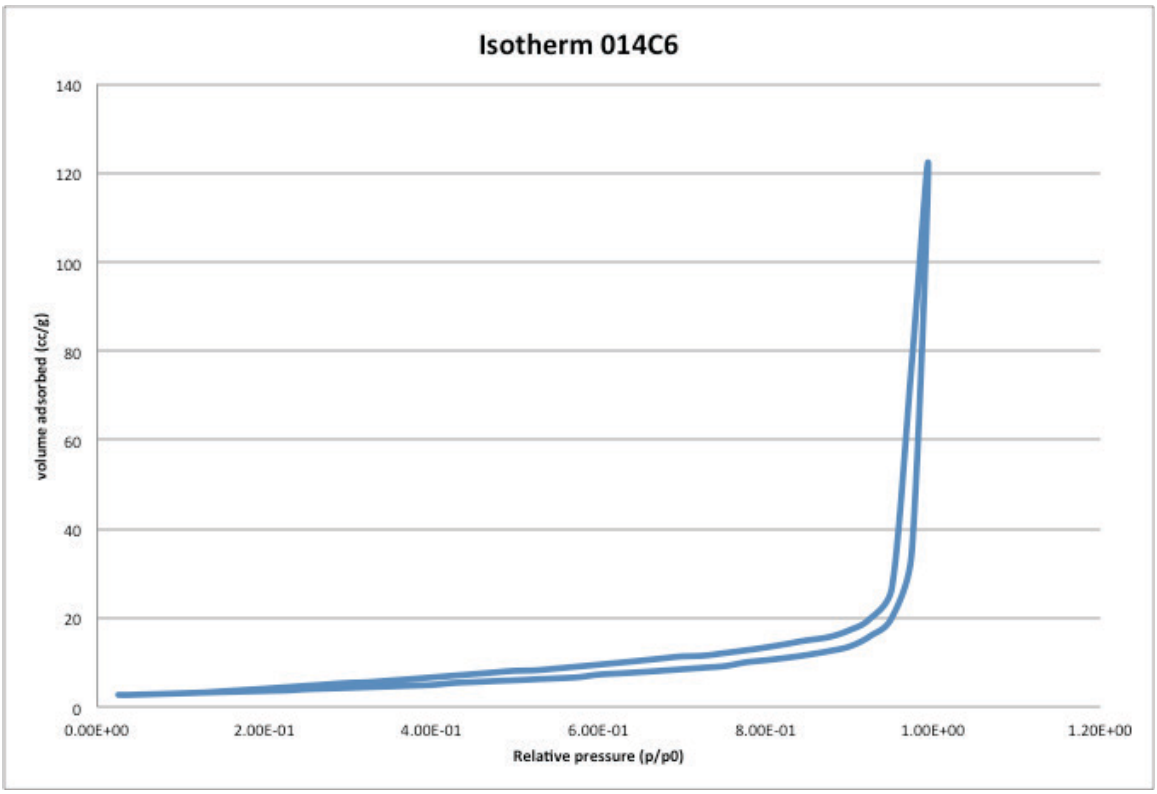

Figure 185 isotherm of sample 014C6 synthesized from cerium hydroxide, triton-X, water, ethanol, and sodium hydroxide, calcinated at 873K

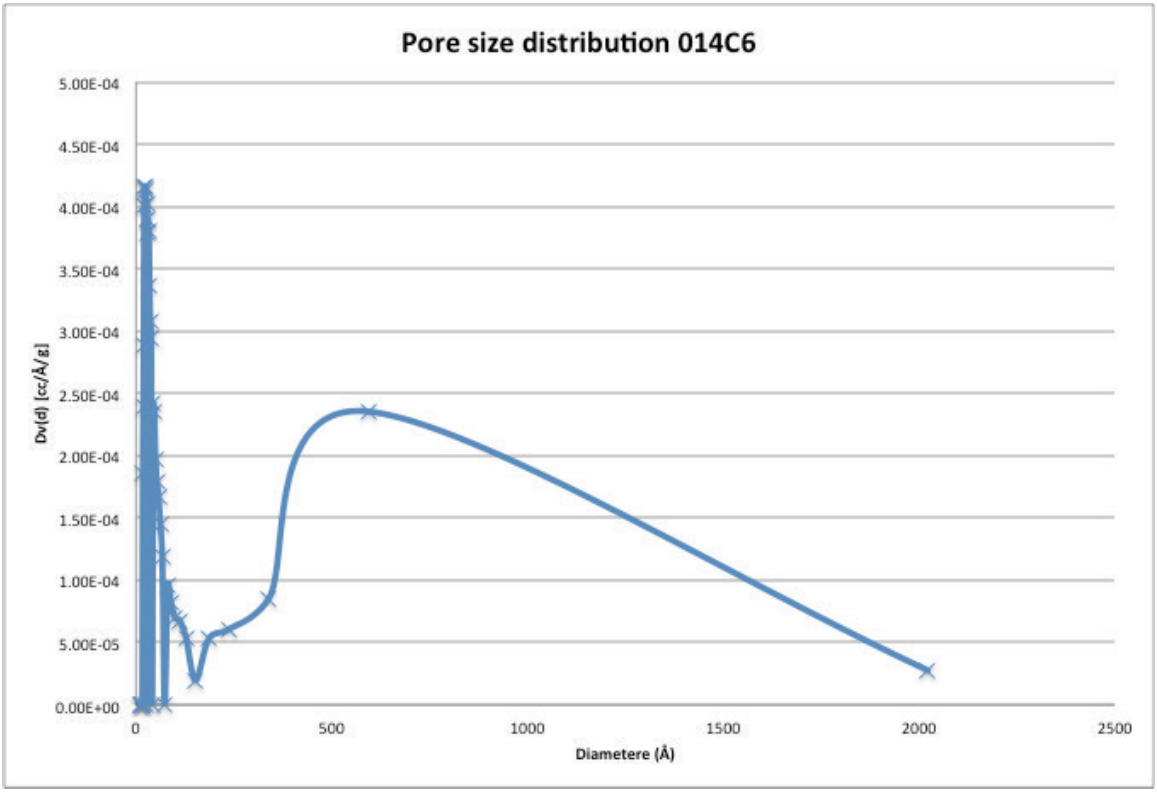

Figure 186 pore size distribution of sample 014C6 synthesized from cerium hydroxide, triton-X, water, ethanol, and sodium hydroxide, calcinated at 873K

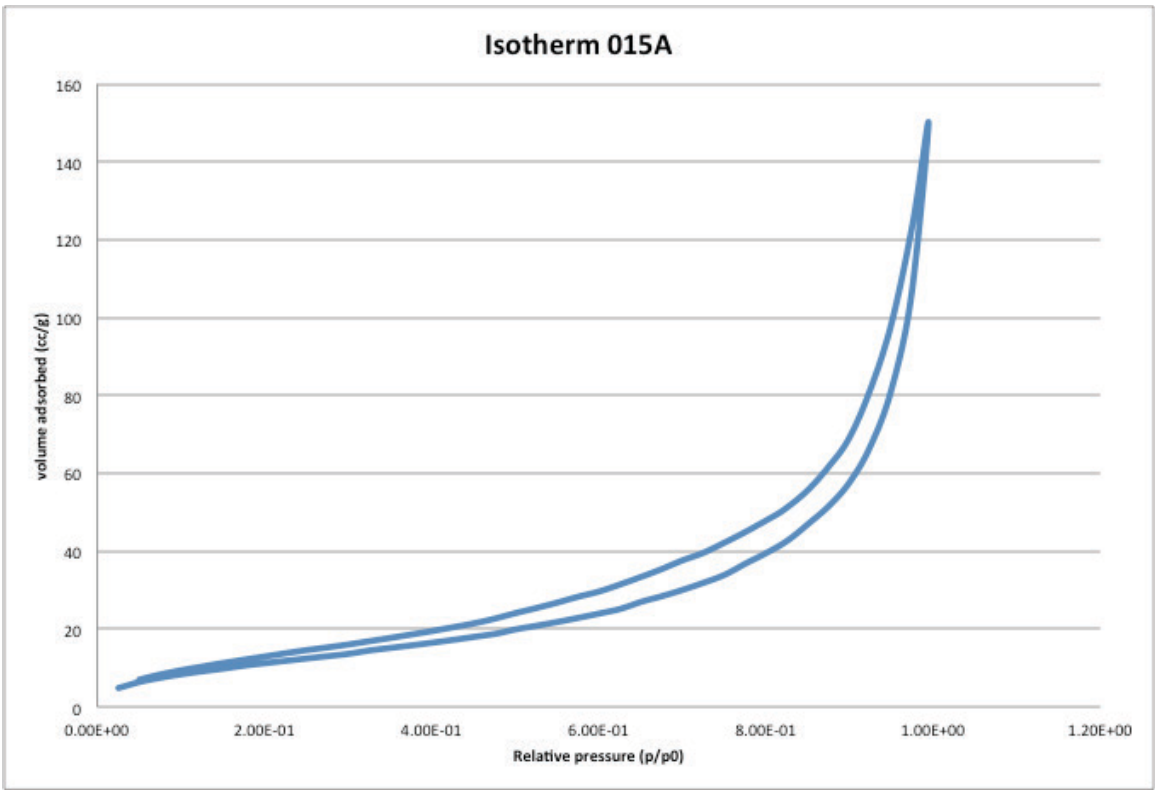

Figure 187 isotherm of sample 015A synthesized from cerium hydroxide, n-hexadecylamine, water, ethanol, and sodium hydroxide, uncalcinated

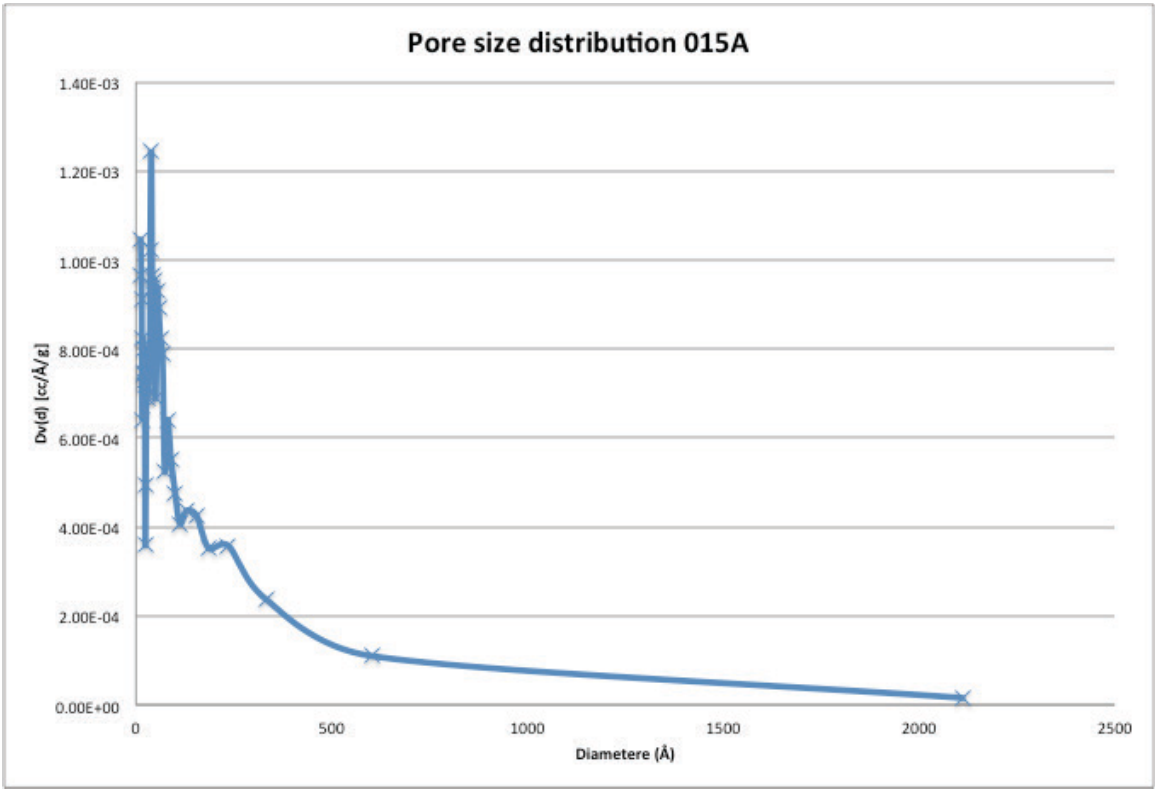

Figure 188 pore size distribution of sample 015A synthesized from cerium hydroxide, n-hexadecylamine, water, ethanol, and sodium hydroxide, uncalcinated

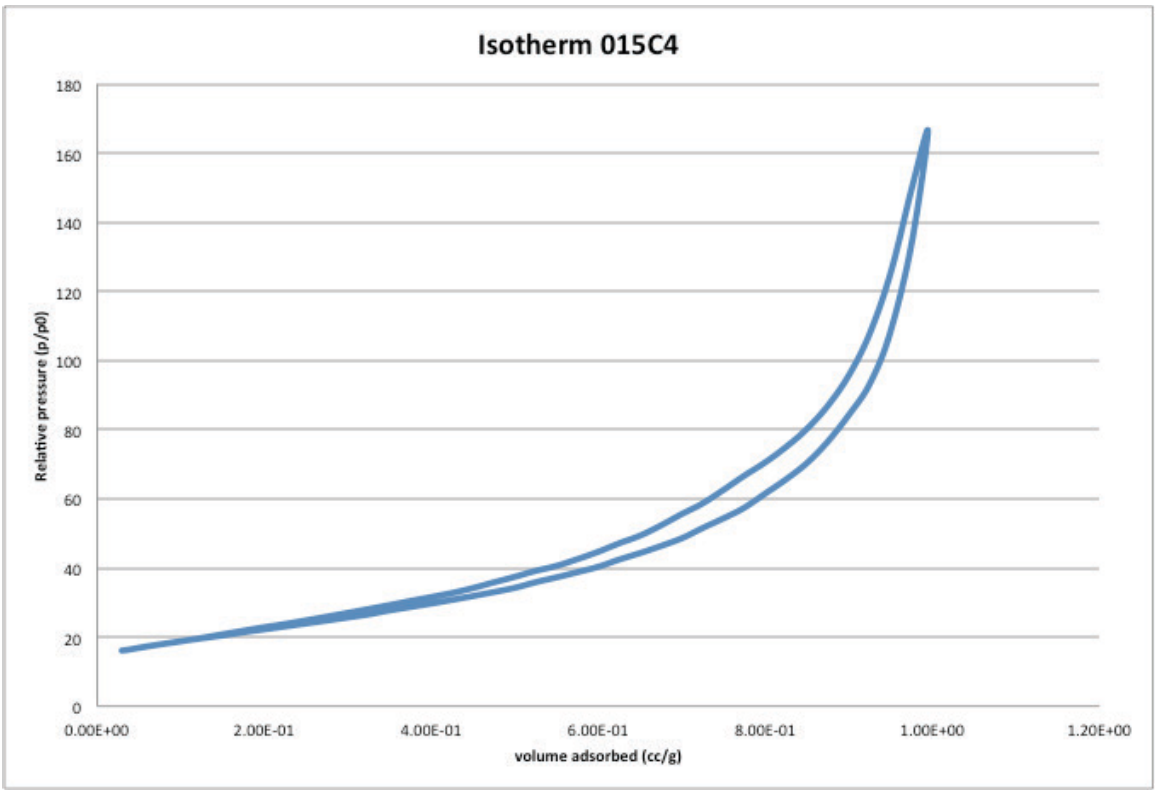

Figure 189 isotherm of sample 015C4 synthesized from cerium hydroxide, n-hexadecylamine, water, ethanol, and sodium hydroxide, calcinated at 673K

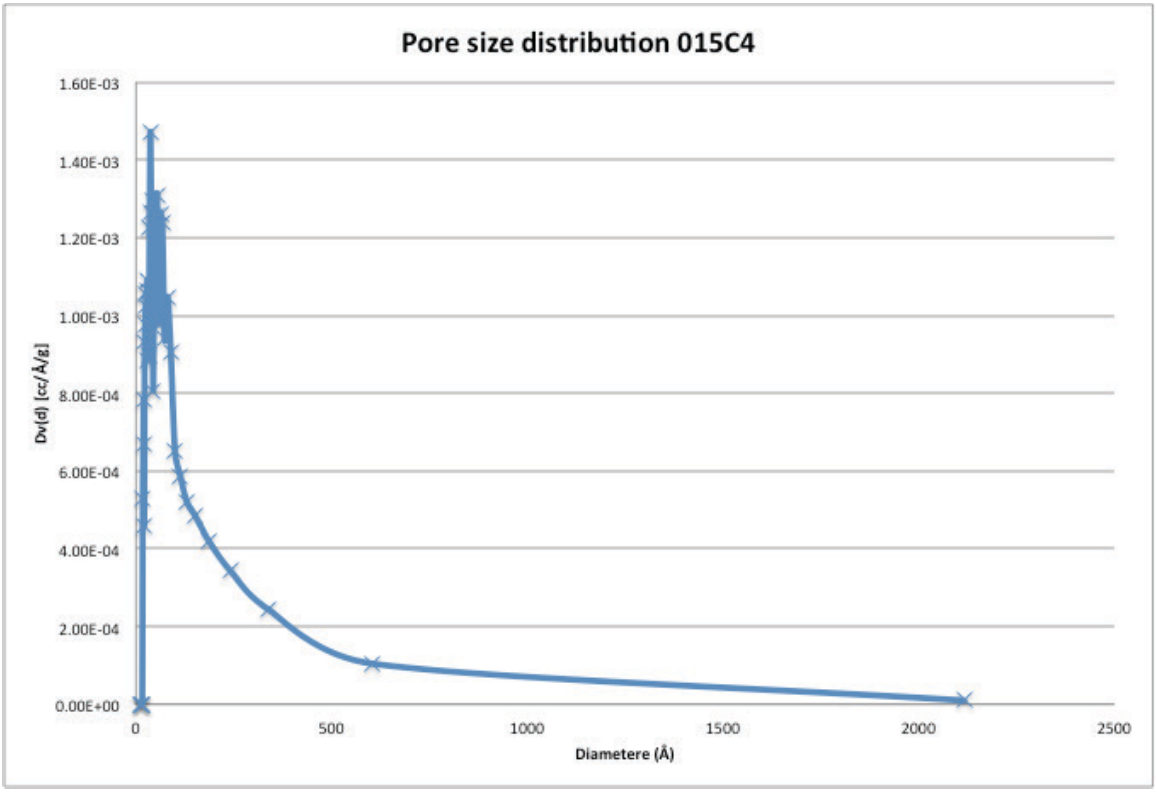

Figure 190 pore size distribution of sample 015C4 synthesized from cerium hydroxide, n-hexadecylamine, water, ethanol, and sodium hydroxide, calcinated at 673K

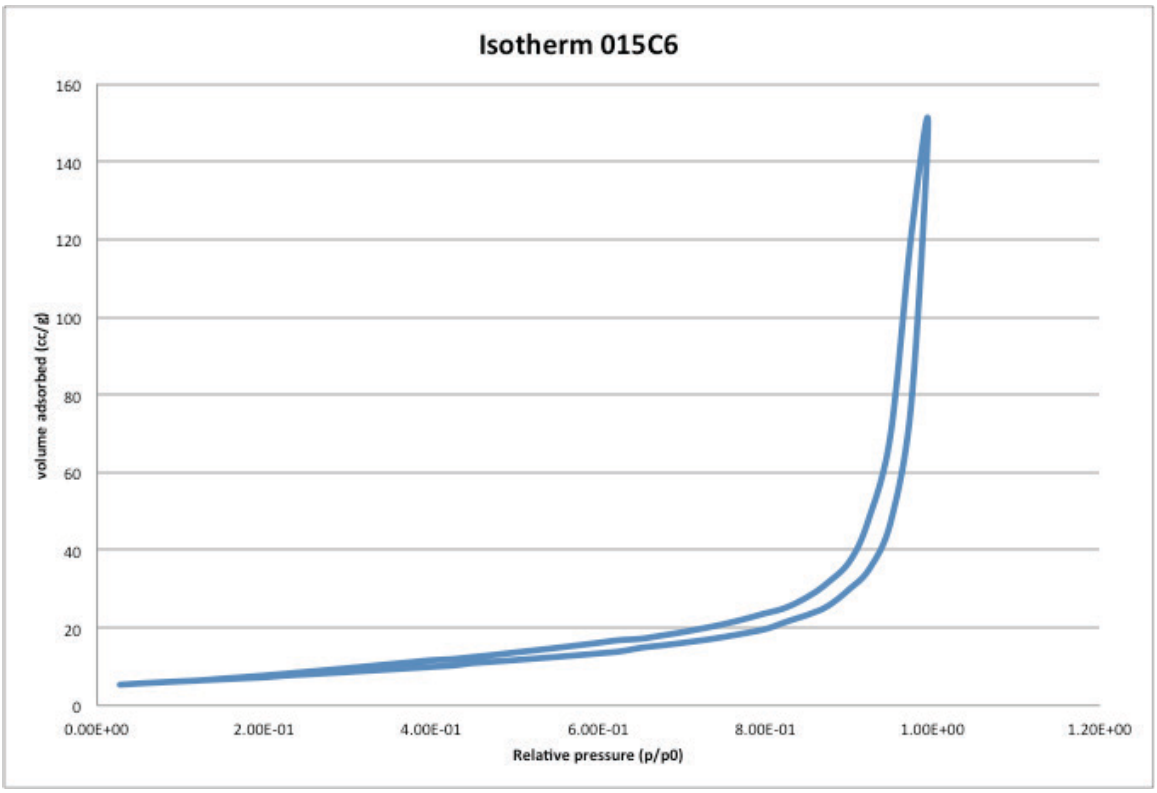

Figure 191 isotherm of sample 015C6 synthesized from cerium hydroxide, n-hexadecylamine, water, ethanol, and sodium hydroxide, calcinated at 873K

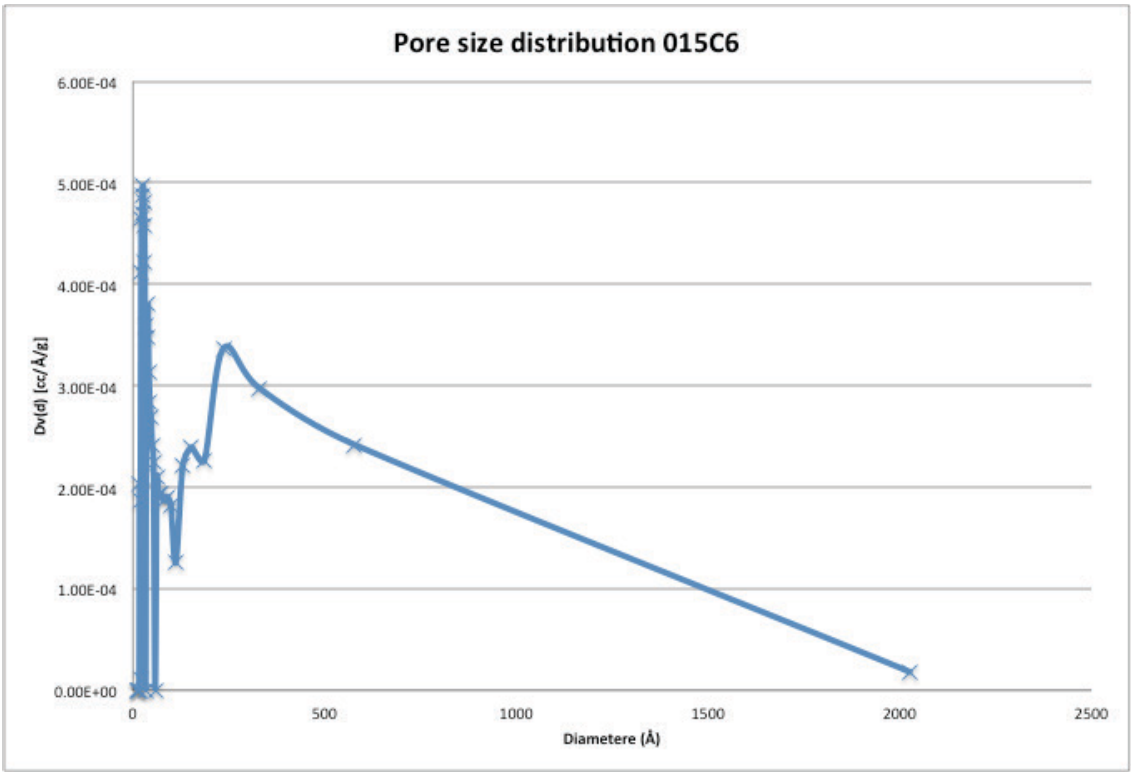

Figure 192 pore size distribution of sample 015C6 synthesized from cerium hydroxide, n-hexadecylamine, water, ethanol, and sodium hydroxide, calcinated at 873K

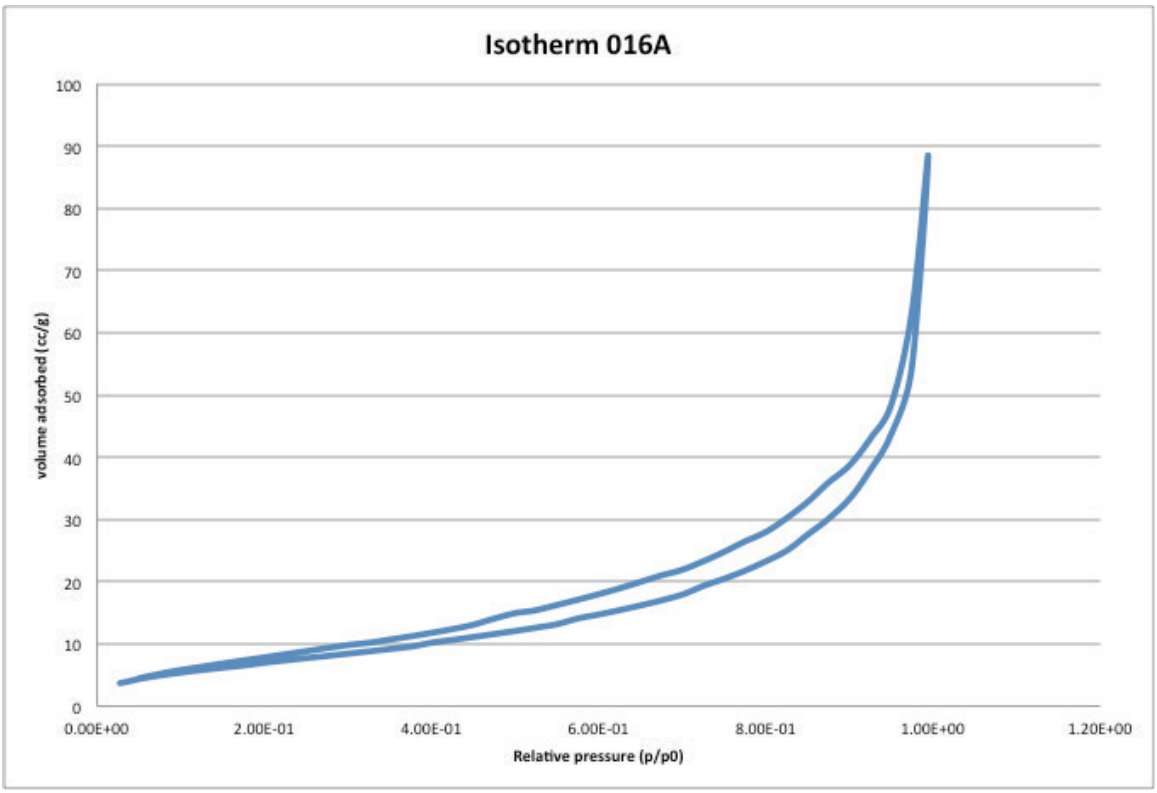

Figure 193 isotherm of sample 016A synthesized from cerium (III) nitrate hexahydrate, samarium (III) nitrate hexahydrate, CTAB, water, ethanol, and sodium hydroxide, uncalcinated

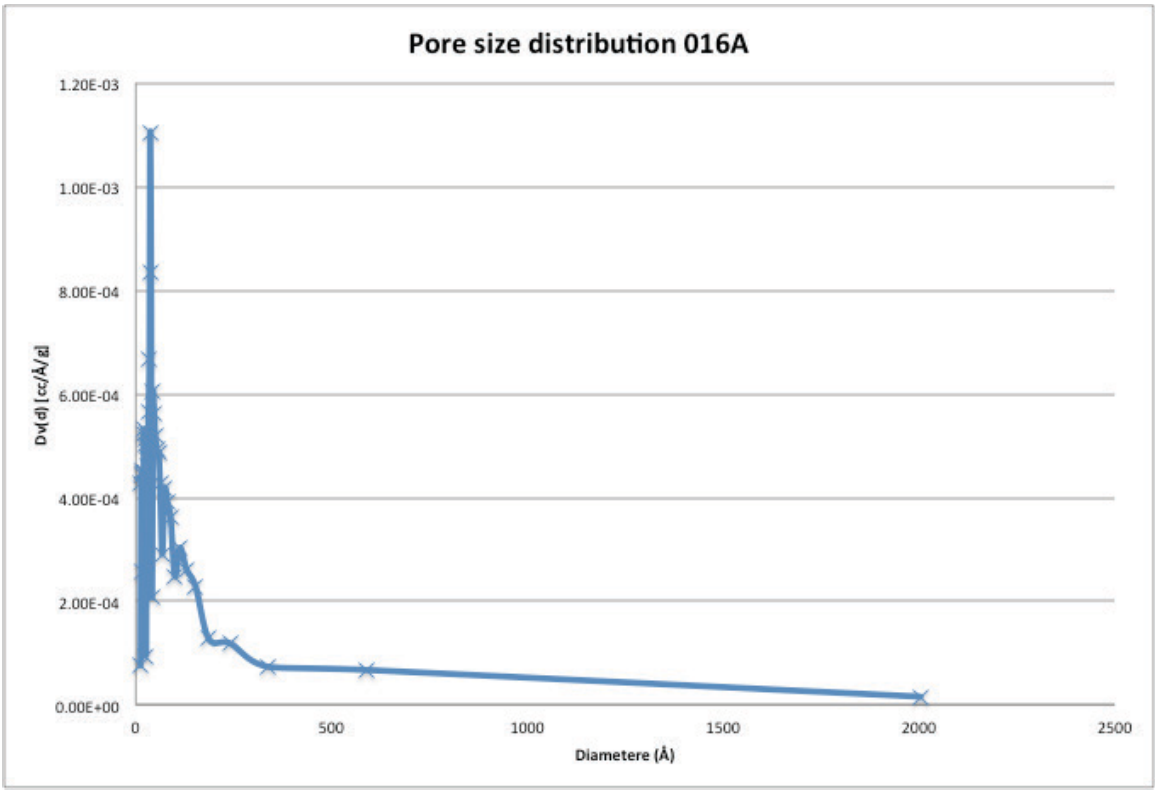

Figure 194 pore size distribution of sample 016A synthesized from cerium (III) nitrate hexahydrate, samarium (III) nitrate hexahydrate, CTAB, water, ethanol, and sodium hydroxide, uncalcinated

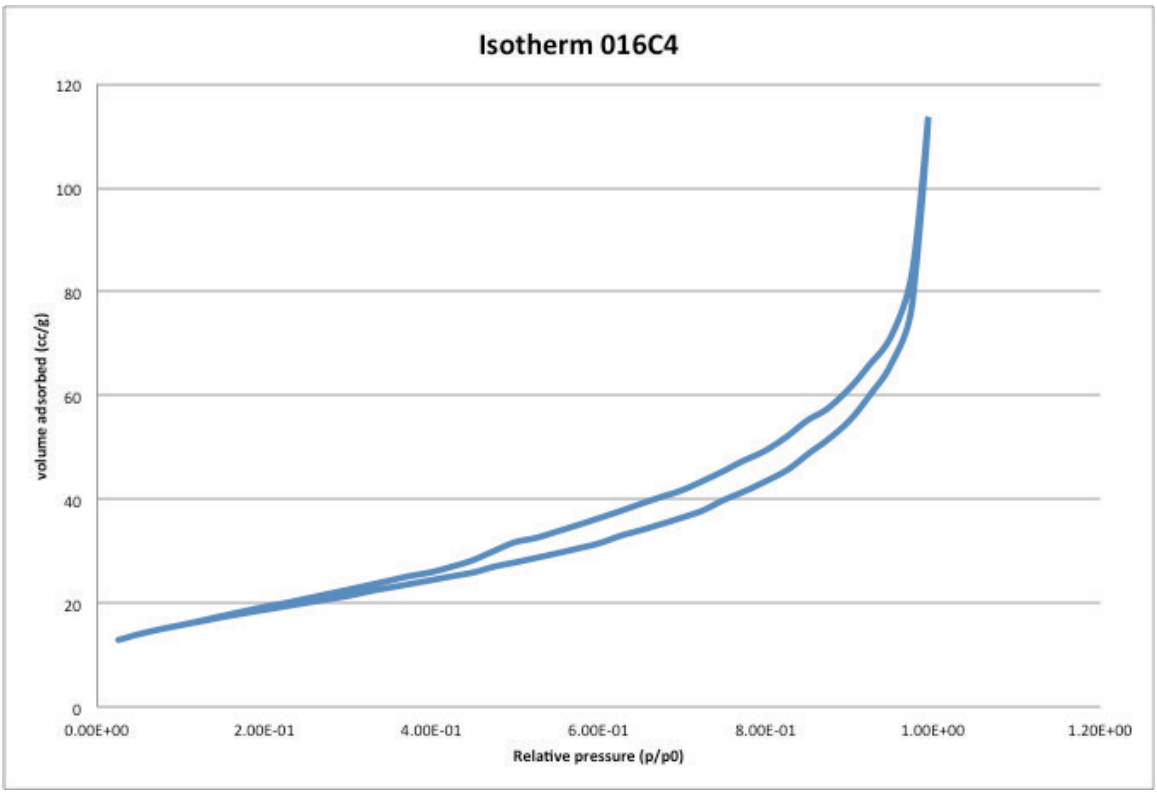

Figure 195 isotherm of sample 016C4 synthesized from cerium (III) nitrate hexahydrate, samarium (III) nitrate hexahydrate, CTAB, water, ethanol, and sodium hydroxide, calcinated at 673K

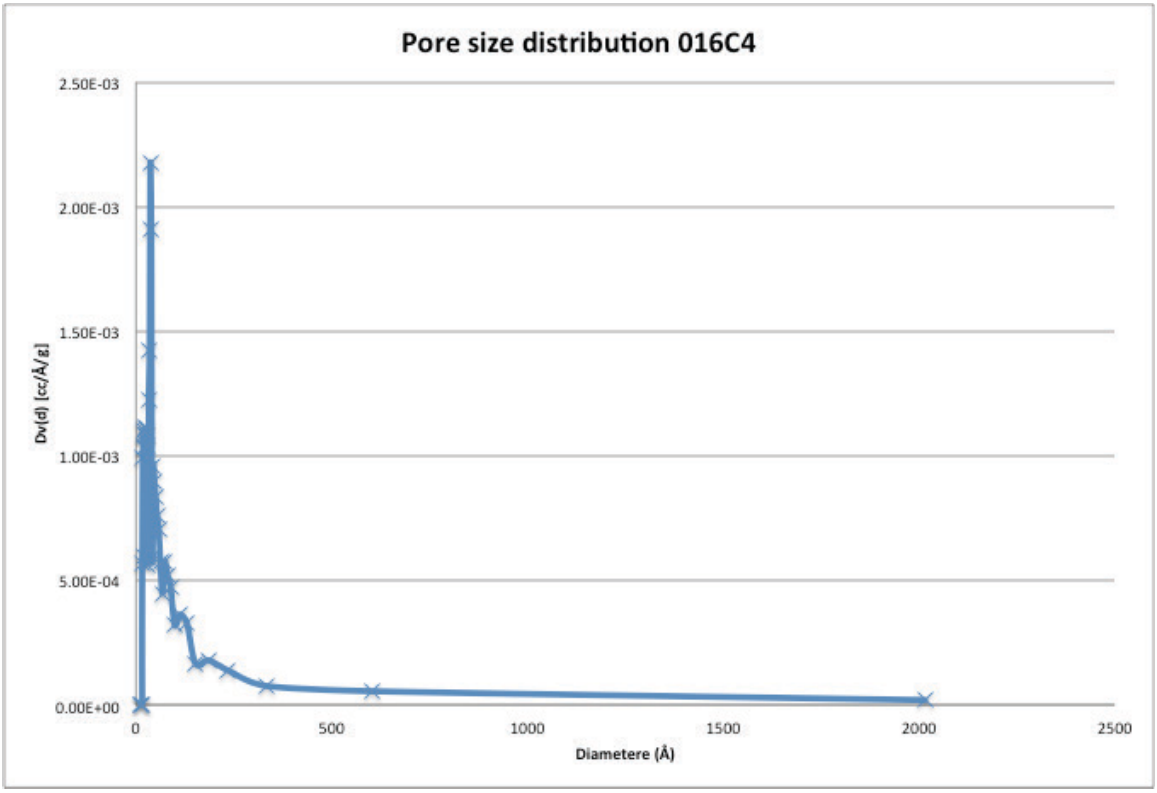

Figure 196 pore size distribution of sample 016C4 synthesized from cerium (III) nitrate hexahydrate, samarium (III) nitrate hexahydrate, CTAB, water, ethanol, and sodium hydroxide, calcinated at 673K

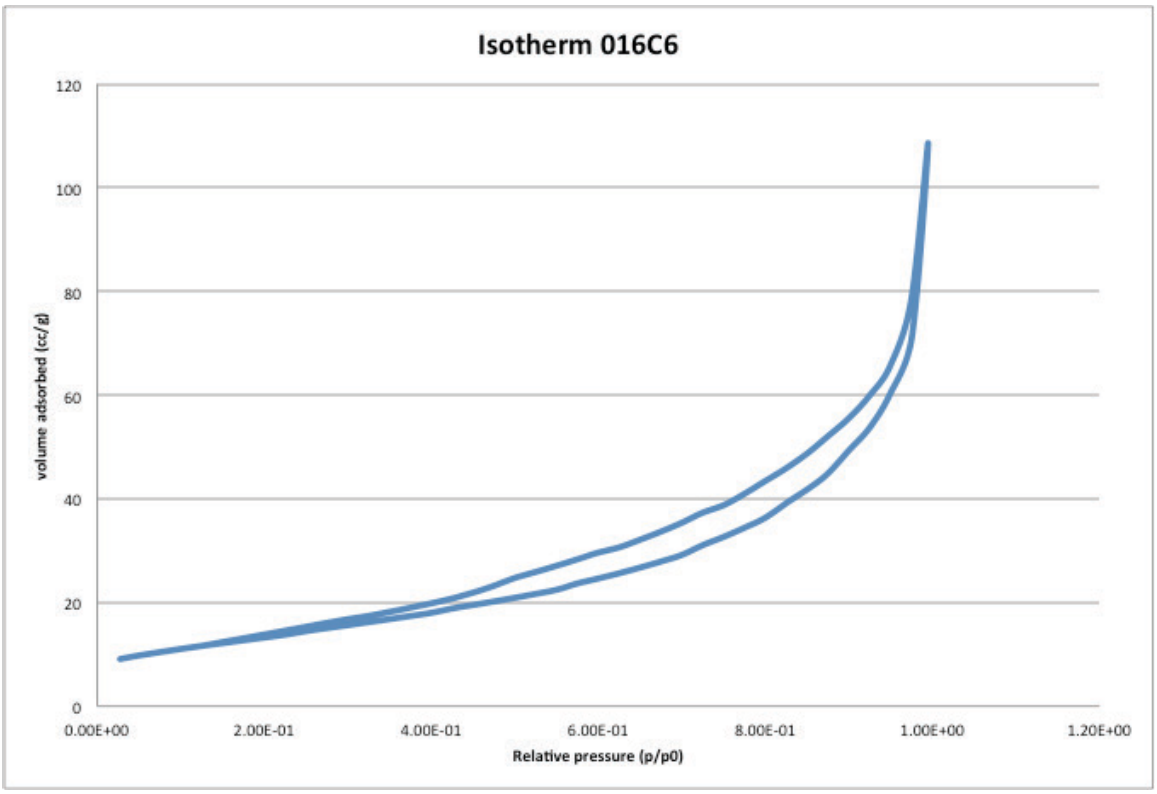

Figure 197 isotherm of sample 016C6 synthesized from cerium (III) nitrate hexahydrate, samarium (III) nitrate hexahydrate, CTAB, water, ethanol, and sodium hydroxide, calcinated at 873K

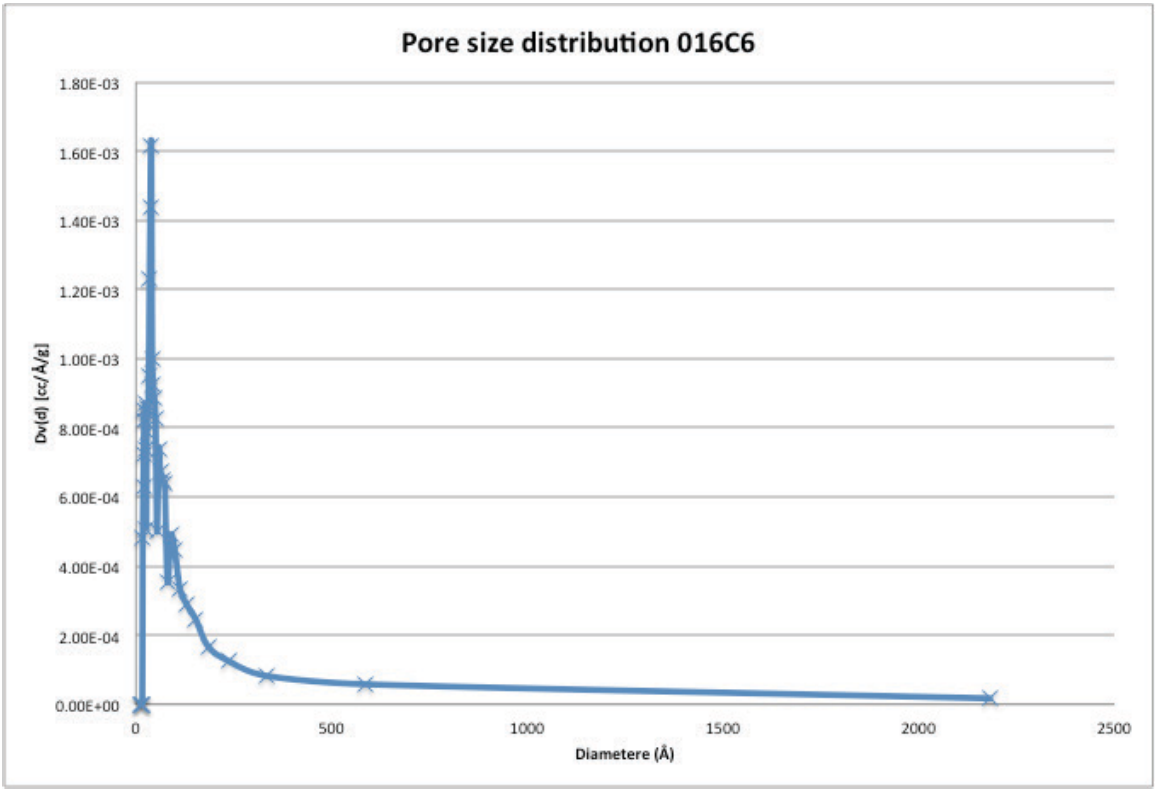

Figure 198 pore size distribution of sample 016C6 synthesized from cerium (III) nitrate hexahydrate, samarium (III) nitrate hexahydrate, CTAB, water, ethanol, and sodium hydroxide, calcinated at 873K

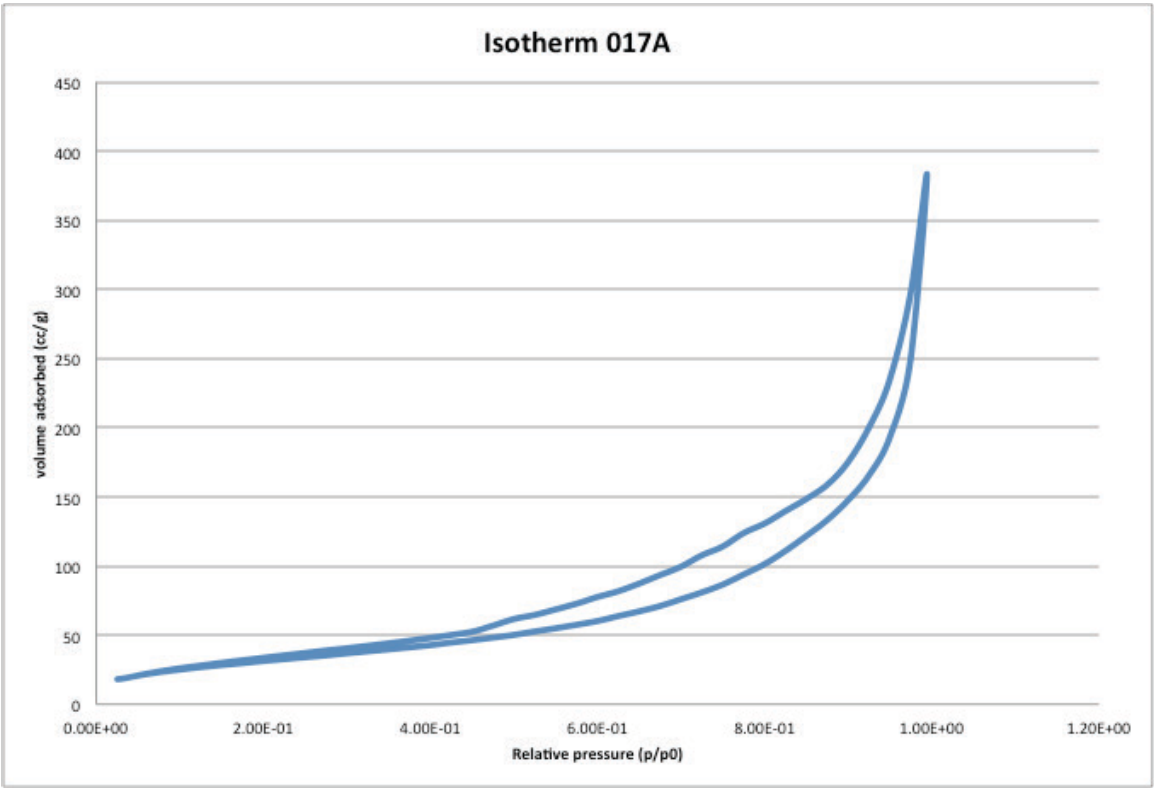

Figure 199 isotherm of sample 017A synthesized from cerium (III) nitrate hexahydrate, titanium isopropoxide, CTAB, water, ethanol, and sodium hydroxide, uncalcinated

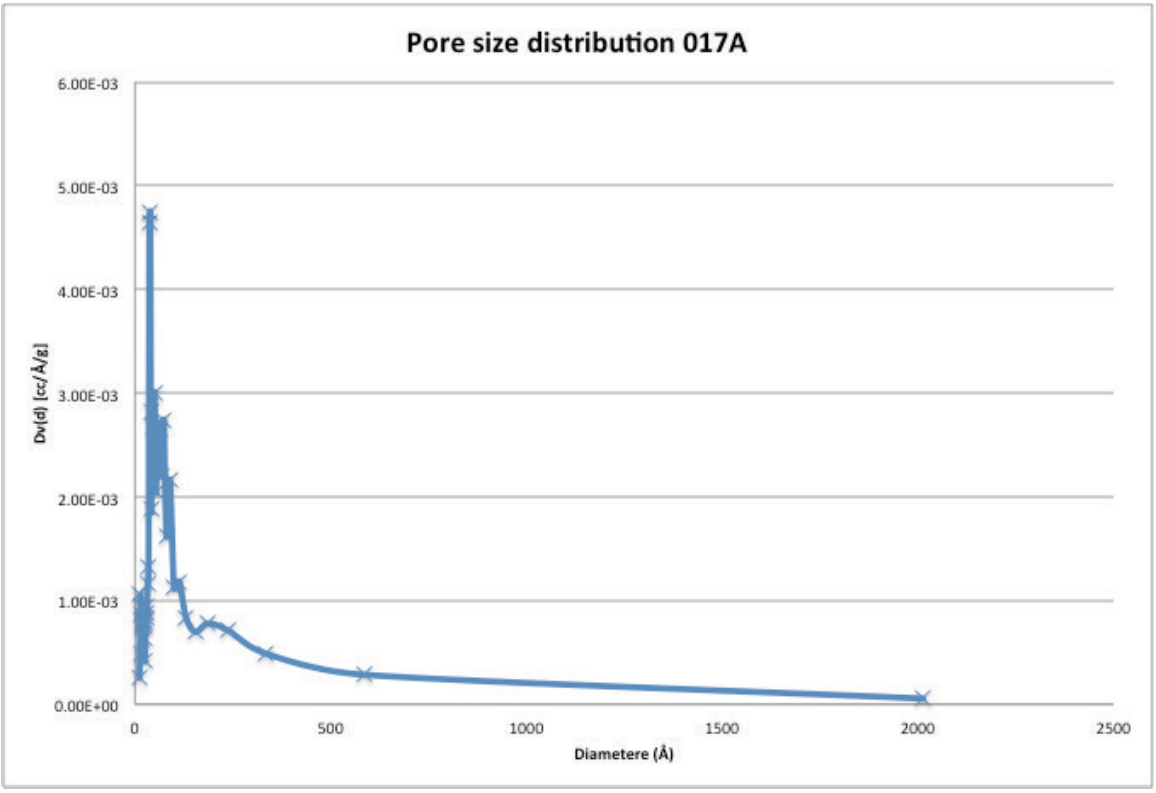

Figure 200 pore size distribution of sample 017A synthesized from cerium (III) nitrate hexahydrate, titanium isopropoxide, CTAB, water, ethanol, and sodium hydroxide, uncalcinated

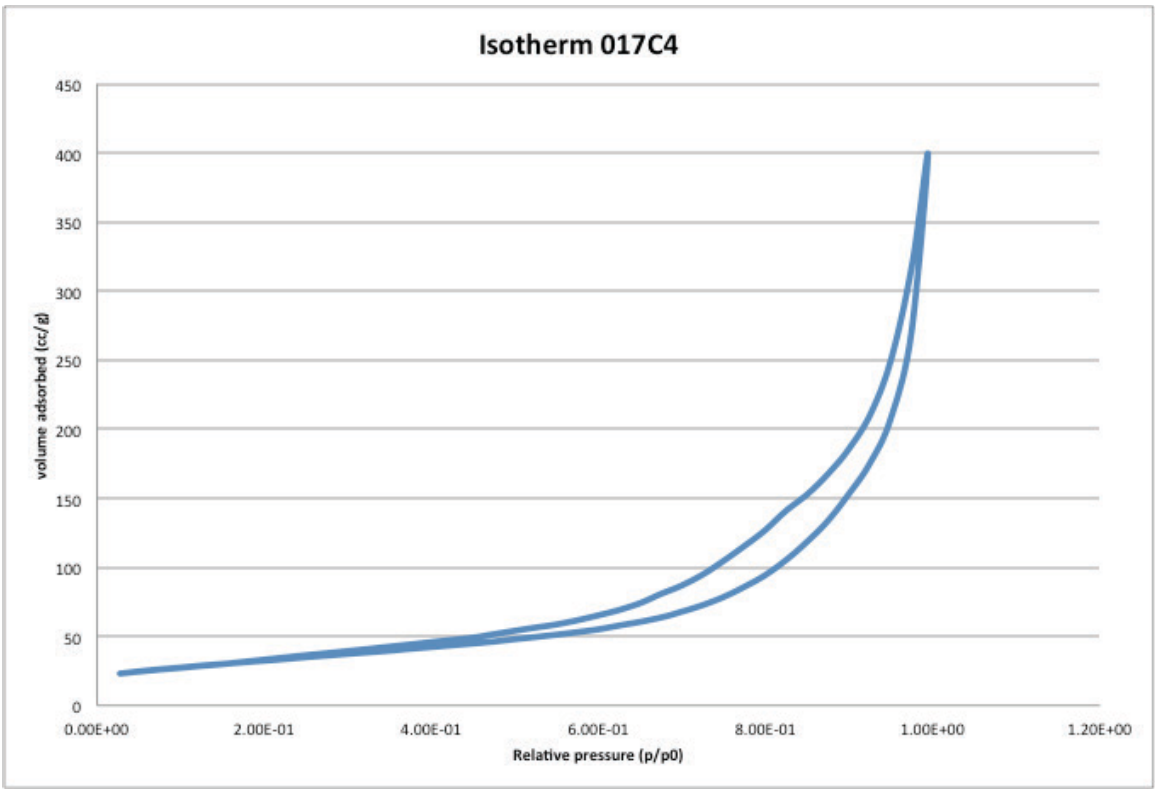

Figure 201 isotherm of sample 017C4 synthesized from cerium (III) nitrate hexahydrate, titanium isopropoxide, CTAB, water, ethanol, and sodium hydroxide, calcinated at 673K

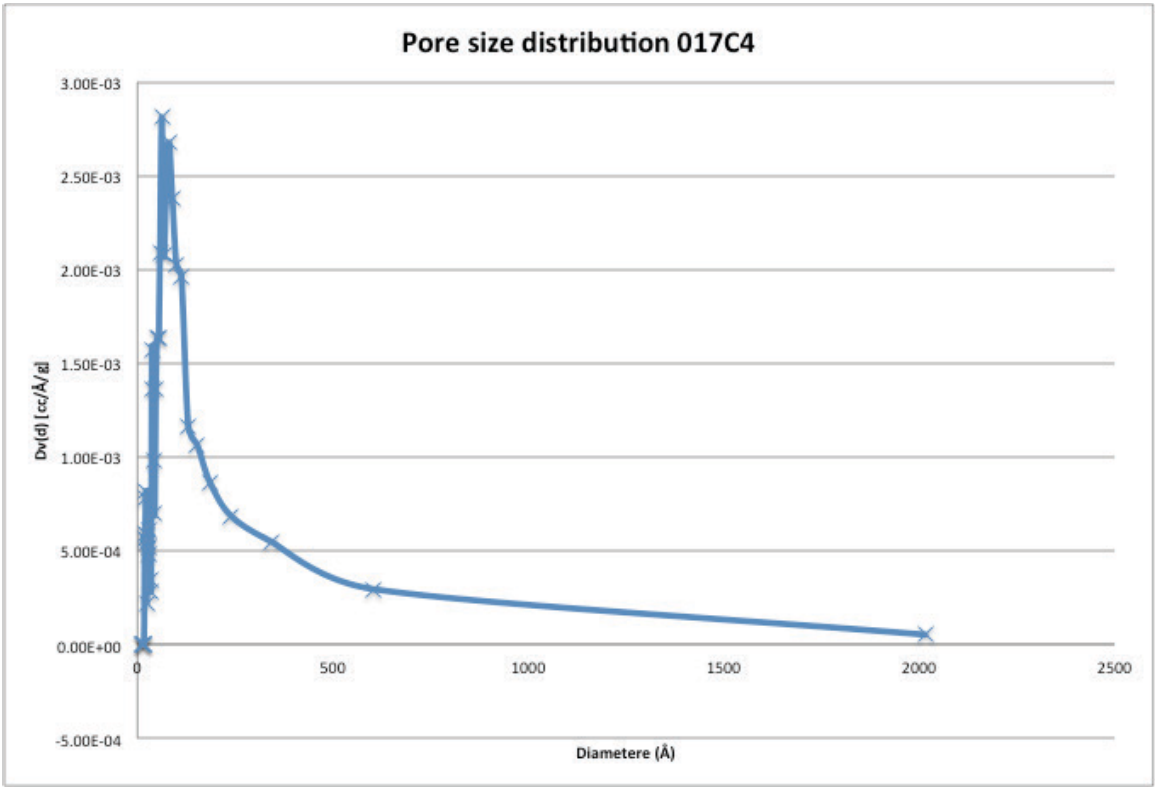

Figure 202 pore size distribution of sample 017C4 synthesized from cerium (III) nitrate hexahydrate, titanium isopropoxide, CTAB, water, ethanol, and sodium hydroxide, calcinated at 673K

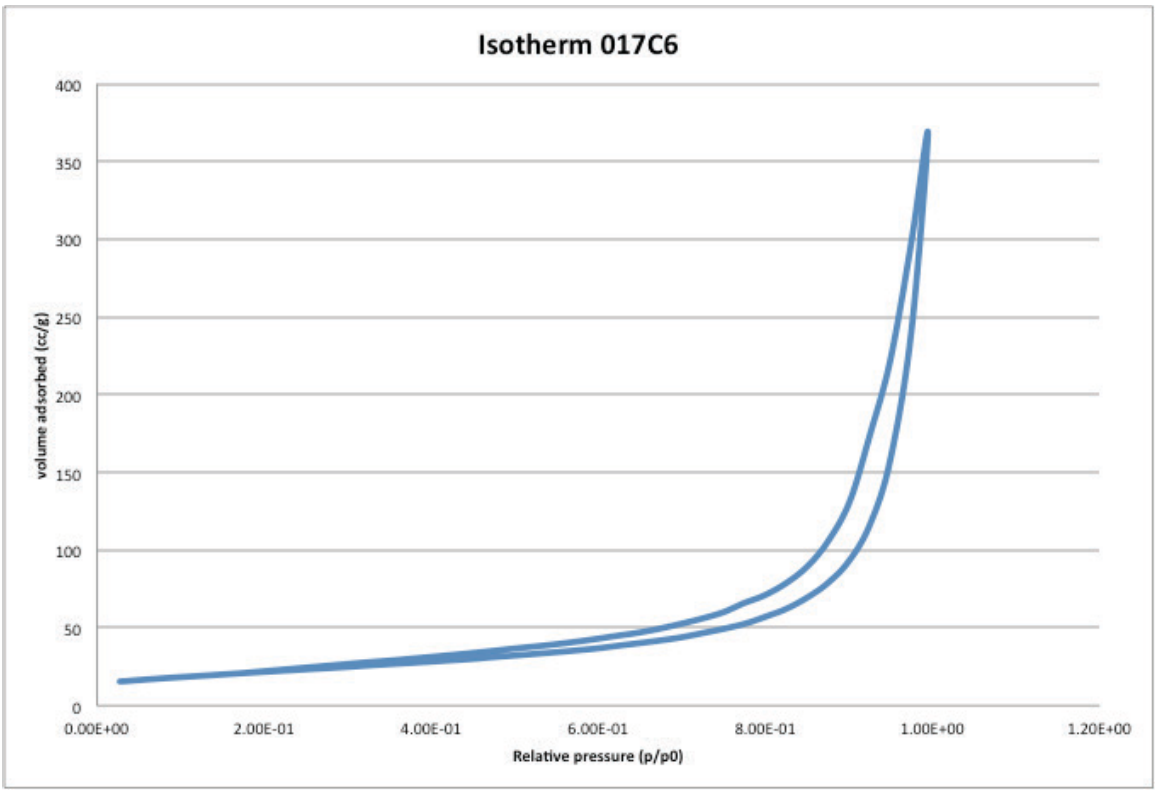

Figure 203 isotherm of sample 017C6 synthesized from cerium (III) nitrate hexahydrate, titanium isopropoxide, CTAB, water, ethanol, and sodium hydroxide, calcinated at 873K

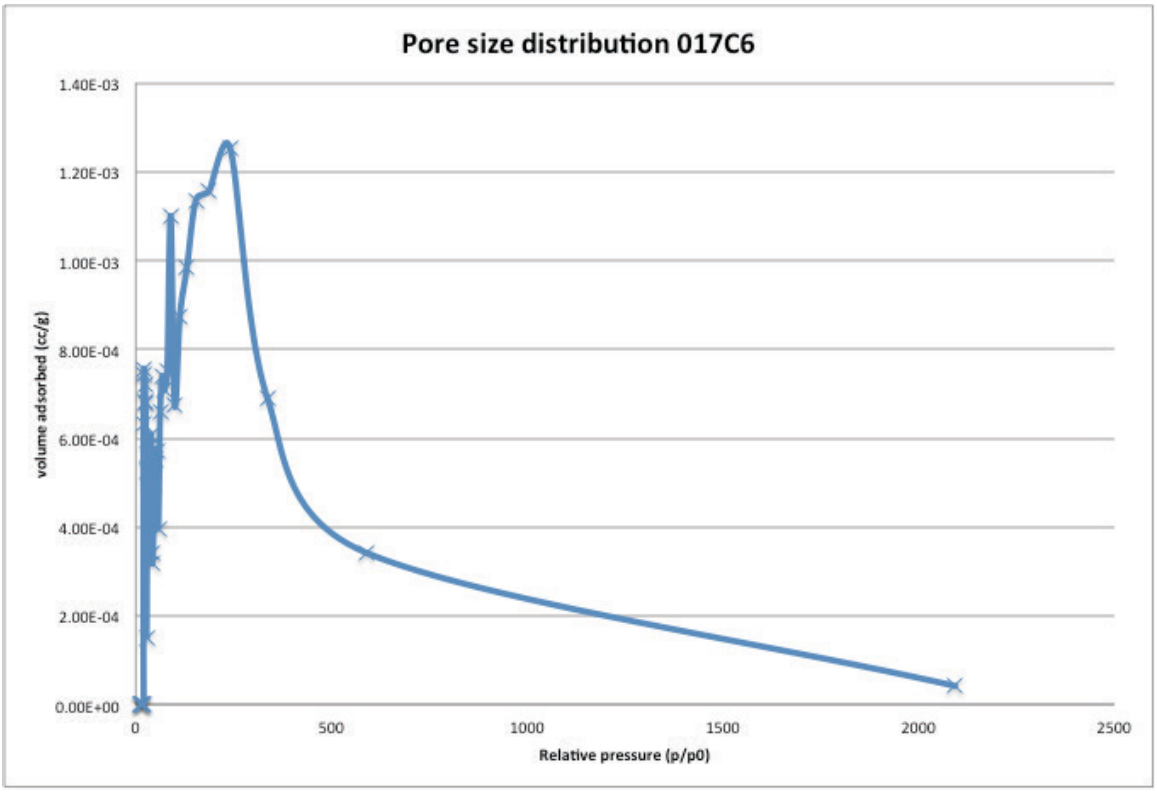

Figure 204 pore size distribution of sample 017C6 synthesized from cerium (III) nitrate hexahydrate, titanium isopropoxide, CTAB, water, ethanol, and sodium hydroxide, calcinated at 873K

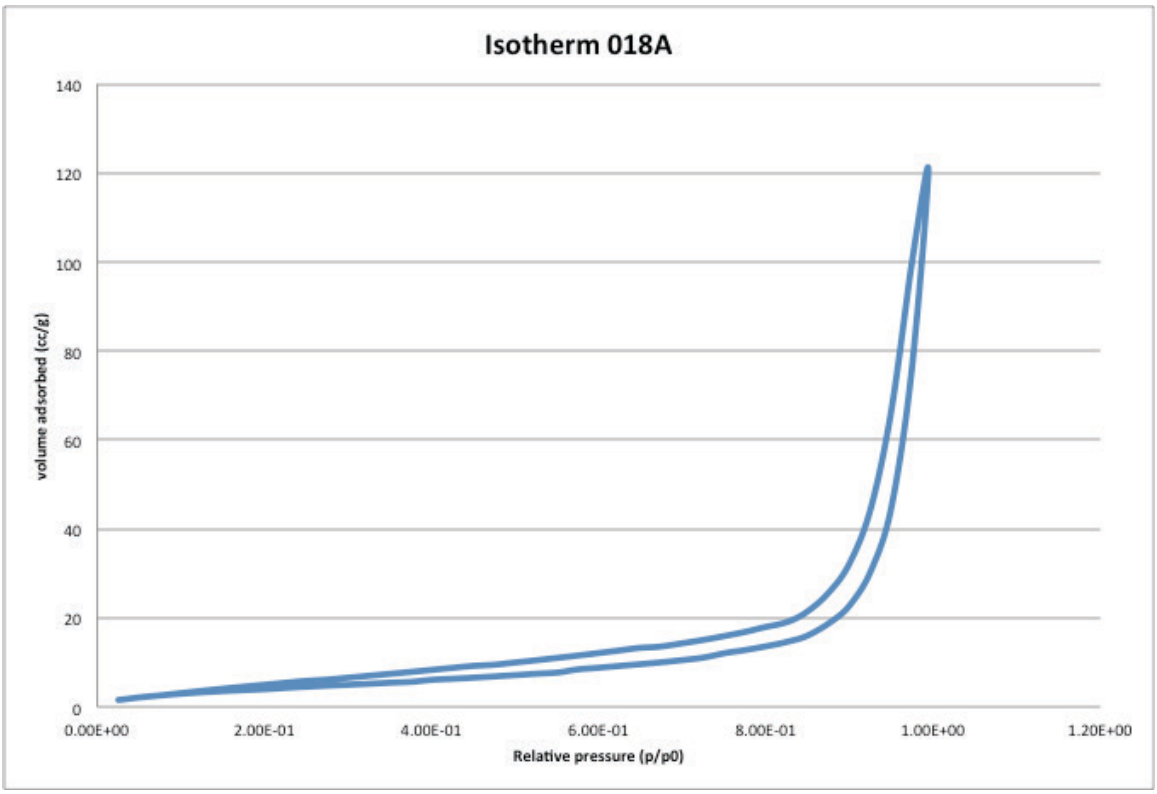

Figure 205 isotherm of sample 018A synthesized from cerium (III) nitrate hexahydrate, copper (III) hemi (pentahydrate), CTAB, water, ethanol, and sodium hydroxide, uncalcinated

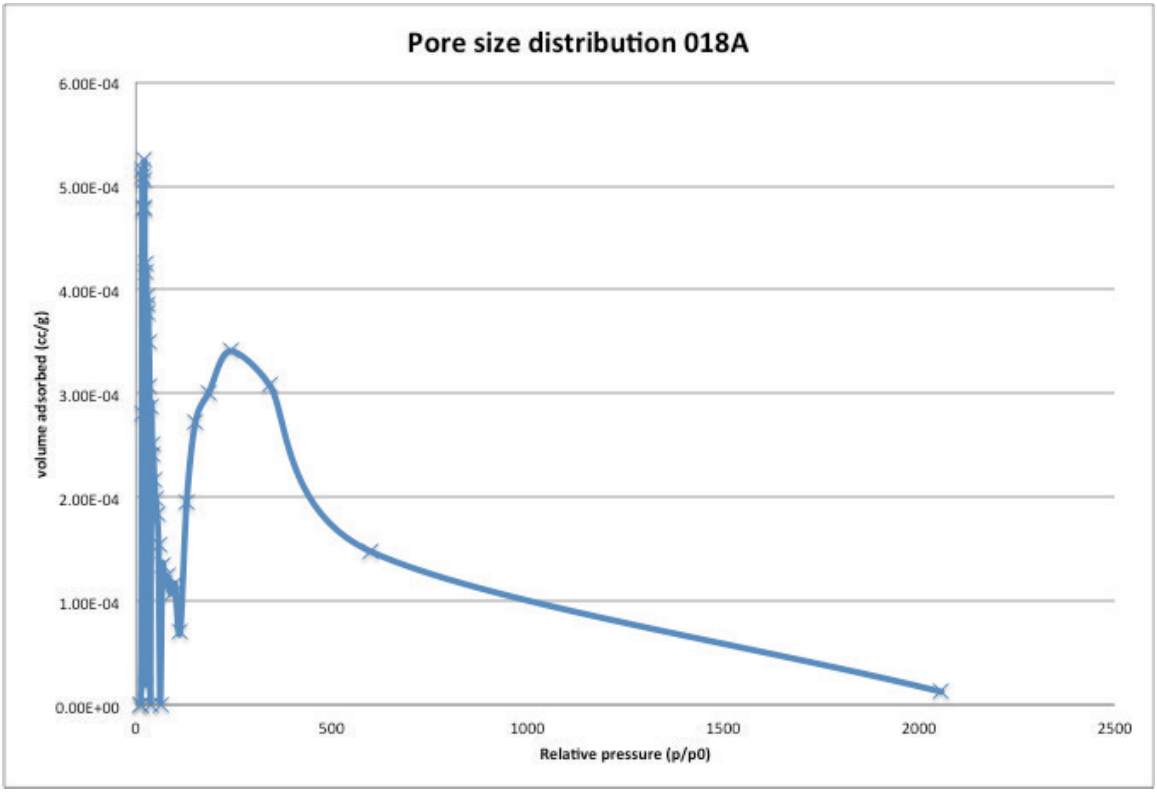

Figure 206 pore size distribution of sample 018A synthesized from cerium (III) nitrate hexahydrate, copper (III) hemi (pentahydrate), CTAB, water, ethanol, and sodium hydroxide, uncalcinated

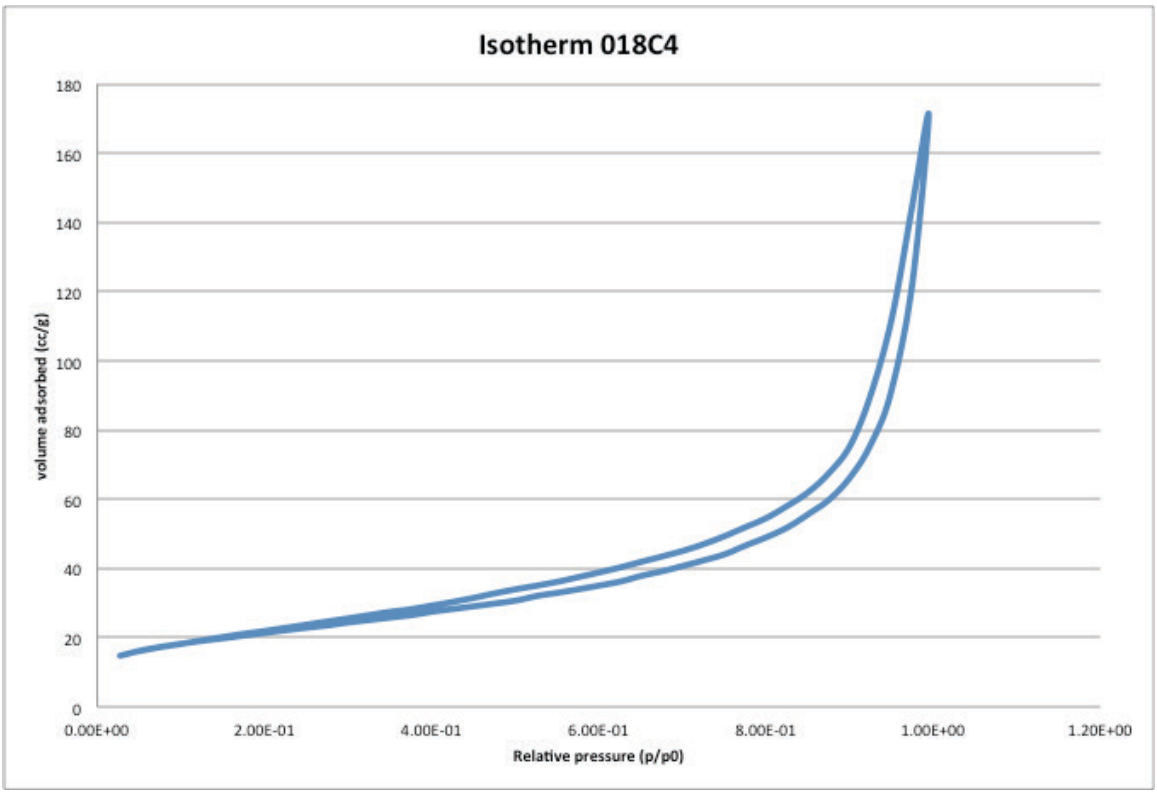

Figure 207 isotherm of sample 018C4 synthesized from cerium (III) nitrate hexahydrate, copper (III) hemi (pentahydrate), CTAB, water, ethanol, and sodium hydroxide, calcinated at 673K

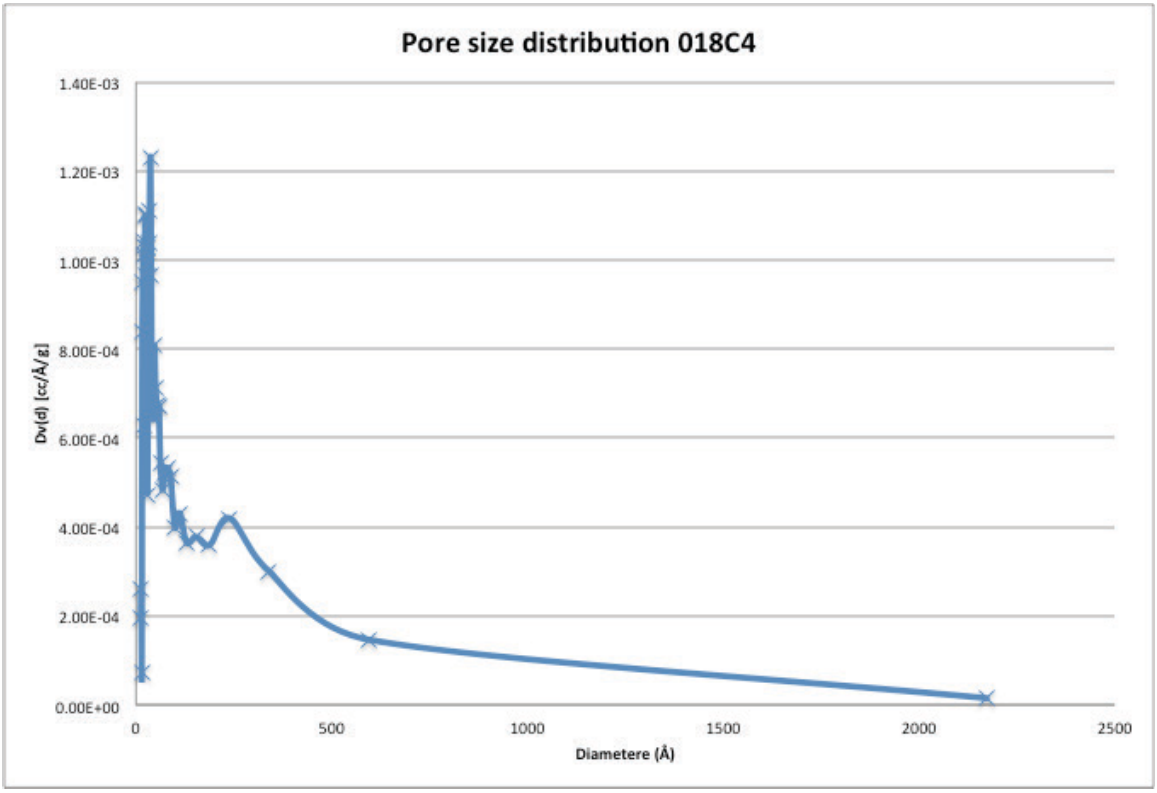

Figure 208 pore size distribution of sample 018C4 synthesized from cerium (III) nitrate hexahydrate, copper (III) hemi (pentahydrate), CTAB, water, ethanol, and sodium hydroxide, calcinated at 673K

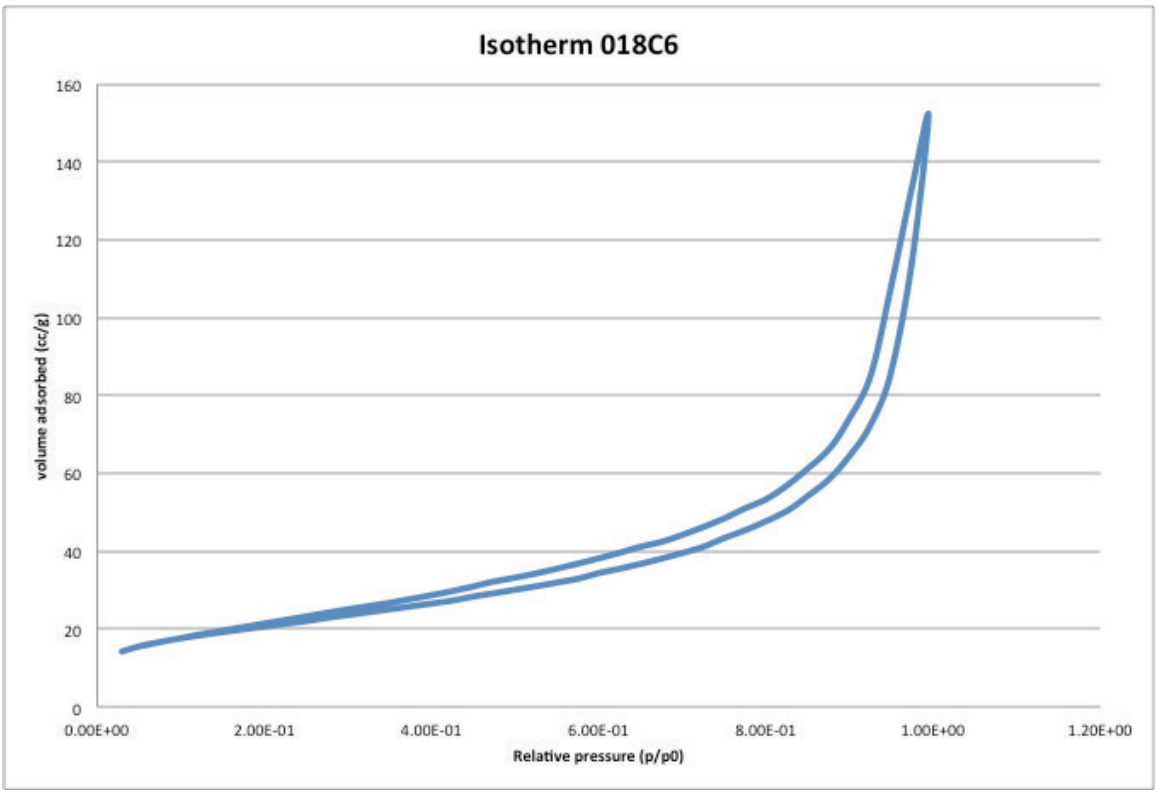

Figure 209 isotherm of sample 018C6 synthesized from cerium (III) nitrate hexahydrate, copper (III) hemi (pentahydrate), CTAB, water, ethanol, and sodium hydroxide, calcinated at 873K

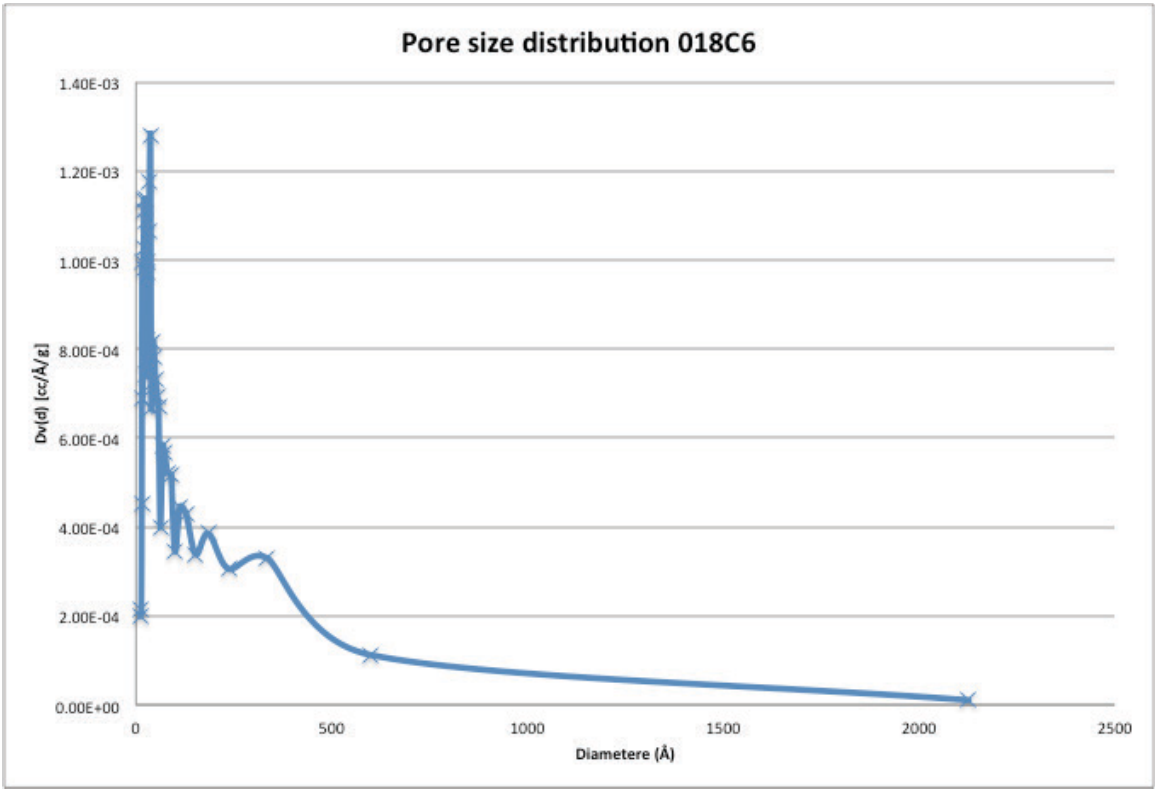

Figure 210 pore size distribution of sample 018C6 synthesized from cerium (III) nitrate hexahydrate, copper (III) hemi (pentahydrate), CTAB, water, ethanol, and sodium hydroxide, calcinated at 873K

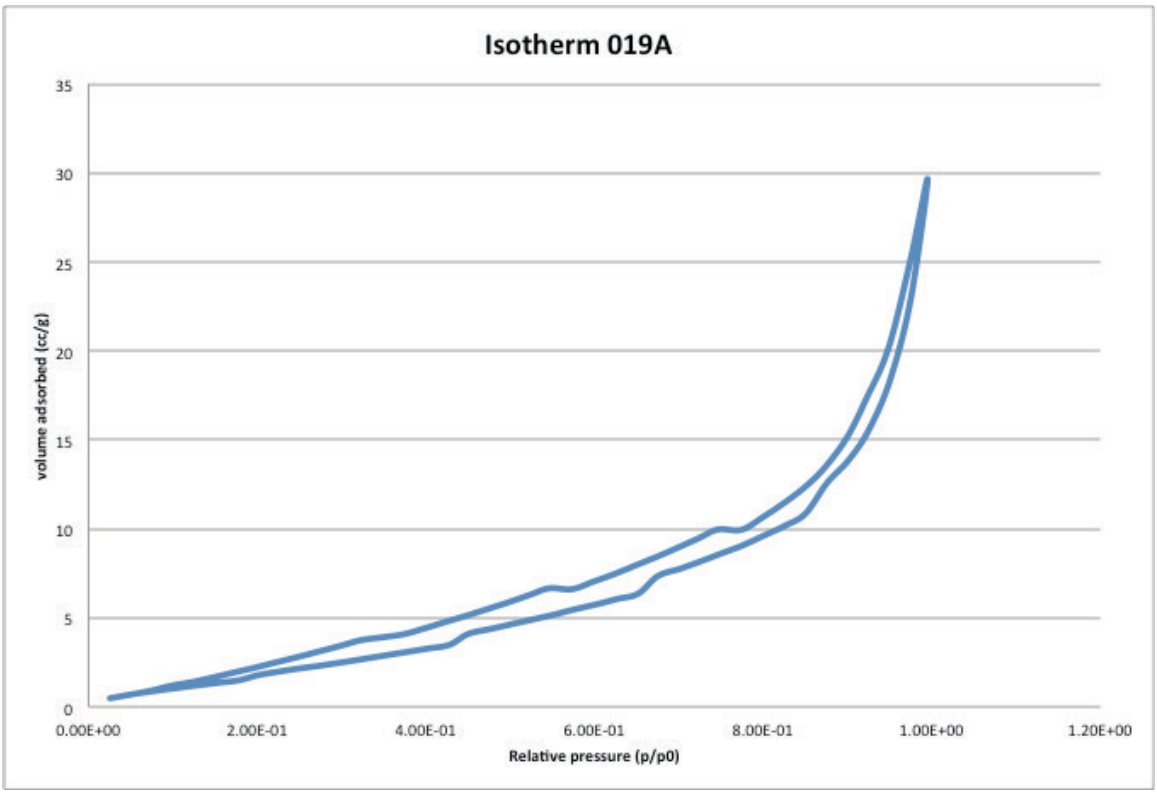

Figure 211 isotherm of sample 019A synthesized from cerium (III) nitrate hexahydrate, copper (III) hemi (pentahydrate), CTAB, water, ethanol, and sodium hydroxide, uncalcinated

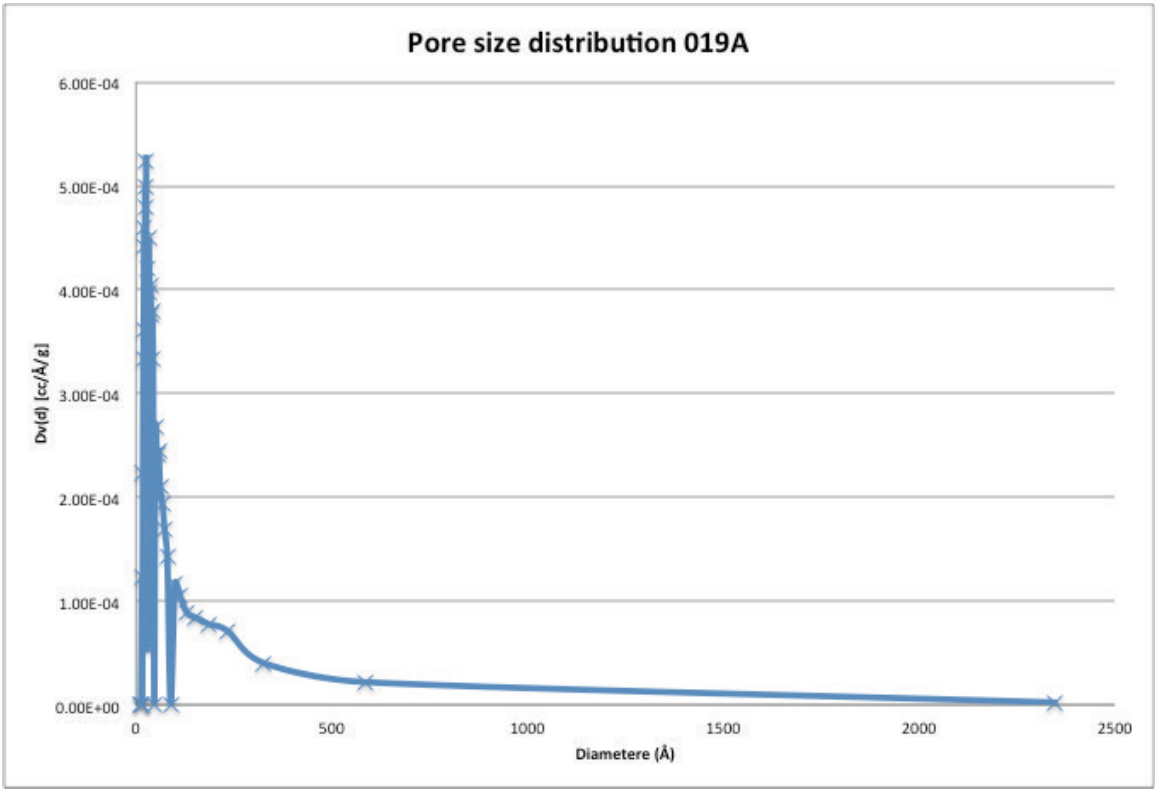

Figure 212 pore size distribution of sample 019A synthesized from cerium (III) nitrate hexahydrate, copper (III) hemi (pentahydrate), CTAB, water, ethanol, and sodium hydroxide, uncalcinated

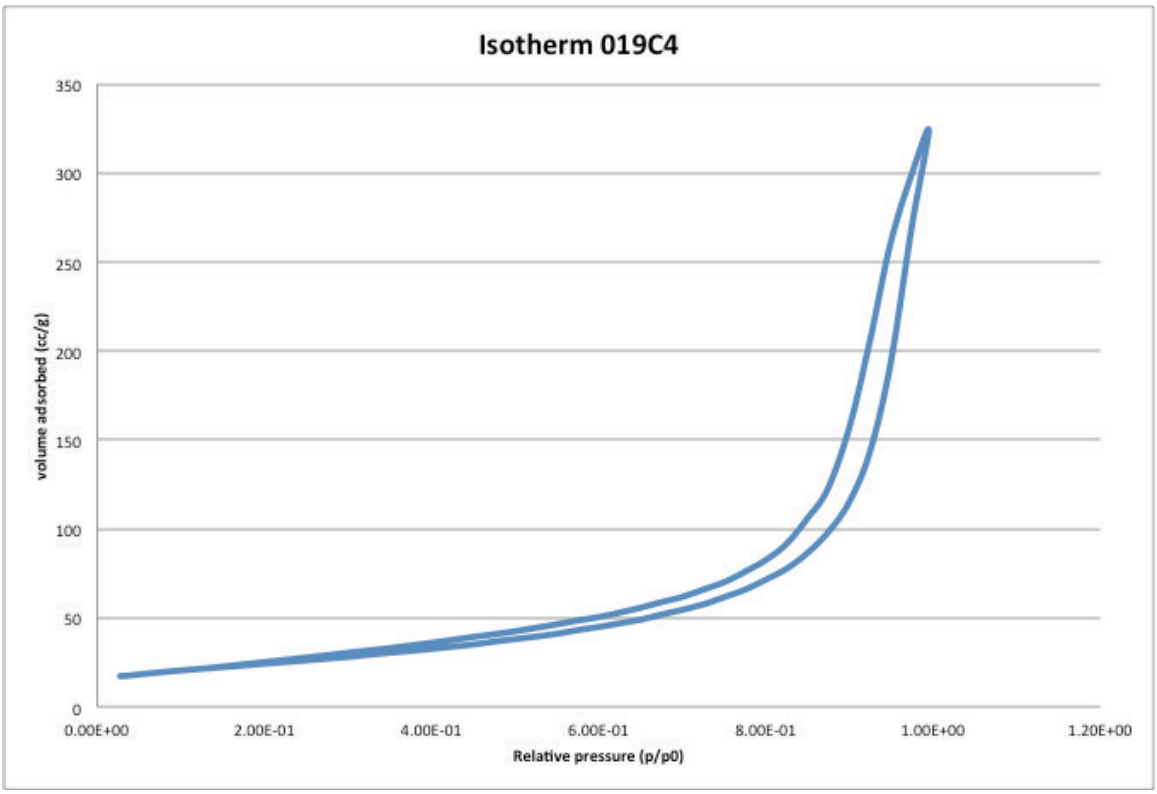

Figure 213 isotherm of sample 019C4 synthesized from cerium (III) nitrate hexahydrate, copper (III) hemi (pentahydrate), CTAB, water, ethanol, and sodium hydroxide, calcinated at 673K

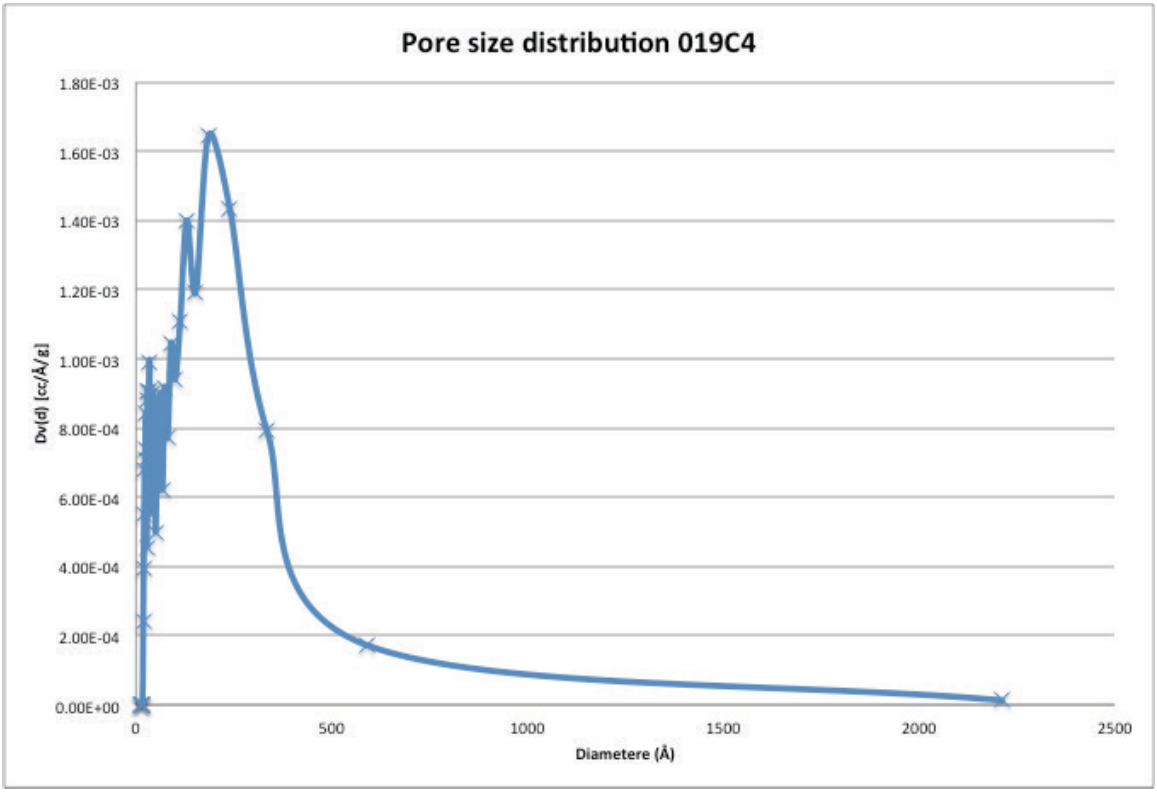

Figure 214 pore size distribution of sample 019C4 synthesized from cerium (III) nitrate hexahydrate, copper (III) hemi (pentahydrate), CTAB, water, ethanol, and sodium hydroxide, calcinated at 673K

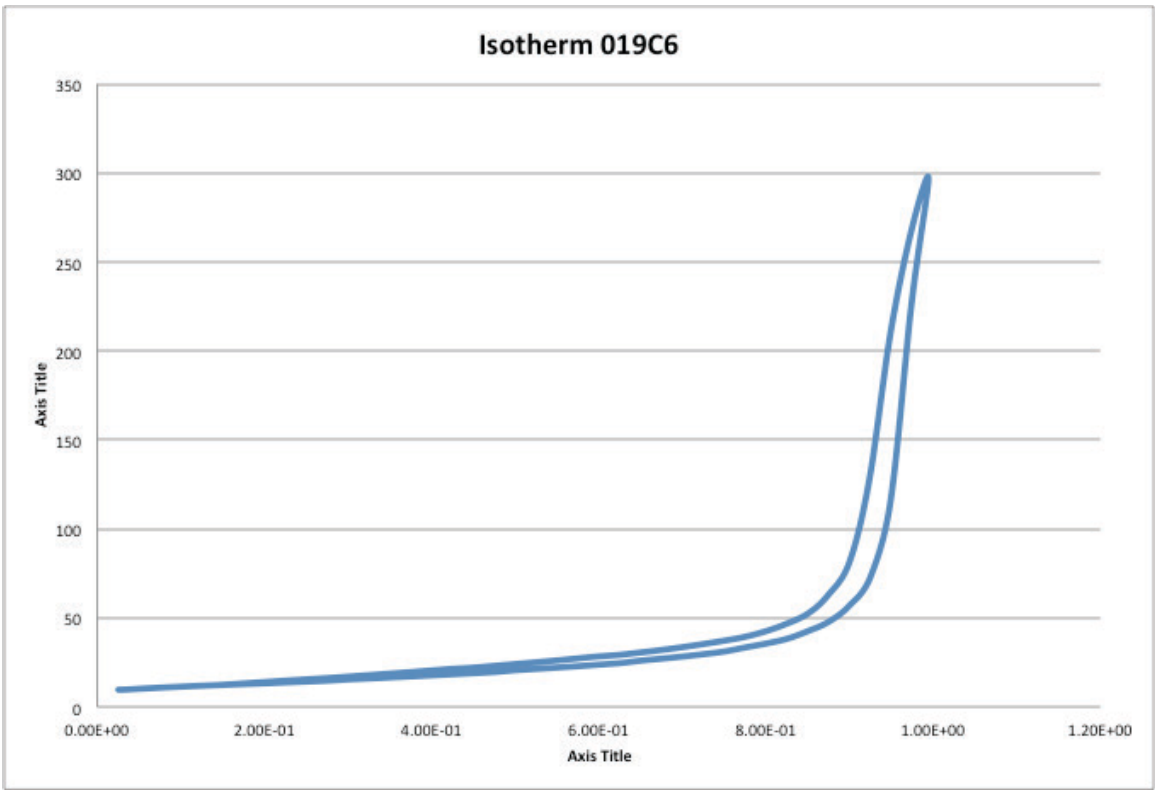

Figure 215 isotherm of sample 019C6 synthesized from cerium (III) nitrate hexahydrate, copper (III) hemi (pentahydrate), CTAB, water, ethanol, and sodium hydroxide, calcinated at 873K

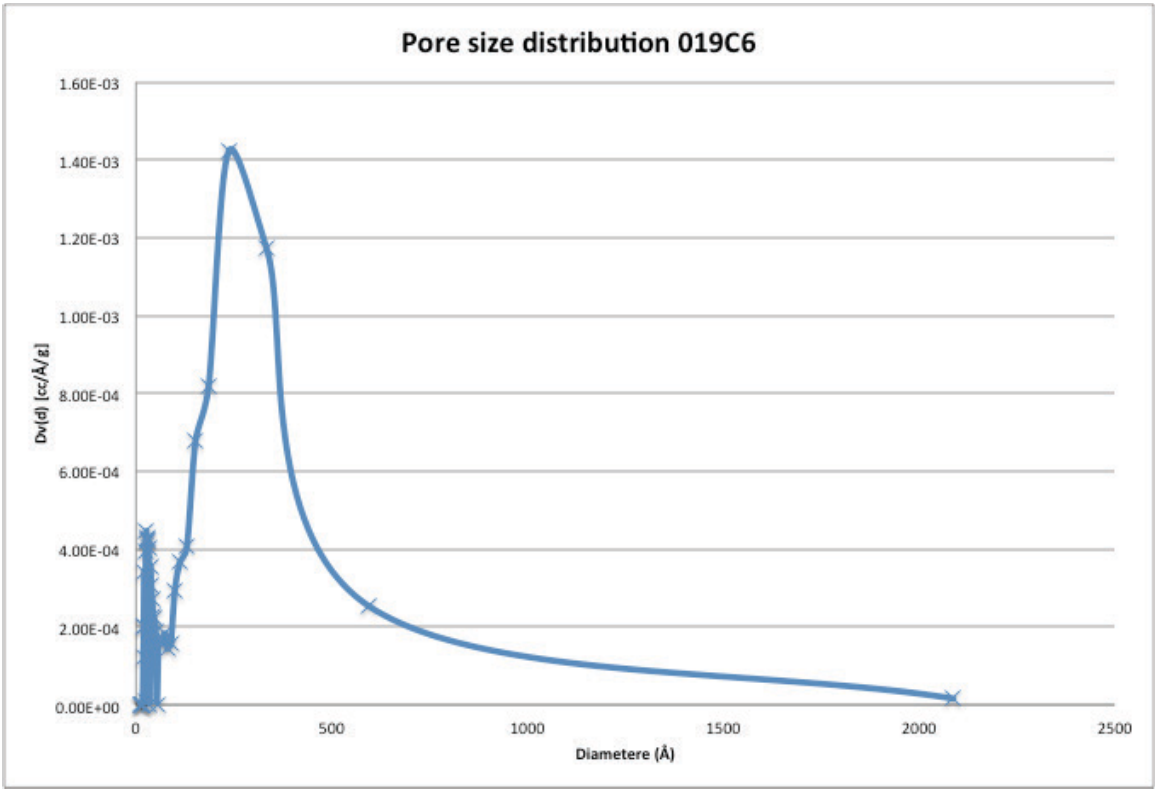

Figure 216 pore size distribution of sample 019C6 synthesized from cerium (III) nitrate hexahydrate, copper (III) hemi (pentahydrate), CTAB, water, ethanol, and sodium hydroxide, calcinated at 873K

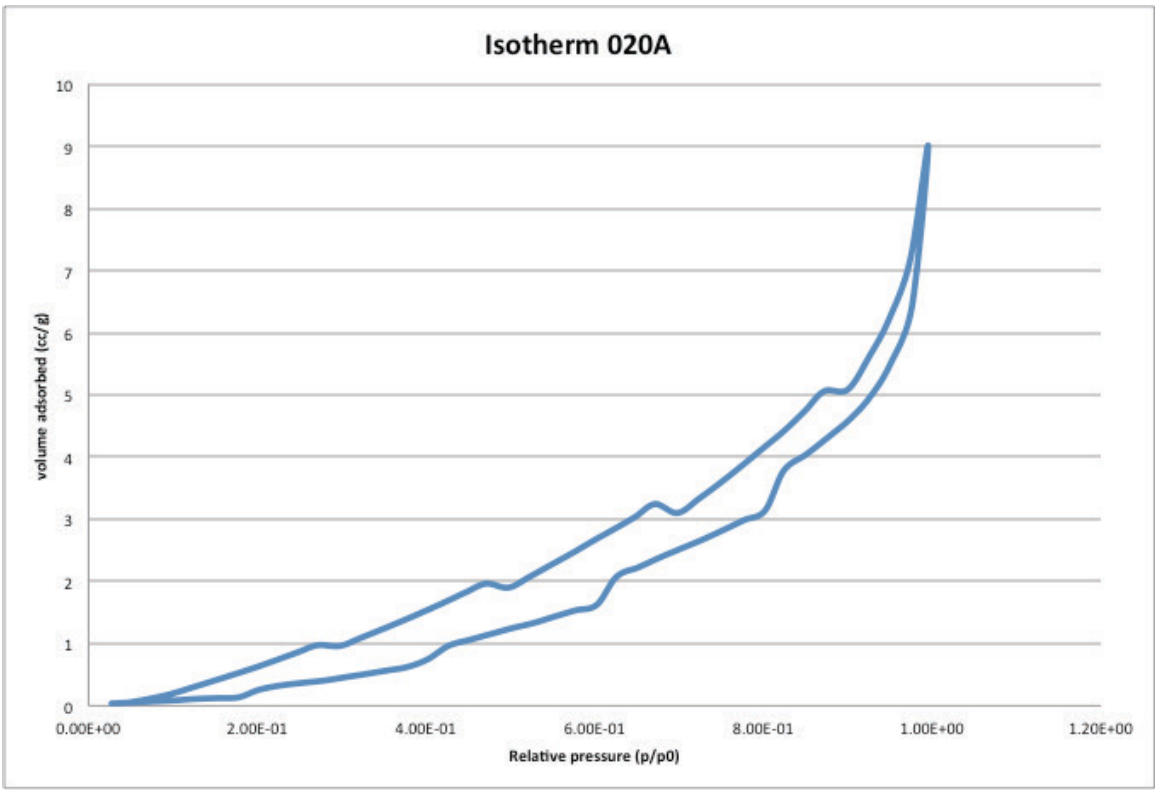

Figure 217 isotherm of sample 020A synthesized from cerium (III) nitrate hexahydrate, samarium (III) nitrate hexahydrate, CTAB, water, ethanol, and sodium hydroxide, uncalcinated

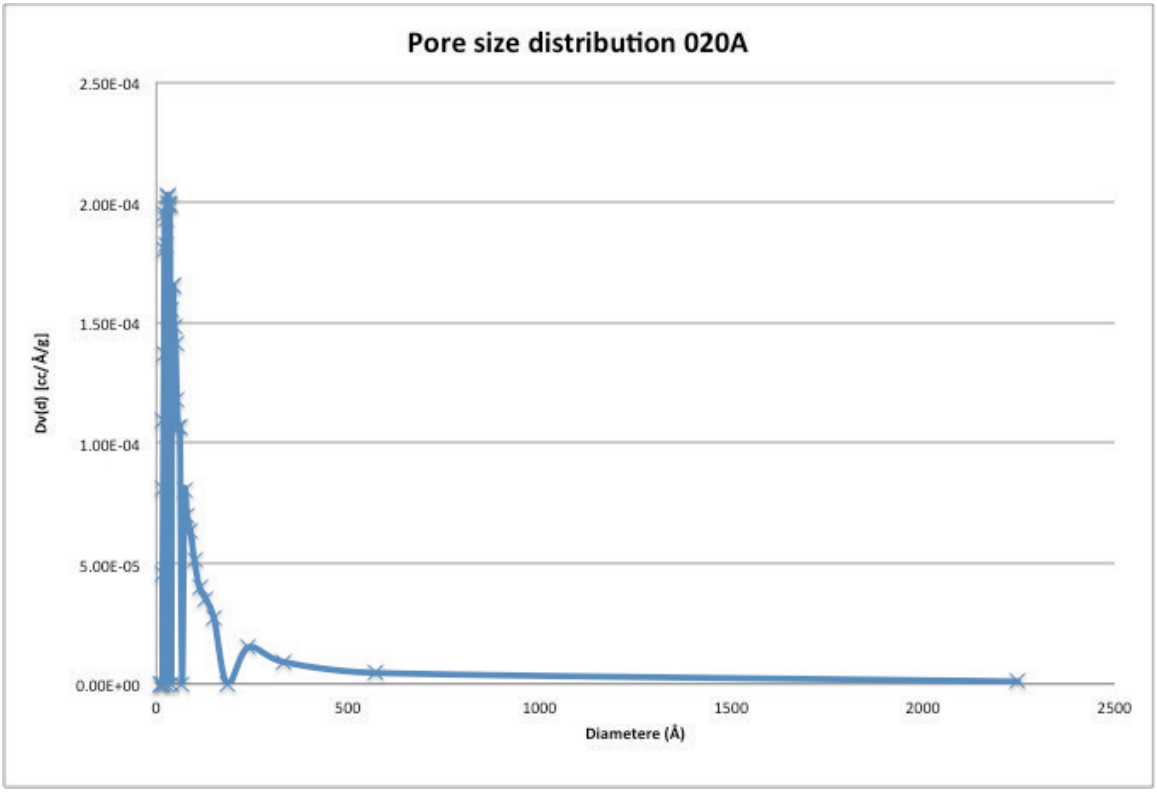

Figure 218 pore size distribution of sample 020A synthesized from cerium (III) nitrate hexahydrate, samarium (III) nitrate hexahydrate, CTAB, water, ethanol, and sodium hydroxide, uncalcinated

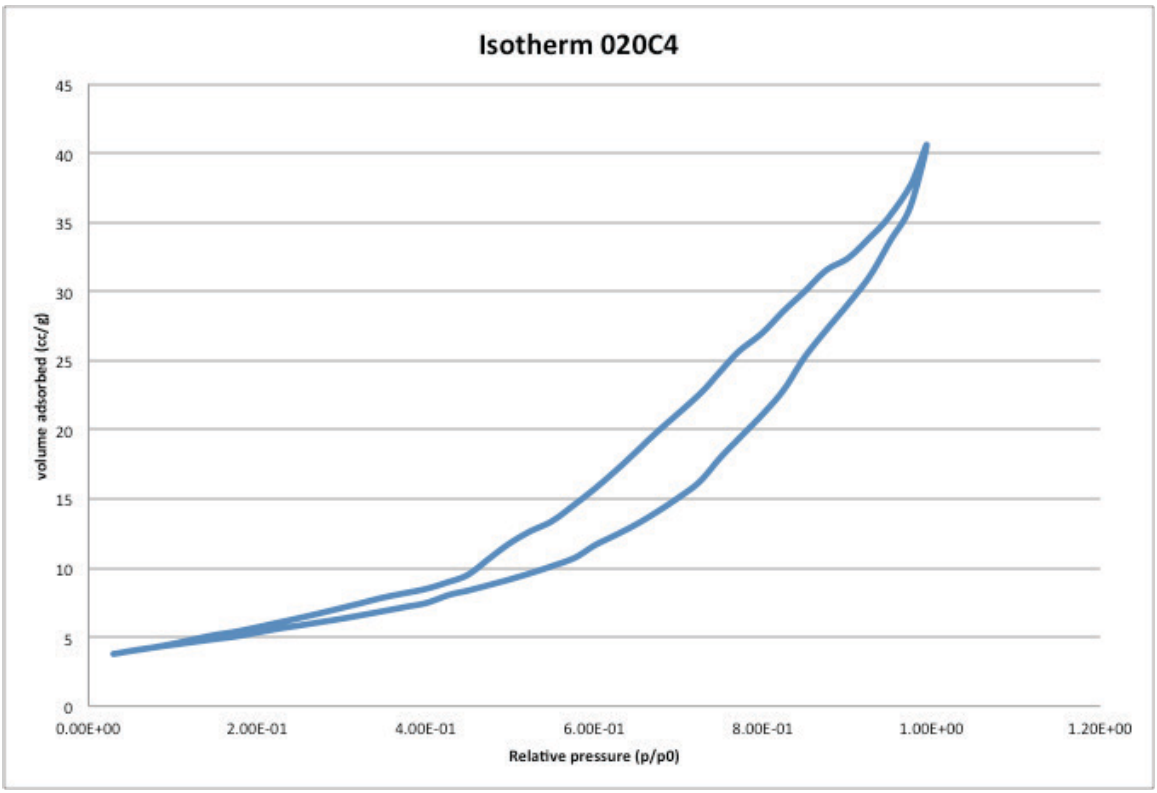

Figure 219 isotherm of sample 020C4 synthesized from cerium (III) nitrate hexahydrate, samarium (III) nitrate hexahydrate, CTAB, water, ethanol, and sodium hydroxide, calcinated at 673K

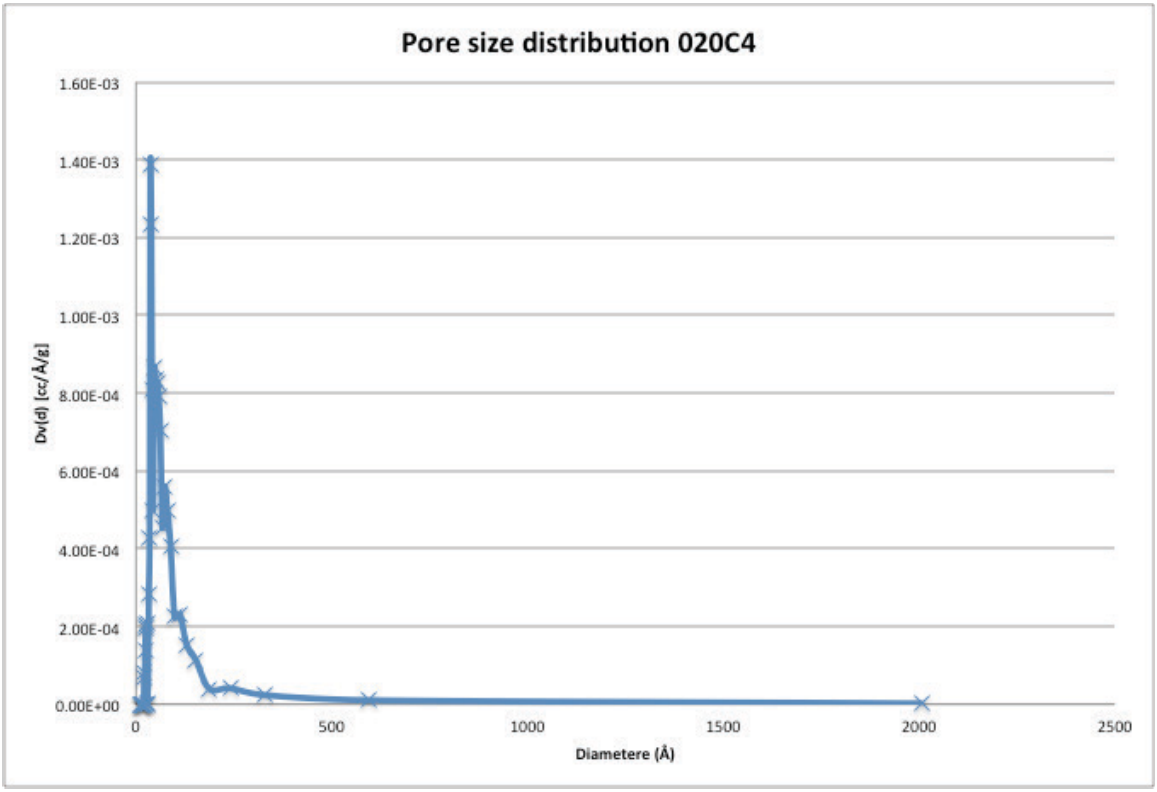

Figure 220 pore size distribution of sample 020C4 synthesized from cerium (III) nitrate hexahydrate, samarium (III) nitrate hexahydrate, CTAB, water, ethanol, and sodium hydroxide, calcinated at 673K

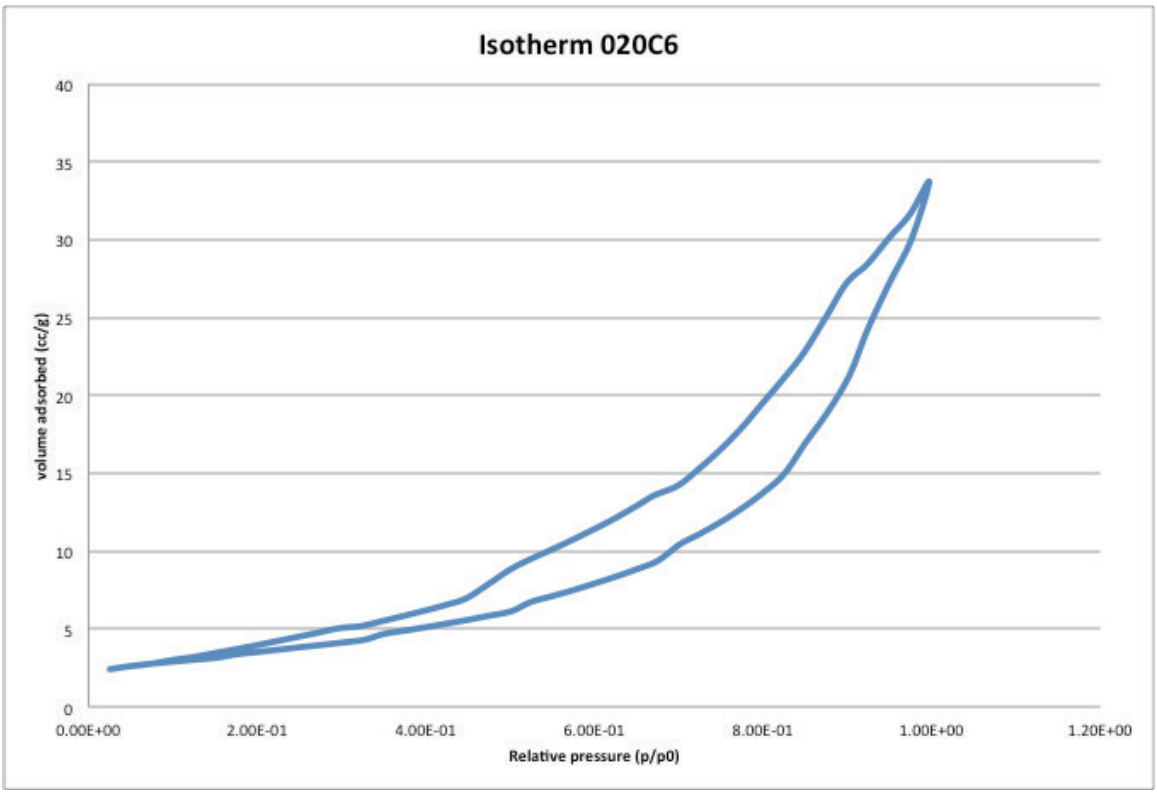

Figure 221 isotherm of sample 020C6 synthesized from cerium (III) nitrate hexahydrate, samarium (III) nitrate hexahydrate, CTAB, water, ethanol, and sodium hydroxide, calcinated at 873K

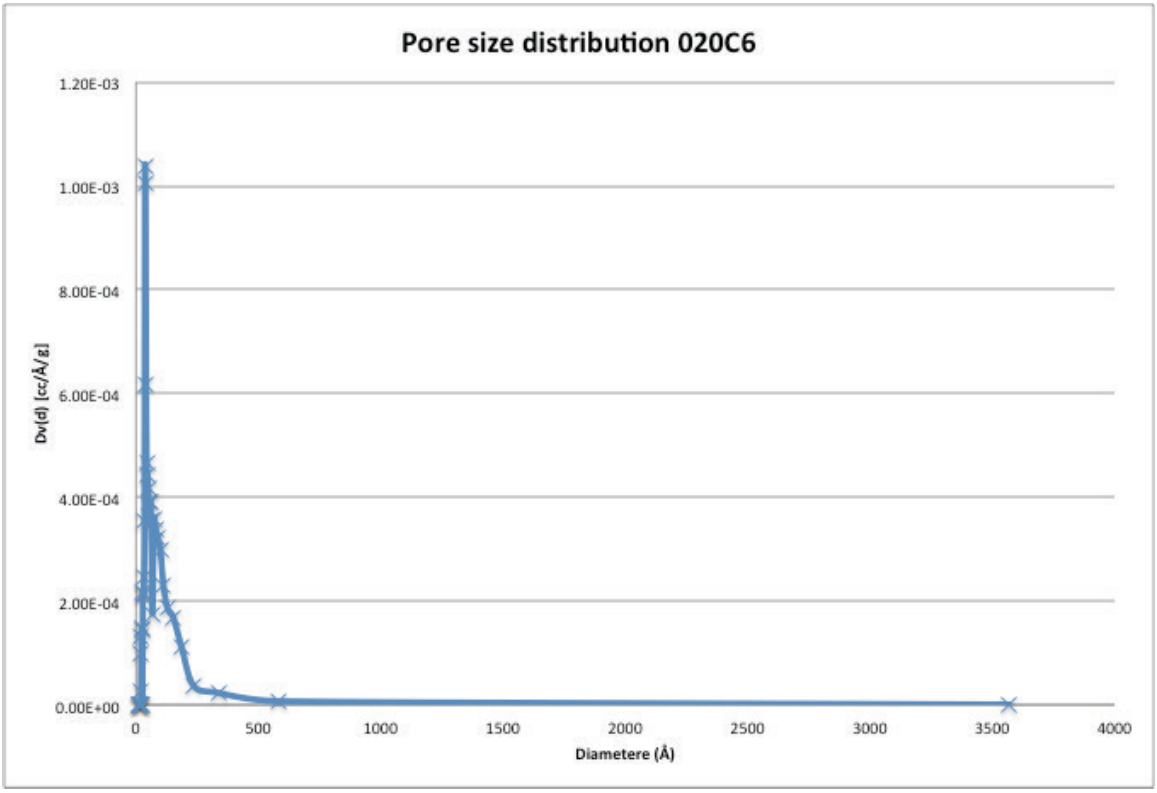

Figure 222 pore size distribution of sample 020C6 synthesized from cerium (III) nitrate hexahydrate, samarium (III) nitrate hexahydrate, CTAB, water, ethanol, and sodium hydroxide, calcinated at 873K